Spectroscopic and Theoretical Studies of Lytic Polysaccharide Monooxygenases

Alessandro Paradisi

PhD

University of York

Chemistry

June 2020

Abstract

Lytic polysaccharide monooxygenases (LPMOs) are monometallic copper enzymes able to depolymerize polysaccharides through an oxidative mechanism, using O_2 or H_2O_2 as co-substrates, involving hydroxylation at the C1 or C4 carbon of the polysaccharide chain and leading to subsequent cleavage of the glycosidic bond. In this work we present a multi-spectroscopic and theoretical study of the enzyme/substrate complex, using an LPMO from the auxiliary activity (AA) family 9 and cellohexaose as substrate. We were able to characterize the active site electronic structure in which the Cu ligand environment forces the Cu(II) semi occupied molecular orbital (SOMO) in a particular orientation which allows the formation of a covalent bond with exogenous ligands in the equatorial plane, with potential implications for O_2 activation during catalytic turnover of the enzyme. A similar study was performed also with an AA11 LPMO that showed a very similar active site electronic structure as compared to the AA9 LPMO and therefore suggesting similar O_2 reactivity with between the two families. Furthermore, when hydrogen peroxide is used as a co-substrate by LPMOs instead of O_2, the rate of reaction is high but it is accompanied by rapid inactivation of the enzymes, presumably through protein oxidation. Herein, we present a multi-spectroscopic study, augmented with mass spectrometry and density functional theory calculations, to show that the product of reaction of an AA9 LPMO with H_2O_2 at higher pHs is a singlet Cu(II)−tyrosyl radical species, which is inactive for the oxidation of polysaccharide substrates. The Cu(II)−tyrosyl radical center entails the formation of significant Cu(II)−(•OTyr) overlap, which in turn requires that the plane of the SOMO of the Cu(II) is orientated toward the tyrosyl radical. We propose from the Marcus cross-relation that the active site tyrosine is part of a “hole-hopping” charge-transfer mechanism formed of a pathway of conserved tyrosine and tryptophan residues, which can protect the protein active site from inactivation during uncoupled turnover.

List of contents

List of figures

List of tables

Acknowledgments

This thesis is the end of a long journey that has been rewarding and challenging from both a personal and scientific point of view. During these years in York, I met fantastic people and friends and surely, I have learned much more than I could have ever imagined at the beginning. This is definitely an experience that I will remember for the rest of my life.

I would like to say thank you to my supervisors Paul Walton and Gideon Davies who gave me this wonderful scientific opportunity. I would like to thank them for their input and suggestions in this work, but also for giving me the space to test my own ideas and hypothesis. A special mention goes to Paul, for having motivated and inspired my scientific thinking during these years and for the 'endless' scientific discussions between us and the rest of the group. I have enjoyed them a lot!

I would also like to thank Peter Karadakov for his encouragement and suggestions throughout the development of this project. A sincere thank you goes also to Mrs Lesley Wild for having kindly donated a PhD scholarship to the University and allowing me to move and study in York. None of this would have been possible without her help.

A great thank you also goes to Luisa for the all help and support inside and outside the 'lab' during these years and, most importantly, for being a sincere friend. I will always be grateful. Thanks also to all the fantastic friends I made here, Martin, Peter, Will, Nina, George, Ben, Lewis, Daniel, Esther, Monika, Claire and Saioa. You are the people that defined my time here in York and your friendship and support means a lot to me.

Thanks to my parents, Franco and Patrizia and to my brother Simone, for having encouraged me to take on this challenge from the beginning and for the constant support along the way. Finally, a special thank you also goes to Valentina, whose support, help and patience have been really significant for me during these years.

Author's declaration

The work presented in this thesis has been carried out by the author, unless otherwise stated in the text. I declare that this thesis is a presentation of original work and I am the sole author. This work has not previously been presented for an award at this, or any other, University. All sources are acknowledged in the **Bibliography** section.

The data presented in **Chapter 3** were published in the following paper:

Paradisi *et al*., *J. Am. Chem. Soc.* 2019, 141, 46, 18585–18599

Work carried out by other persons:

- The *Ls*AA9 LPMO was produced and purified by Novozyme A/S
- The EPR spectra presented in **Chapter 2** were collected by Dr. Luisa Ciano. The simulations of these spectra were carried out by Dr. Luisa Ciano
- The purple species formation kinetics and the resonance Raman spectra in **Chapter 3** were collected by Dr. Esther Johnston
- X-ray absorption spectra in **Chapter 3** were collected under the guidance of Dr. Esther Johnston and Dr. Gianantonio Cibin, at Diamond Light Source
- MCD spectra were collected under the guidance of Dr. Esther Johnston and Prof. Jonathan McMaster, at University of Nottingham
- The LC-MS/MS data presented in **Chapter 3** were performed and analysed by Dr. Adam Dowle, at University of York Technology Facility

1. Introduction

1.1 The potential of biomass for renewable biofuels

Lignocellulosic biomass represents an abundant carbon-neutral renewable resource for the production of mixed sugars which can then be fermented through to biofuels and other biomaterials. Indeed, given the scale of lignocellulosic biomass, its use as a commodity feedstock has long been recognized as a key element in any future sustainable low carbon economy. Renewable energy, obtained from carbon neutral sources, is an important factor for long-term sustainability and to slow-down the impact of climate change.[1] Today, the energy derived from biomass accounts for around 10% of the global energy demand (mostly in form of biofuel) and is expected to grow further in prominent low-carbon scenarios.[1,2] Moreover, the use of lignocellulosic biomass as an energy source also avoids the direct fuel-*versus*-food competition that occurs when corn and sugarcane feedstock are used for production of fuels and biochemicals in biorefineries (which define the so called first generation biofuels).[3,4] As such, the scientific and economical challenge is to shift the energy source to second generation biofuels derived from dedicated energy (non-food) crops or agricultural, forestry and food waste material (for example it is estimated that 30–40% of the food is wasted globally).[5,6] These sources are typically lignocellulosic biomass that, from a chemical point of view, is composed of cellulose, hemicellulose, chitin and lignin.

Despite its promise, the exploitation of lignocellulosic biomass still faces substantial technological challenges to achieve financial viability on a large industrial scale.[7] One of the biggest issues in harnessing the sugars contained in lignocellulose is overcoming its high recalcitrance of cellulose to chemical or enzymatic deconstruction. Plants have evolved complex structural and chemical mechanism to resists attacks to their structural sugars from the microbial, fungal and animal kingdom. One of these factors is cellulose's high level of crystallinity due to an extensive network of hydrogen bonds between the polysaccharide chains, which makes it resistant to acid and enzymatic hydrolysis (see **Figure 1.2** below).[3]

A typical biorefinery comprises of four major sequential processes: feedstock harvest and storage, thermochemical pretreatment, enzymatic hydrolysis, and finally sugar fermentation to bioethanol (or the use of these sugars for other chemical transformations). In the first step the biomass is pretreated by chemical, physical and/or mechanical methods to make the recalcitrant material more accessible to the enzymes.[2] Then, the pretreated biomass undergoes enzymatic hydrolysis and depolymerisation using a combination of many different enzymes (including glycoside hydrolases (GHs) and auxiliary activity enzymes (AA)), which are able to produce sugar monosaccharides. Because of the heterogeneity of the starting biomass from a chemical point of view, a diverse range of enzymes with different sugar specificities is required to achieve a high level of depolymerisation of the starting material.[5] These enzymatic mixtures are often called enzymatic cocktails when they are used in industrial applications. These cocktails, which have commercial names like Celluctast (Novozymes), Spezyme CP (DuPont), C1184 (Sigma-Aldrich), *etc.* are mainly composed by enzymes produced by the filamentous fungi *Aspergillus nidulans*, *Aspergillus niger*, *Penicillium* spp. and *Trichoderma reesei*.[2] In the last step, the saccharides are fermented into ethanol by microorganisms, typically yeasts or bacteria, or used in other chemical processes for the synthesis of carbohydrate based products. The polysaccharide degradation and fermentation processes can be performed separately (called separate hydrolysis and fermentation) or simultaneously (called simultaneous saccharification and fermentation).[2,5]

In the past, a plethora of enzymes capable of degrading cellulose, hemicellulose and lignin have been biochemically characterized, however, new ones are continuously being discovered from different sources. It is without doubt a very active field of scientific research and the focus is now on obtaining enzymes that can perform efficient biocatalysis to produce biofuels in an industrial setting. Properties of the enzymes, such as broad specificity and/or thermo-stability, are important characteristics when considering potential applications.[5]

1.2 The structure of lignocellulose biomass

The plant cell wall is a complex matrix of diverse polymers, which surrounds the plant cell and serves to provide structural rigidity and pathogen defence to the plant. The plant cell walls are the major sources of carbohydrates in lignocellulosic biomass. In fact, the this matrix is mainly composed of polysaccharides like cellulose, a β-1,4-linked glucose polymer arranged in a crystalline fashion; hemicellulose, a predominantly β-1,4-linked polymer formed from arabinose, galactose, glucose, xylose and mannose, with exact composition varying depending on the plant source; pectin a family of complex polysaccharides containing β-1,4-linked galacturonic acid, and lignin which, rather than being a polysaccharide, is comprised of three phenolic compounds p-coumaryl alcohol, coniferyl alcohol and sinapyl alchohol – cross-linked together to form a highly complex and poly-aromatic structure.[8]

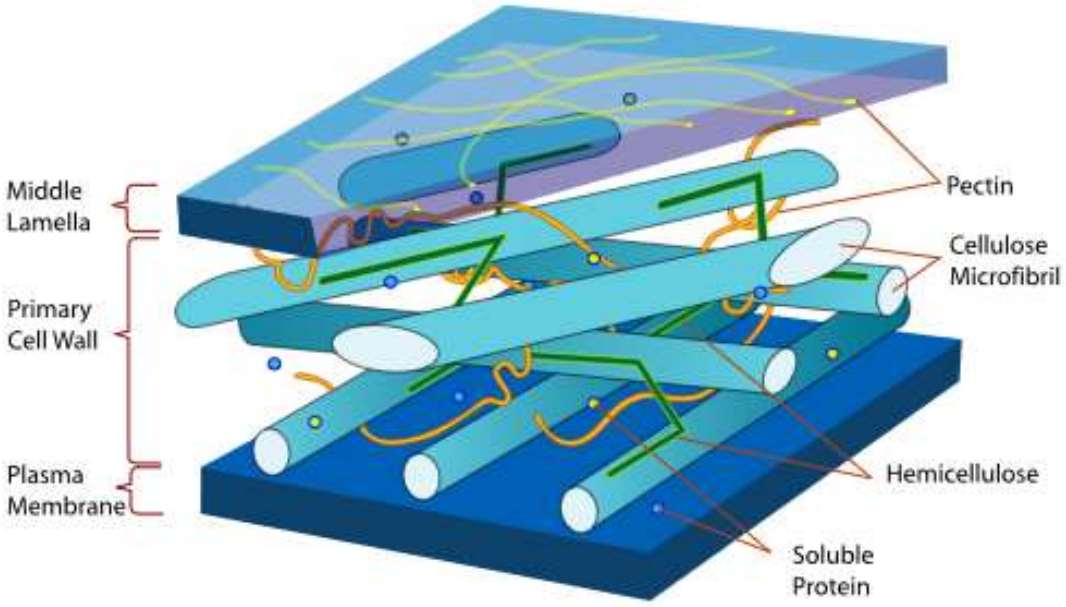

Figure 1.1 Scheme of a plant cell wall structure, showing cellulose microfibrils linked with hemicellulose and pectin. Lignin penetrates the spaces in the cell wall between cellulose, hemicellulose and pectin components, driving out water and strengthening the wall. The plasma membrane is the membrane of the plant cell, while the middle lamella, a layer rich in pectin, forms the interface between adjacent plant cells. Image free for public use from www.wikimedia.org.

During its growth, the plant cell primary wall, is mainly constituted of hemicellulose and pectin, with small amounts of cellulose and lignin, but when the cell has reached its final shape and size the cell wall becomes thinker and its composition changes to primary cellulose, xylan and lignin. In general, a primary cell wall is constituted by polysaccharides surrounded by water (60–70% in mass, **Figure 1.1**). The water content also depends on the amount of lignin present because of the hydrophobic nature of the aromatic polymer. The exact composition in terms of polysaccharides of the cell walls varies per major plant types; therefore, in industrial applications the optimal composition of the enzymatic cocktails for biomass degradation varies according to the source of the biomass.[9,10]

1.2.1 Cellulose

Cellulose is a polymer of *β*-1,4-linked *β*-D-glucose monomers and it is the major structural components of plant cell (**Figure 1.2**). It is the most stable and abundant polysaccharide in Nature and is produced in plants and bacteria by the cellulose synthase enzyme. From a molecular perspective, the O–glycosidic bonds in *β*-1,4-linked polysaccharides are readily hydrolysed in the presence of acids or glycosidases, but the rate of un-catalyzed hydrolysis of a glycoside bond in water is very slow ($k \sim 10^{-14}/10^{-15}$ s^{-1} at 25 °C).[11] An important study by Wolfenden *et al*. estimated that the un-catalyzed half-life of O–glycosidic linkages such as those found in cellulose, chitin and other polysaccharides are 2 and 4 orders of magnitude more stable than DNA or peptide bonds, respectively, with an half-life of 5 million years at neutral pH.[11] Moreover, cellulose chains are tightly packed in microfibrils, characterized by ordered crystalline regions, interspersed with smaller and less organized amorphous regions. In these crystalline lattices only a fraction of the polysaccharide chains are accessible to enzymatic attack on the microfibril surface.

Various crystalline forms (or polymorphs) of cellulose have been identified, which differ in chain orientation, arrangement and hydrogen-bonding patterns. Natural systems produce cellulose I which, in turn, is divided in two different polymorphs called cellulose Iα (found in algae and bacteria) and cellulose Iβ (found in higher plants). Small differences in interlayer chain stacking and in hydrogen bonding patterns differentiate the

two forms (**Figure 1.2**) however, in both forms the hydrogen bonds only exist within single layers with no inter-sheet hydrogen bonds.[12]

Chemical treatments with alkali (like sodium hydroxide) and ionic liquids convert cellulose I into other polymorphs characterized by a structure with antiparallel chains and inter-sheet hydrogen bonding, called cellulose II.[13] Treatment of cellulose I and II with anhydrous ammonia results in cellulose III_I and III_{II}, respectively. cellulose III is the result of ammonia-induced swelling of the crystal to a metastable phase that returns to cellulose I upon heating.[14] Amorphous cellulose, with a low degree of crystallinity, is usually produced by dissolution of cellulose in phosphoric acid and subsequent extensive washing with water. The resulting phosphoric acid swollen cellulose (PASC), is a model substrate for characterization of cellulase enzymes, active on cellulose as substrate.[15]

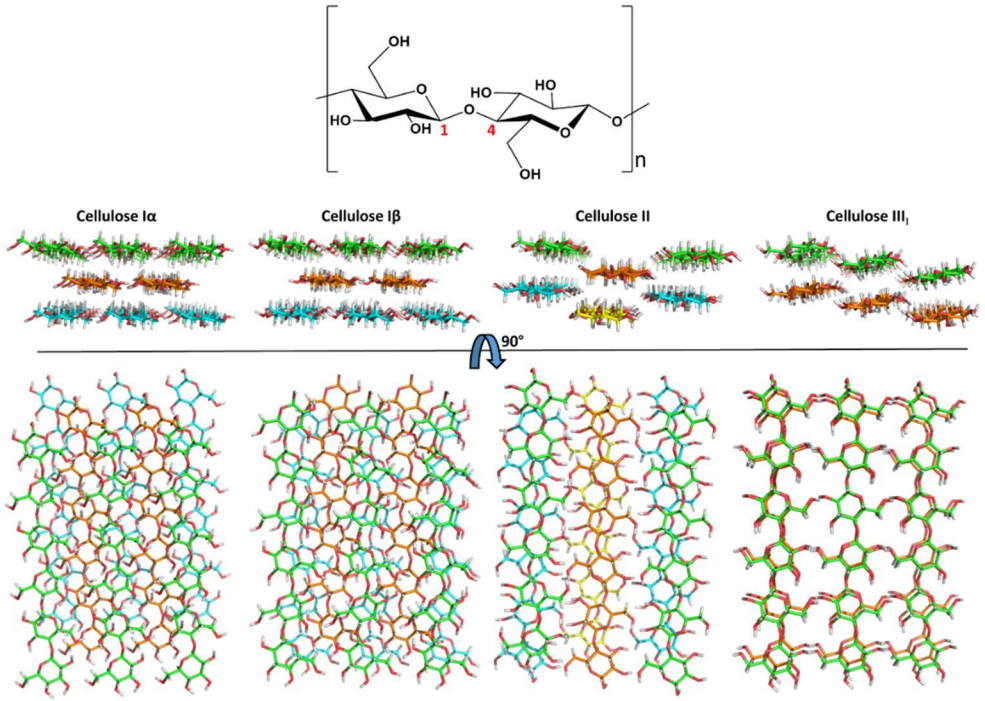

Figure 1.2 Molecular structure of cellulose with the repeating structural unit cellobiose indicated in brackets. Position 1 and 4 of the glucose ring are indicated with red labels (top). Structures of cellulose Iα, cellulose Iβ, cellulose II and cellulose III_I (bottom). The crystal structures were generated with Cellulose-Builder.[16]

1.2.2 Hemicelluloses

Hemicelluloses are the second most abundant component of the plant cell wall, after cellulose. These polysaccharides have a *β*-1,4-linked backbones with an all equatorial configuration, and include xylans, mannans and glucomannans and *β*-1,3-1,4-linked glucans (**Figure 1.3**). These backbones can be decorated with other sugars along the chain generating a wide variety of different structures. For example, in xylans the backbone constituted of xylose monomers, singly (*α*-1,2 or *α*-1,3) or doubly (*α*-1,2–1,3) substituted with glucuronic acids, methyl-glucuronic acids, arabinofuranose and acetil groups; in mannans, a portion of the mannose units is branched with *α*-1,6-galactopyranose units.[17] The precise structure of hemicelluloses and their abundances vary between different plant species and cell types. The most important biological role of hemicellulose is to strengthen the cell wall by interaction with cellulose. Compared to cellulose, hemicelluloses have less tendency to aggregate in compact crystalline forms, exhibiting instead a mostly amorphous structure, the degree of which depends on the type of sugars that constitute them. For a detailed discussion on hemicelluloses structures and their functional roles, the reader is referred to the excellent review by Scheller *et al.*[17]

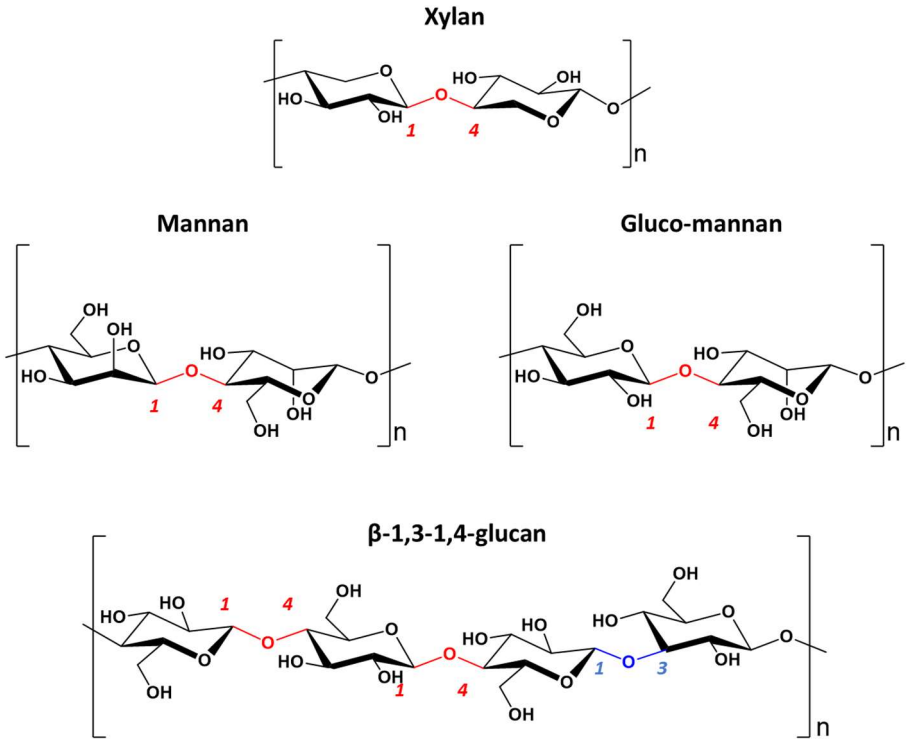

Figure 1.3 Main type of hemicelluloses backbone building blocks. The characteristic equatorial *β*-1,4 (red) and *β*-1,3 (blue) glycosidic bonds are highlighted, together with the respective labelling of the carbon atoms involved in the bonds.

1.2.3 Pectin and lignin

Pectins are a family of complex polysaccharides containing α-1,4-linked galacturonic acid, which form the chain backbone (**Figure 1.4**). The polysaccharide chain can be α-1,2 and α-1,6 substituted by a large variety of different sugars, generating complex branching patters which may even be cross-linked together through ester bonds. Pectins are found in cell walls during the cell growth and form a gel-like matrix which can be altered to allow cell elongation and providing protective barriers for the cell.[18]

Lignin is a heteropolymer constituted by various phenols monomers, mainly 4-hydroxypropanoids, which are connected by both ether and carbon–carbon bonds. The three main building blocks are *p*-cumaryl alcohol, coniferyl alcohol and sinapyl alcohol (**Figure 1.4**), that are polymerized through a free radical process, generally mediated by peroxidase enzymes, with a weight-average molecular weight of 25000 g mol^{-1}.[18] Lignin is found in plant cell walls to provide structural strength and acting as diffusion barrier; its exact composition varies between different plant species and tissues type.[19]

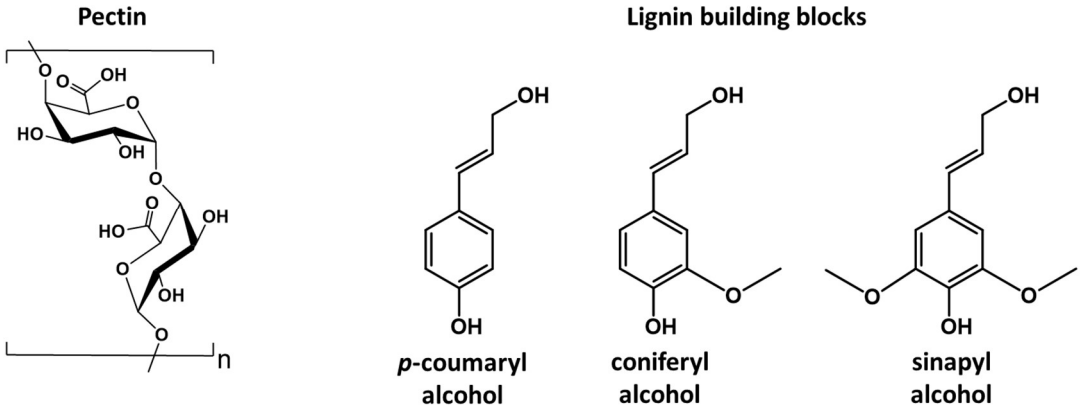

Figure 1.4 Schematic representation of pectins' backbone chain, showing two galacturonic acid molecules linked by a α-1,4 glycosidic bond (left). Structures of the three major lignin monomers (right).

1.2.4 Chitin

Chitin is an abundant polysaccharide constituted by *β*-1,4-linked *N*-acetilglucosamine monomers and is found in the cell walls of fungi, egg shells and the exoskeleton of arthropods (including crustaceans, insects, and arachnids).[20] Chitin is not strictly classified as part of the *lignocellulosic* biomass, as it not found in plant cell walls. However, it is a polysaccharide closely related to cellulose with which it shares many features. The *N*-acetylglucosamine chains form tightly packed crystalline structures, held together by many interchain hydrogen bond interactions (**Figure 1.5**). In Nature, chitin can be find in three different crystal structures *α*, *β* and *γ* forms, which differ in the orientation of the chains and the degree of hydration.[20] In *α*-chitin the chains are arranged in an antiparallel orientation with respect to each other, resulting in tight packing, while in *β*-chitin they are arranged in a parallel orientation; γ-chitin, instead, features both parallel and antiparallel oriented chains. Because of their structure, *β* and *γ*-chitin are more hydrated than *α*-chitin, resulting in a softer and more flexible structure, hence somewhat more accessible to enzymes and therefore enzymatic degradation.

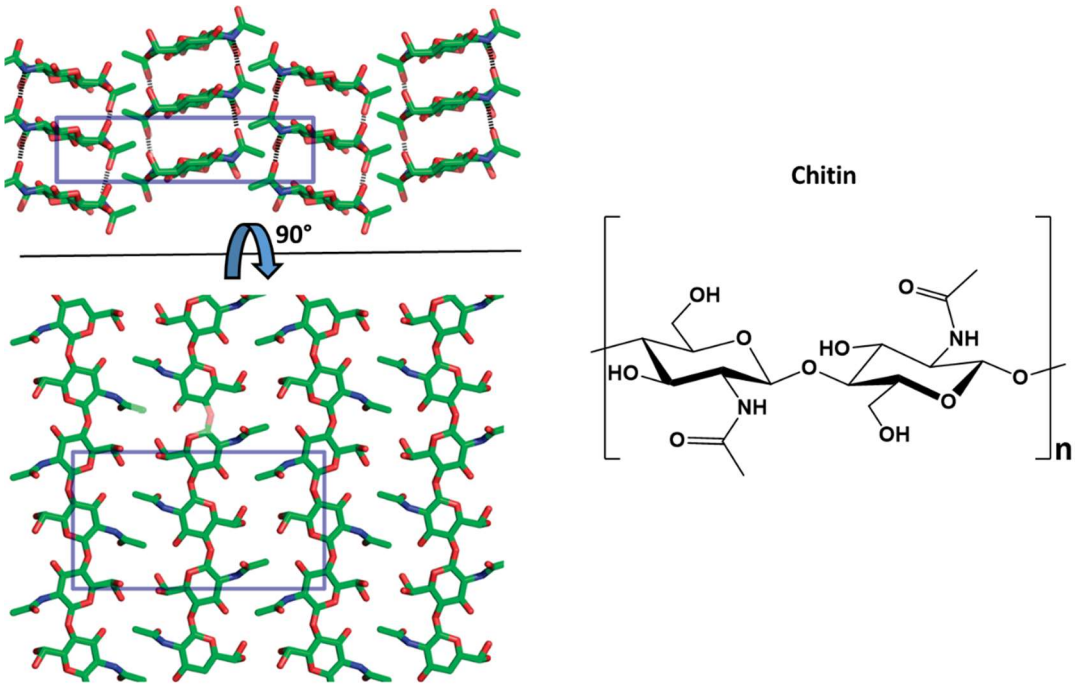

Figure 1.5 Molecular structure of chitin highlighting H-bonds between different chains as black dotted lines. Dimension of the unit cell is shown as a blue rectangle (left). The repeating structural unit chitobiose is indicated in brackets (right). In the crystal lattice, hydrogen bonds are formed between the *N*-acetilglucosamine and hydroxide functional groups. The figure was reproduced and adapted from Sikorski *et al*. [21]

Chitin is an important polysaccharide in the context of biomass recycling for industrial application because it is estimated that 10^{11} tons of chitin are produced annually,[22] most of which is found in the oceans and constitutes a waste product of fishery and aquaculture industries. This biomass could be recovered and exploited in industrial, agricultural and pharmaceutical applications.[23]

1.3 The role of lytic polysaccharide monooxyganases in the enzymatic degradation of polysaccharides

In Nature, fungi and bacteria are the predominant organisms which are capable of degrading recalcitrant plant biomass. As such they account for a large fraction of the global carbon cycle.[24] As described above, biomass is a complex mixture of different polysaccharides and lignin, generating a wide variety of structures and compositions. As a consequence, the lignocellulose-degrading organisms have equipped themselves with a wide variety of enzymes which are secreted onto the biomass and have many different activities complementary to the multiple different structures which are present within the biomass.[4] In this context, the 'canonical model' for enzymatic deconstruction of complex polysaccharides, like cellulose or hemicellulose, is comprised of several different classes of enzymes. These classes include hydrolytic cellulase enzymes, which are further classified as cellobiohydrolases CBH enzymes that attack carbohydrate chains from the end to release disaccharide units, and endoglucanases, EG enzymes, that randomly hydrolyse β-1,4-glicosidic linkages primarily in amorphous regions of polymer fibre. The cellobiose units resulting from the synergistic action of the two classes (indicated by a higher hydrolytic activity than it would be predicted by the sum of the activities of the single enzymes) are finally hydrolysed to monomers by β-glucosidases (**Figure 1.6**).[24] In addition, the catalytic domain of glycoside hydrolases are sometimes found attached to so-called carbohydrate binding modules (CMBs), which are non-catalytic domains involved in substrate targeting, enhancing the enzyme binding to the relevant substrate (see **Section 1.6.2**).[4,25]

These hydrolytic enzymes typically use general acid/base catalysis to hydrolyse glycosidic bonds, using acidic groups provided by aspartic acid or glutamic acid residues (**Figure 1.7**).[26] The active sites of these hydrolytic enzymes can be described as 'grooves'

or ‘tunnels’ which can accommodate single isolated substrate chains. In this model, the rate limiting step for depolymerisation of cellulose is the separation of the single glucan chain from the crystalline bulk of the substrate (de-crystallization) because of the high energy required to break the H-bond network of cellulose. Indeed, the action of many glycosidase enzymes on crystalline substrates is generally orders of magnitude lower with respect to the same activity on soluble polysaccharides.[26]

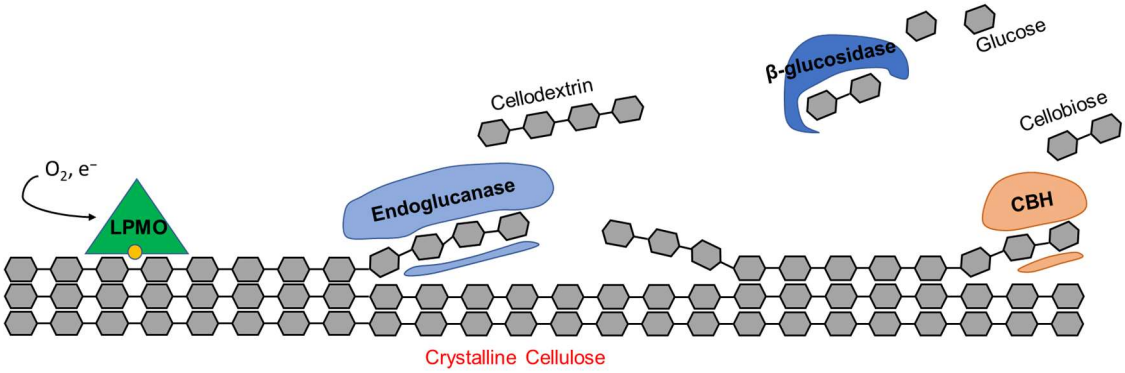

Figure 1.6 Cartoon representing the current enzymatic model for cellulose degradation. Endoglucanases and cellobiohydrolases (CBH, also called exoglucanases) attack isolated chains of cellulose, producing oligosaccharide (cellodextrin) and cellobiose units, respectively, hydrolysing the glycosidic bonds of the polysaccharide chains. The *β*-glucosidase enzymes hydrolyse the cellobiose units generated into glucose monomers. Lytic polysaccharide monooxyganases (LPMOs) break glycosidic bonds through an oxidative mechanism using O_2 and an external electron donor (or H_2O_2 without electron donors); they can act on the crystalline regions of the substrate, generating new chain ends, which can be subsequently used by the other hydrolysing enzymes. The LPMOs action is synergic to the action of the other glycoside hydrolase enzymes, effectively boosting their ability to degrade cellulose. The grey hexagons represent the single glucose monomers, connected by *β*-1,4-glycosidic bonds, to form cellulose chains; the Cu active site of LPMOs is represented by a yellow circle.

In recent years, the ‘canonical model’ of biomass degradation has been challenged by the discovery of a new class of copper-dependent enzymes called lytic polysaccharide monooxyganases (LPMOs) or polysaccharide monooxyganases (PMOs).[27] LPMOs are widespread in Nature and are found in many different organisms such as fungi, bacteria, mollusks, insect and some animals.[28] These copper-dependent enzymes are able to de-polymerize cellulose, cleaving the glycosidic bonds through an oxidative mechanism, instead of an hydrolytic one. This mode of action involves the hydroxylation of C–H

bonds in position C1 or C4 of the glycosidic chain, followed by cleavage of the glycosidic bond *via* an elimination reaction. The reaction produces an oxidized polysaccharide chain end: an aldonolactone (C1 oxidation) or a 4-ketoaldose (C4 oxidation), as shown in **Figure 1.7**. As co-substrates, LPMOs use O_2 and an external electron donor for the necessary reducing equivalents,[27] or H_2O_2 without an external electron donor (see **Section 1.9** below for a discussion of the catalytic mechanism).[29]

The Cu active site is positioned on a flat solvent-exposed surface of the enzyme.[27,30,31] This flat surface allows LPMOs to bind an extended substrate even in regions with high crystallinity, where the polysaccharide chains are tightly packed, without the need for isolation of single polysaccharide chains. The action of LMPOs during lignocellulose degradation has been shown to be highly synergic to the action of the other cellulases. In fact, they can generate new chain breaks in crystalline regions of the substrate, which can be exploited by other hydrolytic enzymes to produce more oligosaccharides, greatly improving the yield of the degradation process (**Figure 1.6**).[32] In support of this mode of action, recent work from Eibinger *et al*. demonstrated a reduction of cellulose surface crystallinity after treatment with LPMOs.[33]

Many organisms capable of lignocellulose biomass degradation encode one or several LPMO genes in their genome, of which expression is up-regulated together with glycoside hydrolases during their growth on recalcitrant polysaccharides. Species that contain multiple LPMOs genes can display substrate-dependent expression profiles.[34]

The discovery of LPMOs is a breakthrough also for industrial applications; their inclusion in the classic hydrolases enzymatic cocktails used for biomass degradation leads to significant improvement in monosaccharaides yields (like glucose from the digestion of cellulose) at the end of the degradation process. The ability of LPMOs to boost the activity of glycoside hydrolases has been one of the key drivers behind the surge of research in this area,.[8,32]

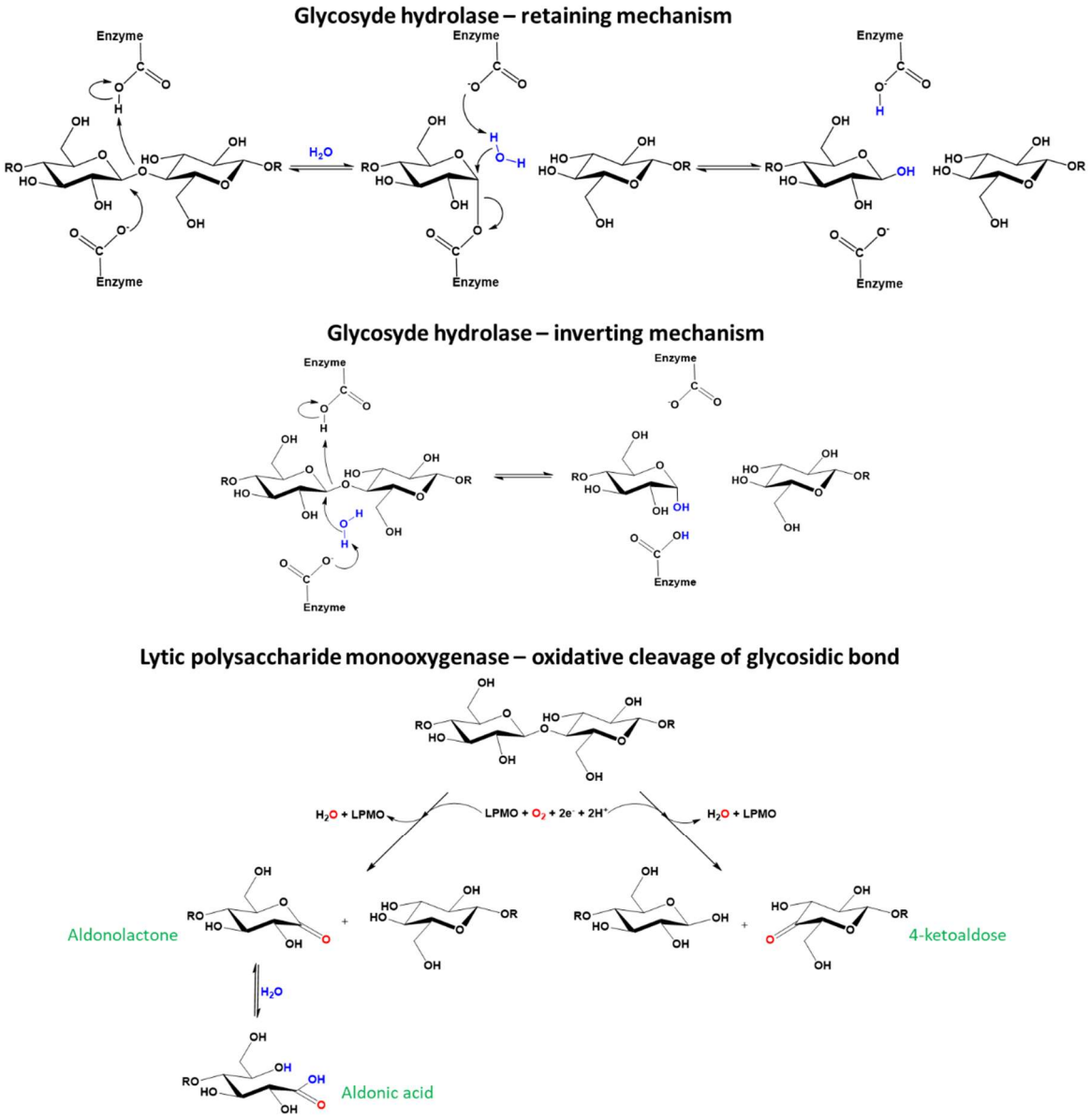

Figure 1.7 Reactions schemes describing the hydrolytic and oxidative cleavage of glycosidic bonds in polysaccharides. The glycoside hydrolases glycosidic bond hydrolysis with retaining mechanism, where the β configuration of the anomeric carbon is retained in the reaction product (top). The glycoside hydrolases glycosidic bond hydrolysis with inverting mechanism, where the β configuration of the anomeric carbon is inverted to α in the reaction product (middle). General scheme for the oxidative cleavage of glycosidic bonds performed by lytic polysaccharide monooxygeneases (bottom). The enzyme oxidizes the C–H bond in position C1 or C4 of the polysaccharide chain, leading to subsequent cleavage of the glycosidic bond and generating an aldonolactone or a 4-ketoaldose, respectively. The aldonolactone can hydrolyse further to the relative aldonic acid form.

1.4 The CAZy classification of LPMOs

The diversity and complexity of polysaccharides found in nature is seen in the large number of enzymes which, often in combination with each other, carry out the assembly or the breakdown of the polysaccharides. These enzymes are generally defined as Carbohydrate-Active enZymes (CAZymes) and are classified according to amino acid sequence similarities and their enzymatic function in the CAZy database (www.cazy.org), updated since 1998.[35] The database is accompanied by CAZypedia, an encyclopaedic resource featuring the description of the various classes of CAZymes.[36] The CAZy database currently covers several classes of enzymes as glycoside hydrolases (GHs), glycosyltransferases (GTs), polysaccharide lyases (PLs), carbohydrate estherases (CEs) and the auxialiary activity enzymes (AAs). , The database also includes carbohydrate binding modules (CBMs), which are non-catalytic proteins which enhance substrate binding[25] CBMs are often found to be attached to GH enzymes through a flexible peptide chain linker.

LPMOs are classified in CAZy as auxiliary activity (AA) enzymes, together with other redox enzymes mostly involved in lignin degradation. Like the other CAZymes, LPMOs are divided into families according to similarities in their amino acid sequences and, currently, there are seven known different families: AA9,[30,31] AA10,[27] AA11,[37] AA13,[38] AA14,[39] AA15[40] and AA16.[41]

The AA9 and AA10 families are the two families which have been bestcharacterized over the years. From a sequence perspective, AA9 family members, mainly of fungal origin, show low sequence homologies between themselves and, as such, are further divided in several sub-families. These sub-families correlate with different reaction specificities of the LPMO on the substrate (*i.e.* whethercellulose oxidation occurs at position C1 or at position C4 of the polysaccharide chain, see **Figure 1.7**).[42] The CAZy database further shows that while most AA9s are single domain enzymes, about ~20% of them have a cellulose binding domain (CMB1) attached at the C-terminus end of the LPMO. Somewhat in contrast to AA9 LPMOs, AA10 LPMOs are mostly found in bacteria and are divided in two phylogenetic clades which are distinguished by a different substrate specificity: one is active one chitin, while the other one is active on cellulose.[43]

The other LPMO families have been discovered more recently than the AA9 and AA10 and fewer reports are available on their characterization. The AA11, AA13 and AA16 family members are found in fungi and are chitin- (C1 and C4 oxidation)[37], starch- (C1

oxidation),[38] and cellulose-active (C1 oxidation),[41] respectively. AA14 LPMOs are found in fungi and have been reported to be active on xylans (with C1 and C4 oxidation).[39] Lastly, the AA15 LPMOs are found in insects, crustaceans and molluscs with reported activity on both cellulose and chitin (C1 oxidation).[40]

1.5 The discovery of LPMOs

In 1950 Elwyn Reese *et al*. published a key paper reporting the activities of cellulolytic and non-cellulolytic organisms on cellulose and its derivatives.[44] The authors, on the basis of microbiological studies, proposed that cellulolytic organisms were able to degrade native cellulose into smaller oligosaccharides which could then be exploited by certain cellulase enzymes to produce glucose monomers. On the other hand, non-cellulolytic organisms, despite having cellulase enzymes in their secretomes as well, were lacking the capacity of efficiently break down native cellulose and therefore this polysaccharide was not a viable food source for these organisms. The authors therefore suggested that the cellulolytic organisms possessed a 'C1' activity, able to destroy the structure of cellulose and allowing the action of other cellulases. In 1974, Eriksson *et al*. published another milestone paper, reporting the action of an enzyme, secreted by the fungus *Sporotrichum pulverolentum*, able to oxidize cellulose and improve the yield of cellulose degradation by endo- and exoglucanases, with respect to the same mixture of glucanases but without this oxidizing enzyme.[45] Together, these two papers suggest that certain organisms are able to produce enzymes which can enhance the action of canonical cellulases, *via* an oxidative mode of action on native cellulose as substrate.

In early 2000s a new group of enzymes was identified from fungal secretomes with the potential of being involved in cellulose degradation. On the basis of their reported weak endoglucanase activity, they were assigned as family 61 glycoside hydrolases (GH61). The structure of one of these enzymes (named *Tr*Cel61A from the fungus *Trichoderma reesei*) revealed a highly conserved flat surface, very different with the usual tunnel or 'cleft' active site found in standard cellulases.[46] This flat surface contained a metal binding site occupied by a nickel ion derived from the crystallization buffer. This clue, together with the reported endoglucanse activity several hundredfold lower than that of other *Trichoderma* endoglucanases, suggested this family of enzymes could not be

glycoside hydrolases. Despite this work, however, this action of this class of enzymes was enigmatic.

Finally, all the relevant pieces were put together by Vaaje-Kolstad *et al*. in 2010 who reported the oxidative mode of action and the crystal structure of a bacterial metallo-enzyme (called CPB21 and classified in the CBM33 family, at the time), able to oxidize chitin as substrate and also able to boost the degradation of chitin by chitinases.[27] This work also demonstrated the incorporation of an oxygen atom derived from O_2 into the oxidized products (chito-oligosaccarides) and the need of a reducing agent to perform the oxidative reaction (**Figure 1.7**). This particular activity was reported to be dependent on Mg(II) or Zn(II), metal ions that would not be naturally associated with an ability to activate molecular O_2 to perform catalysis. Soon after, it was shown that similar enzymes (belonging to the GH61 family) were active also on cellulose, cleaving the glycosidic bond of the substrate by oxidising position C1 or C4 of the polysaccharide chain.[30,31,47] Several crystal structures were reported with different metals in the putative enzyme active site: Ni,[48] Zn[49] and Na.[27] Finally, in 2011 in work partly carried out in York, Quinlan *et al*. used a combination of EPR spectroscopy and X-ray crystallography to demonstrate that the active site of these enzymes contained a monomeric type 2 copper ion, in a particular coordination geometry which employs an N-terminal histidine and a further histidine side-chain to coordinate to a copper ion in a coordination arrangement named as the histidine brace (**Figure 1.8** and also **Section 1.6.1** for a detailed description of the active site).[30] Moreover, at about the same time, Phillips *et al*. confirmed that the activity on these monooxyganase enzymes was only dependent on Cu and not on other ions.[31] The confusion about the metal in the literature previous to Quinlan *et al*. and Philips *et al*. was likely to be due to the very high affinity of the histidine brace for Cu(II) (with dissociation constant $K_d \sim 10^{-9}$),[30,31] making it difficult to eliminate completely the Cu from the active site in metal dependencies studies, and the fact that protein crystallization buffers often contains various metal ions including Cu.

Following these discoveries the new enzymes were called lytic polysaccharide monooxyganases (LPMOs), or simply polysaccharide monooxyganases (PMOs), and the relative families GH61 and CBM33 were then re-named as auxiliary activity 9 (AA9) and auxiliary activity 10 (AA10) families in the CAZy database (see **Section 1.4**). The word 'lytic' refers to the ability of these enzymes to break and loosen polysaccharide chains, in contrast to the other mono-, oligo- and polysaccharide monooxyganases, such as

galactose oxidase, that do not break chains. According to some authors, the use of *lytic* in the name should be avoided as there is no evidence that the enzyme participates in the cleavage of glycosidic bond after the hydroxylation step; therefore, the term polysaccharide monooxyganases better describes the catalytic activity of these oxidative enzymes.[28]

In the last few years research activity on LPMOs has increased dramatically, with discoveries of new families, structures, functions and diversity of these enzymes. However, despite their importance, many important questions about their reactivity still need to be answered.[8,50] The following sections will provide a brief summary of LPMO characteristics discovered so far and highlight the key areas which require further investigation.

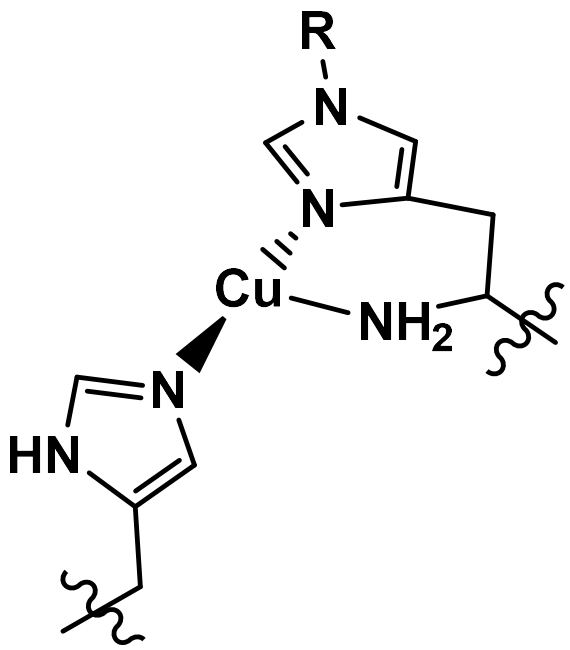

Figure 1.8 Scheme representing the His brace coordination environment in LPMOs. The –R group represents a –H or a $–CH_3$ group as the His-1 of some fungal LPMOs is N–methylated.

1.6 The structure of LPMOs

Despite the low sequence homology between different LPMOs (even among those belonging to the same families), the available structures show that they all share an immunoglobulin-like β-sandwich core, in which the different β-strands are connected by loops of different lengths and structures (**Figure 1.9**).

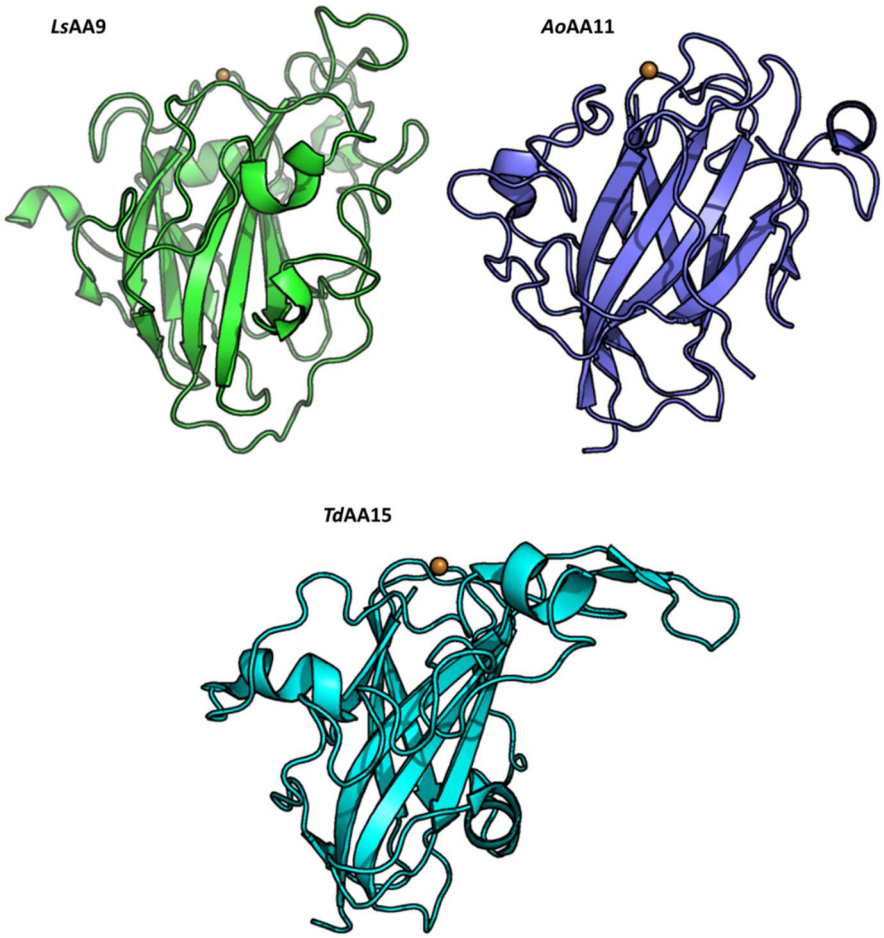

Figure 1.9 Cartoons representing the tertiary structure of several LPMOs from different families: *L. similis* AA9 (PDB 5ACH), *A. oryzae* AA11 (PDB 4MAI) and *T. domestica* AA15 (PDB 5MSZ). The Cu active site positioned on the enzyme flat surface is represented as gold sphere.

Moreover, all LPMOs feature a flat (or near flat) substrate-binding surface, which harbours the mononuclear Cu active site. The structural diversity among the LPMOs is generated by the various loops that connect the β-strands, generating different dimensions and topologies of the substrate binding surface. Although these surfaces can be generally

described as flat, they do show some topological variability which can be related to substrate specificity (**Figure 1.9**).[51] Indeed, the substrate binding surface is characterised by high sequence variability across different LPMOs, suggesting an explanation for the wide variety of substrates displayed by LPMOs, not only in terms of what glycosidic bond they break, but also in terms of varying substrate topologies which occur in different types of plant cell walls. As described in **Section 1.2**, plant cell walls are not homogenous structures, but instead they feature very complex compositions that change from plant to plant.[52]

1.6.1 The Cu histidine brace

The active site is conserved in all LPMO families and consist of a mononuclear Cu site, where a Cu ion is coordinated by two histidine residues: the N-terminal histidine chelates the Cu through its NH_2 group and the δ-N of the imidazole side chain, together with the ε-N of the imidazole ring of the second His residue, in an overall T-shaped geometry called 'histidine brace' (or His brace), as shown in **Figure 1.10**.[30] A particular feature of the histidine brace, is the methylation of the ε-N atom of His-1 found in several fugal LPMOs which is introduced as post-translational modification. The functional role of this methylation is currently not clear but a recent report suggested that it has little effect on the catalytic activity but may help to protect the enzyme from oxidative damage.[53] This feature is not found in bacterial LPMOs (like those in the AA10 family) as these organisms lack the necessary enzymatic machinery to introduce this type of post translational modification.

In addition, it should be noted that some protein sequences currently belonging to the AA9 family display a natural N-terminal His to Arg substitution (Arg-AA9).[54] These are found almost entirely in the phylogenetic fungal class *Agaricomycetes* and are associated with wood decay, but no function has been demonstrated yet for any Arg-AA9. The overall fold of these proteins is very similar to the characteristic fold of AA9 LPMOs, but with significant changes in the region equivalent to the canonical LPMO copper-binding site (indeed no copper binding has been reported). Hence, even if Arg-AA9s are part of the AA9 family, they cannot be classified as LPMOs as they do not show the same enzymatic activity.

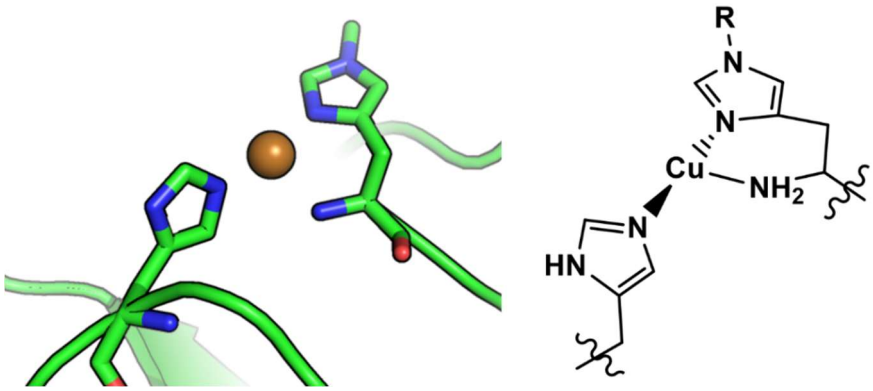

Figure 1.10 Cartoon representing the histidine brace active site in *Hj*AA9 LPMO (PDB 5O2X) (right), together with a general scheme of the His brace (left). R = Me or H depending on the LPMO considered.

In addition to this strictly conserved structural unit, the diversity across the different LPMO families is generated by the identity and different positions of the residues in the secondary coordination sphere of the copper (**Figure 1.11**).[8] The ~50 available crystal structures of different LPMOs show that there is very little variation within the Cu primary coordination sphere, suggesting that the histidine brace could be viewed as a fixed structural unit where the reactivity is finely tuned by secondary coordination sphere interactions.[55] Indeed, several of these residues in the secondary coordination sphere are always conserved within a specific LPMO family and are involved in hydrogen bonding networks with the Cu ligands and the substrate, when bound to the enzyme (see the discussion about substrate binding in **Section 1.7**).[56]

The reduced Cu(I) state is very similar in all LPMOs, where the Cu ion is coordinated only by the His brace residues, no exogenous ligand and is characterized by a Cu−NH_2 bond longer (~2.1–2.3 Å) than the other two Cu−N(imidazole) bonds (~2.0–2.1 Å). In addition to these bonds distances, it should be noted that the two imidazole ring planes are always spatially arranged to form an angle of about 65° between them; this angle appears to be dependent on the presence of the metal in the active site as in the few available *apo* structures this angle is ~30°.[57] In addition, this angle is significantly different from the analogous angle found in many *trans*-N-heterocyclic Cu(II) complexes, where it is usually much less than 30° (because of the conformational demands of the chelate rings of ligands).[55] It is currently unclear if this difference is an important factor in the enzyme reactivity, however it has been suggested that the π-interaction capacities

of the N-heterocycles can play a role in the stabilization of the relevant Cu–oxygen intermediate (**Section 1.9**).[55]

All LPMO families, apart from some AA10s, also feature a Tyr residue in the axial position with respect to the Cu coordination plane (**Figure 1.11**); however, its distance from the metal (Cu−O(Tyr) ~2.5–3.0 Å) is too large to be considered formally bonded to the metal.[8] The oxygen of this Tyr residue is generally considered protonated as shown by the neutron structure of *Neurospora crassa* AA9 LPMO (*Nc*AA9D, see also **Figure 1.14** below).[58]

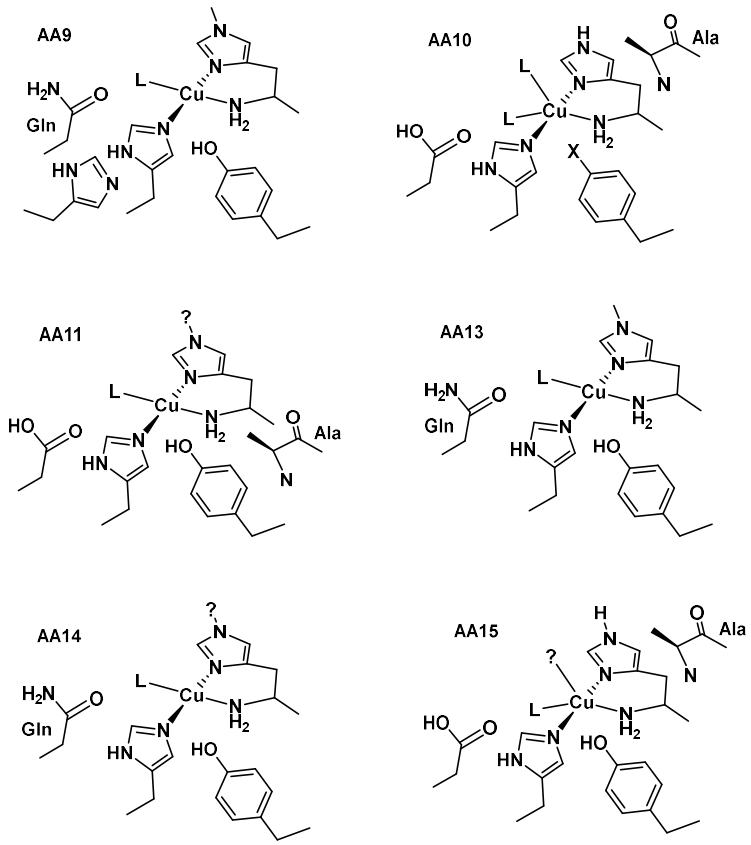

Figure 1.11 The active site structures of LPMOs, classified according to the CAZy database, showing conserved residues in the active site. 'L' refers to exogenous ligands, usually H_2O/OH^- or Cl^-. The wild-type AA11 and AA14 LPMOs may contain a methylated N-terminal histidine side chain (depicted as '?'), like AA9, but this is unknown as the production systems (*E. coli* or *Pichia pastoris*) used to produce these enzymes lack the necessary enzymatic methylation apparatus. The AA16 class is not included in the scheme, as no structure is yet available.

The Cu(II) resting state of the enzyme is characterised by the same T-shaped geometry of the Cu(I) form, but presents two additional water molecules. The crystal structure of *Hypocrea jecorina Hj*AA9A (PDB 5O2X)[59] is representative of this resting state: one water molecule coordinates the Cu(II) in the His brace equatorial plane at ~2.0 Å, *trans* to the amino terminus while the second one occupies the second axial position at ~2.4 Å, *trans* to the Tyr residue, in an overall Jahn-Teller distorted octahedral geometry (**Figure 1.12**).

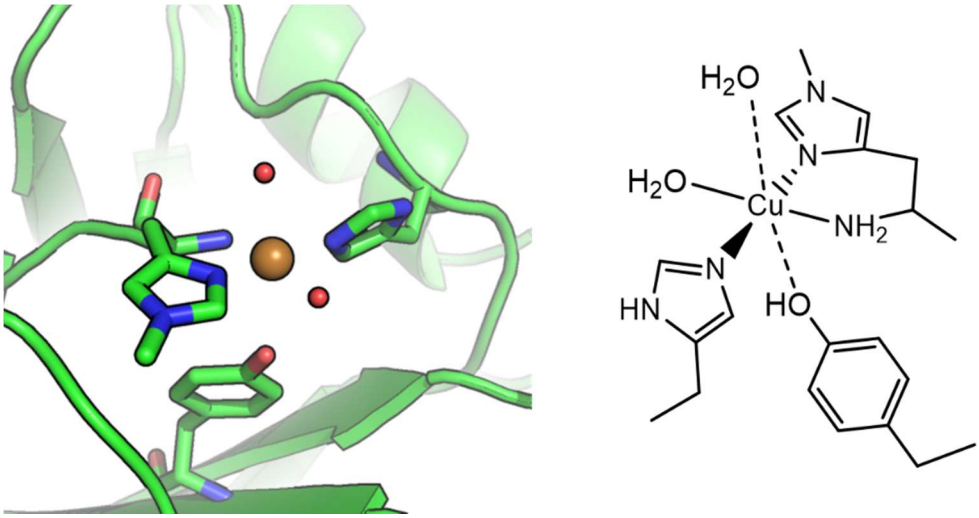

Figure 1.12 Copper active site of Cu(II)–*Hj*AA9 (PDB 5O2X), highlighting the Cu (gold sphere) first coordination sphere.

Some LPMOs belonging to the AA10 family are an exception to this picture because they feature a phenylalanine residue in place of the axial Tyr and they show a distorted coordination geometry with respect to the one described above. As an example, in the structure of *Enterococcus faecalis Ef*AA10 (PDB 4ALC)[60] the equatorial plane of the His brace is significantly distorted: the three N ligands together with one of the exogenous H_2O molecule form the base of a square pyramid, while the second H_2O molecule completes the coordination sphere in the 'axial' position of this distorted pyramid (**Figure 1.13**). This arrangement is sometimes referred as a trigonal bipyramidal coordination (with the amino terminus and the two H_2O molecules forming the base of this bipyramid), however EPR analysis of the Cu(II) resting state indicates a mainly $d(x^2–y^2)$ ground state SOMO, reflecting more a tetragonal structure rather than a true trigonal bipyramidal

geometry (which would have a mainly d(z^2) SOMO ground state).[61,62] Hence, the Cu coordination geometry in these AA10s is better described as distorted square-pyramidal.

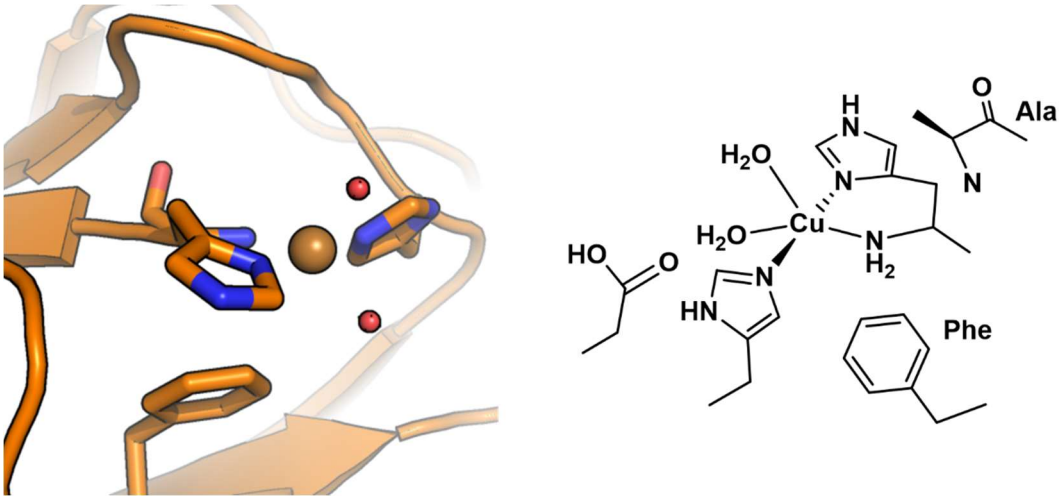

Figure 1.13 Copper active site of Cu(II)–*Ef*AA10 (PDB 4ALC), highlighting the Cu (gold sphere) first coordination sphere.

The two structures presented above were chosen as examples of the Cu(II) resting state in AA9 and AA10 LPMOs, but many more can be found in the protein data bank (PDB), even for other classes of LPMOs. However, it is worth noting that it is not always easy to correctly assign the redox state of the Cu ion in a given crystal structure. The Cu active site in these enzymes appears to be very sensitive to photo-reduction during data collection due to the X-ray beam and therefore the measured Cu–ligand bond distances might not be representative of the real Cu(II) redox state.[60,61,63] Indeed, the bond lengths between the Cu and the exogenous water ligands, as well as the Cu−O(Tyr) vary considerably across the LPMOs published structures.[57] In this respect, a recent analysis of LPMOs structures using the bond valence sum (BVS) method to estimate the Cu redox state form the measured bond distances found that many LPMO structures where the metal was originally assigned in the Cu(II) state were better described as in the Cu(I) state.[64]

The His brace in LPMOs have been proposed to enforce critical and geometric constraints on the Cu active site which are key for favourable binding of O_2/H_2O_2 at the beginning of the catalytic cycle, as well as for assuring a low reorganization energy for

transition between the oxidized and reduced states.[55,63] The O_2/H_2O_2 binding site is thought to be the free equatorial position of the Cu(I) oxidation state, *trans* to the N-terminal amine (which is occupied by H_2O, in the resting state).[8] This hypothesis is supported by the substrate-bound structures obtained for *Lentinus similis Ls*AA9 with soluble cello-oligosaccharides (PDB 5ACI, see discussion below), as the substrate effectively blocking the Cu axial position *trans* the Tyr residue.[65] In agreement with this model, two recent X-ray/neutron diffraction studies reported a structure of the enzyme with an O_2 molecule modelled in the active site (**Figure 1.14**).

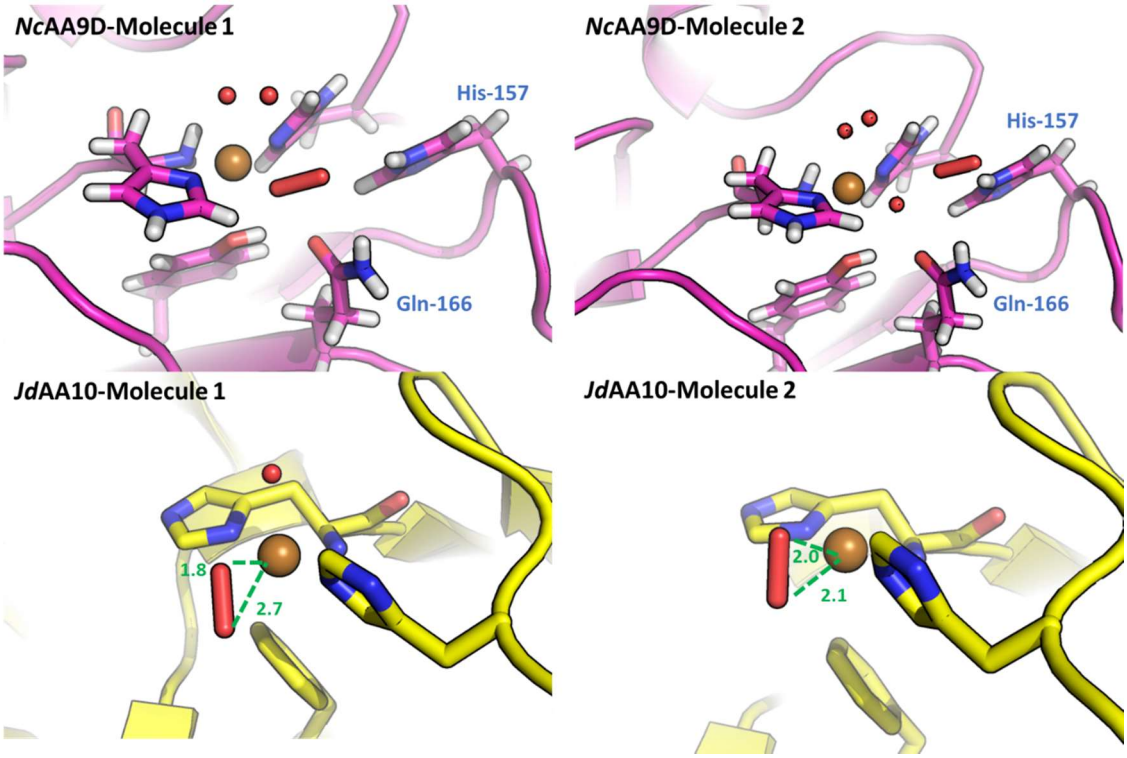

Figure 1.14 Neutron structure of the *Nc*AA9D Cu active site showing two different molecules in the asymmetric unit (top, PDB 5KTH). In Molecule 1 the Cu–O_2 distance is 1.9 Å, while in Molecule 2 is 3.6 Å. X-ray structure of the *Jd*AA10 Cu active site (bottom, PDB 5VG0), showing O_2 in two different coordination geometries: end-on coordination (Molecule 1) and side-on coordination (Molecule 2). Cu–O bond distances are reported in green (Å).

O'Dell *et al*. reported the high resolution structure of *Neurospora Crassa Nc*AA9D (PDB 5TKH), showing two different monomers in the asymmetric unit of the crystal.[58] In the first monomer, the O_2 was modelled as peroxide (with O–O ~1.4 Å) bound in the

equatorial position of the Cu(II), with Cu–O distance of 1.9 Å. In the second monomer, an O_2 molecule (O–O ~1.2 Å) was identified in a 'pre-bound' state at 3.6 Å from the Cu(II), interacting with the distal residues His-157 and Gln-166, adjacent to the Cu(II) equatorial coordination position. Interestingly, a mutational study on a similar AA9 enzyme (the *Myceliophthora thermophile Mt*AA9) found that the distal His and Gln residues affect the dioxygen reactivity of the enzyme.[56] Despite these structural data, however, there currently is no experimental evidence to support or refute the existence of this 'pre-bound' O_2 state.

On the other hand, Bacik *et al*. reported the structure of *Jonesia denitrificans Jd*AA10A LPMO (PDB 5VG0) with a peroxide ion (O−O ~1.5 Å) bound in the equatorial position of the Cu(II).[66] Again, two different monomers are found in the crystallographic asymmetric unit, with O_2 in two slightly different binding modes: one similar to an end-on coordination and a second one resembling more a side-on coordination to the Cu (**Figure 1.14**). The assignment of a peroxide bound to the active site in the equatorial position is certainly interesting in discussing LPMO reactivity, however it should be considered that currently there is no spectroscopic evidence that confirms the existence of a Cu(II)–peroxide species.

1.6.2 CBM modules

Several LPMOs are multi-modular enzymes formed by a catalytic domain and a carbohydrate binding module (CBM) domain. CBMs are non-catalytic domains able to direct the action of the enzyme enhancing substrate binding and/or targeting specific regions of the crystalline polysaccharide.[26] These domains are not only found in LPMOs, but are widespread among the carbohydrate active enzymes: currently there are 79 characterized different CBM families reported in the CAZy database.[67]

The most common family of CBMs found attached to the AA9 LPMO sequences is the CBM1 family, a fungal-specific module known to interact with cellulose.[8,68] Among bacterial AA10 LPMOs it is possible to find both cellulose specific (e.g. CBM1s) and chitin specific binding domains (e.g. CBM5s).[8] These modules generally present a flat glycan binding site (**Figure 1.15**), rich in aromatic residues such as tyrosine and tryptophan, which are used to bind the crystalline surface of cellulose or chitin mainly

through CH–π stacking interactions (also referred as carbohydrate–aromatic stacking interaction).[26] A study on the *Streptococcus coelicolor Sc*AA10C (a cellulose active LPMO) tested the enzymatic activity with and without the native CBM module and showed that only 25−30% of the activity of the full-length enzyme was retained upon removal of the CBM. On the other hand, the product profile seemed not to be affected by the presence or absence of a CBM.[69] Moreover, a recent investigation on the *Neurospora Crassa Nc*AA9C demonstrated that the full length enzyme (comprising the CBM) showed a higher affinity for the substrate with respect to the LPMO catalytic domain alone, but again the product profile did not seem to be affected by the truncation.[70] These two examples suggest that CBM modules are an important factor in the substrate interaction/binding with the enzyme, but do not affect significantly the catalysis at the active site. Indeed, EPR studies of the enzyme Cu(II) resting state showed no dependence of the EPR spectrum on the presence/absence of the CBM module.[59]

The CBM module is connected to the C-terminus of the catalytic domain through a linker region which can have various lengths. These regions generally lack hydrophobic residues but are more rich in proline, serine and threonine residues, with Ser and Thr residues often the target of *O*-glycosylation.[26]

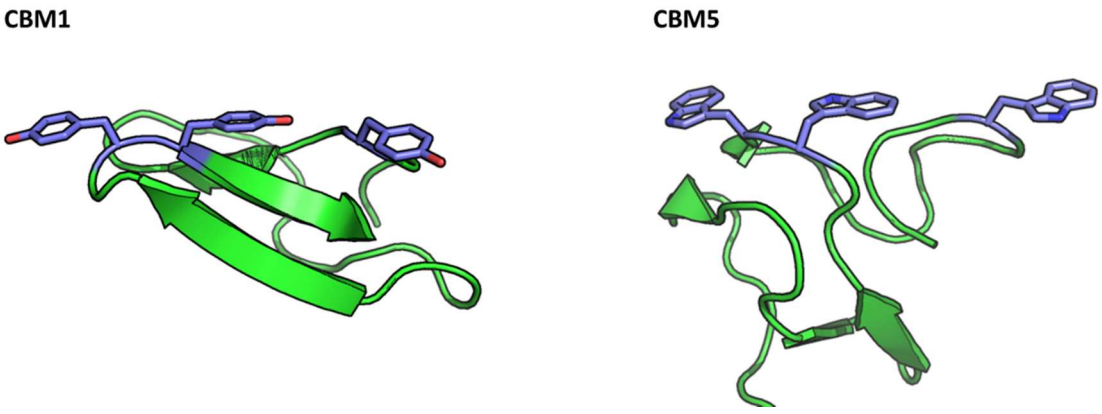

Figure 1.15 Structure of the CBM1 (cellulose binding) *T. reesei* Cel7A cellobiohydrolase (PDB 2MWK) and structure of the CBM5 domain of *M. marina* chi60 chitinase (PDB 4MB4). The important aromatic residues involved in substrate binding are represented in blue.

1.6.3 Glycosylation

Glycosylation in LPMO enzymes does not only occur in the linker region, but is typically found also in the catalytic domain. Glycosylation is a post-translational modification of proteins where carbohydrates are appended to certain residues side chains and can be of two types: *N*-linked (or *N*-glycosylation), when a glycan is attached to the N_δ nitrogen atom of an asparagine residue, or *O*-linked (or *O*-glycosylation) where a glycan is attached to the O_γ of a serine or threonine residue. The role of glycosylation in LPMOs (and in carbohydrate active enzymes more in general) is not fully understood, but it has been shown to affect the structure, the thermal- and proteolytic stability of an enzyme, together with its substrate binding capacity.[71] In LPMOs, glycosylation is often found in those enzymes secreted by fungi: *N*-linked glycosylation always starts with a *β*-N-acetylglucosamine (GlcNac) unit which then can be further decorated with different glycans; whereas *O*-linked glycosylation always features an *α*-mannose as its first unit. Both types of glycosylation also exist in some bacterial proteins.[72] Generally, in structural studies the preparation of the sample for crystallization involves a de-glycosylation step in order to make the sample more homogeneous and to favour the crystallization of the enzyme; this step generally reduces glycosylation to one small glycan per site. Hence, crystal structures do not necessarily represent the glycosylation and structure of the native enzyme. An additional confounding factor is the organism used as host for the recombinant production of enzyme, as not all host organisms can generate the same glycosylation patterns. Indeed, many bacterial systems commonly used to produce LPMOs (like *E. coli*) cannot introduce any glycosylation at all; hence, none of the available bacterial AA10 LPMO structure models contain glycosylation.[8]

1.7 Substrate binding

1.7.1 Substrate specificity

Since the original discovery of LPMO activity toward chitin, LPMOs with activities toward various plant polysaccharides have been described, including cellulose,[30,31,47] soluble cello-oligosaccharides,[73] xyloglucan and other *β*-glucans containing *β*-1,4-linkages,[74] starch[38,75] and xylan.[39] Most of these substrates are insoluble and present significant challenges in the study of LPMO–substrate interaction as they limit the number of experimental techniques available for the study. An early work by Aachmann *et al*. on the chitin active *Serratia marcescens Sm*AA10 LPMO (also known as CPB21) with NMR spectroscopy, showed that substrate binding mainly involves polar interactions and a contribution from a single Tyr residue (Y54) on the flat substrate binding surface of the enzyme[76] (**Figure 1.16**). Moreover, a recent molecular dynamics study of *Sm*AA10 on crystalline chitin corroborated the hypotheses that the residues Tyr-54, Glu-55, Thr-111, His-114, Gln-57, and Asn-182 are important in mediating the enzyme–substrate interaction (**Figure 1.16**).[77]

Fungal AA9 LPMOs often show more than one aromatic residue on the substrate binding surface, arranged in a similar way to those found in other proteins that bind carbohydrates, like CBM modules, where the interaction with the substrate is mediated through CH–π stacking interactions. Indeed, on the basis of the interaction of CBMs with crystalline cellulose, Wu *et al*. studied the *Phanerochaete chrysosporium Pc*AA9D interaction with the hydrophobic face of cellulose using molecular dynamics simulations.[78] Among the residues on the substrate binding surface, three Tyr residues had the highest interaction energies: two of these interacted with pyranose rings on the same central cellulose chain while the third one interacted with a pyranose ring on an adjacent parallel cellulose chain.

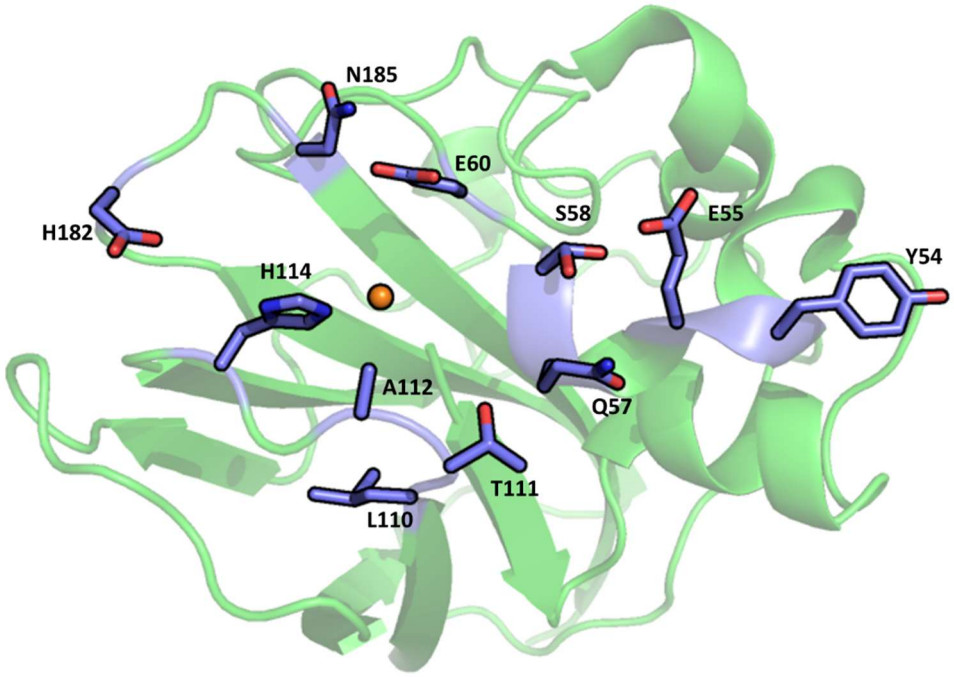

Figure 1.16 Residues on the surface of *S. marcescens Sm*AA10 LPMO (green, PDB 2BEM) which have been shown important for binding to insoluble β-chitin by NMR (blue).[76] The Cu active site is represented as a gold sphere.

The discovery of LPMOs active on soluble oligosaccharides permitted the use of X-ray crystallography to study the enzyme-substrate interaction, together with NMR spectroscopy.[73] A milestone in the LPMO research was reached by the X-ray structure of the *Lentinus similis Ls*AA9 in complex with glucose oligosaccharides (cellotriose and cellohexaose), from which a very detailed picture was obtained of the relevant interactions on the substrate binding surface.[65] This study by Frandsen *et al*., showed that the enzyme-ligand interaction is dominated by polar interactions and by several hydrogen bonds contributing *via* both direct and water-bridged hydrogen bonds (**Figure 1.17**). Two additional interactions were also found: the glycosyl unit in the –3 position of C6 seems to have CH–π stacking interaction with a Tyr residue (Y203), which is conserved in the AA9 family; the glycosyl unit in the +1 position stacks with the imidazole ring of His-1 forming a lone pair–π* interaction (**Figure 1.17**). (Note: the numbering of the pyranose rings follows the general definition used for general definition used for glycoside hydrolases, where the subsites for pyranoses are numbered beginning on each side of the cleavage site and with integers of −1 toward the non-reducing end and +1 toward the reducing end of the glycan respectively).[79]

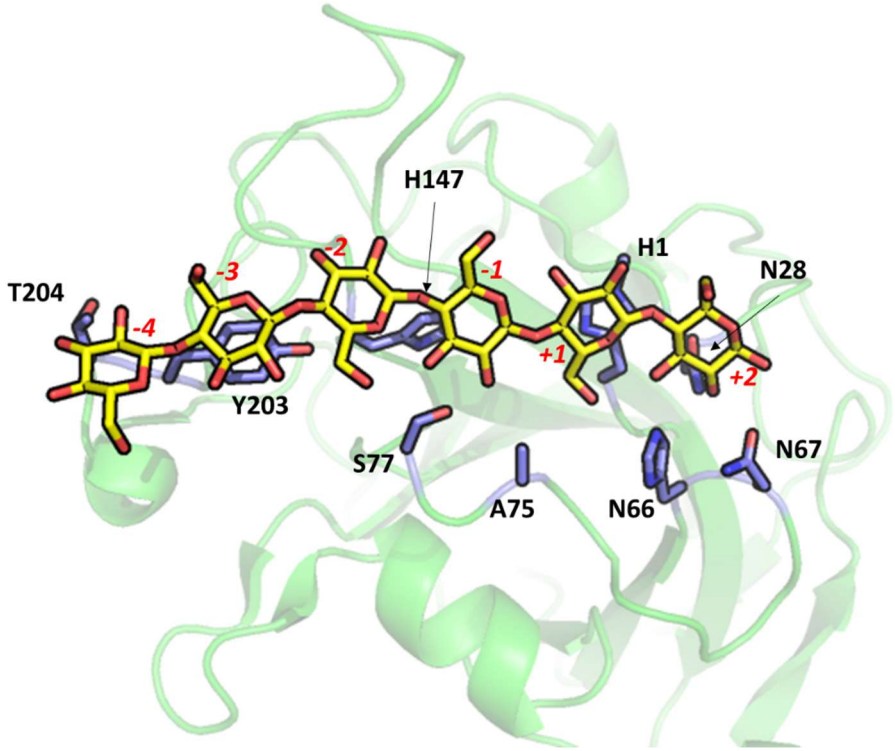

Figure 1.17 Structure of *L. similis Ls*AA9 in complex with cellohexaose (PDB 5ACI), highlighting the residues (blue) that interact with cellohexaose (yellow). Numbering of the cellohexaose pyranose rings is indicated in red.

A NMR study on cellulose and cellohexaose binding with a similar AA9 LPMO, *Neurospora crassa Nc*AA9C further corroborated this picture showing that the interacting area includes the histidine brace as well as the neighbouring residues Ala-80 and His-155 (**Figure 1.18**).[80] Notably this His residue is part of the enzyme active site in the Cu secondary coordination position and is strictly conserved in the AA9 family.[52] On the other hand, many of the residues involved in polar interactions with the substrate found in *Ls*AA9 and *Nc*AA9 are specific to the particular LPMO and not conserved in the family. This observation also holds for the AA10 family where very few of the surface residues involved in substrate bind are strictly conserved in the family.[81]

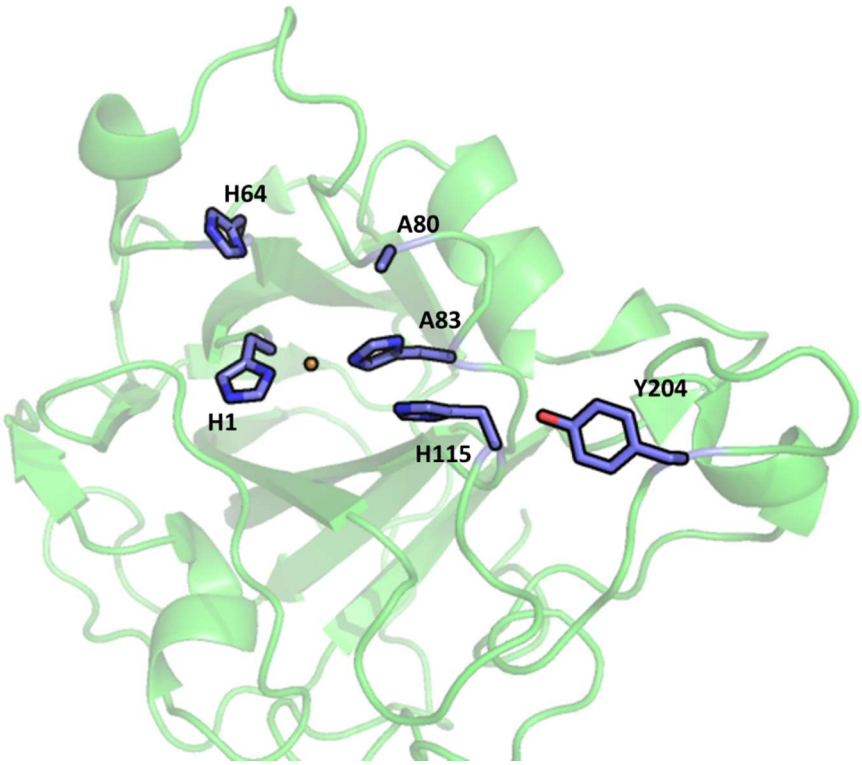

Figure 1.18 structure of *N. crassa Nc*AA9C LPMO showing the residues (blue) involved in cellulose binding as determined by NMR spectroscopy. The Cu ion is represented as gold sphere.

Looking at the active site in more detail, the X-ray structure of *Ls*AA9 and C6 shows that the oligosaccharide does not coordinate directly to the Cu(II) ion but it positioned directly above the His brace coordination plane. In this way the substrate effectively displaces the H_2O molecule in the Cu(II) axial position and affects the H-bond network in the active site (**Figure 1.19**): The C2–OH group of the –1 pyranose unit hydrogen bonds with the –OH group of Ser-77 which in turn is H-bonded coordinating His-77; the C6–CH_2–OH group of the +1 pyranose unit formed hydrogen bonds with the C3–OH group of adjacent pyranose unit (+2 unit) and with the 'pocket' water molecule (O–O, 2.8 Å). The hydrogen bonding pattern around this pocket water further include the N terminus (N–O, 2.9 Å), thereby connecting the substrate to the N terminus and the copper.[65] Moreover, this interaction with the active site results in a perturbation of the Cu(II) EPR spectrum (see later) of the enzyme with respect to the resting state spectrum, consistent with a perturbation of the Cu site electronic structure due to substrate binding.[65,82] Binding of the substrate is unlikely to be influenced by the presence of the Cu(II) in the active site, as Courtade *et al*. showed that the *apo*-enzyme is characterized by a very similar binding constant with respect to the *holo*-enzyme.[80]

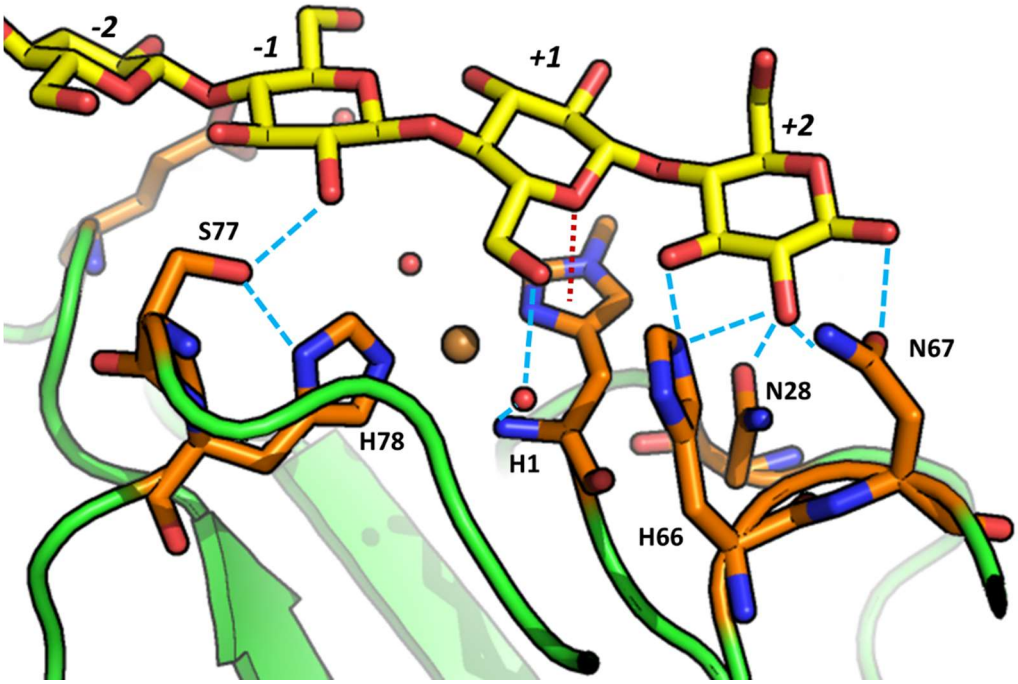

Figure 1.19 Cartoon showing the *L. similis Ls*AA9 copper active site in the enzyme–substrate bound complex (PDB 5ACI). Copper is represented as gold sphere, the coordinating H_2O as red spheres. Residues involved in substrate interaction, near the active site, identified by X-ray crystallography. The light blue dashed lines represent the hydrogen bonding interactions involving the enzyme and the substrate, while the lone pair–aromatic interaction is in dark red.

The particular substrate binding mode leaves only one Cu coordination position available for exogenous ligands coordination: the equatorial coordination position *trans* to the NH_2 group, occupied by a water molecule in the resting state. In the reduced Cu(I) state, the exogenous water molecule is not bound to the metal, hence leaving this position free for O_2/H_2O_2 binding. This model is likely to be valid not only for AA9s enzymes but also for chitin active AA10 LPMOs. Despite the lack an enzyme–substrate complex crystal structure for AA10 LPMOs, two recent investigations, combining NMR and EPR spectroscopy together with DFT calculations, showed that chitin binding to the active site effectively displaces the H_2O molecule in the Cu axial position.[62,77]

Furthermore, several studies showed that substrate binding affinity is significantly enhanced by the presence of chloride or cyanide ions in solution. Both are potential mimics of a negatively charged reactive oxygen species. The dissociation constant K_D for cellohexaose with *Ls*AA9 reduced from ~1 mM to 0.004 mM in absence and presence of Cl^-, respectively.[65] Similarly, the cellohexaose K_D for *Nc*AA9C reduced from 0.8 mM to

0.1 mM with and without CN^- in solution, respectively.[80] When *Ls*AA9 was crystallized in presence of cellohexaose and Cl^-, the chloride was found coordinating the Cu(II) in the equatorial position.[65] The increased affinity is consistent with favourable binding of a reduced oxygen-derived species during turnover, however it is currently unclear whether anion binding enhances substrate binding or vice versa (see also the discussion in **Chapter 2**).

In summary, the binding of LPMOs to a crystalline substrate involves a large portion of the flat substrate binding surface of the enzyme and is mainly driven by electrostatic interactions involving polar residues, together with contributions from CH–π interactions with aromatic residues (mainly tyrosine residues) and lone pair-to-π* interactions.[65] The variety of interactions together with the fact that many of the residues that are part of the substrate binding surface is not conserved between different LPMOs, greatly complicating the understanding of the structural determinants of substrate specificity of LPMOs. Despite recent progress, these factors remain largely unknown. There are data indicating that surface topological differences between chitin and cellulose active AA10 LPMOs,[51] however there are no examples of engineered LPMOs with changed substrate specificity.[52]

1.7.2 Oxidation regioselectivity

A closely related topic to substrate specificity is substrate oxidation regioselectivity. From this point of view, LPMOs can be divided in strictly C1-oxidizers, strictly C4-oxidizers and mixed C1/C4-oxidizers. From the discussion above it is clear that there are many factors that can affect the orientation of the substrate with respect to the active site or even the positioning of the reactive oxygen species relative to the scissile C–H bond in the substrate. So far, there are very little data available on the structural determinants of substrate regioselectivity. However, a comparison between structures of AA9 and AA10 LPMOs revealed an interesting structural correlation.[81] A conserved alanine in the active site of AA10s (**Figure 1.11**) has been suggested to provide steric congestion at the Cu axial position, generating the distorted square pyramidal geometry observed in AA10 LPMOs.[61] Subsequent research showed that the loop hosting this alanine adopts different conformations in C1- and C1/C4-oxidizers AA10s, making the Cu axial position in the C1/C4-oxidizer *Streptomyces coelicolor Sc*AA10B more solvent-exposed than in

the C1-oxidizer *Sc*AA10C.[51] Furthermore, a similar structural comparison in AA9 LPMOs revealed that, strictly C1-oxidizing AA9s have a conserved tyrosine in the secondary coordination sphere, close to the Cu axial position occupied by a water molecule, whereas C4-oxidizing AA9s do not present a Tyr residue in the same position (see *Hj*AA9 active site in **Figure 1.12**).[70] Thus, the accessibility of solvent-exposed Cu axial coordination position, could be a determinant of C4-oxidizing regioselectivity.[81] Nevertheless, recent investigations have reported that mutations affecting accessibility of this axial position did not change the regioselectivities of *Phanerochaete chrysosporium Pc*AA9D and *Ma*AA10B.[83,84] Further experimental studies are needed to test this possible correlation.

1.8 His brace spectroscopic properties

1.8.1 EPR spectroscopy

EPR spectroscopy has been extensively used to gain insight into the Cu environment in LPMOs. The resting state of the enzyme is characterized by a d^9 Cu(II) state which has a single unpaired electron ($S = {}^1/_2$ Kramers doublet), making it EPR active. In terms of spin Hamiltonian parameters that characterize the Cu(II) state, LPMOs can be divided into two broad categories which can be easily seen in the Peisach–Blumberg plot (P-B plot) reported in **Figure 1.20**.[85] The first one is characterized by an axial set of g values (with $g_3 > g_1/g_2$ and g_3 ~2.26–2.28) and a large Cu $|A_3|$ (~400–600 MHz), consistent with a Jahn-Teller elongated octahedral coordination of the Cu(II) ion (**Figure 1.12**). This active site can be classified as a typical type 2 copper site according to the P-B classification of Cu(II) sites.[85] LPMOs from the AA9, AA11, AA13, AA15 families present this type EPR spectrum.[57,86] On the other hand, many LPMOs from the AA10 family are characterised by a more rhombic Cu(II) center that features reduced $|A_3|$ (300–400 MHz) and g_3 (2.25–2.26) values , but larger $|A_1|$ and $|A_2|$ values, with respect to the first category.[62,77] The rhombicity of these EPR spectra is due to the distorted square pyramidal coordination geometry of the Cu(II) that characterize these LPMOs (**Figure 1.13**). However, not all AA10 LPMOs have a rhombic EPR spectrum: those where the active site Phe residue is substituted by a Tyr residue (positioned in the Cu axial

coordination position, similarly to AA9s) show an axial resting state spectrum; indeed, in the P-B plot they are found in the same region of the other LPMO families (**Figure 1.20**).

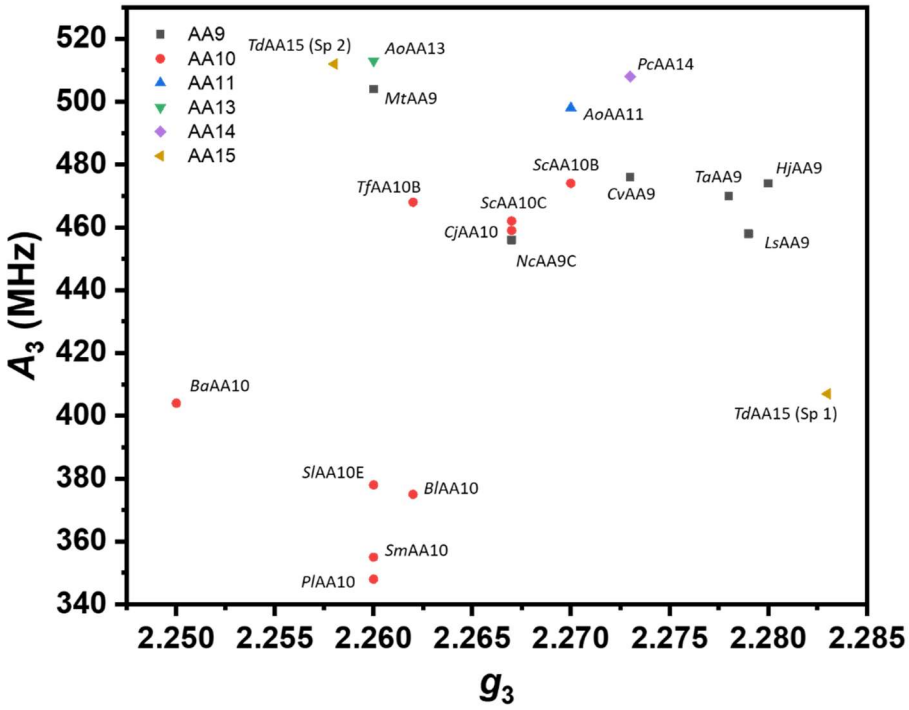

Figure 1.20 Peisach–Blumberg plots of published EPR data for LPMOs Cu(II) resting state (data and references reported in **Table 1.1**). The labels Sp 1 and Sp 2 refer to the two different species reported for *Td*AA15.

Table 1.1 Table of g_3 and $|A_3|$ LPMO Cu(II) resting state EPR values, used for the plot in **Figure 1.20**

LPMO	g_3	A_3 (MHz)	Reference
*Nc*AA9C	2.267	456	Borisova *et al.*[70]
*Ta*AA9	2.267	470	Quinlan *et al.*[30]
*Hj*AA9	2.278	474	Hansson *et al.*[59]
*Mt*AA9	2.28	504	Span *et al.*[56]
*Cv*AA9	2.26	476	Simmons *et al.*[82]
*Ls*AA9	2.273	458	Frandsen *et al.*[65]
*Ba*AA10	2.25	404	Hemsworth *et al.*[61]
*Cj*AA10	2.267	462	Forsberg *et al.*[83]
*Sm*AA10	2.26	348	Forsberg *et al.*[69]
*Sc*AA10C	2.267	459	Forsberg *et al.*[69]
*Bl*AA10	2.262	340	Courtade *et al.*[62]
*Tf*AA10B	2.262	468	Forsberg *et al.*[69]
*Sc*AA10B	2.27	474	Forsberg *et al.*[51]
*Sl*AA10E	2.26	378	Chaplin *et al.*[87]
*Pl*AA10	2.260	355	Munzone *et al.*[88]
*Ao*AA11	2.27	498	Hemsworth *et al.*[37]
*Ao*AA13	2.26	513	Lo Leggio *et al.*[75]
*Pd*AA14	2.273	508	Couturier *et al.*[39]
*Td*AA15 (Sp 1)[1]	2.283	407	Sabbadin *et al.*[40]
*Td*AA15 (Sp 2)[1]	2.258	512	

[1]-The labels Sp 1 and Sp 2 refer to the two different species reported for *Td*AA15.

Despite these differences, all LPMOs EPR spectra are consistent with a mainly $d(x^2–y^2)$ singly occupied molecular orbital (SOMO) ground state.[55] In addition, it should be noted that there is high degree of variability in the published EPR parameters of Cu(II)–LPMOs (**Figure 1.20** and **Table 1.1**) even for enzymes that, from a structural point of view, show the same coordination environment (like LPMOs belonging to the same family).[55,57,86] The origin of this variability is currently not clear, but it is possible that small differences in the H-bonding network around the active site can affect the Cu(II) EPR spectra. Indeed, Span *et al*. reported that the mutation of secondary coordination sphere residues involved in the H-bonding network around the active site was able to perturb the EPR spectra of the *Mt*AA9 resting state.[56]

Furthermore, for several LPMOs it has been shown that substrate binding to the enzyme induces marked changes in the EPR spectra, suggesting that the copper active site is significantly perturbed in the presence of substrate.[62,65,70,77,82] In fact, structural and computational studies showed that the substrate displaces the Cu axial H_2O molecule and is involved in the H-bonding network within the active site, in both AA9s and AA10s (**Section 1.7** and **Figure 1.19**).[62,65,77,82] It has been suggested that these changes of the Cu(II) electronic structure might be important in oxygen activation and hence catalysis, and they will be subject to a detailed investigation for an AA9 LPMO in **Chapter 2**.[62,65,82]

Finally, some authors have used DFT calculations of EPR Spin Hamiltonian parameters to enhance the interpretation of EPR data. Generally, it is not possible to obtain quantitative accuracy (with respect to the experimental data) in EPR parameters predictions with DFT calculations, in transition metal containing molecules.[89,90] However, DFT calculations have been applied with success in reproducing the experimental trends in spin Hamiltonian parameters shift upon β-chitin binding to AA10 LPMOs,[62,77] and allowed to obtain further insight in the active site electronic structure changes induced by the substrate.[62] Again, we refer to **Chapter 2** and **Chapter 4** for a more detailed discussion about EPR parameters prediction with DFT and its application to AA9 and AA11 LPMOs resting state.

1.8.2 Electronic spectroscopy

The information available about LPMOs electronic spectra is scarce and limited to the Cu(II) resting state. The copper(II) center of LPMOs exhibits typical weak dipole-forbidden d-d transition bands between 800–700 nm and with molar extinction coefficient (ε) of 50–150 M^{-1} cm^{-1}.[59,63] These bands are absent in the Cu(I) state (because it is a d^{10} species) and their appearance was utilized to monitor the rate of reaction of Cu(I)–*Ta*AA9 with O_2, using UV-vis stopped flow spectroscopy.[63] Recently, further details on the ligand field transitions in *Hj*AA9 were obtained using a combination of UV-vis, circular dichroism (CD) and magnetic circular dichroism (MCD) spectroscopies.[59] For the Cu(II) resting state of *Hj*AA9 it was possible to resolve three out of the four d-d transitions: the excitation from the d(xz/yz), d(xy) and d(xz/yz) orbitals to the $d(x^2–y^2)$ SOMO were observed at ~764 nm (13000 cm^{-1}), ~720 nm (13890 cm^{-1}) and ~640 nm (15630 cm^{-1}), respectively. The fourth ligand field transition from the $d(z^2)$ orbital remained unresolved

in the electronic spectra. Furthermore, this study showed that the presence or absence of the associated CMB module at the C-terminus of the enzyme did not perturb the electronic spectrum of the enzyme (as well as the relative EPR spectrum), suggesting that the CBM module do not interact with the *Hj*AA9 active site, despite having a significant effect on the substrate binding efficiency of the enzyme.[59]

1.8.3 X-ray absorption spectroscopy

X-ray absorption spectroscopy (XAS) has been used to obtain information about the Cu redox state and its coordination environment in solution, in order to evaluate potential differences with the coordination derived from crystal structures of the enzyme. The XAS spectra of Cu(I)–*Ta*AA9 showed an intense pre-edge peak at ~8984 eV,[63] of which shape and intensity is typical for three coordinate Cu(I) species, and assigned to a dipole allowed Cu 1s to 4p transition.[91] This result was similar to that obtained for the Cu(I) state of *Ba*AA10, suggesting the same Cu(I) coordination geometry.[61] On the other hand, the Cu(II) state of *Ta*AA9 is characterized by a weak pre-edge feature assigned as a dipole forbidden Cu 1s to 3d transition, which is typical for Cu(II) complexes (see **Section 3.3.3.1** for detailed discussion about pre-edge XAS spectra).[91]

Moreover, the extended X-ray absorption fine structure (EXAFS) spectrum of Cu(I)–*Ta*AA9 was best simulated with three first-sphere O/N ligands, two at 1.90 Å and one at 2.25 Å from the Cu (all with estimated standard deviation of ±0.02 Å), consistent with a three-coordinated description of the Cu(I) ion. The two Cu–N(His) bonds were found slightly shorter than the Cu–NH_2 bond, in agreement with X-ray structures of LPMOs (**Section 1.6.1**). The EXAFS spectrum of Cu(II)–*Ta*AA9 instead was best simulated with four Cu–O/N bonds at an average distance of 1.98 ±0.02 Å from the metal, consistent with square planar coordination geometry for the Cu(II) site.[63] Furthermore, it should be noted that, if compared with crystal structures, these distances are more similar to those in the high-resolution crystal structures of other AA9s (PDBs 4QI8, 5O2X, and 5ACG, with resolution 0.9–1.2 Å, **Section 1.6.1**)[59,65,92] than to those in the crystal structure of *Ta*AA9, which is at a lower resolution (PDB 2YET, resolution 1.50 Å, Cu–NH_2 2.4 Å, Cu–N_δ 2.1 Å, Cu–N_ε 2.3 Å, Cu–OH_2 2.2 Å).[30,57] Lastly, the EXAFS spectrum of Cu(II)–*Nc*AA13, an LPMO from the AA13 family characterized by a Cu first coordination sphere very similar to that of AA9s (**Figure 1.11**), was best fit with a 5/6 coordinate Cu(II) ion

consisting in four Cu–O/N bonds ~2.0 Å, 1 Cu–O/N bond ~2.2 Å and 1 Cu–O/N bond at ~2.4 Å, consistent with a Jahn-Teller distorted coordination of the Cu(II).[38]

1.9 The catalytic mechanism

Over the years, there have been many reports on the LPMO–substrate interaction and the products profiles generated by LPMOs. However the catalytic mechanism of these enzymes remains essentially unresolved. Indeed, this aspect of LPMOs has proved to be an area of great research activity, not least because the oxidising species generated at the active site has to be potent enough to cleave the C–H bond on the substrate, the strength of which is estimated to be around 100–104 kcal mol^{-1}.[93] In terms of mechanism, it is known that both oxygen and hydrogen peroxide are co-substrates for polysaccharide oxidation by LPMOs, and different mechanisms have been proposed and extensively reviewed.[8,94,95] Here we summarize the main evidence about the different proposals for the LPMO catalytic cycle. As a side note, the discussion about the Cu–O_2 reactive species is not limited only to LPMOs enzymes but is also relevant in other Cu oxygenases and related model complexes; for an recent comprehensive review on this subject we refer to the work of Courtney *et al*.[96] and Liu *et al*.[97]

The first insights in the catalytic mechanism were obtained by Vaaje-Kolstad *et al*.[27] in one of the early reports on LPMOs. They showed that LPMO catalysis was observed neither in the presence of O_2 nor reducing agent. Moreover, ^{18}O isotope labelling experiments showed that molecular oxygen was the source of oxygen atoms inserted into the oxidized products (see also discussion on H_2O_2 below). The enzymatic action was not inhibited by catalase or superoxide dismutase suggesting that the binding of O_2 the active site could be a critical step in the catalytic cycle and that free superoxide or peroxide species were not released in solution. In addition, it was shown that reaction of Cu(I)–LPMO with O_2 in the absence of polysaccharide reaction (non-coupled turnover *vs* coupled turnover in presence of the polysaccharide) generated H_2O_2 in solution, and was proposed to be side reaction.[27] Using similar methods, the same conclusions were obtained also for AA9 LPMOs by Beeson *et al.*[98] Overall, these studies allowed a proposal for the following general reaction:

$$O_2 + 2e^- + 2H^+ + R\text{–}H \xrightarrow{\text{Cu(II)–LPMO}} R\text{–}OH + H_2O$$

Mechanisms that rely on O_2 activation all share a common starting point in which the Cu(I) reacts with O_2 to form a Cu(II)–superoxide complex, $[Cu(II)–O_2]^+$. From here various possible mechanism differ in terms of the timing of proton and electron transfers to the active site, and in terms of which Cu–oxygen species is able to perform hydrogen atom abstraction (HAA) from the substrate: Cu(II)–superoxide, a Cu(II)–oxyl species $[Cu(II)–O^\bullet]^+$ or a Cu(III)–hydroxide species, $[Cu(III)–OH]^{2+}$.[94] Cellulose and chitin have very strong C1–H/C4–H bonds, with bond dissociation energies (BDEs) in the order of 100–104 kcal mol^{-1}, hence an important thermodynamic consideration is that the active Cu–oxygen intermediate needs to have the oxidising power to be able to abstract a hydrogen atom from the substrate.[93] Following this consideration, Hedergård *et al.* calculated the BDEs for various possible Cu–oxygen intermediates using DFT and found that HAA from a Cu(II)–superoxide intermediate always yielded an endothermic reaction, while HAA from a Cu(II)–oxyl or a Cu(III)–hydroxide generated an exothermic reaction.[93] Thus, these last two intermediate were the preferred candidates for HAA from the substrate. However, it should be noted that arguing against the $[Cu(III)–OH]^{2+}$ unit as the active oxidant in LPMOs is the likely inability of the initial product HAA, the $[Cu(II)–OH_2]^{2+}$ unit, to undergo rebound to yield the final hydroxylated product (see **Figure 1.21**).

The current understanding of the LPMO catalytic mechanism (with O_2 activation) is essentially based on theoretical studies, as there are no experimentally characterized Cu–O_2 intermediates in the catalytic cycle. These computational studies, which are based on DFT cluster models of the active site[99] or QM/MM models including the entire enzyme,[100,101] indicate a Cu–oxyl intermediate as the likely intermediate capable of HAA from the substrate (**Figure 1.21**).

From an experimental point of view, Kjaergård *et al*. investigated O_2 reactivity with an AA9 LPMO, *T. aurantiacus Ta*AA9, with a combination of stopped-flow absorption and freeze−quench EPR spectroscopy.[63] They showed that the reaction of Cu(I)−*Ta*AA9 with O_2, in the absence of substrate, rapidly regenerated the resting state Cu(II) signals with a minimum rate constant > 0.15 s^{-1} (estimated second order rate constant ~500 M^{-1} s^{-1} at 20 °C). On the basis of reported redox potentials for AA9 LPMOs ~275 mV (*vs* SHE) and the potential for the one-electron reduction of O_2 to O_2^- , –165 mV (*vs* SHE),

they calculated a rate of an hypothetical outer-sphere electron transfer of $\sim 4.5 \times 10^{-4}\ s^{-1}$, using Marcus theory, which was $\sim 10^3$ slower than the rate of Cu(I) re-oxidation derived form of the EPR and stopped-flow data. Therefore, they suggested that the one-electron reduction from Cu(I) to O_2 was likely to proceed via in inner-sphere mechanism involving rapid formation of $[Cu(II)–O_2]^+$. However, they did not directly observe a bound Cu(II)–superoxo intermediate. In addition, a recent study on a similar AA9 LPMO, *Hj*AA9, observed a much slower rate of re-oxidation of the Cu(I) by O_2, with a second order rate constant of ~50 $M^{-1}\ s^{-1}$ at 20 °C.[102] However, even this slower rate would still be too fast compared to the estimated rate for an outer-sphere electron transfer; hence the inner-sphere mechanism still remains the favourite one as compared to the outer-sphere mechanism.

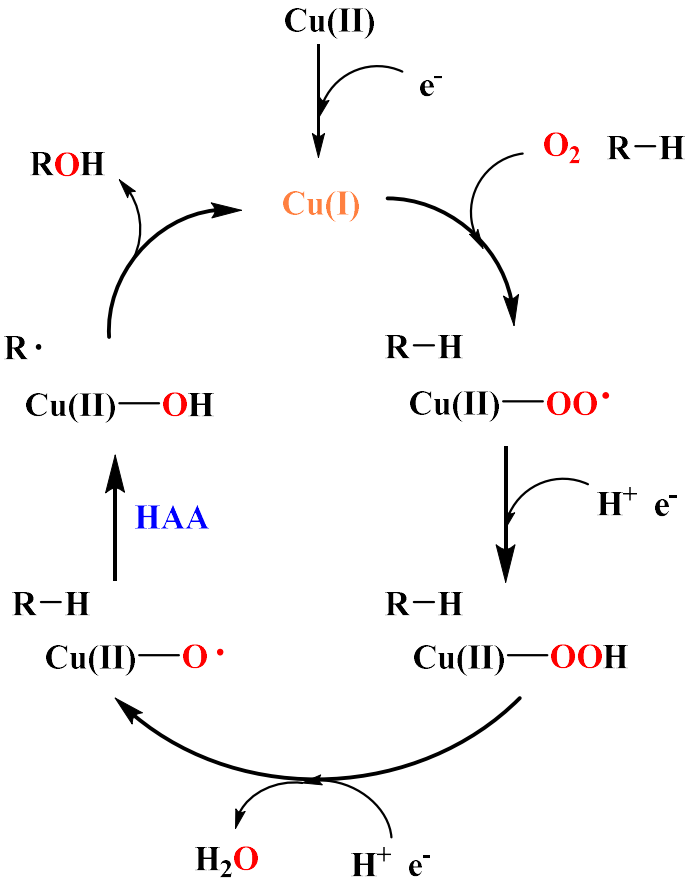

Figure 1.21 Schematic summary of the proposed mechanism for hydrogen atom abstraction (HAA) by an LPMO using O_2 and an external reducing agent.

In 2017, a study from Bissaro *et al.* demonstrated that LPMO reactions can be driven by H_2O_2 and suggested hydrogen peroxide could be the relevant oxidant used by the enzyme.[29] This claim was supported by several factors: in the absence of O2 and by controlling the H_2O_2 supply, fast reaction kinetics were achieved that formed the same type of products obtained with O_2 as oxidant. Moreover, isotope labelling experiments using $H_2{}^{18}O_2$ showed that the oxygen atoms inserted into the products derived from hydrogen peroxide. On the other hand high level of H_2O_2 in solution was found to be detrimental and led to enzyme inactivation. This type of reactivity was shown for both AA9s and AA10s LPMOs and for both cellulose and chitin as substrates (although with different reaction rates). Lastly, they reported that under turnover conditions using only O_2 as the oxidant, the addition of horseradish peroxidase inhibited LPMO activity. The lack of inhibition previously reported (and again demonstrated by Bissaro *et al.*)[27] by catalase was attributed to the substantially lower Michaelis constant K_m of peroxidase, allowing it to compete more effectively with the LPMO for available peroxide. Overall, the enzymatic activity is consistent with the following reaction:

$$H_2O_2 + R\text{–}H \xrightarrow{\text{Cu(I)–LPMO}} R\text{–}OH + H_2O$$

The authors suggested various potential mechanism, including a possible involvement of $^{\bullet}$OH radicals generated through a Fenton-like mechanism. Following this study, several theoretical investigations have studied the H_2O_2 activation pathway, in order to identify the key reactive intermediate that perform HAA from the substrate. With the use of QM/MM calculations, Wang *et al*. addressed H_2O_2-dependent catalysis in the *Ls*AA9–cellotriose complex showing that there is an efficient mechanism to break the O−O bond in H_2O_2 *via* a one-electron transfer from the LPMO-Cu(I) to form an $^{\bullet}$OH radical and a Cu(II)−OH species.[103] In addition, the calculations showed that the formed $^{\bullet}$OH radical preferred to abstract a hydrogen atom from the $[Cu(II)-OH]^+$ species, to form a $[Cu(II)\text{-}O^{\bullet}]^+$ species, rather than directly abstracting a hydrogen from the substrate. After this step, it is the $[Cu(II)\text{-}O^{\bullet}]^+$ which is able to perform HAA from the C4 atom of the substrate, as shown in **Figure 1.22** (the same favoured reactive intermediate found in the O_2 catalytic cycle, see above). A key concept of this study is that the $^{\bullet}$OH radical formed after the O–O bond cleavage is not free to diffuse in solution, but instead is stabilized

though a series of H-bonding interactions with the enzyme, that form a sort of 'cage' that orients it to perform HAA on the $[Cu(II)-OH]^{+}$.[103] (It is worth noting that generation of free hydroxyl radical in solution would likely to be inconsistent with regioselective C1 or C4 oxidation.) Moreover, a subsequent QM/MM study by Bissaro *et al*. on the *Sm*AA10 LPMO and chitin as substrate, found a similar result where the generated OH radical appeared to be confined and oriented by hydrogen bonds, from both the substrate and the protein, in order to perform HAA from the $[Cu(II)-OH]^{+}$.[104] Their overall proposed mechanism is consistent with that shown in **Figure 1.22**.

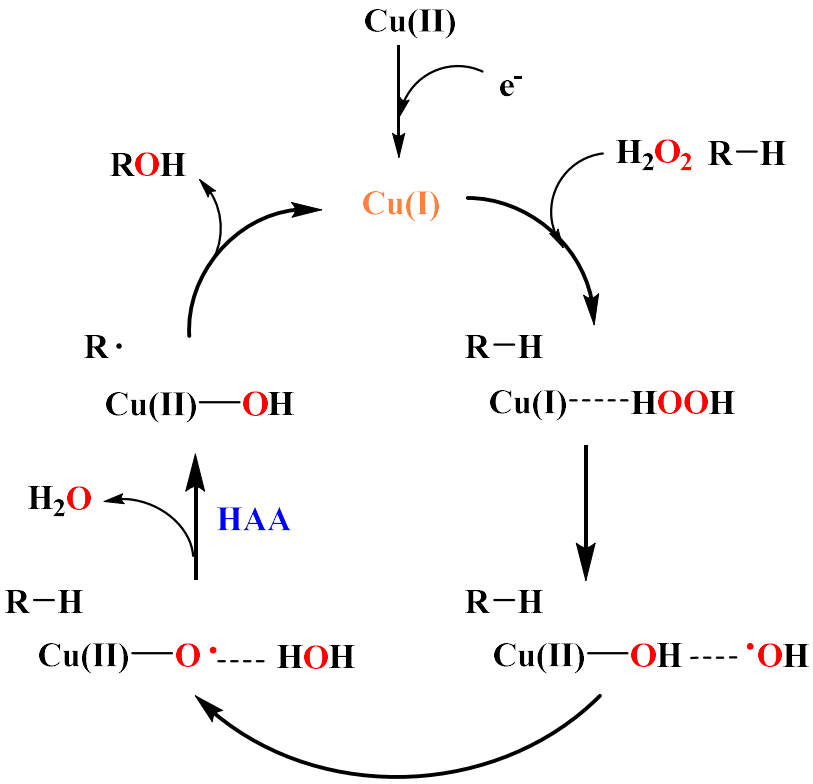

Figure 1.22 Schematic summary of the proposed mechanism for hydrogen atom abstraction (HAA) by an LPMO using H_2O_2. Note that the scenarios for H_2O_2-driven catalysis generally imply that the copper stays reduced in between catalytic cycles and no external reducing agents are required, as opposed to the O_2-driven catalysis shown in **Figure 1.21**

Overall, these theoretical studies suggest that the relevant Cu-based active intermediate responsible for the HAA from the substrate is always a $[Cu(II)\text{-}O^{\bullet}]^{+}$ species, irrespective of whether H_2O_2 or O_2 is activated by the Cu(I) active site in LPMOs. This

intermediate remains a very elusive species that has never been characterized before, not only in LPMOs chemistry but neither in other Cu enzymes or model complexes; it will certainly be the focus of much research effort in the future.

Currently, it is not clear which is the most relevant co-substrate between O_2 and H_2O_2 and if certain reaction conditions always favour one pathways with respect to the other. However, during turnover conditions with O_2 as co-substrate, low levels of H_2O_2 could be generated *via* several known mechanisms. The most direct source of H_2O_2 generation would be by Cu(I)−LPMOs that are not bound to the substrate reacting with O_2 to form superoxide which could then disproportionate to O_2 and H_2O_2 (non-coupled turnover), as mentioned above.[28] In cases where excess reducing agent would be present under turnover conditions in the presence of O_2, peroxide will be generated by LPMOs that are not bound to the substrate. Hence, because of the generally faster enzymatic kinetics obtained when H_2O_2 is used as co-substrate (see **Section 1.10**), some authors argued that H_2O_2 is the only relevant kinetic co-substrate in LPMO catalysis.[95] Lastly, it should be noted that in the H_2O_2 mechanism an external source of electrons is required to activate the Cu(II) site (*i.e.*, reduction to Cu(I)) but is not required for turnover with peroxide, as H_2O_2 contributes the two electron equivalents required for the reaction and therefore potentially solving the issue of how the reducing equivalents are delivered to the Cu active site during catalysis.[8]

1.10 LPMOs enzymatic kinetics

Detailed enzymatic kinetic analyses are scarce because of the difficulties in measuring them with insoluble substrates, however some available reports offer a basis for discussion.[95] In the early report from Vaaje-Kolstad *et al*. a rate of 0.017 s^{-1} was reported for the oxidation of β-chitin by SmAA10A using O_2 as oxidant. Another study on the *Nc*AA9C LPMOs reported a rate of 0.03 s^{-1} for the oxidation of cellulose, using O_2 as co-substrate.[74] Moreover, Frandsen *et al*. measured the kinetics of the *Ls*AA9 catalysed oxidation of a soluble oligosaccharide (cellotetraose, C4) allowing for the first time to use a Michaelis-Menten model for the enzymatic kinetic. They found a k_{cat} 0.11 s^{-1} and a K_m for C4 of 43 μM (k_{cat}/K_m of 2.6×10^3 M^{-1} s^{-1}). Overall, these data suggest that the reaction rates with O_2 are relatively slow, regardless of the substrate used.

On the other hand, reaction rates using H_2O_2 instead of O_2 are typically much higher. Using [^{14}C]-labelled chitin, Kuusk *et al*. reported Michaelis-Menten kinetics for the oxidation of chitin by *Sm*AA10A LPMO, with a k_{cat} of 6.7 s^{-1} and a K_m of 2.8 μM for chitin and H_2O_2 (k_{cat}/K_m for H_2O_2 is 2×10^6 M^{-1} s^{-1}).[105] In a subsequent study, Hangasky *et al*. measured the kinetics of *Myceliophthora thermophile* AA9 (*Mt*AA9E) catalyzed oxidation of cellohexaose (G6) evaluating both O_2 and H_2O_2 as cosubstrates.[106] They reported a k_{cat} of 0.28 s^{-1} and a K_m of 230 μM for O_2, as compared to a k_{cat}/K_m value for H_2O_2 of 1×10^3 M^{-1} s^{-1}. When H_2O_2 was used as a co-substrate, observed rates were much higher, too fast to be accurately measured.[106] Hence, on the assumption that more than 50% of added H_2O_2 had been consumed, the authors estimated observed rate constants (k_{obs}) of 4.8−15 s^{-1} for concentrations of H_2O_2 ranging from 12.5 to 100 μM.

The study from Hangasky *et al*. also found that the reaction with H_2O_2 leads to nonspecific oxidation of the polysaccharide (hence not only limited to position C4 of the polysaccharide) while the O_2 reaction leads to regioselective substrate oxidation. This observation is consistent with an oxidation mechanism of a hydroxyl radical-based mechanism as compared to the more controlled reaction with O_2. However, this effect was not observed in other reports where the products obtained through H_2O_2-driven catalysis were indistinguishable with respect to those obtained via O_2-driven catalysis.[29,102]

On this point, an interesting consideration is that different oligomer substrates have different binding modes on the same enzyme, with significant effects on the spatial arrangements near the Cu active site, as demonstrated by Simmons et al.[82] The QM/MM studies show that in order to have a controlled generation of $^{\bullet}$OH radicals, interaction of the active species with both the active site residues and the substrates is fundamental. Therefore, it is conceivable that specific background reactions occur for certain LPMO-substrate combinations, where substrate binding is not ideal/optimal.[82] This consideration, together with the fact that in presence of reducing agents both coupled and non-coupled turnover (generation H_2O_2) can happen, yields an overall complicated picture where reaction conditions are important in determining which catalytic pathway may prevail. Currently, it is not clear whether the O_2 mechanism or the H_2O_2 mechanism is the more biologically relevant and further studies are needed to better understand the LPMO reactivity.

1.11 Electron transfer and the role of reducing agents

The reduction of LPMO-Cu(II) to LPMO-Cu(I) is generally accepted as a necessary step to activate the enzyme resting state and after this step additional reducing equivalents may or may not be necessary, depending on the co-substrate (O_2 or H_2O_2). It has been demonstrated, that this reduction step can be carried out by a wide variety of reducing agents, including small organic molecules, such as ascorbic acid,[27] reduced glutathione,[27] cysteine,[75,107] a wide range of plant biomass or fungal phenolic compounds,[108] lignin and its fractions,[49,109] and oxidoreductases.[31,110]

The standard reduction potentials $E°$ reported for AA9s at pH 6 are ~150−330 mV *vs* the SHE and potentials of AA10s have been reported in the range ~220−370 mV *vs* SHE.[8,107] Currently, no reduction potentials have been reported the other families of LPMOs, although they are likely to be within the same range. The positive reduction potential and the easily accessible position of the Cu ion on the enzyme surface explain why the Cu(II) is easily reduced by many reductants. The rate of reduction of the resting state by small organic reductants like ascorbate is generally very fast, in the millisecond time range (for both AA9s and AA10s), which if compared with the much slower enzymatic turnover rate (in the minutes range), suggests that the activation of the Cu(II) resting state is not the rate limiting step of an O_2 driven LPMO reaction.[104,108] In order to facilitate LPMO catalysis, an electron donor must have a potential that is close to or below that of the LPMO copper active site (≤200−300 mV). Indeed, Kracher *et al*. studied a series of reducing agents and found that those with lower potentials were correlated with higher LPMO turnover rates.[108] A similar correlation was obtained by Frommhagen *et al*. using variation in pH to manipulate redox potentials of reductants.[111] Several studies have shown that higher concentrations of reluctant lead to higher catalytic rates and higher consumption of O_2, during O_2-driven catalysis.[73,112] However, high concentration of reducing agents also led to faster inactivation of the LPMO. It should be noted that higher reductants concentrations are also more likely to favour side reactions like un-coupled turnover, and that most of these reductants can react with O_2 themselves generating H_2O_2, further complicating the system.

One of the most characterized reducing agents for AA9 LPMOs is cellobiose dehydrogenase (CDH)[31,107,113] an extracellular flavocytochrome enzyme that is capable of storing two electrons and donating them to the LPMO active site. CDH is thought to

be one of the most relevant *in vivo* reducing agents for LPMOs; indeed the deletion of the CDH-encoding gene in LPMO-expressing fungi results in reduced cellulose activity that is partially restored upon reintroduction of a CDH to the deletion variants.[31,50]

The CDH consists of a flavin adenine dinucleotide (FAD)-binding domain, a cytochrome *b* domain, and some CDHs have a CBM domain. The FAD-binding domain is rapidly reduced by cellobiose (which is an abundant substrate available during cellulosic biomass degradation, see **Figure 1.6**) which then transfers the electrons to the cytochrome *b* domain. Cyclic voltammetry and rapid kinetic measurements show that the cytochrome domain ($E°$ ~100–150 mV *vs* SHE) of the CDH is responsible for ET to the LPMO.[108] Even though the existence of a putative CDH "docking" site on AA9 LPMOs has been proposed,[114] experimental data and computational modeling suggest direct electron transfer at the active site of the LPMO.[80,92] It is however unclear if this direct interaction can happen also during LPMO catalysis as this interaction is likely not possible because the active-site surface will be blocked by substrate binding. Further studies are warranted to identify the nature and timing of the interaction between LPMOs and CDH as electron donor.

1.12 Aims of this work

The discovery of LPMOs has certainly represented a breakthrough for the understanding of enzymatic biomass degradation and its industrial implementation for the production of biofuels. From a molecular point of view, LPMOs are also very interesting enzymes because they offer new insights into copper–oxygen chemistry and into how enzymes catalyse the oxidation of strong C–H bonds in a wide variety of polysaccharides. Despite the progresses in the last ten years from their discovery in 2010, there are still many outstanding questions that need to be answered in order to fully understand the LPMOs mode of action.[8,28,95] Among these, there is the already mentioned identity of the key Cu–oxygen intermediate, able to perform HAA from the target C–H bond (but the identity of the other intermediates of the catalytic cycle remain to be elucidated as well); which is the relevant co-substrate in physiological conditions between O_2 and H_2O_2 and, in case of O_2 reactivity, how electrons are delivered to the Cu active site while the enzyme is bound to its substrate. Furthermore, another key challenge lies in the multitude of

reactions that may take place at the Cu site (coupled and non-coupled pathways), which often complicate the interpretation of experimental results. This issue is even more relevant when using 'industrial' substrates (*i.e.*, co-polymeric and complex), as opposed to 'clean' substrates like oligosaccharides or pure forms of cellulose of chitin.[95]

In this respect, several experimental and computational studies showed that the presence of the correct substrate for a particular LPMO is important in directing the reactivity towards the target C–H bond and to avoid deleterious non-coupled pathways, leading to enzyme damage and inactivation (see **Section 1.7** and **1.9**). Moreover, the binding of substrate to some LPMOs significantly perturb the EPR spectrum of the Cu(II) resting state, suggesting that significant changes occur at the copper active site in the presence of substrate, which might be of key importance for O_2/H_2O_2 activation and hence catalysis.[65,70,77,82] In order to obtain a more detailed picture of the substrate effect on the Cu(II) site electronic structure, we report a multi-spectroscopic (EPR, UV-vis, CD and MCD) and theoretical (DFT and CASSCF) study of the Cu(II) resting state and of the relative enzyme/substrate complex for the cellulose-active *Ls*AA9 LPMO, used as model enzyme. Furthermore, the same methodology was also applied to study the active site of a chitin-active LPMO from the AA11 family, the *Ao*AA11 LPMO. Potential similarities and differences between *Ls*AA9 and *Ao*AA11 spectroscopic properties due to differences in the Cu active site will be discussed and also compared with the available data for the chitin-active AA10 LPMOs.

When hydrogen peroxide is used as a co-substrate by LPMOs instead of O_2, the rate of reaction is high but it is accompanied by rapid inactivation of the enzymes, presumably through protein oxidation. Moreover, as mentioned above, this protein oxidation is more significant if the enzyme reacts with H_2O_2 in the absence of substrate. Herein, we present a multi-spectroscopic study, augmented with mass spectrometry and DFT calculations, to show that the product of reaction of *Ls*AA9 LPMO with H_2O_2 at higher pHs is a singlet Cu(II)−tyrosyl radical species, which is inactive for the oxidation of polysaccharide substrates. On the basis, we propose from the application of Marcus theory that the active site tyrosine is part of a "hole-hopping" charge-transfer pathway formed of a network of conserved tyrosine and tryptophan residues, which can protect the protein active site from inactivation during non-coupled turnover.

2 *Ls*AA9 interaction with cellohexaose

2.1 Introduction

The auxiliary activity 9 (AA9) family of lytic polysaccharide monooxyganases is a family of enzymes widely distributed among filamentous fungi and mostly active in cellulose degrading processes. Originally classified as glycoside hydrolase family 61 (GH61) in the CAZy database, after the first reports of endoglucanase activity in enzymes belonging to this family,[46] Quinlan *et al*. (following the previous discovery of chitin active LPMOs by Vaaje-Kolstad *et al*.)[27] demonstrated that the enzymes members of this family are not glycoside hydrolases but are instead LPMOs.[30] Therefore, the GH61 family was reclassified as AA9 family in the CAZy database.[25] The amino acid sequence similarity among the AA9 LPMOs is low, even between those secreted by the same fungi species, but they share the same three dimensional structure and the Cu active site (see **Section 1.6**). Fungi can secrete many LPMOs, ranging from several to more than thirty different ones, which can have different substrate specificities and regioselectivities, with respect to oxidation at position C1/C4 of the polysaccharide chain. The wide diversity of AA9 LPMOs in the fungal kingdom and their substrate specificities has been recently reviewed by Zhang *et al*.[115]

One of the major challenges in the characterization of LPMOs reactivity is represented by the insoluble nature of their substrates (like crystalline cellulose or chitin), as it severely limits the number of the standard experimental techniques which can be used; for example the study of their enzymatic kinetics, as generally requires soluble substrates. However, some AA9 LPMOs are able to act on shorter soluble oligosaccharides and, even though the biological relevance of this reactivity could be questioned, they are excellent candidates for laboratory studies.[65,70,73,80,82,116]

Frandsen *et al*. reported the first crystal structures of an LPMO-substrate complex, obtained by soaking crystals of *Lentinus similis* AA9 (*Ls*AA9) LPMO in a solution containing cello-oligosaccharides substrates. The cellohexaose (C6) does not coordinate directly to the Cu ion, but instead it is positioned directly above the Cu equatorial coordination plane, displacing the axial H_2O and stacking the +1 glycosyl unit on top of the His-1 imidazole ring. Moreover, the C6 forms several interactions with the active site residues: hydrogen bonds involving Asn-28, His-66, Asn-67, Ser-77, His-78 and the 'pocket water' molecule, and a lone pair–aromatic interaction with His-1 (**Figure 2.1**).

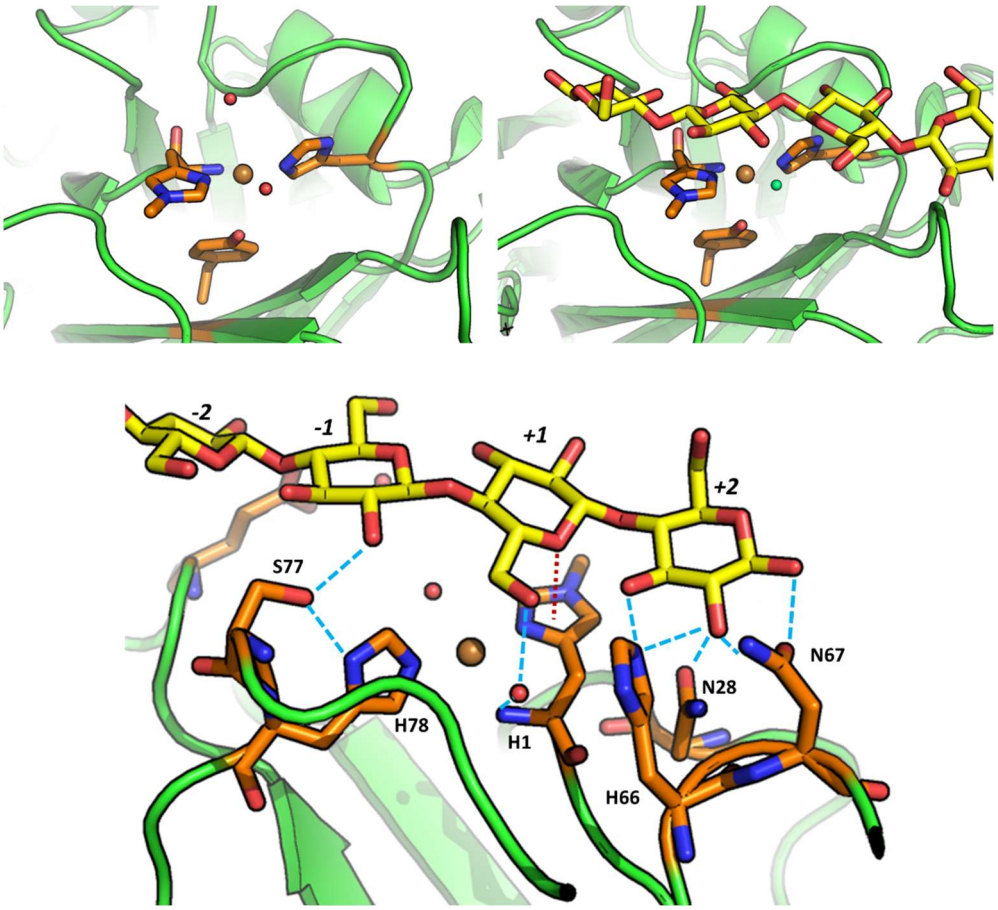

Figure 2.1 *Ls*AA9 copper active site in the resting state (top left, PDB 5ACH) and in the enzyme-substrate bound complex (top right, PDB 5ACF). Copper is represented as gold sphere, the coordinating H_2O as red spheres and the Cl^- as green sphere. The histidine and the tyrosine ligands are coloured in orange, the cellohexaose substrate in yellow and the enzyme secondary structure is in green. Residues involved in substrate interaction, near the active site, identified by X-ray crystallography (bottom, PDB 5ACI). The light blue dashed lines represent the hydrogen bonding interactions involving the enzyme and the substrate, while the lone pair–aromatic interaction is in dark red.

These structures suggested that the most likely position for O_2 (or H_2O_2) to bind is the equatorial position *trans* to the N-terminal amine. Moreover, the same structures revealed that this equatorial position was occupied by a chloride ion, which could be considered a potential mimic of superoxide or another activated oxygen species.[65]

EPR spectroscopy, on the other hand, showed that the substrate binding to the active site is accompanied by a significant perturbation of the Cu(II) spin Hamiltonian parameters, and both large crystalline substrates (like cellulose) and shorter oligosaccharides (like C6) produced the same perturbations in the EPR spectrum, suggesting very similar substrate binding modes to the enzyme active site.[65,70,82]

Various substrate binding studies demonstrated that in presence of anions such Cl^- or CN^-, the enzyme substrate affinity is greatly enhanced suggesting a cooperative effect of the anion and substrate binding, although the nature of this effect is not currently well understood. These observations, together with the consideration that Cl^-/CN^- can behave as O_2^- mimics, suggest that the events leading to the ternary complex formation (enzyme/substrate/O_2) are coupled, in line with a recent kinetic study on an AA9 LPMO by Hangasky *et al.*[116]

In this context, we report here a multi-spectroscopic (EPR, UV-vis, CD and MCD) and theoretical (DFT and CASSCF) study of the enzyme/substrate complex, using the *Ls*AA9 LPMO and cellohexaose as substrate. We were able to determine spin Hamiltonian parameters and d-d transition energies for all the complex studied, which describe an overall Cu(II) electronic structure consistent with a tetragonally distorted octahedral coordination geometry. Furthermore, the His brace ligand environment forces the Cu(II) SOMO in a particular orientation which allows the formation of strong covalent bonds with exogenous ligands in the equatorial plane, which carried potential implications for O_2 activation during catalytic turnover of the enzyme.

2.2 Methods

2.2.1 Cloning, Protein Production and Purification

The *Ls*AA9 LPMO was produced and purified by Novozyme A/S following the procedure already reported by Frandsen *et al*.[65]

Briefly, the gene encoding *Ls*AA9 was PCR amplified from genomic DNA of *Lentinus similis* and cloned in *E. coli* using the forward primer F-P247JK (5′-ACACAACTGGGGATCCACCATGAAGT ACTCCATCCTCGGGCT-3′) and reverse primer R-P247JK (5′-CCCTCTAGA TCTCGAGCCTTGTCGAGCGACTCT ATCCA-3′), containing insertion sites for the vector pDau109 used for cloning. The fragments were then cloned into BamHl- and XhoI-digested pDau109 using an IN-FUSION Cloning Kit. Cloning of the genes into BamHl- and XhoI-digested pDau109 resulted in transcription of the *Ls*AA9 encoding gene under the control of a NA2-tpi double promoter. The treated plasmids and inserts were transformed into One Shot TOP10F chemically competent *E. coli* cells (Invitrogen) according to the manufacturer's protocol, spread onto Luria-Bertani (LB) plates supplemented with 0.1 mg/mL ampicillin and incubated at 37 °C overnight. Colonies of each transformation were cultivated in LB medium supplemented with 0.1 mg/mL ampicillin and plasmids were isolated using a QIAPREP Spin Miniprep Kit (QIAGEN).

The *Ls*AA9 gene was expressed in *Aspergillus oryzae* MT3568. A transformant producing the recombinant *Ls*AA9 was inoculated in 2 L of Dap-4C medium and incubated at 30 °C for 4 d. Mycelia were removed by filtration, and the medium was collected for purification. Ammonium sulfate was added to the sterile filtered medium to a conductivity of 200 mSi cm^{-1} and the pH adjusted to 7.5. The broth was applied to a 50/15 Butyl Toyopearl column (Tosoh Biosciences) equilibrated with 25 mM Tris, 1.5 M ammonium sulfate, pH 7.5. The column was washed in the same buffer and eluted with a gradient to 25 mM Tris, pH 7.5. Fractions containing *Ls*AA9 were combined and washed with milliQ water by ultrafiltration (10 KDa MWCO, PES filter, Sartorius) to a conductivity of 1.2 mSi/cm. The pH was adjusted to 8.0 and applied to a 50/40 Q Sepharose FF column (GE Healthcare) equilibrated with 20 mM Tris, pH 8.0. The column was washed in the same buffer and the enzyme eluted with a gradient from 0 to 0.5 M sodium chloride. Fractions containing *Ls*AA9 were combined and concentrated by

ultrafiltration using VivaSpin 20 (10 KDa MWCO, PES filter) spin concentrators. The purified enzyme was then frozen and stored at –20 °C before further characterization.

2.2.2 EPR Spectroscopy

Continuous wave (cw) X-band frozen solution EPR spectra were acquired on a Bruker EMX spectrometer operating at ~9.30 GHz, with modulation amplitude of 4 G, modulation frequency 100 kHz and microwave power of 10.02 mW (3 scans) at 165 K. *Ls*AA9, prepared as described above, was at 0.25 mM concentration in 20 mM sodium phosphate buffer at pH 6.0 with 10% *v/v* glycerol and, for the substrate-bound spectra, three equivalents of cellohexaose and 200 mM NaCl or NaBr were added to the protein solution. Note: presence/absence of glycerol does not affect the spectra.

Q-band spectra were acquired on a Jeol JES-X320 spectrometer operating at ~34.7 GHz, with modulation width 1 mT and microwave power of 0.75-1 mW at 113 K. The spectra of *Ls*AA9 (1.1-3.2 mM solutions) were collected in 20 mM sodium phosphate buffer at pH 6.0 with 10% *v/v* glycerol and, for the substrate-bound spectra, in the presence of two equivalents of cellohexaose and 200 mM NaCl or NaBr.

Spectral simulations were carried out using EasySpin 5.0.3 integrated into MATLAB R2016a software on a desktop PC.[117] Simulation parameters are given in **Table 2.1**. g_3 and $|A_3|$ values were determined accurately from the absorptions at low field. It was assumed that g and A matrices were axially coincident. Accurate determination of the g_1, g_2, $|A_1|$ and $|A_2|$ was obtained by simultaneous fitting of both X- and Q-band spectra. The superhyperfine coupling values for the nitrogen atoms could not be determined accurately, although it was noted that satisfactory simulation could only be achieved with the addition of two or three nitrogen atoms with the coupling values reported in **Table 2.1**. All data collection and spectra simulations with EasySpin were performed by Dr. Luisa Ciano.

Anisotropy between g_1/g_2 (degree of rhombicity) was quantified as R_g according to the following equation ($\Delta g_{\mathrm{i}} = g_{\mathrm{i}} - 2.0023$):[118]

$$R_g = \frac{2(\Delta g_2 - \Delta g_1)}{\Delta g_2 + \Delta g_1}$$

Table 2.1 EPR spin Hamiltonian parameters from simulations of cw X-band and cw Q-band spectra, collected at 165 K and 113 K respectively.

Parameter		*Ls*AA9		*Ls*AA9_C6_H_2O		*Ls*AA9_C6_Cl		*Ls*AA9_C6_Br	
		X-band	**Q-band**	**X-band**	**Q-band**	**X-band**	**Q-band**	**X-band**	**Q-band**
g values	g_1	2.051	2.051	2.053	2.053	2.038	2.045	2.034	2.036
	g_2	2.075	2.075	2.064	2.061	2.064	2.065	2.073	2.069
	g_3	2.278	2.278	2.270	2.270	2.234	2.234	2.220	2.222
A^{Cu} (MHz) [1]	A_1	50	50	35	35	10	10	10	10
	A_2	125	125	46	46	77	77	55	55
	A_3	465	465	518	515	517	517	525	525
A^N (MHz) [1]		32, 40, 43	32, 40, 43	32, 43, 40	32, 43, 40	19, 31, 36	19, 31, 36	31, 36	31, 36
A^X (anisotropic) (MHz) [1]	A_1	-	-	-	-	40	40	40	40
	A_2					43	43	335	335
	A_3					40	40	60	60
g strains (g_1, g_2, g_3)		-	-	0, 0.0005, 0	0, 0.0005, 0	-	-	0.005, 0, 0.005	0.005, 0, 0.005
A^{Cu} strains (MHz)				40, 40, 60	70, 40, 120	20, 30, 50	10, 30, 70	25, 50, 70	10, 45, 70
Line widths (Gaussian, Lorentzian)		0.6, 0.6	4.0, 4.0	0.3, 0.4	1.0, 1.0	0.2, 0.2	2, 2	0.5, 0.5	4, 4

[1] -The sign of the hyperfine coupling cannot be determined from the simulations, therefore they are all reported as positive. The nitrogen ligands are reported as single values as it is not possible to determine their anisotropicity from the experimental spectra; each reported value corresponds to a different nitrogen atom and is presumed to be the major axial coupling from nitrogen to the Cu(II). For the Cl^- and Br^- ligands the hyperfine tensor principal values along the g_1, g_2 and g_3 directions are reported. Estimated experimental errors: ±0.002 for *g* values; ±5 MHz for A_3^{Cu} values; ±10–15 MHz for A_1^{Cu} and A_2^{Cu}; ±4 MHz for A^N in *Ls*AA9 and *Ls*AA9_C6_Br, while ±2 MHz in *Ls*AA9_C6 and *Ls*AA9_C6_Br; ±5 MHz for A^{Cl} ; ±10 for A^{Br}.

2.2.3 Electronic Spectroscopy: UV-vis, CD and MCD

The UV−vis absorption spectra were acquired on a PerkinElmer Lambda 465 diode array spectrophotometer. CD spectra were recorded on a Jasco J810 spectropolarimeter. The spectra were recorded at room temperature with 0.5 mM Cu(II)–*Ls*AA9 in 20 mM Na phosphate pH 6.0, and with 3 equivalents of cellohexaose, 200 mM NaCl or 200 mM NaBr, where relevant. MCD spectra were recorded on a Jasco J-810 spectropolarimeter adapted to incorporate an Oxford Instruments Spectromag SM4000 magnetocryostat at the University of Nottingham. The sample solutions were loaded into cells of ca. 2 mm path length constructed from quartz discs separated by a rubber ring spacer and frozen in liquid nitrogen. The spectra were collected at ±3, ±5 and ±7 T magnetic fields and temperatures between 5 and 15 K. The sample composition for the resting state sample was: Cu(II)–*Ls*AA9 0.9 mM, 50% w/v sucrose in 20 mM Na phosphate pH 6.0, and with three equivalents of cellohexaose, 200 mM NaCl or 200 mM NaBr, where relevant. Sucrose was used as glassing agent. For the enzyme-substrate samples, the enzyme concentration was 0.4 mM for the *Ls*AA9_C6 complex, 0.4 mM for *Ls*AA9_C6_Cl complex and 0.9 mM for the *Ls*AA9_C6_Br complex; all other conditions were the same as the resting state one.

After the Gaussian deconvolution of UV-vis and MCD spectra of each sample, the C_0/D_0 ratio for each transition was determined with the following equation:

$$\frac{C_0}{D_0} = \frac{kT\ A_{MCD}}{\beta B\ A_{UV-vi}}$$

where A_{MCD} is the area under the MCD band, A_{UV-vis} is the area under the absorption band, k is the Boltzmann constant, β is the Bohr magneton, while T and B are the temperature and the field at which the MCD spectra were recorded respectively.

2.2.4 Theoretical calculations

Geometry optimizations were performed using the ORCA 4.1 software package.[119] The starting point of the geometry optimized structures was obtained from the coordinates of the *Ls*AA9 resting state structure (PDB 5ACI) and from cellohexaose-bound *Ls*AA9 crystal structure (PDB 5ACH) and included seven amino acid residues (His-1, Pro-29 Ser-77, His-78, His-147, Gln-162 and Tyr-164) with the following modifications:

carbonyl of His-1 and Pro-29 were replaced by a methyl group; Ser-77 was truncated by methyl substitution of Cα; His-78, His-147 and Tyr-164 were truncated by methyl substitution of Cβ, Gln-162 was truncated by methyl substitution of Cγ.[63] The choice of the Cu secondary coordination sphere residues included in the modelling was based on different considerations: His-147 and Gln-162 are conserved in the AA9 family and were shown to affect the catalytic activity of AA9 LPMOs;[56] Ser-77 forms an hydrogen bond with the Cu ligand His-77 and with the substrate, in the enzyme/substrate complex;[65] Pro-29 was found to be important in keeping the His-1 imidazole ring in the correct position, during geometry optimizations. The equatorial and axial H_2O ligands were retained in the resting state (Model1_2H_2O), while for the substrate-bound models two glucose units of the cellohexaose substrate were retained (those directly above the Cu ion, Model2_Sub_H_2O). Additionally, the 'pocket' water molecule that is hydrogen bonded to the amino terminus and the substrate was included in the model. The histidine brace equatorial H_2O ligand was then replaced with Cl^- or Br^- to generate the two halogen bound structures (Model3_Sub_Cl and Model4_Sub_Cl, respectively). A fifth model was built starting from the resting state, but with a deprotonated tyrosinate residue (Model5_Tyr). Asterisks in **Figure 2.2** indicate the atoms kept fixed during the optimization. The protonation states of the residues were assigned according to those obtained from the neutron crystal structures of an AA9 LPMO (PDB 5KTH) at pH 5.6 (pD 6.0).[58]

All geometry optimizations were performed at the DFT level of theory, using UBP86 (with RI approximation) as a functional.[120] As basis set, Def2-TZVP [121] was used on the Cu(II), the first coordination sphere nitrogen and oxygen atoms, or on the halide ions where relevant; Def2-SVP was used on all the remaining atoms. Empirical dispersion correction was accounted for using Grimme's D3 method with Becke−Johnson damping (D3BJ);[122] solvation effects were included with the conductor-like polarizable continuum model (CPCM, $\varepsilon = 4.0$), as implemented in ORCA. This solvation model was already employed with success in previous DFT cluster model studies on AA9 LPMOs active site.[63,103] Frequency calculations were performed on all optimized structures to ensure that the structures were local minima containing no imaginary frequencies aside from those due to the constrained atoms.[103]

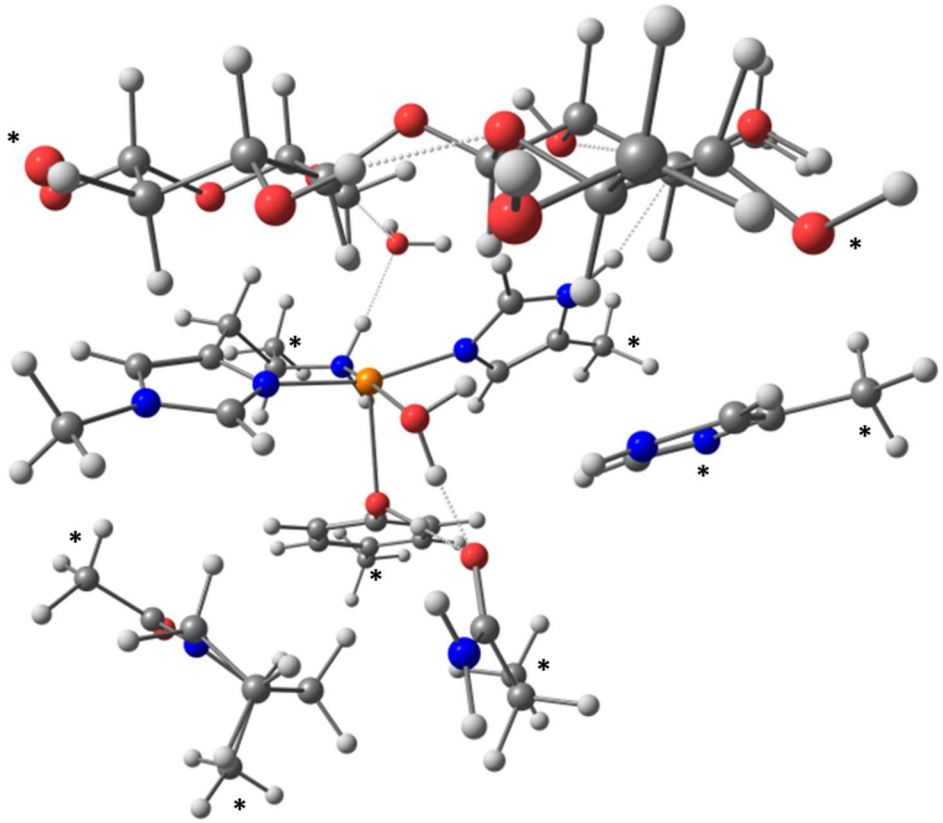

Figure 2.2 Cluster model of the substrate-bound *Ls*AA9A active site (Model2_Sub_H_2O). Atoms with fixed coordinates during the geometry optimization are indicated with asterisks. For the models without substrate, the same atoms were kept fixed apart from the two O atoms on the substrate. The Cu is shown in orange, the O atoms in red, the N atoms in blue, the C atoms in dark grey and the H atoms in white light grey.

EPR parameters were calculated at the DFT level of theory using B3LYP or B3LYP with 38% Hartree-Fock exact exchange.[123] The copper ion was described with the CP(PPP) basis set;[124] the amino terminus nitrogen atom, the coordinating water molecules and all the atoms on the imidazole rings were described with the IGLO-III basis set;[125] all the remaining atoms were treated with the Def2-SVP basis. The integration grid was kept large through all the calculations (AngularGrid = 7 for all the atoms and IntAcc = 6 on the Cu(II) ion) to ensure that the core density was correctly described. Solvation effects were included with the Conductor-like polarized continuum model (CPCM, $\varepsilon = 4.0$).

The *g* tensor principal values were calculated through the solution of the coupled perturbed Kohn-Sham equations (with perturbations represented by the Zeeman interactions with the external magnetic field), as implemented in ORCA.[126] The origin was chosen as the center of the electronic charge.[127] The calculations included the

relativistic mass correction, diamagnetic spin-orbit, and paramagnetic spin-orbit terms. The hyperfine coupling calculations included the Fermi contact term, the spin–dipolar contribution and the spin–orbit coupling correction (SOC) for the Cu(II) and the halide ions. The paramagnetic SOC term was calculated with the spin–orbit mean field concept (SOMF(1X) in ORCA).[128] The calculation of the nitrogen hyperfine tensors only included the first order terms, since SOC corrections are small (< 1 MHz) for light ligand nuclei.[129,130]

For the exited states calculations with TD-DFT and CASSCF methods, the models were reduced in size to reduce the computational cost, removing the Pro-29 and His-147 residues. The TD-DFT UV-vis spectra were calculated using the Tamm−Dancoff approximation,[131] the CAM-B3LYP functional,[132] the Def2-TZVP basis set on all atoms, together with the RIJCOSX approximation with a dense integration grid (ORCA Grid 5).[133]

The CASSCF method[134] was employed for calculation of the ligand field transition energies, together with the Def2-TZVP basis set on all the atoms in the models.[135] A minimal active space CAS(9,5), comprising only d-electrons was used in the calculation, together with the NEVPT2 methodology[136] to calculate the effects of dynamic electron correlation. The effects of spin–orbit coupling were considered using the spin–orbit mean-field (SOMF) approximation,[128] as implemented in ORCA. As a starting point to the CASSCF calculations, quasi-restricted orbitals (QROs) from DFT calculations (B3LYP/Def2-TZVP) were employed.[137]

2.3 Results

2.3.1 EPR Spectroscopy

Continuous wave EPR spectra were collected at both X- and Q-band frequencies on *Ls*AA9 (at 165 K and 113 K, respectively) and its different substrate-bound complexes to determine their spin Hamiltonian parameters (SH). The simultaneous fit of the spectra at both frequencies allowed the determination of accurate values for the Cu(II) g matrix values and metal hyperfine coupling constants (A^{Cu}). In two cases (*Ls*AA9_C6 and *Ls*AA9_C6_Cl), this fitting procedure yielded slightly different values for g_1 and g_2 (Table **2.1**) and therefore the average value of the two was used for data analysis. A summary of SH parameters obtained from the spectra are reported in **Table 2.2**, while the experimental spectra with their relative simulations are shown in **Figure 2.3**.

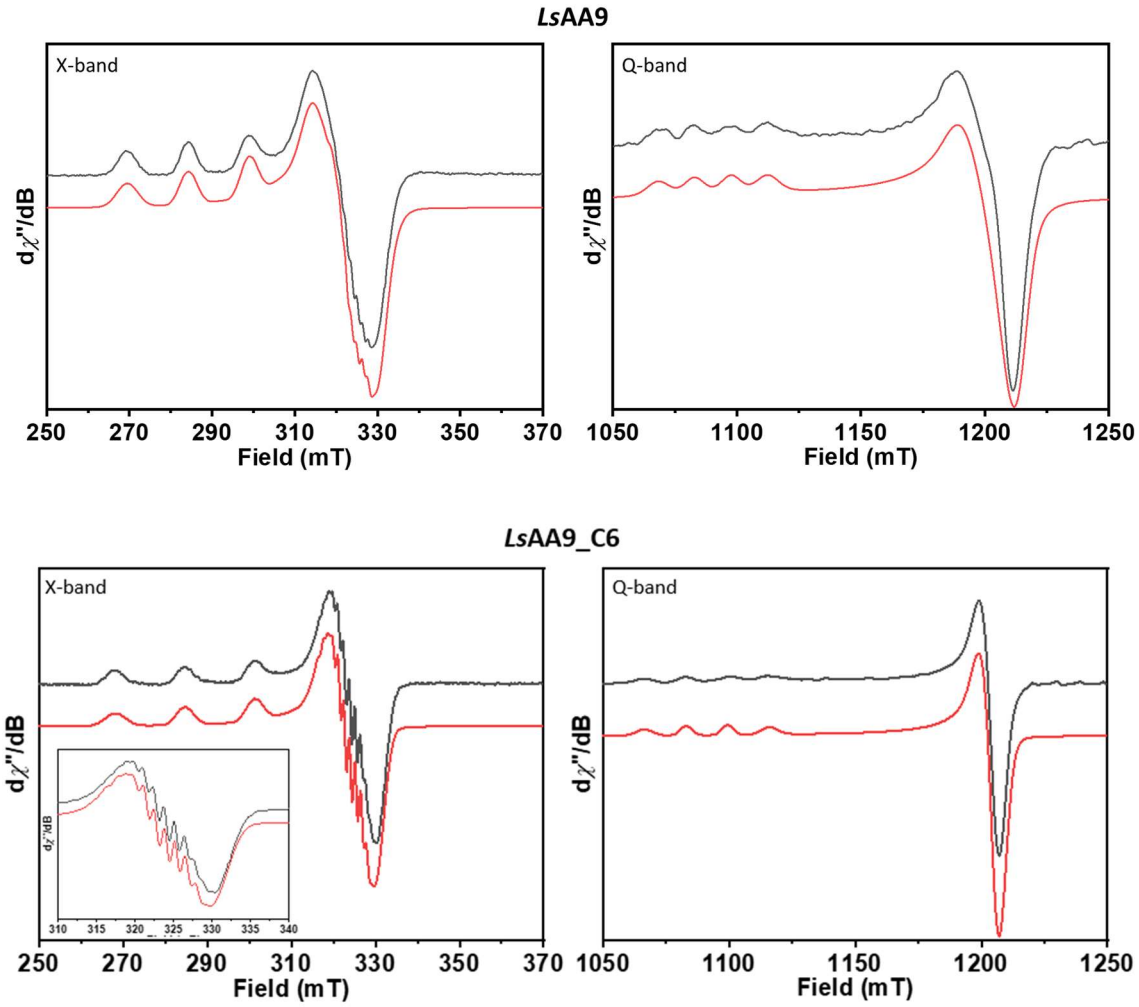

(Figure continued on next page)

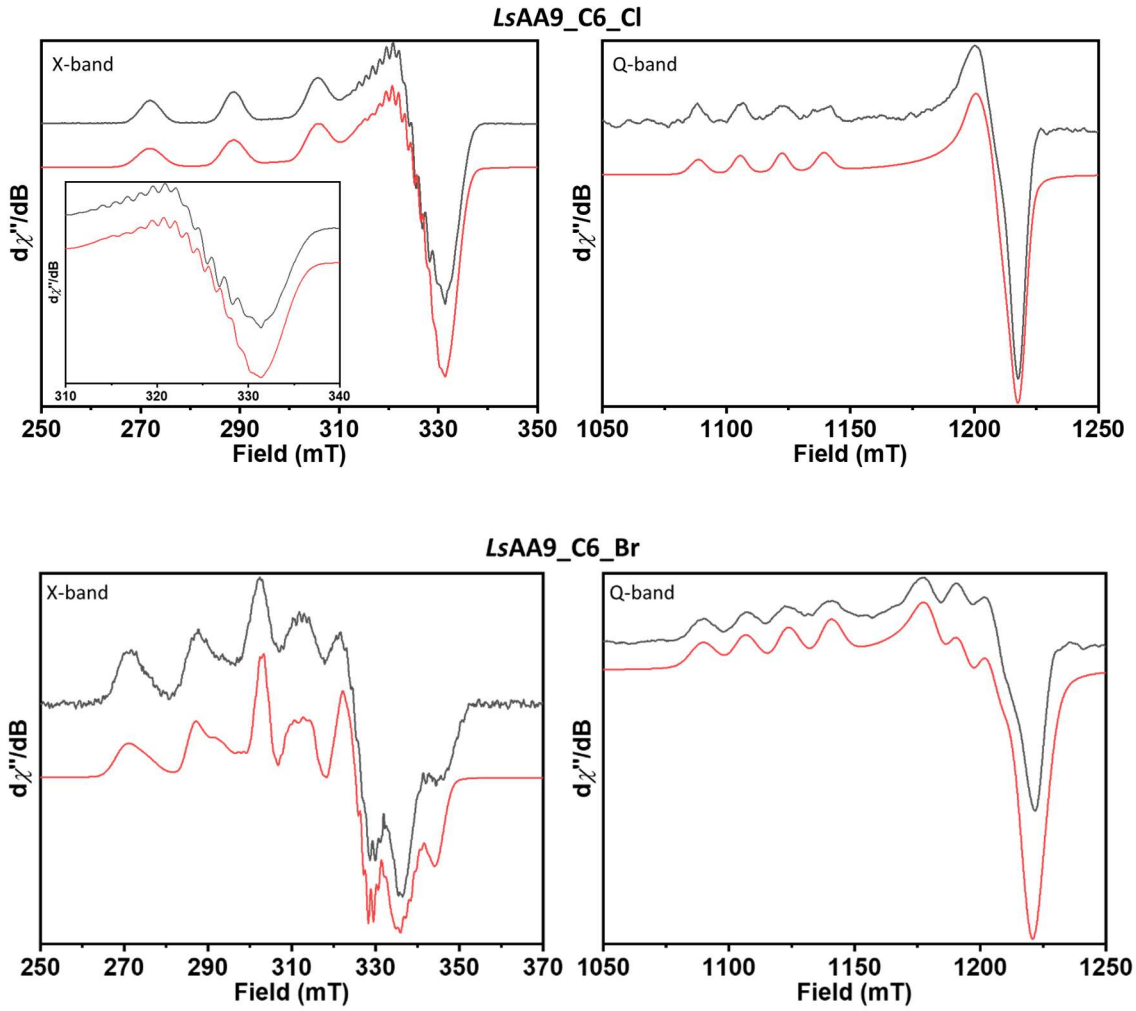

Figure 2.3 X-band and Q-band spectra for *Ls*AA9, *Ls*AA9_C6, *Ls*AA9_C6_Cl and *Ls*AA9_C6_Br (black) together with their respective simulations (red). The insets show a zoom of the g_1/g_2 region of the spectra to better visualize the superhyperfine patterns in *Ls*AA9_C6 and *Ls*AA9_C6_Cl. Simulation parameters are reported in **Table 2.1**.

The resting state (*Ls*AA9) is characterized by a near-axial set of *g* values ($g_3 > g_2 \approx g_1$, $R_g = 0.40$) and with $|A_3^{Cu}| > |A_2^{Cu}| > |A_1^{Cu}|$, with an overall spectral envelope indicating a ground state semi-occupied molecular orbital (SOMO) with mostly $d(x^2–y^2)$ character, typical for type 2 Cu sites found in metalloproteins.[91] These parameters are in good agreement with those already reported for *Ls*AA9 by Frandsen *et al*. on the basis of X-band EPR only,[65] and consistent with a Jahn-Teller distorted octahedral coordination geometry for the Cu ion, as shown in the X-ray structure of the enzyme (**Figure 2.1**). In this structure the equatorial coordination plane is defined by the three nitrogen atoms of the histidine brace and an exogenous water molecule. In the two axial positions, the –OH

group from the Tyr-164 residue and a second water molecule complete the coordination sphere (**Figure 2.4**).

Table 2.2 Experimental *g* matrix and *A* matrix values derived from simulation of frozen solution EPR spectra (continuous wave X- and Q-band). *A* values are reported in MHz.

g_1	g_2	g_3	R_g[1]	$A_1^{Cu\ 2}$	$A_2^{Cu\ 2}$	$A_3^{Cu\ 2}$	$A^{N\ 2,3}$			$A^{Cl/Br\ 2,4}$
***Ls*AA9**										
2.051	2.075	2.278	0.40	50	125	465	32	40	43	-
***Ls*AA9_C6**										
2.053	2.062	2.270	0.26	35	46	518	32	40	43	-
***Ls*AA9_C6_Cl**										
2.042	2.065	2.234	0.45	10	77	517	19	31	36	40 43 40
***Ls*AA9_C6_Br**										
2.035	2.071	2.221	0.71	10	55	525	31	36	-	40 335 40

[1]-Rhombicity calculated as $R_g = 2(\Delta g_2 - \Delta g_1)/(\Delta g_2 + \Delta g_1)$, with $\Delta g_i = g_i - 2.0023$.

[2]-Signs of the hyperfine coupling cannot be determined from the simulations, so only their magnitude $|A|$ is reported. Estimated experimental errors are reported in **Table 2.1**.

[3]-The N atoms hyperfine coupling is reported as single values because the experimental spectra are not resolved enough to allow estimation of their anisotropicity. Estimated experimental errors are reported in **Table 2.1**.

[4]-For the halide hyperfine coupling, it is possible to estimate their *A* matrix principal values, which are reported as couplings along the g_1, g_2, g_3 directions, respectively. Estimated experimental errors are reported in **Table 2.1**.

The addition of cellohexaose (C6) into the sample solution caused a significant change to the EPR spectra of the enzyme (**Figure 2.3**), with an increase of the $|A_3^{Cu}|$ coupling (from 465 MHz to 515 MHz), accompanied by a small decrease in g_3, and the appearance of a well resolved superhyperfine coupling in the g_1/g_2 directions. The overall spectrum is more axial with respect to the sample in the absence of substrate, as evidenced from the smaller splitting between g_1 and g_2 (Rg = 0.26) and between the hyperfine coupling along the same directions ($|A_1^{Cu}|$ = 35 MHz and $|A_2^{Cu}|$ = 38 MHz).

As described by Frandsen *et al*, in the presence of Cl^-, the formation of the enzyme/substrate complex is coupled by coordination of Cl^- to the Cu(II) ion, leading to the addition of superhyperfine features along the g_1/g_2 direction (**Figure 2.3**).[65] Considering the crystal structure of the *Ls*AA9_C6_Cl complex (**Figure 2.1**), an initial

assignment of the orientation of the *g* tensor principal directions can be made, with g_2 directed along the Cl–Cu(II)–NH_2 bond and therefore with the g_1 direction along the Cu–N(His) bonds (**Figure 2.4**); this assignment is corroborated by DFT calculations of the *g* tensor orientation (see **Section 2.3.4.3**). The binding of chloride to the metal (which effectively replaces the equatorial H_2O molecule) is also accompanied by a significant reduction in g_3 (g_3 = 2.234) with respect to the *Ls*AA9_C6 complex, while $|A_3^{Cu}|$ remains essentially constant (518 MHz).

Taking advantage of the apparent increased affinity of the Cu(II) for chloride ions when cellohexaose is bound to the active site, we tested the possibility of binding Br^- instead of Cl^- to the copper ion allowing us to 'tune' the electronic structure of the copper (**Figure 2.4**). Indeed, when bromide was included in the preparation of the *Ls*AA9 substrate complex, the resulting spectrum (*Ls*AA9_C6_Br) showed a noticeable large superhyperfine coupling due to the bromide ion, mainly appearing within the g_2 component of the copper *g* tensor, clearly evident in the Q-band spectrum (**Figure 2.3**). This feature further corroborates the assignment of the g_2 direction as oriented close to the direction of the Br–Cu(II)–NH_2 bonds (under the assumption that the bromide ion binds in the same equatorial position as the chloride). Moreover, as with the *Ls*AA9_C6_Cl complex, the bromide complex also exhibits a reduction in its g_3 value (2.221) from the corresponding H_2O complex (*Ls*AA9_C6, g_3 = 2.271), possibly due to higher covalency of the Cu–halide bond with respect to the Cu–OH_2 one. The slightly lower g_3 value (~2.22) compared to the chloride (~2.23) is consistent with the higher σ-nephelauxetic properties of the bromide ligand.[138]

A detailed analysis of the superhyperfine coupling on the basis of continuous wave X- and Q-band only is often challenging because it is not possible to determine its magnitude with high accuracy (apart from few particular cases where this coupling is of the same order of magnitude as the metal hyperfine coupling, like the coupling of Br^- bound to the Cu). Therefore any conclusion on this topic needs to be drawn with caution. Nevertheless, some general consideration can be made, especially for the substrate-bound complexes, in which the superhyperfine features are well resolved. In the X-band spectrum of the resting state (*Ls*AA9), the superhyperfine coupling due to the ligating N atoms is not well resolved and only some weak features around 3200-3270 G are visible, but the inclusion of three N atoms with coupling around 30–40 MHz in the simulation is necessary to obtain a good simultaneous fit of both X- and Q-band experimental data. As seen above, addition

of cellohexaose to the enzyme generates a stronger and better-defined superhyperfine coupling pattern, which permits more confidence in the simulation of these parameters. Again, as in the absence of substrate, the simulations require the inclusion of three N atoms with couplings similar to those of the resting state. An amino terminus N coupling similar to the coupling of the coordinating imidazole nitrogen atoms, suggests a slightly higher covalence of the Cu(II)–NH_2 bond, with respect to the Cu(II)–N(His) bond; generally sp^3 hybridized N atoms tend to have a smaller isotropic coupling compared to sp^2 hybridized N atoms, because of their smaller *s* orbital content.[139] Hence, a possible explanation for the similarity in isotropic A^N is a higher spin density on the amino terminus N compared to the histidine N atoms.

The substitution of the Cu equatorial water molecule with Cl^- in *Ls*AA9_C6_Cl, reduces one of these couplings to 19 MHz, while the other two remain basically constant. Considering the hybridisation argument outlined above and the fact that the Cl^- binds *trans* to the amino terminus, this N atom with lower coupling was therefore assigned to the –NH_2 group nitrogen. Moreover, the presence of a 19 MHz coupling for this complex was also supported by ENDOR data obtained in our group from a previous work on *Ls*AA9 (see the supporting information in Frandsen *et al.*).[65] Lastly, the presence of a very large superhyperfine coupling due to the Br^- in *Ls*AA9_C6_Br, overlapping with the Cu hyperfine features, greatly complicates the appearance of the X-band spectrum and the simulation of the N superhyperfine coupling. Therefore, in this case, only two N atoms could confidently be included in the simulations with coupling in the order of ~35 MHz.

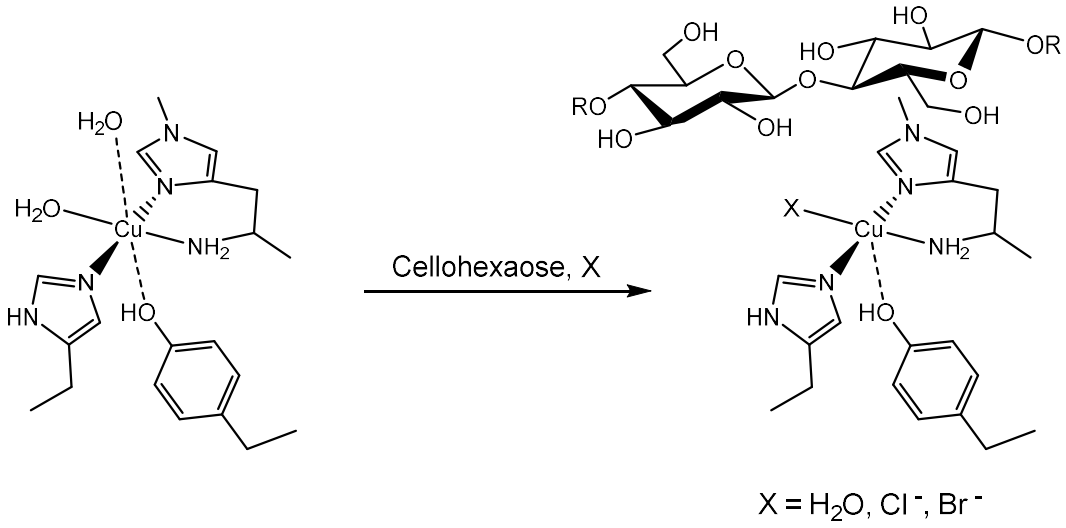

Figure 2.4 Schematic representation of the change in the coordination sphere of the copper ion in *Ls*AA9 upon binding of cellohexaose, with or without Cl^-/Br^-.

2.3.2 Electronic Spectroscopy: UV-Vis, CD and MCD spectra

A combination of UV-vis, circular dichroism (CD) and magnetic circular dichroism (MCD) spectroscopies were performed on the Cu(II) resting state of *Ls*AA9 and on the three complexes with substrate and Cl^-/Br^- to obtain insight into their d-based electronic transitions (**Figure 2.5**). In particular, d-d excited states are key in the interpretation of EPR spin Hamiltonian parameters. In mononuclear Cu complexes, the dipole-disallowed d-d transitions are usually of low intensity (ε~50–100 $M^{-1}cm^{-1}$) with respect to spin-allowed charge transfer (CT) transitions. As such, d-d bands are often not resolved in the UV/vis absorption spectrum of the complex (at the typical concentrations used in metallo-enzyme studies of 1–3 mM).[91,140] However, it is known that in MCD spectroscopy d-d transitions are more intense with respect to CT bands.[141] In addition, being a signed quantity, MCD spectroscopy (together with CD spectroscopy) is often able to provide improved resolution for these transitions as compared to a normal absorption spectrum.

To obtain the most reliable data, CD, MCD and UV/vis spectra were simultaneously fitted with Gaussian functions to determine the energy of the various electronic transitions. Energies were allowed to vary on the order of few hundreds wavenumbers in the MCD relative to the CD and UV-vis spectra due to the difference in temperature at which they were collected, and because of the overall broad band shapes, which lower the resolution. Overall, the error in the energy of the bands was estimated to be in the order of ±50–100 cm^{-1}. The results for all the different complexes studied here are reported in **Table 2.3** together with possible bands assignments. The bands were assigned on the basis of their energy, C_0/D_0 ratio and field/temperature dependence of the MCD spectrum, together with the results of the CASSCF and TD-DFT calculations (see **Section 2.3.5**).

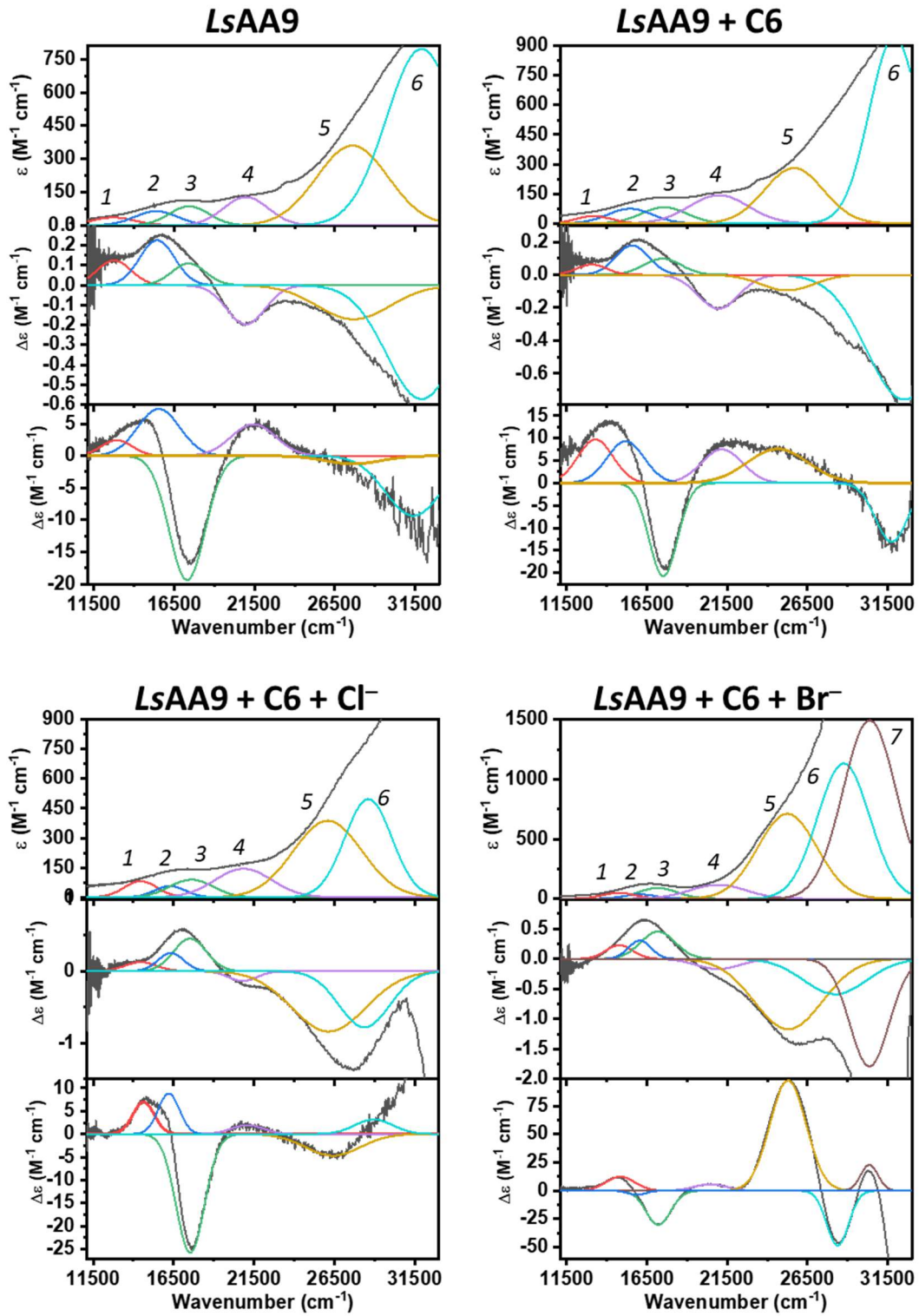

Figure 2.5 Room temperature UV-vis (top), CD (middle) and low temperature, 5 K, 7 T MCD (bottom) spectra of Cu(II)-*Ls*AA9, *Ls*AA9 with cellohexaose (labelled C6 in the figure), *Ls*AA9 with cellohexaose and Cl^-, and *Ls*AA9 with cellohexaose and Br^-, together with their Gaussian bands fitting. The experimental spectra are shown in black while peak fits as coloured lines. Enzyme concentration was 0.9 mM for *Ls*AA9, 0.4 mM for *Ls*AA9_C6, 0.4 mM for *Ls*AA9_C6_Cl and 0.9 mM for *Ls*AA9_C6_Br, 50% w/v sucrose, Na–phosphate 20 mM, pH 6.0. Any added cellohexaose was three times the enzyme concentration, NaCl or NaBr were 200 mM. Bands labelling and fitting data are reported in **Table 2.3**.

Table 2.3 Gaussian band energies (cm^{-1}) for the fitting of the UV-vis, CD and MCD spectra for the different enzyme/substrate complexes of Cu(II)–*Ls*AA9, together with the respective C_0/D_0 ratio and transition assignment.

Band	Energy (cm^{-1})			C_0/D_0	Assignment
	UV-vis	CD	MCD		
***Ls*AA9**					
1	12700	12750	12980	0.066	$d_{z^2} \rightarrow d_{x^2-y^2}$
2	15370	15430	15530	0.120	$d_{xz} \rightarrow d_{x^2-y^2}$
3	17430	17440	17310	0.282	$d_{yz} \rightarrow d_{x^2-y^2}$
4	20980	20960	21400	0.026	$Tyr \rightarrow d_{x^2-y^2}$
5	27600	27600	27640	0.003	CT
6	31900	31890	31620	0.009	CT
***Ls*AA9_C6**					
1	13190	13090	13290	0.273	$d_{z^2} \rightarrow d_{x^2-y^2}$
2	15450	15570	15210	0.109	$d_{xz} \rightarrow d_{x^2-y^2}$
3	17570	17460	17520	0.170	$d_{yz} \rightarrow d_{x^2-y^2}$
4	20980	20950	21080	0.040	Tyr $\rightarrow d_{x^2-y^2}$
5	24790	24750	24640	0.038	CT
6	31580	31500	31740	0.005	CT
***Ls*AA9_C6_Cl**					
1	14450	14450	14630	0.0590	$d_{z^2} \rightarrow d_{x^2-y^2}$
2	16270	16330	16190	0.110	$d_{xz} \rightarrow d_{x^2-y^2}$
3	17600	17510	17530	0.200	$d_{yz} \rightarrow d_{x^2-y^2}$
4	20840	20960	21070	0.008	Tyr $\rightarrow d_{x^2-y^2}$
5	26070	26100	26400	0.010	CT
6	28600	28600	28940	0.005	CT
***Ls*AA9_C6_Br**					
1	14760	14770	14880	0.242	$d_{xz} \rightarrow d_{x^2-y^2}$
2	16050	16050	15880	0.059	$d_{xy} \rightarrow d_{x^2-y^2}$
3	17170	17190	17210	0.227	$d_{yz} \rightarrow d_{x^2-y^2}$
4	20930	20630	20440	0.030	Tyr $\rightarrow d_{x^2-y^2}$
5	25250	25300	25290	0.089	CT
6	28240	28230	28380	0.026	CT
7	30360	30360	30360	0.005	CT

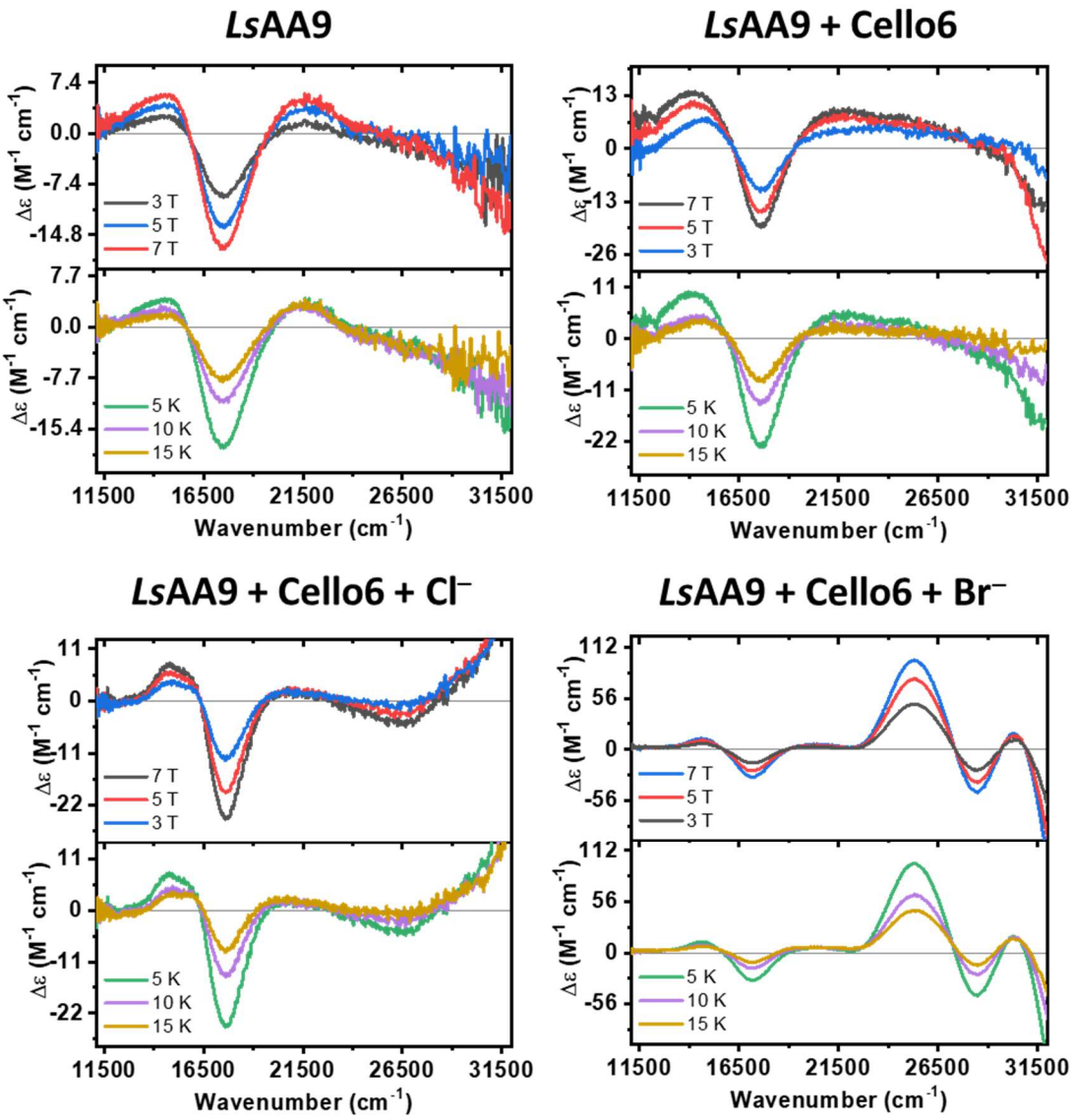

Figure 2.6 MCD spectra field dependence at 5 K (upper half) and temperature dependence at 7 T (bottom half) of *Ls*AA9, *Ls*AA9 with cellohexaose (labelled Cello6 in the figure), *Ls*AA9 with cellohexaose and Cl^-, and *Ls*AA9 with cellohexaose and Br^-. Enzyme concentration was 0.9 mM for *Ls*AA9, 0.4 mM for *Ls*AA9_C6, 0.4 mM for *Ls*AA9_C6_Cl and 0.9 mM for *Ls*AA9_C6_Br, 50% w/v sucrose, Na–phosphate 20 mM, pH 6.0. Were present, cellohexaose was three times the enzyme concentration, NaCl or NaBr were 200 mM.

The electronic absorption spectrum of *Ls*AA9 shows a weak, broad and relatively featureless (ε~100 cm^{-1}) absorption band centred at 16500 cm^{-1} which has a derivative shaped signal in the relatives MCD spectra (**Figure 2.5**). This particular feature is typical for mononuclear Cu complexes and is referred to as pseudo-*A* term, composed of two opposite sign *C*-term features assigned to $d(xz/yz) \rightarrow d(x^2–y^2)$ ligand field transitions which can spin–orbit couple (bands *2* and *3* in **Figure 2.5**).[91,142,143] Gaussian

deconvolution of the combined spectra revealed at least three different bands in the d-d region, centred at ~12800 cm^{-1}, ~15400 cm^{-1} and ~17400 cm^{-1}. These three bands gain substantial intensity with respect to bands *5* and *6* positioned at 27600 cm^{-1} and 31900 cm^{-1}, respectively (**Figure 2.5**, which are, in turn, more intense in the UV-vis spectrum), consistent with their assignment as ligand field (bands *1*, *2* and *3*) and CT transitions (bands *5* and *6*). Moreover, the MCD intensity of transitions *1*, *2*, *3* and *6* is inversely proportional to the temperature, classifying them as MCD *C*-terms (**Figure 2.6**). An expected fourth d-d transition is not resolved in the experimental spectra, and therefore it was not possible to determine its energy. In terms of transition energies, the resulting ligand field spectrum resembles the one reported for *Hj*AA9 LPMO (although the $d(z^2)$ transition was not resolved in this spectrum)[59] and is similar to those reported in several tetragonal mononuclear Cu(II) complexes including α-hydroxylating monooxygenase and the square planar $[Cu(II)(1,2\text{-dmIm})_4](BF_4)_2$ model complex.[59,144] Lastly, it should be noted that the high energy (CT) region of the spectra is basically featureless, therefore it is difficult to determine the correct number of bands present in this region and a precise estimate of their energies; the error on the position of these CT transitions it is likely to be larger than that on the d-d transitions.

In addition to the *C*-term transitions described above, the spectra of the resting state in **Figure 2.5** further reveal a band centred at ~21000 cm^{-1} (band *4*) with low intensity (estimated ε ~120 M^{-1} cm^{-1}), similar to those typical for d-d transitions, but with no temperature dependence of its MCD signal (*i.e.* no *C*-term intensity). This property, together with a low C_0/D_0 ratio (**Table 2.3**), suggests that this band is best assigned as a CT transition with little contribution of the Cu(II) ion. The same band is found also when the enzyme is bound to substrate and is independent on the nature of the exogenous ligand in the Cu equatorial coordination position (H_2O, Cl^- or Br^-); the energy of this band is basically constant across the series (the transition is always labelled as band *4* in **Figure 2.5**). On the basis of the available experimental data it is not possible to make a definitive conclusion about the origin of this transition; however, a reasonable hypothesis is to assign it to a tyrosine/tyrosinate–Cu(II) ligand-to-metal charge transfer (LMCT) band. The possibility of this assignment will be discussed further below and in the computational section. By analogy, in a recent work on the active site of Amine Oxidase (AO, a mononuclear Cu enzyme), Andelson *et al*. demonstrate the presence of a low intensity (ε ~400 M^{-1} cm^{-1}) tyrosinate–Cu(II) LMCT at ~22500 cm^{-1}, involving a tyrosine residue in axial position respect to the Cu(II) coordination plane.[145] The axial positioning

of the ligand means that orbital overlap between the tyrosinate out-of-plane π HOMO and the Cu(II) d(x^2–y^2) SOMO is low, which explains the atypical low intensity for a tyrosinate–Cu(II) LMCT, as compared to other characterized phenolate–Cu(II) complexes.[146] In *Ls*AA9 (and more in general in AA9 LPMOs) the active site Tyr residue is in axial position respect to the His Brace Cu coordination plane, similarly to the AO active site. In this case, the low intensity of the putative tyrosinate–Cu(II) LMCT can be justified considering the low orbital overlap due to the Tyr position and/or the presence of only a small percentage of tyrosinate species at pH 6, with respect to its protonated version. The presence of a neutral axial tyrosine at pH 6 is supported by a neutron crystal structure of the *Neurospora crassa Nc*AA9 LPMO, which shows the protonation of the residues in the active site;[58] therefore the hypothetical tyrosinate fraction, if present, would be a small percentage of the total. Additionally, if we assume an extinction coefficient ε of 400 M^{-1} cm^{-1} for the tyrosinate–Cu(II) LMCT, then the observed ε ~120 gives an estimated concentration of the tyrosinate species of ~30 % of the total enzyme concentration. This percentage is not consistent with the EPR data of *Ls*AA9, which show the presence of a single species in solution (see the discussion on the calculated EPR parameters for the Cu(II)-tyrosinate species in **Section 2.3.4.2**). Lastly, we refer to the discussion about TD-DFT calculations, in **Section 2.3.5.1,** that provide some evidence for an alternative assignment of this transition as a neutral tyrosine–Cu(II) LMCT, instead of a tyrosinate–Cu(II) LMCT.

The complex of *Ls*AA9 with cellohexaose (*Ls*AA9_C6) presents a very similar set of MCD, CD and UV/vis spectra to those of the resting state (**Figure 2.5**). The resolved d-d transitions (bands *1–3*) are at ~13100 cm^{-1}, ~15400 cm^{-1} and ~17500 cm^{-1} demonstrating that the displacement of the Cu axial H_2O molecule does not significantly change the strength of the ligand field at the metal. This observation is consistent with the *g* values obtained from EPR with *Ls*AA9_C6, which are also close to those of the resting state. Moreover, an additional band appears at ~24700 cm^{-1} and is assigned as CT transition on the basis of its energy low C_0/D_0 ratio (band *5*).

The chloride complex (*Ls*AA9_C6_Cl) has some differences with respect to the two previous cases. The first two d-d transitions (bands *1* and *2*) are shifted to higher energy, by ~1000 cm^{-1}, consistent with formation of a higher ligand field due to the strong binding of the Cl^-. This increase in ligand field is counter to what would be expected given the position of chloride in the spectrochemical series (see discussion in **Section 2.4**). The

charge transfer band at ~26200 cm^{-1} (band *5*) has a clear temperature dependence of its MCD signal (**Figure 2.6**), suggesting that the Cu(II) orbitals are involved in this transition. In this particular spectral region there are well characterized $Cl^- \rightarrow$ Cu(II) LMCT bands known for the square planar $[CuCl_4]^{2-}$ complex. These transitions arise from promoting an electron from the predominantly π bonding orbitals with mainly Cl^- character, to the Cu based SOMO.[147,148] Hence, the band at ~26200 cm^{-1} in *Ls*AA9_C6_Cl can be tentatively assigned as a $Cl^- \rightarrow$ Cu(II) LMCT, in agreement with its low C_0/D_0 ratio.

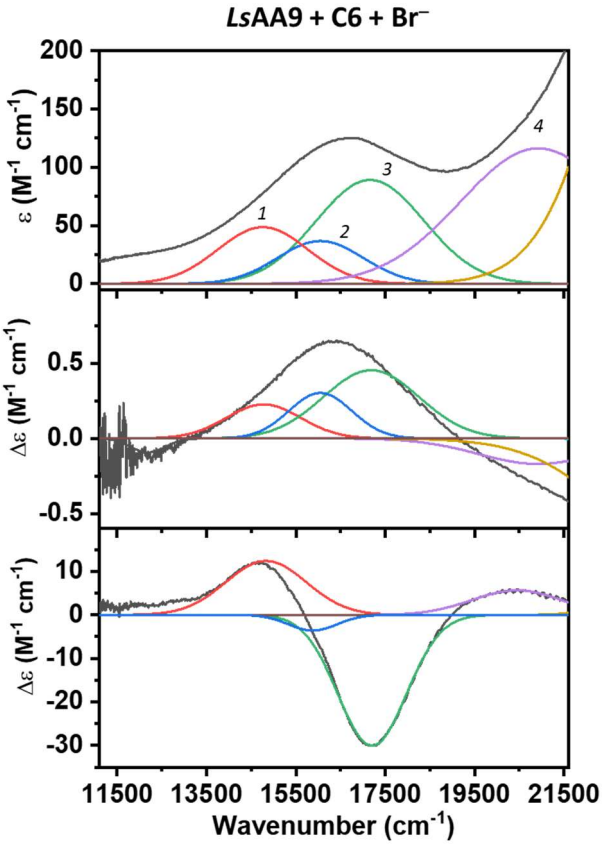

Figure 2.7 Expanded view of the d-d transition region of the UV-vis (top), CD (middle) and MCD (bottom) spectra for *Ls*AA9_C6_Br, together with their Gaussian bands fitting. The experimental spectra are shown in black while peak fits as coloured lines. Enzyme concentration was 0.9 mM, 50% v/v sucrose, cellohexaose 2.7 mM, NaBr 100 mM, Na–phosphate 20 mM, pH 6.0. Bands are labelled according to the numbering in **Table 2.3**.

In the Br^- complex (*Ls*AA9_C6_Br) the first two ligand field transitions (bands *1–2*) are again shifted by ~1000–1500 cm^{-1} with respect to the enzyme resting state (**Figure**

2.7 and **Table 2.3**). Additionally, if bands *1* and *3* are assigned as the pseudo-*A* pair, then band *2* can be assigned as d(xy)→d(x^2–y^2), as this transition is generally negative in MCD spectra of mononuclear Cu complexes (see also the discussion about CASSCF results in **Section 2.3.5.2**).[91,144,145,149] Moreover, in the charge transfer region of the spectra, bands *5* and *6* are much more intense than the bands in all other presented spectra, as shown in **Figure 2.5**. Similar to the *Ls*AA9_C6_Cl case, these two bands can be assigned as Br^- → Cu(II) LMCT from π (in plane and out of plane) bonding orbitals with mainly Br^- character, as reported by Rivoal *et al*. for the $[CuBr_4]^{2-}$ complex in a distorted tetrahedral coordination geometry (D_{2d} symmetry).[150] These types of transitions have contributions from the spin–orbit coupling of the halogen, therefore the much higher MCD intensity of these two bands in the bromide case with respect to the chloride analogue is due to the larger spin–orbit coupling constant of the bromide (2460 cm^{-1}), *cf.* chloride (590 cm^{-1}).[150]

2.3.3 Theoretical calculations: geometry optimizations

Computational models of the *Ls*AA9 active site were generated using the cluster model approach. The model was build considering the Cu ion, its first coordination sphere and several other residues in the secondary coordination sphere (see **Section 2.2.4** for details about the choices). The Cu exogenous ligands (water/hydroxide, chloride, bromide) were included depending on the model considered. For the resting state of the enzyme (Based on the Cu(II) X-ray structure with PDB 5ACH), two H_2O ligands for the Cu were included (one in the His brace equatorial plane and one in *trans* to Tyr-164, Model1_2H_2O). On the other hand, the models involving the substrate were built starting from the X-ray structure of *Ls*AA9 in complex with cellohexaose (PDB 5ACI) and including the appropriate Cu equatorial ligand: H_2O (Model2_Sub_H2O), Cl^- (Model3_Sub_Cl) and Br^- (Model4_Sub_Br). Lastly, given the hypothesis described above of a possible Cu(II)–tyrosinate species present in small amount in the resting enzyme, a fifth model was generated from Model1_2H_2O, but with deprotonated Tyr-164 (Model5_Tyr). Geometries were optimized at the DFT level of theory using BP86 as functional, the Def2-TZVP basis set on the Cu and its ligating atoms, and the Def2-SVP basis set on all remaining atoms. All the optimized geometries, apart from the one of Model5_Tyr (see discussion below), were in excellent agreement with the crystallographic structures (**Table 2.4**), showing some structural relaxation but without unreasonable distortions, as

shown in **Figure 2.8**. The root mean square deviation (RMSD) for of the calculated Cu–ligand bond distances for Model1 to Model4, with respect to the experimental distances, is 0.13 Å, with the largest variations observed for the two Cu axial ligands. It should be noted that for the resting state structure (5ACH) the resolution of 1.28 Å, a very good resolution for typical protein structures, allows to estimate a bond distance RMSD of ~0.1 Å.[151] However, this value includes the entire protein and does not necessarily apply to the metal active site, where it could be even larger.[152]

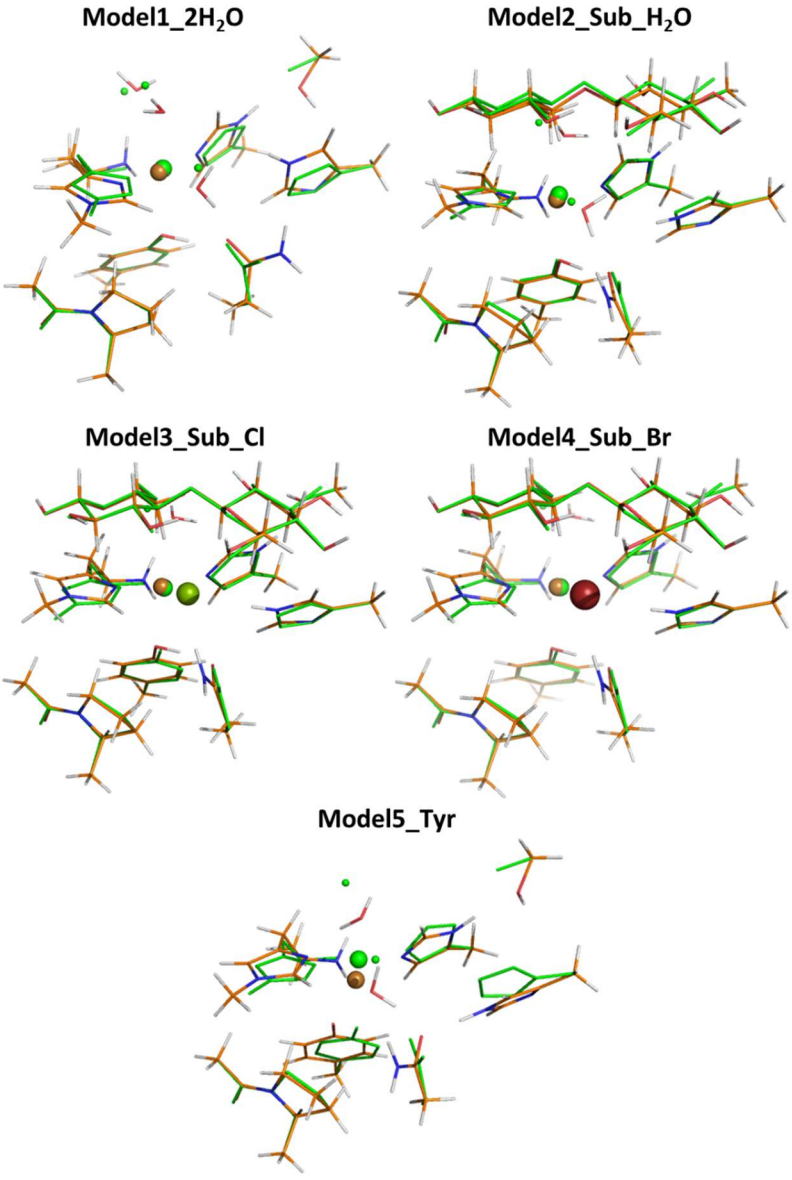

Figure 2.8 DFT-optimized geometries of the different *Ls*AA9 active site models (orange), overlaid with the respective crystal structure geometry (green). For the models without substrate, the reference is the PDB 5ACH structure, while for those with substrate the reference is the PDB 5ACI structure. The Cu(II) is in gold (green sphere in the crystal structure), the Cl^- in dark green and the Br^- in dark red; water molecules in the crystal structure are represented as small green spheres.

In the enzyme resting state, the optimized geometry maintains the tetragonally distorted Cu coordination geometry observed in the X-ray structure, with four ligands in the equatorial plane of the His Brace, plus the axial H_2O and Tyr oxygen atom at ~2.5–2.6 Å. These two calculated distances are shorter than those measured in the experimental structure, especially for the axial water molecule (**Table 2.4**). A similar consideration also holds for the Cu–NH_2 bond, which is systematically calculated as shorter (~ 0.1 Å) than it is in the crystal structure. This issue is not new in the LPMO field and was already reported in other theoretical studies (always using DFT, but with different functionals).[63,100] A likely explanation for the discrepancy between the calculated and experimental Cu–NH_2 bond lengths is that the active site is sensitive to photo-reduction to Cu(I) during X-ray data collection, giving the slightly longer experimental bond distances. Indeed, recent neutron structures (which are much less affected by photoreduction) of the *Nc*AA9D LPMO reported by O'Dell *et al*., showed a Cu–NH_2 bond length of 2.0 and 2.1 Å (PDB 5TKI and 5TKG, respectively), consistent with the calculated one.[58]

As already discussed in **Section 2.1**, substrate binding to *Ls*AA9 does not distort the Cu(II) coordination geometry but does displace the axial H_2O *trans* to Tyr-164, and also shortens the Cu(II)–O(Tyr) distance by about 0.2 Å. The inclusion of the substrate in the computational model (Model2_Sub_H2O) reproduced this change, with a shift from 2.55 Å to 2.42 Å in the Cu-tyrosine length, compared to the resting state, in agreement with the experimental data. The models with Cl^- and Br^- in place of the equatorial H_2O (Model3_Sub_Cl and Model4_Sub_Br, respectively) behave in a similar way, but with slightly longer Cu(II)–O(Tyr) distances (~2.5 Å) compared to Model2_Sub_H2O. Also, the Cu–Cl bond is shorter than the Cu–Br bond, as expected due to the larger dimensions of the Br^- anion and expected weaker coordination to the Cu(II) (**Table 2.4**).

The deprotonation of the Tyr-164 residue to tyrosinate generates a Cu(II) coordination geometry which is significantly distorted with respect to the normal histidine brace coordination (**Figure 2.8**, Model5_Tyr). The oxygen atom of the tyrosinate residue moves to 1.97 Å from the Cu(II) and displaces the N_δ of His1 imidazole ring, which moves to 2.41 Å away from the metal. In this situation the Tyr residue is no longer an axial ligand, but is now coordinating to the copper in the distorted equatorial plane. In addition, the axial H_2O is also no longer coordinating to the metal. The final geometry is characterized by a four coordinate Cu(II) with an equatorial coordination plane which is rotated towards

the Tyr residue. Clearly, this optimized geometry, in which the normal His brace arrangement is lost, is significantly different from the one obtained in Model1_2H_2O. The experimental crystal structures do not show any evidence of this distorted arrangement, suggesting that a deprotonated tyrosine coordinating to the copper is an unlikely representative structure of the resting state. In fact, the crystal structures were obtained at pH 5.5, very similar to the pH at which the EPR and electronic spectra were collected (pH 6.0), hence if the tyrosinate species was present in significant amount, it should be visible from the structures.

Table 2.4 Selected bond distances (Å) and angles (°) for the various *Ls*AA9 model optimized geometries, alongside the corresponding metrics from the *Ls*AA9 crystal structures, with and without bound cellohexaose (PDB 5ACI and 5ACH, respectively).

Model[1]	**Cu–NH_2**	**Cu–N_δ**	**Cu–N_ε**	**Cu–O(Tyr)**	**Cu–X_{eq}**[2]	**Cu–H_2O_{ax}**	**N_δ–Cu–N_ε(°)**	**NH_2–Cu–X_{eq}(°)**
5ACH (1.28 Å)	2.2	1.9	2.0	2.8	2.1	3.3	169	167
Model1_2H_2O	2.05	1.98	2.01	2.55	2.11	2.49	172	172
Model5_Tyr	2.05	2.41	2.07	1.97	2.10		128	168
5ACI (1.75 Å)	2.3	1.9	2.0	2.6	2.4		164	175
Model2_Sub_H2O	2.07	1.95	1.99	2.42	2.17		162	172
Model3_Sub_Cl	2.11	1.97	1.99	2.50	2.41		167	177
Model4_Sub_Br	2.01	1.98	1.99	2.49	2.56		166	177

[1]-The resolution for the X-ray structure is reported in brackets.

[2]- X_{eq} = H_2O in Model1_2H_2O, Model2_Sub_H2O, Model5_Tyr, 5ACI and 5ACH; Cl^- in Model3_Sub_Cl; Br^- in Model4_Sub_Br. The *eq* label indicates the coordination position in the histidine brace equatorial plane, while the *ax* label indicates the axial coordination position, *trans* to the Tyr-164 residue.

2.3.4 Theoretical calculations: EPR spin Hamiltonian parameters

The optimized geometries were then used to calculate the EPR spin Hamiltonian parameters, at the DFT level of theory. The next section will discuss the choice of the basis set and the functional dependence of the calculated parameters, while the following section will discuss the correlation of the computational results with the experimental data. In general, the accuracy of EPR parameters calculations with DFT, for systems involving transition metal ions, is variable and depends on the metal considered and its oxidation state. In particular, for Cu(II) systems, the relatively large *g* shifts tend to be underestimated in calculation, due to a combination of a too covalent bonding description and too high d-d transition energies.[89,90] Calculated metal hyperfine contributions suffer from similar problems in the spin–orbit contribution (being related to the *g* shift), and also in the evaluation of the Fermi contact term, as this term depends on the indirect core level spin polarization arising from the unpaired spin density in the valence shell. This spin polarization is difficult to calculate accurately and is generally underestimated.[129] Hybrid functionals tend to be more successful in this type of calculations since they provide a better picture of metal–ligand covalent bonding.[90] In this regard, the amount of Hartree-Fock exchange in a given functional can be adjusted to obtain better calculated parameters. However, this is a highly empirical approach and, because the optimum amount of Hartree-Fock exchange depends on the metal and its oxidation state, it is not possible to determine a general procedure which is valid for every system. Notwithstanding the significant issues associated with calculating EPR parameters, this approach has been used in the past to study Cu complexes in both synthetic and biological systems.[153,154]

2.3.4.1 Basis set and functional dependence

The choice of the basis set can affect the calculated EPR parameters, especially for metal hyperfine couplings because they require a basis set with more flexibility in the core region (Fermi contact term), as compared to standard ones which are designed for accurate treatment of the valence region (*e.g.* Def2-SVP/TZVP). For this reason, several combinations of basis sets (**Table 2.5**) for the metal and the ligands were tested using the B3LYP functional with 38% Hartree-Fock exchange, B3LYP(38HF) (see below for

discussion about the choice of the functional). The model used in this analysis is Model3_Sub_Cl, with both the substrate and a Cl^- bound to the Cu active site.

Table 2.5 Different basis set schemes considered in the study of Model3_Sub_Cl EPR properties.

Scheme	Cu(II)	Cu ligand atoms
1	Def2-TZVP	Def2-TZVP
2	CP(PPP)	IGLOIII
3	CP(PPP)	Def2-TZVP
4	aug-cc-pVTZ-J	aug-cc-pVTZ-J
5	Def2-QZVPP	Def2-QZVP

The first tested scheme (*1*) described all the relevant atoms with the standard Def2-TZVP basis set, while in schemes *2* and *3* the CP(PPP) basis set, from Neese and co-workers, was used for the description of Cu(II). This last basis set is constructed on Ahlrichs's DZ basis set but has additional flexibility in the core region (17s7p3d1f) and was specifically designed for metal core shell properties like hyperfine couplings and Mössbauer shifts.[124] Scheme *4* utilizes the Sauer's aug-cc-pVTZ-J basis set, which has an increased core flexibility, like the CP(PPP), but is more polarized (17s10p7d3f2g).[155] Finally, scheme *5* describes the metal with a Def2-QZVPP basis set (11s6p5d4f2g). On the ligands (the imidazole rings of the two coordinating histidine residues, the amino terminus and the exogenous halide ion), both Def2-TZVP and Def2-QZVP were investigated as basis sets, alongside aug-cc-pVTZ-J and IGLO-III. The latter is another EPR-specialized basis set developed for organic radicals, and is characterized by increased core flexibility respect to the TZVP or QZVP basis.[125]

The calculated *g* and A^{Cu} values for the different schemes are reported in **Table 2.6**. In terms of *g* values, all the tested basis sets performed in a similar way, showing that these parameters are not very sensitive to the basis set. On the other hand, it is clear that describing the metal with the Def2-TZVP basis set is not appropriate for hyperfine coupling values as A_1 (–112 MHz) and A_2 (401 MHz) are too large compared to the experimental values (10 MHz and 77 MHz, respectively). The CP(PPP) basis set strongly

improves the result. However, moving to the larger aug-cc-pVTZ-J and Def2-QZVPP basis sets does not significantly improve the results further. Therefore, the CP(PPP) basis set was chosen to describe the Cu(II) in all calculations. In terms of ligand superhyperfine coupling instead, the Def2-TZVP basis set gives almost identical results to all the other larger basis sets, for both N and Cl^- couplings. This basis set was therefore used for the ligands in calculations over the IGLO-III basis set, as the latter is not defined for the Br^- ion. Scheme *3* was the final choice for productive calculations.

Table 2.6 Experimental and DFT calculated *g* and hyperfine coupling values obtained from the optimized structure Model3_Sub_Cl, for the different basis set schemes considered. Calculations were performed with the B3LYP(38HF) functional. The numbering of the schemes follow that reported in **Table 2.5**.

Basis set scheme	***g* tensor**			**Cu(II) hyperfine (MHz) [1]**			**Ligand superhyperfine A^{iso} (MHz) [1]**			
	g_1	g_2	g_3	A_1	A_2	A_3	NH_2	N_δ	N_ε	Cl^-
Exp.	2.045	2.064	2.234	10	77	517	19	36	31	41
1	2.058	2.081	2.230	–212	401	–453	34	39	37	25
2	2.058	2.076	2.223	–3	36	–594	34	39	36	24
3	2.057	2.078	2.223	–8	41	–593	34	40	37	25
4	2.057	2.080	2.232	0	55	–596	34	38	36	25
5	2.058	2.080	2.233	23	79	–606	33	37	36	24

[1]- Signs cannot be determined form the experiment. Only the isotropic values are reported for the N and Cl^- ligands.

The DFT-calculated EPR parameters are much more sensitive to the choice of the functional than they are to the choice of basis set, and in particular to the amount of Hartree-Fock (HF) exchange included in a given functional, as discussed above. Several different hybrid functionals were tested on Model3_Sub_Cl, as they tend to perform better than pure functionals for transition metal ions; the results are summarized in **Table 2.7**. Among these, B3LYP, PBE0 and TPSSh have been reported to be those with the best

performances for 3d transition metals.[89,90] In addition, previous work carried out in our laboratory had found that B3LYP with increased amount of HF exchange (up to 38%), had an improved performance compared to the standard version (20% HF exchange), therefore this modification was also tested. Previous work by Solomon and co-workers, extensively studied the effects of HF exchange in DFT calculations of Cu(II) complexes, often reporting that a 38%HF exchange gave better performances as compared to the standard amount in various functionals.[91,149,156] Lastly, a recent work by Bissaro *et al.* on calculation of EPR parameters with DFT on an AA10 LPMO[77] employed the PBE0 functional with the zeroth-order regular approximation (ZORA), obtaining reasonable agreement with the experimental data; this possibility was therefore also included in our study.

The obtained results show that g_3 and the Cu hyperfine couplings are the parameters most affected by the choice of the functional, while the ligand superhyperfine coupling is less sensitive. Different functionals performed better for different parameters but none, among those considered, outperformed all the others in g and A tensors prediction. Moreover, we note that, for this system, the inclusion of scalar relativistic effects with the PBE0 functional does not significantly improves the results, compared to PBE0 alone. Overall, the best compromise is represented by B3LYP with 38% HF exchange, which was then used also for the calculations on all the other studied models of *Ls*AA9.

Table 2.7 Experimental and DFT calculated *g* and hyperfine coupling values obtained from the optimized structure Model3_Sub_Cl, using different functional.

Functional (%HF) [1]	*g* tensor			Cu(II) hyperfine (MHz) [2]			Ligand superhyperfine A^{iso} (MHz) [2]			
	g_1	g_2	g_3	A_1	A_2	A_3	NH_2	N_δ	N_ε	Cl^-
Exp.	2.045	2.064	2.234	10	77	517	19	36	31	41
B3LYP(20%)	2.044	2.056	2.159	4	34	–538	38	42	41	29
B3LYP(38%)	2.056	2.080	2.223	6	64	–573	34	34	37	26
TPSSh(10%)	2.038	2.045	2.126	3	27	–542	37	40	39	25
PBE0(25%)	2.048	2.063	2.180	10	–12	–571	37	40	39	26
PBE0(25%) +ZORA	2.049	2.065	2.187	5	–36	–605	35	37	36	24

[1]-The percentage of Hartree-Fock exchange of each functional is reported in brackets.

[2]- Signs cannot be determined from the experiment. Only the isotropic values are reported for the N and Cl^- ligands.

2.3.4.2 EPR parameters of *Ls*AA9/Substrate Complexes

The optimized geometries of the different active site models were used to calculate the relative EPR parameters at the DFT level of theory, using B3LYP with 38% of Hartree-Fock exchange, the CP(PPP) basis set on the Cu(II) and the TZVP on the metal ligands, following the results outlined in the previous section. The results for the five different models are summarized and reported in **Table 2.8**, together with the respective experimental parameters (from **Table 2.2**).

Table 2.8 Calculated *g* values and Cu hyperfine coupling constants (in MHz), together with the experimental values obtained from the EPR spectra simulations.

	g_1	g_2	g_3	R_g [2]	A_1^{Cu}	A_2^{Cu}	A_3^{Cu}
				***Ls*AA9**			
Exp.	2.051	2.075	2.278	0.40	50	125	460
Model1_2H2O	2.051	2.091	2.230	0.58	155	24	–544
				***Ls*AA9_C6**			
Exp.	2.053	2.062	2.270	0.16	35	46	–518
Model2_Sub_H2O	2.056	2.081	2.225	0.38	137	65	–518
				***Ls*AA9_C6_Cl**			
Exp.	2.042	2.065	2.234	0.45	10	77	517
Model3_Sub_Cl	2.046	2.081	2.211	0.57	123	13	–540
				***Ls*AA9_C6_Br**			
Exp.	2.035	2.071	2.221	0.71	10	55	525
Model4_Sub_Br	2.045	2.084	2.210	0.62	106	–1	–551
				***Ls*AA9_Tyrosinate**			
Model5_Tyr	2.065	2.108	2.277	0.51	152	–7	–493

The calculations for the resting state model (Model1_2H_2O) correctly reproduced an almost axial set of *g* values, with small rhombicity (R_g = 0.58) between g_1 and g_2. Overall, the experimental trend in g_3 is correctly reproduced with Model1_2H_2O > Model2_Sub_H2O > Model3_Sub_Cl > Model4_Sub_Br, even if with smaller **Δ***g* shifts as compared to the experiments. The small deviation from perfectly axial symmetry in g_1/g_2 of the DFT models mirrors the experimental trend, where Model2_Sub_H_2O has the smallest R_g, and the bromide complex has the highest R_g. On the other hand, Model5_Tyr represents an exception as it features *g* values which are significantly higher than all other models, which suggests that if the Cu(II)–tyrosinate species were present in solution, then it would be characterized by higher *g* values (especially in g_3). However, the *Ls*AA9 experimental EPR spectra (X/Q-band) only show a single species present in solution, and therefore the presence of a deprotonated Tyr-164 residue is not supported by the experimental data.

For the Cu hyperfine coupling (A^{Cu}) the situation is more complex, with less clear trends. All the calculated models have very similar A_3 values (about –540 MHz) and therefore do not follow the experimental trend, where the enzyme resting state has a

smaller $|A_3|$ (460 MHz) with respect to the substrate bound cases (~520 MHz), as reported in Table 2.8. Interestingly, a certain degree of anisotropy is predicted between the first and the second principal component of the A tensor, with $|A_1| > |A_2|$ (both positive), but this appears to be opposite to the experimental result, where the simulations showed much better fits with the A principal component along the g_1 direction being smaller than the component along the g_2 direction (*i.e.* $|A_1| < |A_2|$). The performance of the calculations for A^{Cu} is worse than for the g tensor, but it should be kept in mind that metal hyperfine coupling is a more difficult property to predict with accuracy since the three contribution from the Fermi contact (A^{FC}), the spin–dipolar (A^{SD}) and the spin–orbit (A^{SO}) coupling are often of similar magnitude but varying in sign. Since the mechanisms that generate these three contributions have different physical origin, quantitative accuracy is not commonplace.[89] Moreover, the systematic underestimation of g_3 compared to the experiment leads to a large error in the calculations of the spin–orbit contribution (A^{SO}), because this quantity is proportional to the $\mathbf{\Delta}g_3$ shift. As A^{SO} is a positive contribution to $A_3{}^{Cu}$, and the Fermi coupling and the spin dipolar contributions are generally negative, the calculated $A_3{}^{Cu}$ tends to be more negative than the experimental one.

The analysis of the hyperfine contributions allows further evaluation of the electronic structure calculations (**Table 2.9**). All models have negative $A_3{}^{FC}$ / $A_3{}^{SD}$ and positive $A_3{}^{SO}$ values, as typical for Cu(II) axial systems. The chloride and the bromide complexes feature a reduced spin-dipolar contribution, compared to complexes with water molecules as ligands, consistent with the expected higher covalency of the Cu(II)–halide bond, which reduces the spin density at the metal. Interestingly, a similar trend would be expected also for the Fermi coupling term, but in the Br^- case, the $A_3{}^{FC}$ is slightly more negative compared to the resting state (Model1_2H_2O). On the other hand, following the trend of the g_3 values, the A^{SO} contribution decreases in magnitude along the series Model1_2H_2O > Model2_Sub_H2O > Model3_Sub_Cl > Model4_Sub_Br, while for Model5_Tyr is much larger, being characterized by a significantly bigger g_3.

Table 2.9 Calculated contributions to Cu A_3 (in MHz) [1].

Model	A_3^{FC}	A_3^{SD}	A_3^{SO}	A_3^{Tot}
Model1_2H_2O	–287	–564	307	–544
Model2_Sub_H2O	–267	–553	302	–518
Model3_Sub_Cl	–289	–539	288	–540
Model4_Sub_Br	–296	–529	275	–550
Model5_Tyr	–315	–540	363	–493

[1]-FC= Fermi coupling term, SD = spin–dipolar term, SO = spin–orbit and Tot = sum of the contributions.

The superhyperfine coupling of the ligating nitrogen atoms is maintained basically constant across the different models suggesting that the displacement of the axial H_2O, or the replacement of equatorial H_2O in the resting state, does not strongly affect the bonding properties of the Cu(II) with the two His ligands, as shown in **Table 2.10**. The table reports only the N isotropic coupling, even if the coupling is in fact anisotropic (with the largest principal component of the tensor along the bond direction), because the experimental data are not resolved enough to obtain the degree of anisotropy, hence only the isotropic value can be estimated. The situation is different for the halide couplings, especially for the Br^-, where the much larger coupling allows to estimate the three principal components of the A^{Br} tensor. Therefore, both their principal components and their A^{iso} values are reported in **Table 2.10**.

The calculated couplings for Model1_2H_2O and Model2_Sub_H_2O compare well with the experimental values for the resting state and its substrate bound version (*Ls*AA9 and *Ls*AA9_C6), where the best fits to the EPR spectra were obtained with three nitrogen atoms each coupling around 30–45 MHz (**Table 2.2**). Because of the very similar couplings between them and the experimental error in the range of ±5 MHz, it was not possible to make an assignment of the single nitrogen atoms by comparison with the calculated values. Interestingly, the DFT calculations support similar coupling between the amino terminus N atom and the two coordinating imidazole N atoms, as already highlighted in the experimental EPR section (**Section 2.3.1**).[139] It should be noted that this apparently high coupling of the amino terminus was also reported in previous EPR/DFT studies on an AA10 LPMO by Bissaro *et al*.[77] and by Courtade *et al*.[62] In these works, the reported A_{iso}^N coupling for the –NH_2 group nitrogen in the resting state and in

the enzyme/substrate (chitin) complex was ~37 MHz, consistent with the values found in our study.

On the other hand, the DFT values for the Model3_Sub_Cl complex are very similar to those of Model1_2H_2O and therefore the amino terminus superhyperfine coupling is not consistent with the experimental one, which is estimated at ~19 MHz. The calculations suggest that the binding of the halide ion *trans* to the NH_2 group does not affect significantly the Cu(II)–NH_2 bond, while the experiment seems to suggest the opposite effect. The halogen ion hyperfine coupling is calculated with a strong degree of anisotropy, with the largest component along the Cu–X^- bond (along the g_2 direction), as expected. The magnitude the Br^- coupling is larger with respect to that of Cl^-, mainly because of its larger nuclear magnetic moment, but they are both slightly underestimated as compared to the experimentally determined values. This is evident in the largest coupling of the A^{Br} tensor, which a calculated value of 266 MHz, lower than the 335 MHz determined in the EPR spectra (with A^{iso} coupling of 135 MHz and 145 MHz, respectively). The Cl^- case, even if the comparison is more difficult because the degree of anisotropy cannot be accurately determined from the experiment, shows a similar situation with a calculated A^{iso} of 30 MHz, against an experimental one of ~40 MHz.

Table 2.10 Calculated ligand hyperfine (superhyperfine) coupling constants (in MHz), for the nitrogen atoms and halogen ions coordinated to the Cu(II).

Model	$A^{NH_2(His1)}$	$A^{N\delta}$ **(His1)**	$A^{N\varepsilon\ (His78)}$	$[A^X]$ (A^{iso}) [1]
Model1_2H_2O	35	36	34	-
Model2_Sub_H_2O	37	32	30	-
Model3_Sub_Cl	36	36	36	[14 60 13] (30)
Model4_Sub_Br	35	36	36	[71 266 68] (135)
Model5_Tyr	31	1	24	-

[1]- For the Cl^- and Br^- ions the three A principal values are reported, together with the relative isotropic value, because they can be estimated to a certain extent from the EPR spectra simulations (**Table 2.2**). The labelling of the principal components follows the [g_1 g_2 g_3] convention.

Löwdin analyses of the spin density can help rationalize the trends in the EPR parameters of the calculated models (**Table 2.11**). As shown in **Figure 2.9**, for Model1_2H_2O the spin density is mainly distributed in the equatorial plane of the histidine brace, with virtually no contribution from the ligands in axial position (less than 0.5% each). The same situation holds also for Model2_Sub_H_2O, Model3_Sub_Cl and Model4_Sub_Br. The spin density distribution reflects a σ* type of bonding between the Cu and the ligands and explains the strong anisotropic nature of the calculated halide hyperfine coupling, because of its localization in the equatorial plane. In Model5_Tyr there is basically no spin density on the His-1 imidazole ring (0.1%), in agreement with the 1 MHz coupling of its N_δ atom; moreover, some delocalization is seen on the Tyr-164 ring (~10% in total on the Tyr residue), but the biggest part of the spin density remains on the Cu(II), ~75%, suggesting that the electronic structure is best described as Cu(II)–tyrosinate species, with no contribution from a Cu(I)–tyrosyl radical species.

The Cu spin population slightly reduces going from the resting state model (76%) to the chloride (71%) and bromide (70%) cases. The spin density on the Br^- is slightly higher with respect to the Cl^- one, in agreement with the nephelauxetic series, where the Br^- forms a more covalent bond with the Cu(II). The spin population of the ligating nitrogen atoms does not change much across the series (apart from the Model5_Tyr) and the amino terminus nitrogen is always characterized by a slightly higher spin population than the two imidazole nitrogen atoms. This distribution is consistent with the superhyperfine coupling constants presented above and offers an explanation for the similar coupling of the sp^3 N and sp^2 N atoms: the Cu(II)–NH_2 bond is more covalent than the Cu(II)–His bonds and therefore has a higher spin density.

Table 2.11 Löwdin spin populations (%) of Cu and inner sphere ligand atoms/residues in optimized models of the *Ls*AA9 active site.

Model	Cu	NH_2(His1)	N_δ (His1)	N_ε (His78)	X^-	O (Tyr164)
Model1_2H_2O	75.9	8.1	5.4	5.0	3.7	-
Model2_Sub_H2O	74.3	9.7	5.3	4.5	4.1	-
Model3_Sub_Cl	71.3	8.6	5.4	5.2	7.7	-
Model4_Sub_Br	70.1	8.6	5.5	5.2	8.9	-
Model5_Tyr	75.3	7.5	0.1	3.5	3.8	6.4

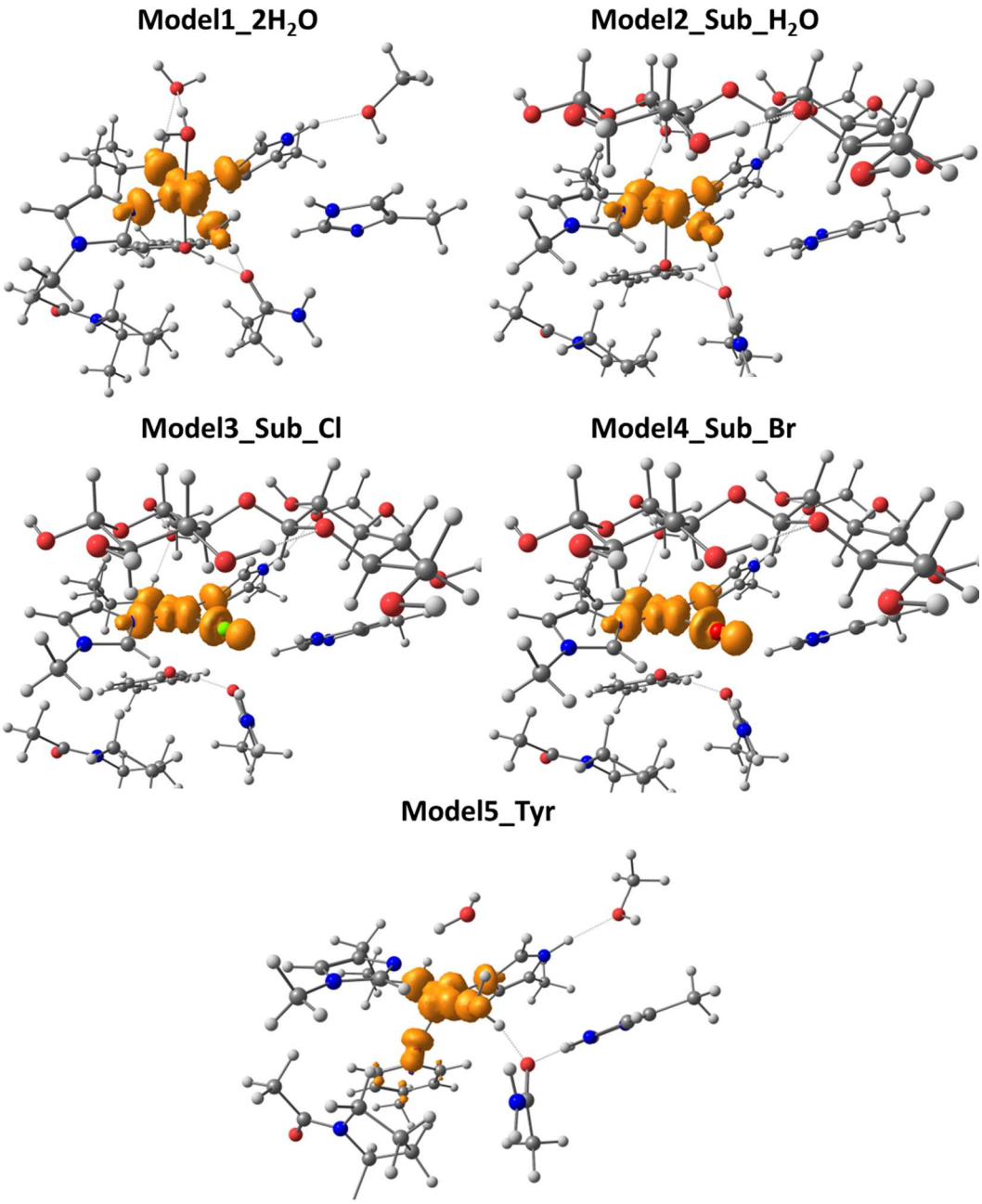

Figure 2.9 Calculated spin density (in orange) for the different models of the *Ls*AA9 active site. The spin density contour level for plotting is chosen at 0.003 e Å^{-3}.

2.3.4.3 Relative orientation of *g* and *A* matrices

The calculation of the SH parameters also affords the orientation of the *g* tensor and A^{Cu} tensor with respect to the reference molecular frame. From these orientations it is possible to make a connection with ligand field models of SH parameters (see discussion in **Section 2.4**). The molecular frame was defined with the origin on the Cu(II) ion, the *X* axis along the Cu–N$_\delta$ (imidazole ring, His1) bond, the *Y* axis along the Cu–N (amino

terminus) bond and the *Z* axis normal to these two vectors. In the resting state model (Model1_2H_2O), the calculated *g* tensor principal components essentially align with the defined molecular frame, with a small rotation (less than 5°) around the *Z* axis of the molecular frame (**Figure 2.10**); therefore it is possible to label the *g* values as follow: $g_1 = g_x$, $g_2 = g_y$ and $g_3 = g_z$. This assignment is in agreement with a qualitative assignment based on ligand field theory for a square planar Cu(II) complex, where the largest *g* value is perpendicular to the Cu coordination plane. The calculated A^{Cu} hyperfine tensor is essentially co-linear with the *g* frame, with a rotation of ~7° around the g_z direction (**Figure 2.10**). The same orientations are obtained also for Model2_Sub_H_2O, Model3_Sub_Cl and Model4_Sub_Br, with their *g* and *A* tensors basically co-linear and aligned with the molecular frame. These results support the fact that in the EPR simulations it is not necessary to include rotation of the *A* tensor against the *g* frame to obtain good fits. The results also confirm the assignment of the g_2 direction along the Cu(II)–halide bond (**Figure 2.3**).

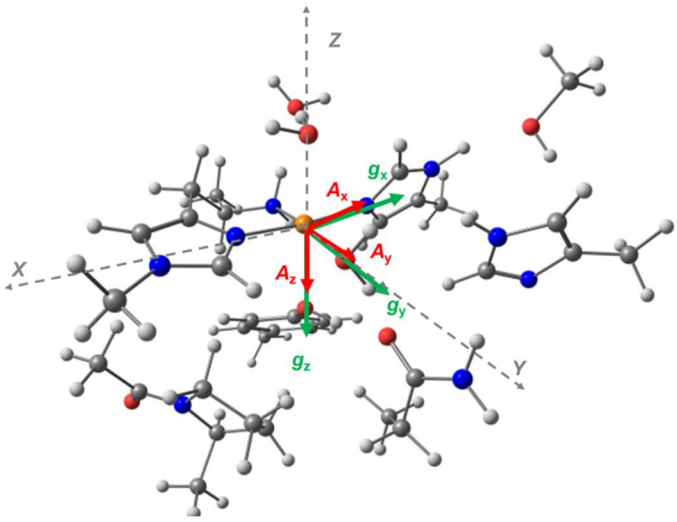

Figure 2.10 Cartoon representation of the calculated relative orientation of the *g* (green) and A^{Cu} (red) tensors principal components with respect to the molecular frame (grey dotted vectors), for Model1_2H_2O.

2.3.5 Theoretical calculations: d-d and charge transfer electronic transitions

To further characterize the electronic structure of the different models, the ligand field (d-d) and charge transfer excited states were calculated at the TD-DFT level of theory

(CAM-B3LYP functional and Def2-TZVP basis set on all atoms). The TD-DFT method allows to calculate excitation energies even in relatively large computational models (more than 100 atoms), without requiring large computational resources. However, this is generally not a very accurate method for transition metal systems, with calculated transition energies very sensitive to the choice of the functional.[89,90] Because d-d transition energies are important for the interpretation of the EPR spin Hamiltonian parameters, the ligand field exited states were also calculated with the CASSCF method, together with NEVPT2 treatment of dynamic electron correlation, distributing all Cu(II) nine electrons in the five molecular orbitals with predominant metal 3d character, namely CAS(9,5). Although more computationally expensive compared to TD-DFT, the CASSCF method is usually able to provide more accurate estimations of the d-d transitions for transition metal complexes, as already extensively studied for type 1 copper sites.[149,157,158] The energies and intensities of the calculated excitations were used to aid the assignment of the experimental electronic transitions (see **Section 2.3.2**). In this regard, in order to provide a meaningful labelling of the d orbitals, the molecular frame reference axes were set in the same way as for the EPR calculations (**Figure 2.10**).

2.3.5.1 TD-DFT

The calculated electronic spectra for the different models of the *Ls*AA9 active site are shown in **Figure 2.11**; the relative transition energies, together with their assignments, are summarized in **Table 2.12** (the labelling of the different excited states follows to the one used in **Figure 2.11**). The assignments were based on the difference density plots of each transition. In all the calculated spectra, the first four excited states correspond to d-d transitions while, at higher energies, the spectra are characterized by LMCT transitions, in qualitative agreement with the results obtained from the experimental spectra.

Overall, the energy of the ligand field transitions are always overestimated with respect to the experimental energies, by about 2000–3000 cm^{-1}, and their calculated intensities (50–150 M^{-1} cm^{-1}) are comparable to the experimental ones. Moreover, the calculated ordering of the d-d exited states is common to all the complexes, from Model1_2H_2O to Model4_Sub_Br, with only exception of Model5_Tyr because of its very different coordination geometry compared to the others. The first excited state is mainly

represented by a d(z^2) SOMO (**Figure 2.11**) and is followed by the second and third exited state, with predominantly d(xz) and d(xy) character, respectively. Finally, the last ligand field exited state is represented by a d(xy) SOMO. The first exited state is the one that shows the highest variability across the different models moving from 11910 cm^{-1} to 14440 cm^{-1} in Model3_Sub_Cl. The other d-d transitions are less affected by the change in Cu(II) coordination environment, with variations in the order of 500–1500 cm^{-1}, in agreement with the limited variations obtained from the experimental electronic spectra (**Table 2.3**). However, the obtained order of the ligand field excited states is not fully consistent with the MCD spectra, as they show that the two highest energy transitions are those forming the pseudo-*A* pair, d(xz)/d(yz) → d(x^2–y^2), while the TD-DFT calculates the d(xy) → d(x^2–y^2) as the highest energy transition. Lastly, the tyrosinate model (Model5_Tyr) is characterized by significantly lower d-d transition energies (**Table 2.12**), likely due to the distorted coordination geometry with respect to the enzyme resting state, which reduces the ligand field splitting of the d-orbitals.

Considering the charge transfer transitions, the comparisons with the experimental data are more difficult because, with the exception of *Ls*AA9_Sub_Br, the transitions in this region of the spectra are not well resolved and so their energies are not accurately determined. In addition, charge transfer transitions are known to be challenging for TD-DFT calculations, as their energies are dependent on the choice of the functional and on the polarity of the environment.[90] However, despite these limitations, some useful correlations with the experiment can be obtained from these calculations.

The calculated transition *5* (**Figure 2.11**) is the first charge transfer transition after the ligand field energy region and can be assigned as a tyrosine → Cu(II) SOMO LMCT, which appears at lower energies with respect to the His → Cu(II) LMCT. Therefore, this transition suggests an alternative assignment for the experimental band *4* in the electronic spectra of the complexes (**Table 2.3**): this band does not represent a tyrosinate → Cu(II) LMCT, but instead a tyrosine → Cu(II) SOMO LMCT. The calculated energy for this transition in the different models (24750–26800 cm^{-1}) is always higher with respect to the experimental one (~21000 cm^{-1}), but its low intensity (50–100 M^{-1} cm^{-1}) and position with respect to the other LMCT transitions, are consistent with the characteristics of the experimental band *4*. On the other hand, the calculated UV-vis spectrum of Model5_Tyr shows a very intense tyrosinate → Cu(II) SOMO LMCT, due to the significant overlap between the tyrosinate π HOMO and the Cu based SOMO (which is typical in Cu(II)–

phenolate model complexes).[146,159] Hence, it can be argued that if a species corresponding to Model5_Tyr was present in the enzyme resting state, even in small amounts, it should be possible to observe its characteristic LMCT transition.

The first two His → Cu(II) SOMO LMCTs are found at higher energy, ~31000 cm^{-1}, and close to each other (transitions *6* and *7* in Model1_2H2O). This provides a reasonable assignment for the band at 31800 cm^{-1} in the electronic spectra of the resting state as a histidine based LMCT (**Figure 2.5**), also given the weak temperature dependence of its MCD signal (**Figure 2.6**). Upon addition of substrate (Model2_Sub_H_2O), the calculated spectrum suggests a large energy splitting between the two LMCTs, because the His-1 → Cu(II) SOMO LMCT is now predicted at 24400 cm^{-1}, while the other one (from His-64) remains ~31000 cm^{-1}. Even if it is possible that the substrate induces a difference in the energies of the two LMCTs, because of its lone pair–aromatic interaction only with His-1 (**Figure 2.1**), such a large effect is not consistent with the *Ls*AA9_C6 experimental spectrum, where significant MCD temperature dependence can be only detected for the band at ~31600 cm^{-1} (**Figure 2.6**). In the Model3_Sub_Cl, these two histidine based LMCTs are mixed the Cl in-plane p orbital (**Figure 2.11**), generating two LMCT transitions at 28800 cm^{-1} and 33490 cm^{-1}, with mixed Cl/His character and of higher intensity with respect to those in Model2_Sub_H_2O. For the Br^- complex, two additional transitions are predicted (23660 cm^{-1} and 26100 cm^{-1}), both corresponding to Br^- → Cu(II) SOMO, from the in-plane and out-of-plane p orbitals of the Br^-. The energy of these two LMCT is lower with respect to the chloride based LMCTs, in agreement with the experimental results (**Figure 2.5**).

In summary, the performance of TD-DFT for prediction of LMCT excited states is variable and not fully reliable for the prediction of the transition energies when compared with experiment. However, it is useful in aiding possible assignments for the experimentally determined bands.

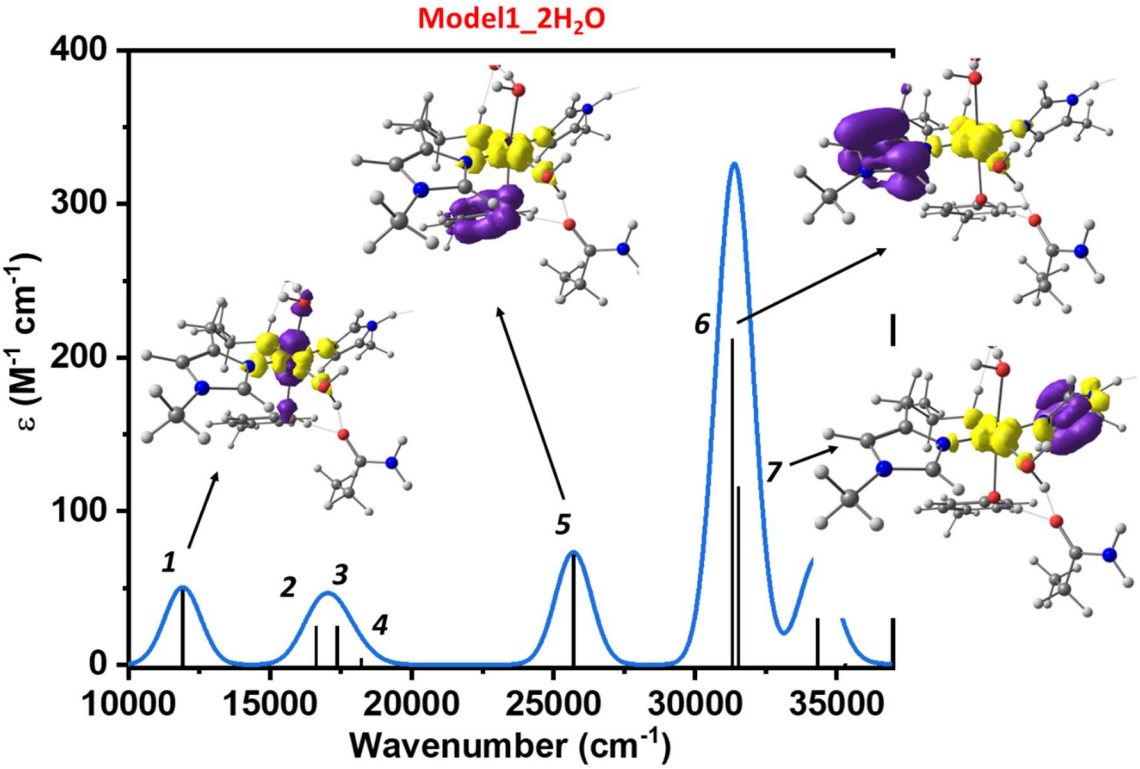

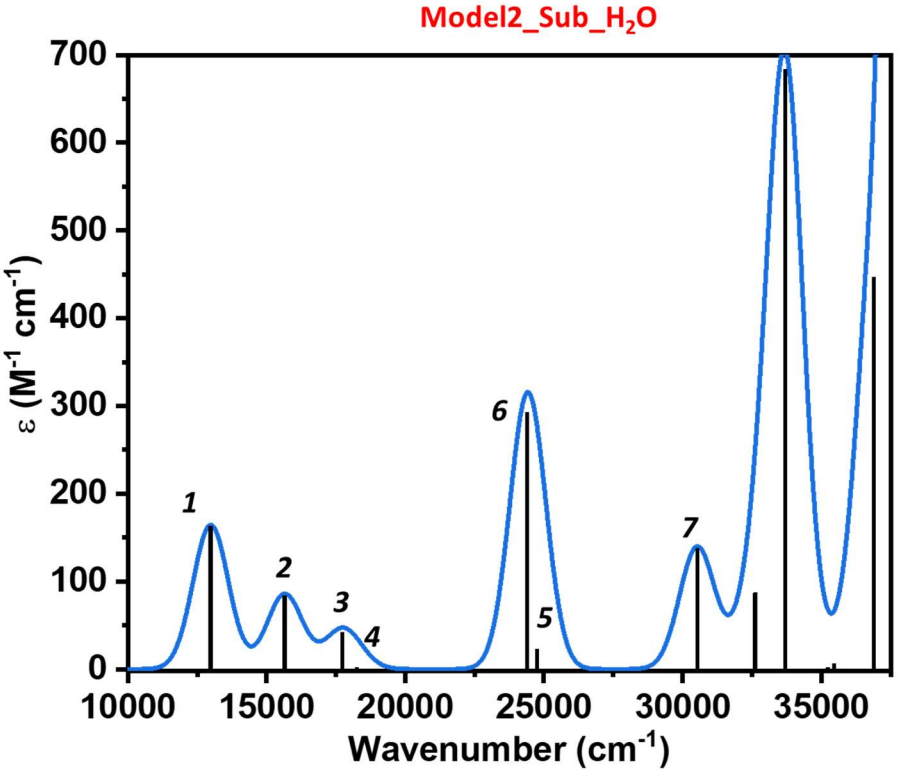

(Figure continued on next page)

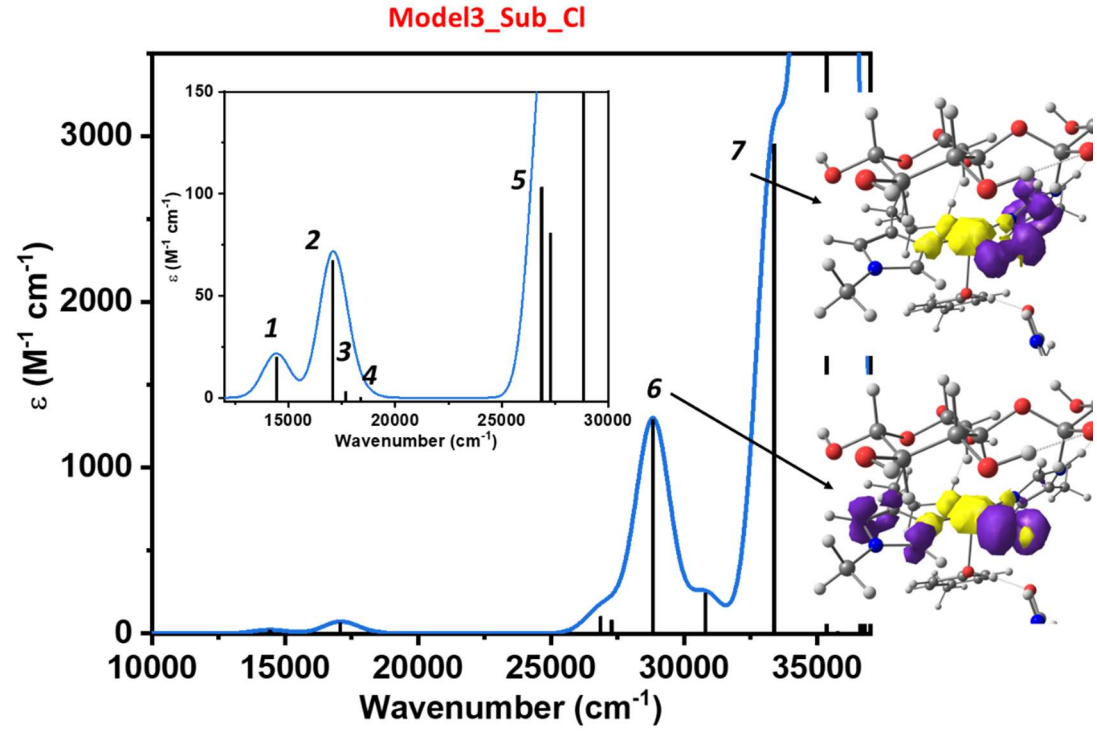

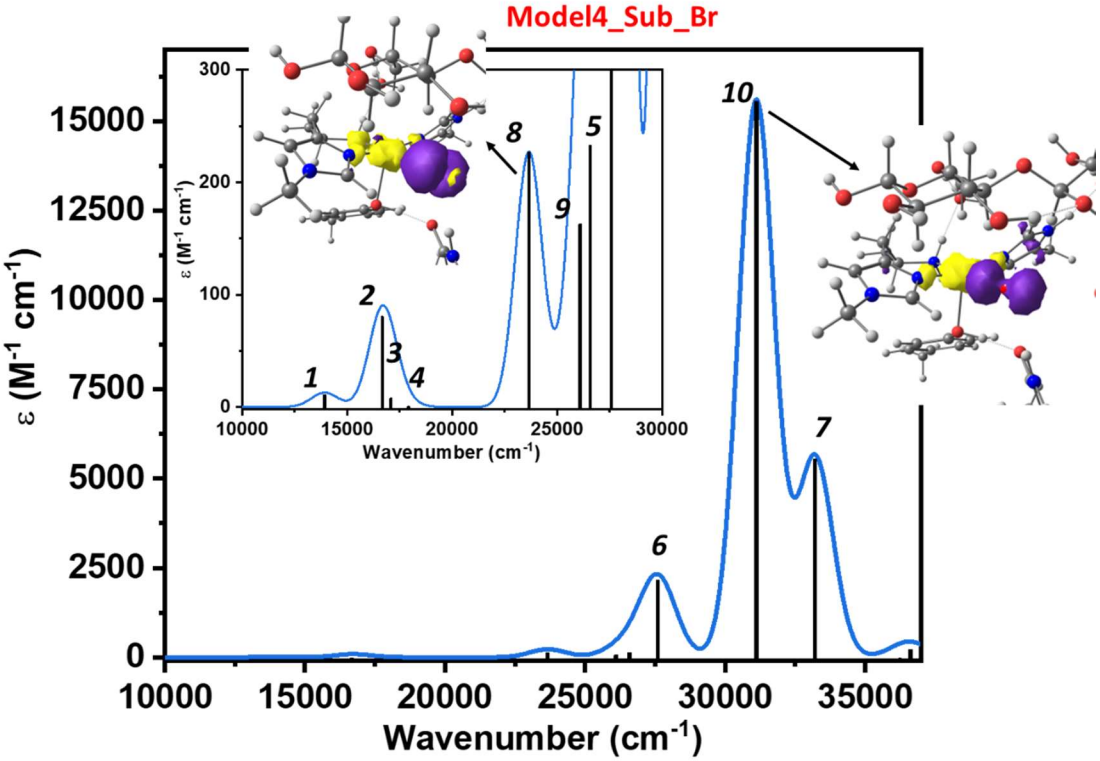

(Figure continued on next page)

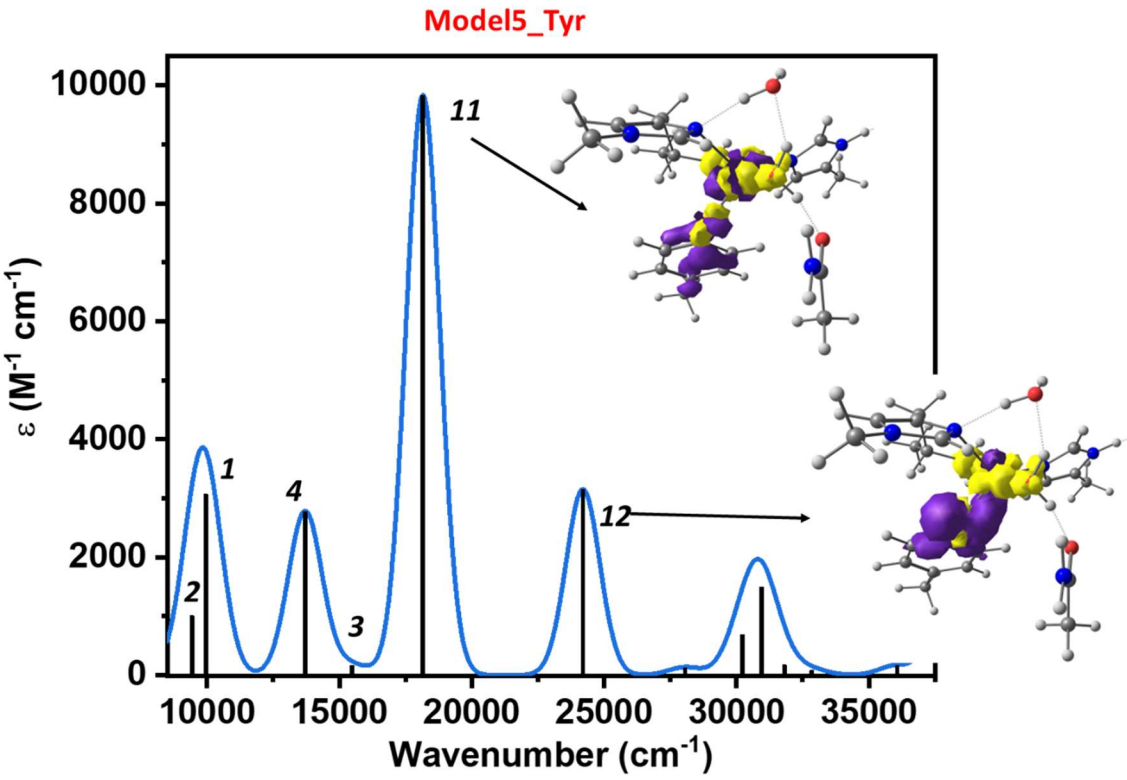

Figure 2.11 Calculated TD-DFT UV-vis spectra (blue) for the different models of the *Ls*AA9 active site. A band broadening of 1500 cm^{-1} was applied to each vertical transition. Vertical excitations are represented as black bars. The numbering of the transitions corresponds to the one reported in **Table 2.12**. The insets show the expanded d-d regions for Model3_Sub_Cl and Model4_Sub_Br. Difference density plots for selected transitions are reported as insets: yellow indicated positive electron density and purple indicates negative electron density. The plotted surfaces were generated with a 0.003 e/$Å^3$ cut-off.

Table 2.12 TD-DFT calculated energies (cm^{-1}) for selected transitions in the UV-vis spectra of *Ls*AA9 active site models, together with their respective assignments.[1]

Nr.	Excitation	Model1_2H_2O	Model2_Sub_H_2O	Model3_Sub_Cl	Model4_Sub_Br	Excitation	Model 5_Tyr
1	$d_{z^2} \rightarrow$					$d_{xz} \rightarrow$	
	$d_{x^2-y^2}$	11910	12990	14440	13930	$d_{x^2-y^2}$	9430
2	$d_{xz} \rightarrow$					$d_{xy} \rightarrow$	
	$d_{x^2-y^2}$	16630	15660	17070	16670	$d_{x^2-y^2}$	9950
3	$d_{yz} \rightarrow$					$d_{z^2} \rightarrow$	
	$d_{x^2-y^2}$	17360	17740	17680	17090	$d_{x^2-y^2}$	15480
4	$d_{xy} \rightarrow$					$d_{yz} \rightarrow$	
	$d_{x^2-y^2}$	18210	18260	18390	17920	$d_{x^2-y^2}$	13710
5	$Tyr \rightarrow$						
	$d_{x^2-y^2}$	25710	24748	26870	26590		
6	$His_1 \rightarrow$						
	$d_{x^2-y^2}$	31310	24400	28830	27595		
7	$His_{64} \rightarrow$						
	$d_{x^2-y^2}$	31530	30530	33390	33210		
8	$Br\ \pi_{ip} \rightarrow$						
	$d_{x^2-y^2}$				23660		
9	$Br\ \pi_{op} \rightarrow$						
	$d_{x^2-y^2}$				26100		
10	$Br\ \sigma \rightarrow$						
	$d_{x^2-y^2}$				31114		
11						$Tyr^- \rightarrow$	18160
						$d_{x^2-y^2}$	
12						$Tyr^- \rightarrow$	24200
						$d_{x^2-y^2}$	

[1]-The numbering of the bands corresponds to the one used in **Figure 2.11**. The *op* and *ip* labels stand for out-of-plane and in-plane, respectively.

2.3.5.2 CASSCF/NEVPT2

The ligand field exited states, together with the respective excitation energies, were calculated with the CASSCF/NEVPT2 method and are summarized in **Table 2.13**. If compared to the experimental energies obtained from the fitting of UV-vis/CD/MCD spectra, the calculated transitions are in reasonable agreement, with deviations in the order of 1500–2000 cm^{-1} compared to the Gaussian band maxima. This is a typical correlation between experiment and theory for this type of calculations. Overall, this methodology had a better performance as compared to the TD-DFT methodology.

Table 2.13 CASSCF/NEVPT2 calculated d-d excited states for the different models of the *Ls*AA9 active site.

Excitation	Model1_2H_2O	Model2_Sub_H_2O	Model3_Sub_Cl	Model4_Sub_Br	Excitation	Model5_Tyr
$d_{z^2} \rightarrow d_{x^2-y^2}$	11680	12620	13380	12870	$d_{xz} \rightarrow d_{x^2-y^2}$	8890
$d_{xy} \rightarrow d_{x^2-y^2}$	13430	13160	13840	13420	$d_{xy} \rightarrow d_{x^2-y^2}$	9860
$d_{xz/yz} \rightarrow d_{x^2-y^2}$	14470	14280	14950	14510	$d_{z^2} \rightarrow d_{x^2-y^2}$	10850
$d_{xz/yz} \rightarrow d_{x^2-y^2}$	15840	15980	16390	16000	$d_{yz} \rightarrow d_{x^2-y^2}$	12650

For all the models considered here, the predicted ground state SOMO is mainly $d(x^2–y^2)$ on the metal and is of σ* character type with respect to the ligands in the equatorial plane, in agreement with what already derived from the EPR spectra and the spin density distribution from DFT calculations (**Figure 2.9**). Again, with the only exception of Model5_Tyr, the ordering of the d-d excited states is common to all models, but with small differences in the excitation energies across the series. The first excited state features predominantly $d(z^2)$ character, while the second excited state is mainly of d(xy) character. The two excited states with highest energy have mainly d(xz) and d(yz) character, with some mixing between them due to spin–orbit coupling: the d(xz) orbital

mostly contributes to the third excited state, while the d(yz) mainly contributes to the fourth d-d transition (**Figure 2.12**). The transition energy that appears to be mostly affected by the change in the Cu(II) ligand set is the first excited state, which shifts ~1500 cm^{-1} higher in energy when the substrate is bound in the active site (**Figure 2.12**). This observation could be explained by a stronger interaction of the axial Tyr out-of-plane π HOMO with the Cu $d(z^2)$ orbital, consistent with the shortening of the Cu(II)–O(Tyr) distance, obtained upon substrate binding.

The calculated d-d excited states in Model3_Sub_Cl are shifted to slightly higher energies by about 500–1000 cm^{-1} with respect to the Model2_Sub_H_2O, suggesting a stronger interaction of the equatorial Cl^- with the Cu, which is able to produce a larger splitting between the $d(x^2–y^2)$ SOMO and the other d orbitals, compared to the splitting generated by H_2O ligand. This result reproduces the observation obtained earlier from the experimental electronic spectra, where the Cl^- induced a stronger ligand field on the Cu(II). A similar effect was calculated also for the Br^- ligand (Model4_Sub_Br), but with a general lowering of the electronic transitions by 500 cm^{-1} with respect to Model2_Sub_H2O. The Br^- forms a longer bond with the Cu(II) than Cl^- (2.56 Å and 2.41 Å, respectively), therefore generating a smaller effect on the metal ligand field.

On the other hand, Model5_Tyr with a fully deprotonated tyrosine is characterized by excited states with much lower energies than the resting state model, indicating a lower strength of the ligand field, not in accord with experiment. Moreover, the order of the excited states is different, with the first excited state mainly represented by the d(xz) orbital, followed by d(xy), $d(z^2)$ and d(yz), in order of increasing energy. The smaller magnitude of the ligand field also explains the larger *g* shifts obtained for Model5_Tyr compared to those obtained for Model1_2H_2O. Thus, the addition of substrate possibly drives a stronger Cu-tyrosine interaction, but not to the extent that the tyrosine deprotonates.

The calculated excited states ordering can be used to help the assignment of the experimental d-d transitions in the electronic spectra (**Table 2.3**). In the experimental spectra there are three bands which can be assigned as d-d excitations, on the basis of their C_0/D_0 ratio. Of these, the two with highest energy form the MCD pseudo-*A* pair and assigned as $d(xz/yz)\rightarrow d(x^2–y^2)$ transitions, in agreement with the CASSCF calculations: the transition with the highest energy of the two is always assigned as $d(yz)\rightarrow d(x^2–y^2)$ while the other one as $d(xz)\rightarrow d(x^2–y^2)$. Following the ordering, the lowest energy band

in the experimental spectrum can be assigned to $d(z^2)/d(xy) \rightarrow d(x^2-y^2)$. In general, the $d(xy) \rightarrow d(x^2-y^2)$ transition is characterized by a negative sign in MCD spectra of mononuclear Cu(II) complexes, while the $d(z^2) \rightarrow d(x^2-y^2)$ is usually positive.[91,144,145,149] Therefore, even if it is not possible to assign with certainty the experimental band *1*, it can be tentatively assigned as $d(z^2) \rightarrow d(x^2-y^2)$; the leftover $d(xy) \rightarrow d(x^2-y^2)$ transition then remains unresolved in the experimental spectra. However, the *Ls*AA9_C6_Br complex is an exception to this picture: here the fitting of UV-vis, CD and MCD spectra shows a negative band positioned in between the two states that form the pseudo-*A* pair and hence tentatively assigned $d(xy) \rightarrow d(x^2-y^2)$, while the $d(z^2) \rightarrow d(x^2-y^2)$ transition is missing possibly because it is now overlapped with the d(xz) based excitation. We note that in this case, the experimental result suggests a d(xy) excited state higher in energy than the d(xz) one, but the CASSCF calculations predict the former at lower energy with respect to the d(xz) excited state. Because the $d(xy) \rightarrow d(x^2-y^2)$ transition is not resolved in the other experimental spectra, it is not possible to conclude if its energy is systematically underestimated by the CASSCF calculations or the *Ls*AA9_C6_Br represents an exception.

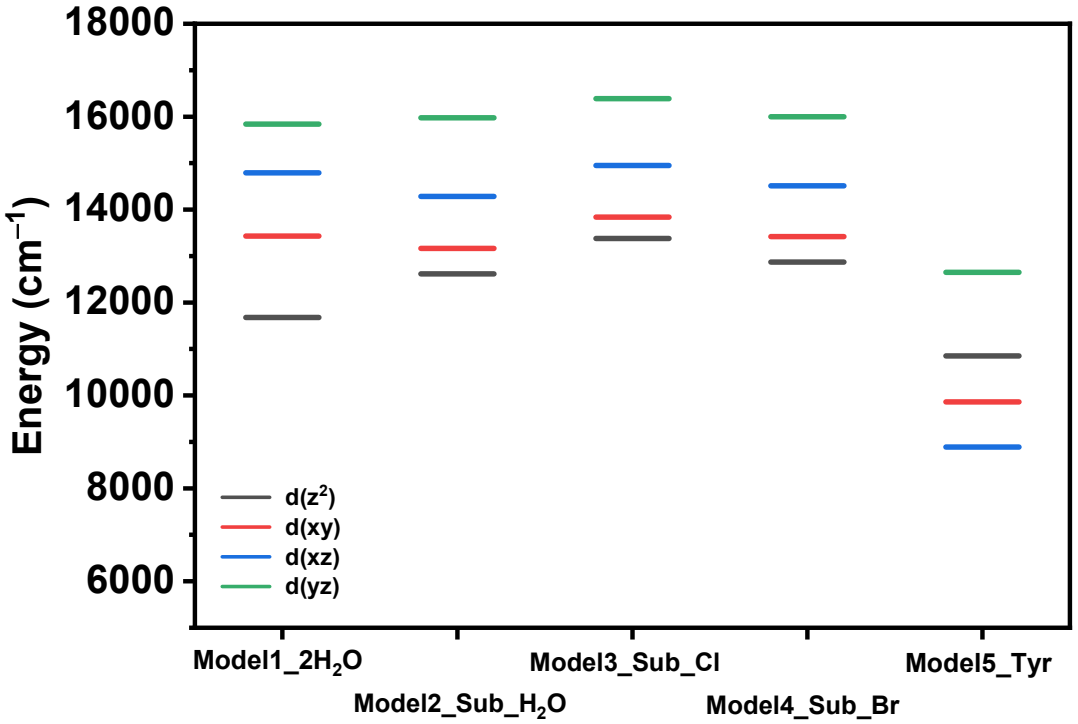

Figure 2.12 CASSCF/NEVPT2 calculated excited states for the different models of the *Ls*AA9 active site. Excited states are labelled according to the d orbital that mainly represent the location of the unpaired electron. The ground state is labelled as d(x^2–y^2) and set at 0 cm^{-1}.

2.4 Discussion

Exploiting the ability of *Ls*AA9 LPMO to act on soluble oligosaccharides as substrates, we were able to perform a detailed investigation of the electronic structure of the enzyme/substrate complex, through the use of EPR, UV-Vis, CD and MCD spectroscopies coupled with theoretical calculations. Previous structural investigations showed that the substrate (cellohexaose, in this case) does not coordinate directly the Cu(II) ion upon binding to the enzyme, therefore any change in spectroscopic properties brought about by it must be due to an interaction with the Cu(II) outer coordination sphere.[65] The binding of the substrate to the Cu(II)–*Ls*AA9 active site is always accompanied by a characteristic perturbation of is EPR spectrum. Very similar perturbations were also reported for other two AA9 LPMOs, *Cv*AA9 and *Nc*AA9C upon cellohexaose/cellulose binding, suggesting that the observed effect is not only particular for *Ls*AA9 studied here, but more relevant to all the AA9 family.[70,82] Hence, the analysis of the EPR spin Hamiltonian parameters can help understanding the effects of the substrate on the Cu electronic structure.

In this context, ligand field theory (LFT) provides a useful model to aid interpretation of SH parameters from EPR spectra.[160] Within this model, the assigned d-d transitions, the experimental *g* values and the Cu hyperfine contributions, $A^{Tot} = A^{Fermi} + A^{Spin\text{-}Dipolar} + A^{Spin\text{-}Orbit}$ are used to calculate ground (γ_{GS}^2) and excited states ($\gamma_{xy}^2, \gamma_{xz}^2$ and γ_{yz}^2) Cu(II) d-orbital characters together with the amount of d(z^2) mixing into the ground state SOMO, using the following equations (see **Appendix 1** for full details about the methodology):

$$\Delta g_z \approx \frac{8\zeta_{\mathrm{Cu}}\,\gamma_{GS}^2\,\gamma_{xy}^2\,a^2}{\Delta E_{xy\rightarrow x^2-y^2}}$$

$$\Delta g_x \approx \frac{2\zeta_{\mathrm{Cu}}\,\gamma_{GS}^2\,\gamma_{yz}^2\,(a-\sqrt{3}b)^2}{\Delta E_{yz\rightarrow x^2-y^2}}$$

$$\Delta g_y \approx \frac{2\zeta_{\mathrm{Cu}}\,\gamma_{GS}^2\,\gamma_{xz}^2\,(a+\sqrt{3}b)^2}{\Delta E_{xz\rightarrow x^2-y^2}}$$

$$A_{iso} = P_d\left[-K + \frac{1}{3}\left(\Delta g_x + \Delta g_y + \Delta g_z\right)\right]$$

$$A_z = P_{\mathrm{d}}\left[-K - \frac{4}{7}\gamma_{GS}^2(a^2-b^2) + \Delta g_z + \frac{\Delta g_y\left(3a-\sqrt{3}b\right)}{14(a-\sqrt{3}b)} + \frac{\Delta g_x\left(3a+\sqrt{3}b\right)}{14(a-\sqrt{3}b)}\right]$$

ζ_{Cu} represents the one-electron quasi-atomic copper spin–orbit coupling constant (usually taken as –830 cm^{-1}), the γ values are reduction factors which are sometimes associated with the 'covalent dilution' of the metal d-orbitals with the relative ligand orbitals, the ΔE values are excitation energies of the ligand field transitions, while *a* and *b* measure character of d(x^2–y^2) and d(z^2) in the ground state (GS), respectively ($a^2 + b^2 = 1$). $P_{\mathrm{d}}=g_e g_{\mathrm{Cu}}\mu_e\mu_{\mathrm{Cu}}$ is the quasi atomic parameter usually taken as 1180 MHz, while the term $-P_{\mathrm{d}}K$ represents the isotropic Fermi contact, which is treated phenomenologically in LFT. Lastly, A_{iso} is the isotropic Cu hyperfine coupling, the average of the hyperfine coupling over the *x*, *y* and *z* directions. Despite not being quantitatively accurate, these equations are useful tools which aid interpretation of spin Hamiltonian parameters and give chemical insight into the electronic structure of the Cu(II) ion.[160]

From these relationships it can be reasoned that differences in g_x and g_y can arise from differences in transition energies of the d(xz) and d(yz) transitions, or in differences in the excited state covalencies (γ_{xz}^2 and γ_{yz}^2), or by d(z^2) mixing into the ground state (b^2).

Following the work proposed by Gewirth *et al*. the value of b^2 can be estimated from the rhombicity parameter (R_g) using the following expression:[161]

$$R_g = \frac{2(\Delta g_y - \Delta g_x)}{\Delta g_y + \Delta g_x} \approx 2\frac{\Delta E_{\mathrm{yz}}\left(a+\sqrt{3}b\right)^2 - \Delta E_{\mathrm{xz}}\left(a-\sqrt{3}b\right)^2}{\Delta E_{\mathrm{yz}}\left(a+\sqrt{3}b\right)^2 + \Delta E_{\mathrm{xz}}\left(a-\sqrt{3}b\right)^2}$$

With $a^2 + b^2 = 1$ and assuming $\gamma_{xz}^2 \approx \gamma_{yz}^2$.

The calculated values for b^2, γ_{GS}^2 and the different contributions to A_z, for the *Ls*AA9/cellohexaose complexes are summarized in **Table 2.14**. In all cases the amount of d(z^2) mixing into the ground state is very small, as expected on the basis of their nearly axial EPR spectra. However, R_g is a steep function of b^2, and a small amount of mixing is required in the equations to fully account for the g_x/g_y splitting observed experimentally.

Table 2.14 Contributions to Cu A_z (MHz) and γ_{GS}^2 for the different *Ls*AA9/cellohexaose (C6) complexes, calculated with ligand field theory model.

Complex	A_z^{total}	A_z^{FC}	A_z^{SD}	A_z^{SO}	γ_{GS}^2	b^2 (d_{z^2}%)
***Ls*AA9**	–460	–251	–565	356	0.85	0.3
***Ls*AA9_C6**	–518	–294	–567	344	0.84	0.0
***Ls*AA9_C6_Cl**	–517	–275	–543	300	0.81	0.3
***Ls*AA9_C6_Br**	–525	–279	–531	286	0.80	0.4

The binding of the substrate to the enzyme resting state is accompanied by an increase in $|A_z|$ (from 460 MHz to 518 MHz), a change readily explained by an increase in the magnitude of the Fermi coupling contribution ($|A^{FC}|$), from 251 MHz to 291 MHz for *Ls*AA9 and *Ls*AA9_C6, respectively. On the other hand, the overall covalency of the SOMO remains constant, suggesting that the displacement of the Cu axial H_2O does not significantly affect the covalency of the His brace. Indeed, this is corroborated by the DFT calculated spin density, which shows virtually zero delocalization on the axial H_2O. The amount of Fermi coupling at the Cu is affected by the core orbitals spin polarization (negative contributor), valence shell spin polarization (negative contributor) and 4s

orbital mixing with the SOMO (positive contributor).[154] The 4s orbital content of the SOMO is generally proportional the amount of d(z^2) orbital into the SOMO therefore,[162] given the low rhombicity of *Ls*AA9 and *Ls*AA9_C6, its contribution to the change in A^{FC} is probably negligible. On the other hand, core orbitals spin polarization generally is proportional to the degree of spin density at the Cu, which remains essentially constant upon substrate binding. Hence, the observed shift in A^{FC} is likely related to an increase in the magnitude of the valence shell spin polarization (i.e. more negative A^{FC}). Indeed, previous studies in Cu(II) complexes emphasised the importance of the valence shell contribution to A^{FC}, especially when there are changes in coordination geometry and/or in the number of ligands, which here goes from 6 to 5 Cu ligands.[154] A similar effect was also reported in a recent study on *Bl*AA10 LMPO by Courtade *et al*. where, upon substrate binding, the number of Cu ligands changed from 5 to 4 and the coordination moved from a distorted square pyramidal geometry to an essentially square planar geometry.[62] This effective change in geometry and number of Cu ligands was accompanied by a significant reduction of the A^{FC}, going from –134 MHz (no substrate) to –320 MHz (with substrate). Lastly, we note that the DFT calculations (**Table 2.9**) appear to underestimate this effect for Model2_Sub_H_2O as the A^{FC} contribution shifts in the opposite direction as compared to the LFT model (–287 MHz and –267 MHz for Model1_$2H_2O$ and Model2_Sub_H_2O, respectively), and generating the inconsistency between the calculated and experimental *A* principal components (**Table 2.8**).

Through a combination of UV-vis stopped flow and freeze-quench EPR data, Kjaergaard *et al*. showed that the reaction of the Cu(I) state with O_2 in *Ta*AA9 LPMO, in the absence of substrate, rapidly regenerated the spectroscopic features of the Cu(II) resting state, with an overall rate constant $k > 0.15$ s^{-1}.[63] They demonstrated that this process was the result of an inner sphere process, with the formation of a Cu(I) + O_2 bound species (although no Cu–O_2 intermediate was detected). In this reaction, the formation of a strong bond Cu–O_2 bond is fundamental to drive the thermodynamically unfavourable one-electron reduction of O_2 to O_2^- ($E^{o}_{Cu(II)/Cu(I)}$in AA9 LPMO ~250–275 mV, $E^{o}_{O_2/O_2^-}$= –165 mV *vs* SHE) . In agreement with this observation, our DFT modelling shows that the histidine brace coordination environment generates an almost perfectly flat Cu equatorial coordination plane where all the Cu(II) spin density is confined in this plane (**Figure 2.9**). This particular arrangement guarantees that the overlap between the Cu(II) based SOMO and the O_2 π^* frontier molecular orbital is maximized in order to form a

strong covalent bond between the two. In the same study, using DFT modelling, Kjaergaard *et al.* also showed that the bound superoxide species could be easily displaced by the axial H_2O, regenerating the enzyme resting state with H_2O bound in the equatorial position.[63] As already seen, the binding of the substrate displaces this axial H_2O, disrupting this O_2^- dissociation mechanism and possibly increasing the stability $[Cu–O_2]^+$ intermediate.

The binding of Cl^- in place of the equatorial H_2O ligand, in *Ls*AA9_C6_Cl, is accompanied by a large reduction in g_z with respect to *Ls*AA9_C6, but with a very similar A_z, as compared to *Ls*AA9_C6. The g_z reduction generates a reduction in the A^{SO} contribution which is counter-balanced by a reduction in the magnitude A^{FC} and A^{SD}, because of an increase in covalency due to the formation of Cu(II)–Cl bond ($\gamma_{GS}^2 = 0.81$, **Table 2.14**). Together with the increased covalency, the electronic spectra of *Ls*AA9_C6_Cl show an increase in the ligand field strength at the Cu(II), shifting the d-d transitions to higher energy (especially for the $d(xy) \rightarrow d(x^2–y^2)$ transition) and providing a second mechanism for the reduction of g_z. A similar argument can be formulated also for the *Ls*AA9_C6_Br complex and supported by the CASSCF calculations, which give slightly higher ligand field excitations for the chloride and the bromide complexes with respect to *Ls*AA9_C6 (**Figure 2.12**). This result is surprising since the shift in the energy of the d-d transitions across the $H_2O/Cl^-/Br^-$ series is counter to what is expected from the spectrochemical series. According to the spectrochemical series the H_2O is a stronger ligand than Cl^- and Br^- and therefore the *Ls*AA9_C6 complex should be the one with the highest ligand field. This observation suggests that chloride and bromide are able to induce an unusually strong ligand field to the Cu(II) in the *Ls*AA9 active site.

A previous study on the *Ls*AA9-cellohexaose interaction by Frandsen *et al.* demonstrated a strong cooperative effect between chloride and cellohexaose in increasing the substrate and anion binding to the active site: the dissociation constant K_d for C6 decreased from ~1 mM to 3.7 μM after addition of 200 mM Cl^- in solution. On the other hand in the absence of the substrate, a Cl^- concentration 200 mM could only generate a minor species (~20 % detected by EPR spectroscopy) in solution.[65] We have found a similar effect also with the Br^- ion, as the complex could only be formed in presence of cellohexaose. Moreover, the Cl^-/substrate enhanced binding is not an exclusive feature of the *Ls*AA9 LPMO but was observed also in other AA9 LPMOs, like *Cv*AA9 and

*Nc*AA9C, with very similar changes in in the enzyme relative EPR spectrum: significant reduction of g_z, a larger A_z and appearance of the characteristic superhyperfine pattern.[70,82]. A similar effect of increased substrate affinity in presence of CN^- was also reported for *Nc*AA9C by Courtade *et al*.[80] In these works, it was suggested that small anions, like CN^- and Cl^-, could be considered as superoxide analogues and that this increased affinity was consistent with a favourable binding of a reduced O_2 species (like O_2^-), in the initial step of the enzymatic catalytic cycle.[65,80]

The EPR data, together with DFT calculations for the *Ls*AA9_C6_Cl and *Ls*AA9_C6_Br complexes, show that these complexes are slightly more covalent compared to *Ls*AA9 and *Ls*AA9_C6, resulting in a reduced spin density on the Cu, and a higher spin density on the Cl^-/Br^- as compared to the H_2O, in agreement with a higher nephelauxetic effect for the halides. It is possible to speculate that a similar effect would be obtained upon formation of a strong covalent bond with O_2 (a π acceptor ligand), allowing to delocalize some spin density from the Cu(II) and obtaining a stabilizing effect due to nephelauxetic expansion (reduced electron repulsion on the Cu). A strong bonding interaction is also consistent with the increased ligand field obtained for the chloride and bromide cases, with respect to *Ls*AA9 resting state.

On the other hand, the binding of substrate to the enzyme resting state induces the appearance of a well-defined superhyperfine pattern in the *Ls*AA9_C6 complex X-band EPR spectrum (**Figure 2.3**), possibly due to an increase of the N ligating atoms coupling (and increased covalency in the His brace plane).[65] EPR spectra simulations reported here gave similar N couplings across the complex series for the ligating imidazole N atoms, while for the amino terminus, the A^N tensor is essentially constant in moving from *Ls*AA9 to *Ls*AA9_C6 (~30–35 MHz) , but then drops upon binding of Cl^- in *Ls*AA9_C6_Cl (~19 MHz). The DFT calculated SHF couplings supports the picture of essentially constant coupling with the ligands, but do not reproduce the drop obtained in *Ls*AA9_C6_Cl. Hence, given the apparent disagreement between the experimental and the calculated values and the relatively large error in the determination of SHF coupling from X-band EPR spectra only it is difficult to define a clear model for a substrate induced effect on SHF couplings. Hence, even though it is possible that the substrate induces a perturbation in the ligating nitrogen coupling with the Cu(II), more detailed investigation on N SHF coupling through ENDOR and HYSCORE spectroscopies are needed to clarify this subject.

Another important consideration about the electronic structure of the *Ls*AA9 Cu active site is the ordering of the d-d excited states. In the resting state, the electronic spectra of the enzyme, together with the CASSCF calculations, assign a mainly d(z^2) character to the first excited state, while two highest ones have mainly d(xz) and d(yz) character, respectively. Therefore, in terms of ligand field splitting schemes, the coordination geometry is best described as a tetragonally distorted coordination (Jahn-Teller distortion), rather than a square planar coordination, as shown in **Figure 2.13**. This consideration suggests that the Cu axial ligands, even if they have long bond distances with the metal, are important in defining the electronic structure of Cu(II). As a comparison, one of the two mononuclear Cu sites (Cu_M site) in PHM enzyme, characterized by histidine residues coordination in the metal equatorial plane, but without axial ligands, the d(z^2) SOMO excited state is found as the one highest in energy, while the d(xy) orbital represents the first excited state.[144] Moreover, the results from the CASSCF/NEVPT2 calculations, shows that this orbital splitting remains the same also in the substrate bound models, indicating that the Tyr-164 alone is enough to yield the d(z^2) orbital as the first excited state SOMO.

Moreover, the spectroscopic and computational data obtained here suggest that Tyr-164 residue is also involved in a weak LMCT transition with Cu(II). Mutational studies targeted the replacement of Tyr-164 with other non-coordinating residues (like a phenylalanine) would be necessary to definitively prove the origin of this transition, however—even in the absence of such studies—its features are consistent with the proposed assignment: the weak intensity and lack of measurable *C*-term dependence are due to the axial positioning this ligand, resulting in a very low overlap with the d(x^2–y^2) based SOMO.

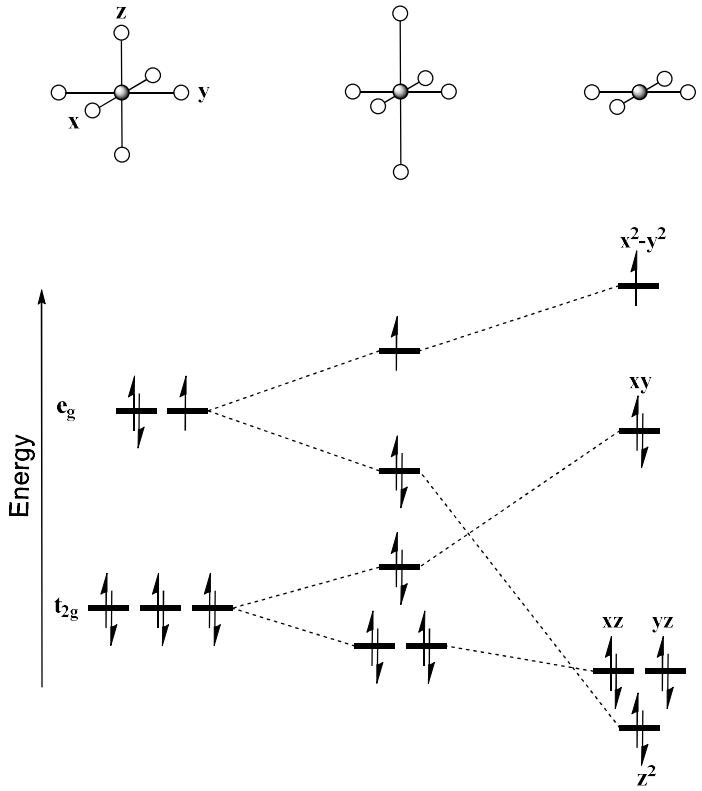

Figure 2.13 Cu(II) d orbital splitting scheme upon changing the coordination geometry from a octahedral to a square planar coordination geometry *via* elongation of the Cu–L bonds along the Z axis.

This tyrosine is a conserved residue in the AA9 family however, to date, there are only few studies that investigated its role in enzymatic catalysis. In an early study, Harris *et al*. demonstrated that replacing this Tyr with a Phe residue significantly reduced the enzymatic activity in *Tt*AA9E, but it was not completely abolished.[49] Moreover, Span *et al*. showed that the modification of the H-bonding network in which the axial Tyr is involved affect the Cu(II) EPR spectrum of the resting state,[56] consistent with hypothesis of the axial Tyr being an important part in defining the active site electronic structure. Various proposals have been suggested for the role of the active site Tyr in the catalytic mechanism of LMPOs. Among these, there is the hypothesis that the Tyr is part of an electron transfer chain that delivers electrons from an exogenous reducing agent to the copper during catalysis,[75] or help protecting the active site from highly oxidizing reactive intermediate, generated during uncoupled catalysis.[163] Indeed, the possibility of a LMCT transition with the Cu(II) reported here is consistent the previous hypothesis. The potential redox activity of Tyr-164 will be further investigated in the next chapter.

2.5 Conclusions

Multi-frequency CW-EPR spectroscopy, together with UV-vis, CD and MCD spectroscopies, enabled the determination of accurate Cu(II) spin-Hamiltonian values and d-d transition energies, for the *Ls*AA9 LPMO resting state and for the enzyme-substrate complex, with different ligands in the Cu(II) equatorial position (H_2O, Cl^- and Br^-). These data, in combination with DFT and CASSCF calculations, gave an accurate description of the Cu active site electronic structure. We found the Cu d orbital splitting is consistent with a Jahn-Teller distorted octahedral geometry and where the particular His brace ligand environment generates a well-defined Cu(II) based SOMO, which is oriented in order to have optimized interaction (high orbital overlap) with an equatorial exogenous ligand. Indeed, this is a key requirement for efficient O_2 activation, where the energetic cost of the one-electron reduction of dioxygen is counterbalanced by the formation of a strong covalent Cu–O_2^- bond. Addition of substrate to the Cu(II) resting state of the enzyme causes small changes to the active site electronic structure which are consistent with a shift from a 6 coordinate to a 5 coordinate Cu complex, where the axial H_2O ligand is displaced by the substrate. The enzyme-substrate complex can bind small anions (like Cl^- and Br^-) in this equatorial position, forming complex characterized by higher covalence and higher ligand field with respect to an H_2O ligand in the same position. Moreover, the presence of a low energy and low intensity Tyr → Cu(II) LMCT was demonstrated, suggesting a potential involvement of Tyr-164 in electron transfer processes to the metal, during the enzyme catalytic cycle.

3 Formation of a Cu(II)-Tyrosyl complex in *Ls*AA9

3.1 Introduction

Lytic polysaccharide monooxygenases (LPMOs, also known as PMOs) are copper-containing enzymes that catalyze the oxidative cleavage of polysaccharides by dioxygen or hydrogen peroxide.[8,27,29–31,50] The active site of LPMOs contains a single copper ion coordinated by an N-terminal histidine through the NH_2 of the amino terminus and the π-N of its imidazole side chain.[65] A T-shaped coordination geometry at the Cu is completed by the τ-N atom of a further histidine side chain. This structural unit is known as the histidine brace (**Figure 3.1**).[55] There is interest in LPMOs, not only for their use in commercial bioethanol production and bacterial/fungal virulence,[32,95] but also for the—as yet unknown—details of their catalytic mechanism(s),[94] especially the means by which the enzyme oxidizes a C–H bond in the polysaccharide substrate, the bond dissociation energy (BDE) of which is calculated to be *ca.* 100 kcal mol^{-1}.[164]

Studies of LPMOs have concentrated on the active site, with more recent attention focusing on the role of amino acid residues within the secondary coordination sphere of the Cu center.[56] Here, the situation is complicated by the fact that LPMOs exist in at least seven distinct phylogenetic groups (listed as classes AA9,[30] AA10,[27] AA11,[37] AA13,[38,75] AA14,[39] AA15[40] and AA16[41] in the CAZy database).[35] Each class presents a subtly different active site structure, due to differences in the identities and positions of amino acid residues in the secondary coordination sphere of the copper (**Figure 1.11**).[52]

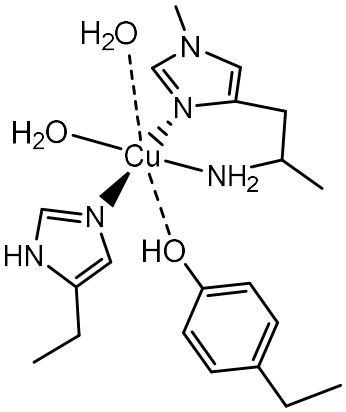

Figure 3.1 Scheme of the active site structure of a Cu(II)–AA9 LPMO, depicting the histidine brace, the axially-positioned tyrosine and equatorial and axial water molecules. The Cu–O distance with the axial ligands are > 2.5–2.6 Å, too long to be considered a formal bond interaction.

The secondary coordination sphere of the copper ion in proteins can have profound effects on the reactivity of any exogenous ligands bound to the copper.[165] Indeed, in the context of LPMOs, on-going site directed mutagenesis work coupled with activity studies and EPR spectroscopic measurements have highlighted the critical role, in terms of catalytic activity, of the glutamine in the active site of AA9 LPMOs, and the important roles of a tyrosine and non-coordinating histidine that are also found in the secondary coordination sphere.[49,56] Also, the significance of an alanine side chain in AA10 LPMOs has recently been demonstrated, in which the methyl group of the alanine likely restricts coordination of exogenous ligands in the axial position of the copper coordination sphere.[61,166] Among these residues however, the role of the tyrosine found in all LPMO classes (except some AA10 LPMOs), and which is always positioned in the axial coordination position of the copper ion, has attracted most attention, not least because it is not clear how this side chain is not oxidized in preference to the substrate during catalytic turnover; BDE (O–H), ~88 kcal mol^{-1}.[167]

In this regard, various proposals exist for the role of the tyrosine in the mechanism of LPMOs. Principal amongst these is that the tyrosine forms part of an electron transfer chain that delivers electrons from an exogenous reducing agent to the copper while the LPMO is in contact with a substrate.[75] There have also been proposals where the tyrosine/tyrosyl radical redox-couple stabilizes an intermediate Cu(II)–oxyl or Cu(III)–OH species, similar to the formation of the porphyrin radical cation seen in Compound I of P450 enzymes.[50] A further proposal is that the tyrosine protects LPMOs from self-

oxidation during the non-substrate-coupled turnover of O_2; this suggestion parallels a similar role for tyrosine(s) in P450 enzymes.[163] In delineating a role for the tyrosine in LPMOs, however, direct experimental evidence is scarce. There have been no spectroscopic determinations of any intermediates, save for a single report from Singh *et al*., who observe tyrosyl radical formation upon treatment of a Cu(II)-LPMO with hydrogen peroxide in the presence of excess reducing agent.[163] Using perpendicular-mode EPR, resonance Raman and UV/vis spectroscopies, the authors of this study proposed the formation of a *S*=1 Cu(II)–(•OTyr) ferromagnetically-coupled pair, which was further suggested to be part of the catalytic cycle of LPMOs. In addition to experimental work, DFT and QM/MM calculations have also been undertaken on several different LPMO systems in the presence of substrate. None of the preferred pathways from these calculations invokes a role for the tyrosine residue within the catalytic mechanism.[99,103,168]

It is in this context that we report a multi-spectroscopic (EPR, VT/VH-MCD, CD, UV/vis, XAS, resonance Raman), mass spectrometry and DFT study into a purple-coloured species that arises during the uncoupled turnover of an AA9 LPMO (*Ls*AA9) with hydrogen peroxide at raised pHs. We show that this species is a stable Cu(II)–tyrosyl radical, akin to those seen in other copper oxidases like galactose oxidase.[169,170] In contrast to galactose oxidases, this tyrosine radical is not covalently modified, nor is it part of the catalytic cycle of LPMOs. Moreover, at physiological pHs (< 7) the purple species does not form to any significant extent, leading to the proposal that the active site tyrosine in LPMOs, along with a nearby tryptophan residue, is part of a hole-hopping pathway which protects LPMOs from oxidation during uncoupled turnover. This study also points to the challenges which highly oxidizing intermediates present to enzymatic systems and the means by which the potentially deleterious effects of these intermediates are mitigated by the protein, not only through the use of hole-hopping residues like tyrosine but also through glycosylation substitutions on the enzyme, a feature also revealed in our current study.

3.2 Methods

3.2.1 Preparation of *Ls*AA9 LPMO

The *Ls*AA9 LPMO enzyme purified as reported previously (see **section 2.2.1**).[65]

3.2.2 Formation of the *Ls*AA9 purple species

The reduced Cu(I) state of *Ls*AA9 was generated by reaction of the enzyme with excess ascorbic acid, inside a N_2 atmosphere glove box. The excess ascorbic acid was then removed *via* buffer exchange with a 10 kDa MWCO VivaSpin centrifuge concentrator. All the solutions used inside the N_2 atmosphere glove box were de-gassed by freeze-pump-thawing on a schlenk line (water, buffers) or by purging the solution with N_2 for 30 min (protein and H_2O_2 solutions). H_2O_2 in appropriate amount was then added to the Cu(I)-*Ls*AA9 solution to initiate the reaction. When starting from the Cu(II) resting state, H_2O_2 was simply added to the protein solution without degassing.

3.2.3 *Ls*AA9 *N*-Deglycosylation

*Ls*AA9 was incubated with a His-tagged Endoglycosidase H (Endo H) in a 10:1 molar ratio in 20 mM Na-phosphate at pH 7.2 for 2 days at room temperature. NaCl and imidazole were added to the solution up to a final concentration of 500 mM and 25 mM, respectively, then the solution was applied to a 1 mL HisTrap FF column to remove the Endo H from the sample. EDTA was added to the flow-through to a final concentration of 2 mM, and then it was incubated for 2 h at room temperature. The flow-through was then applied to a Superdex 75 16/600 column, pre-equilibrated with 20 mM Na-phosphate, 250 mM NaCl at pH 7.2. The eluted fractions corresponding to the deglycosylated *Ls*AA9 were then concentrated, copper loaded with 1 equivalent of $CuSO_4*5H_2O$ and buffer exchanged in 20 mM Na-phosphate at pH 6.0 with a 3 kDa MWCO VivaSpin centrifuge concentrator.

3.2.4 UV-Vis, CD and MCD spectroscopy

The UV-vis absorption spectra were acquired on a Shimadzu UV-1800 spectrometer or on a Perkin Elmer Lambda 465 diode array spectrophotometer. For the kinetics, the Cu(I)-LsAA9 and H_2O_2 solution were prepared as described above. The sample was then transferred to the spectrometer in a sealed cuvette and an appropriate amount of de-oxygenated H_2O_2 was quickly added to initiate the reaction.

CD spectra were recorded on a Jasco J810 spectropolarimeter at room temperature. MCD spectra were recorded on a Jasco J810 spectropolarimeter adapted to incorporate an Oxford Instruments Spectromag SM4000 magnetocryostat. The sample solutions were loaded into cells of *ca*. 2 mm path-length constructed from quartz discs separated by a rubber ring spacer and frozen in liquid nitrogen. The spectra were collected at 3 T, 5 T and 7 T with temperatures between 5 K and 55 K.

3.2.5 EPR spectroscopy

Continuous-wave X-band frozen solution EPR spectra were acquired on a Bruker micro EMX spectrometer operating at ~9.30 GHz, with a modulation amplitude of 4 G, modulation frequency of 100 kHz and a microwave power of 10.02 mW. The spectra are the summation of 3 scans and were recorded at 170 K. The purple colored species samples were generated in the same way as for the UV/vis experiments. EPR spin quantitation, *via* double integration of the spectra, of the paramagnetic Cu concentration was performed using a 0.200 mM $CuSO_4$, 10 mM HCl, 2 M $NaClO_4$ standard solution (single point standardization).

The conversion of the Cu(II)-*Ls*AA9 resting state to the purple species was estimated via EPR spin quantitation. It was assumed that the Cu(II) signal reduction was only due to conversion in the purple species. At pH 10.0, after the reaction with H_2O_2, the final Cu(II) concentration was 75-80% less than the Cu(II) resting state, at the same protein concentration (*i.e.* 75-80% conversion into the purple species). To determine the Cu(II) concentration of the apo-protein after the purple species reduction and treatment with EDTA, the sample was buffer exchanged, under anaerobic conditions, to remove the excess of reducing agent and the $[Cu(EDTA)]^{2-}$ complex. The sample was then taken to

pH 2.0 by adding HCl to denature fully the enzyme. The Cu(II) concentration was then measured by EPR *via* spin quantitation.

3.2.6 X-ray Absorption Spectroscopy

XAS spectra were collected on a 1.0 mM solution of enzyme *Ls*AA9 at pH 10.0, which had been flash-frozen to 77 K. Data were acquired on the sample at 90 K at the B18 Core Spectroscopy beamline at Diamond Light Source, Oxfordshire, UK. At the time of the measurement, the Diamond synchrotron was operating at a ring energy of 3 GeV. The beamline was equipped with a Si(111) double crystal monochromator, and harmonic rejection was achieved through the use of two Pt-coated mirrors operating at an incidence angle of 9 mrad. The monochromator was calibrated using the first maximum in the derivative in the edge region of the XAS spectra of a copper foil placed between the second and third ion chambers at 8979 eV. Data were collected in fluorescence mode from 8770 to 9020 eV using a nine-channel Ge solid-state detector at the copper K absorption edge (~8980 eV) in 1 eV steps. The measurements were collected at 77 K.

3.2.7 Resonance Raman spectroscopy

Samples were prepared in the same way as the UV/vis samples, but using $H_2{}^{18}O_2$, D_2O or $H_2{}^{18}O$ for the isotopically-substituted samples. Spectra were collected using a HORIBA XploRA Raman microscope at room temperature using 532 nm and 785 nm laser wavelength excitations. The spectrometer gratings used were 2400 gr mm^{-1} and 1200 gr mm^{-1}, respectively, together with a confocal pinhole size of 500 µm and slit width of 200 µm. The laser power was ~7 mW. Samples were measured in the liquid state using a 63x/1.0 dipping objective (Zeiss). To test for heating effects, measurements were also made on the samples in the frozen state facilitated by using a LN_2 cooling stage and 100x/0.9 lens, with the rest of the acquisition parameters remaining the same as those used for the liquid sample measurements. The frozen sample results showed no significant spectral differences compared to the liquid state data. Real-time spectral acquisition was also performed to optimise the acquisition parameters (signal-to-noise)

and to verify non-destructive testing. To ensure acceptable measurement statistics, ~40 spectra were collected per sample tested. The spectra were processed (baseline corrected, normalized, averaged) and then analyzed using OriginPro (2018) software, with processing and spectral analysis also independently checked using IGOR Pro (v.6.3.7). Accounting for the measurement statistics, the maximum uncertainty associated with the Raman band positions was found to be ~±2 cm^{-1}.

3.2.8 Analysis of the reaction products

Cellohexaose was used as substrate. 100 µL reactions were set up with 750 µM cellohexaose, 1 mM ascorbic acid, 100 µM H_2O_2 (no H_2O_2 added in the O_2 turnover reactions), 1 µM *Ls*AA9 or purple *Ls*AA9 in 5 mM MES at pH 7.0 and were incubated at 40 °C for 2 hours. The reaction was then quenched by addition of 3 reaction volumes of ethanol (98% *v*/*v*). Reactions with H_2O_2 were performed inside an N_2 atmosphere glove box. 1 µL of sample was then mixed with 2 µL of 10 mg mL^{-1} 2,5-dihydroxybenzoic acid in 50% acetonitrile, 0.1% trifluoroacetic acid on a Bruker SCOUT-MTP 384 target plate. The spotted samples were then dried in air under a lamp, before being analysed by mass spectrometry on a Ultraflex III matrix-assisted laser desorption ionization–time of flight/time of flight (MALDI-TOF/TOF) instrument (Bruker), as described previously.[27] The purple species *Ls*AA9 sample used in the assay, was incubated with EDTA overnight to remove Cu^{2+} from any *Ls*AA9 that had not been converted to the purple species. The resulting $[Cu(EDTA)]^{2-}$ complex was then removed from the solution by ultra-centrifugation through 10 kDa cut-off size-exclusion filters.

3.2.9 DFT

Spin unrestricted density functional theory (DFT) calculations were performed using the ORCA 4.1 electronic structure package.[119] The different cluster models were derived from the X-ray crystal structure of *Ls*AA9 (PDB: 5ACG). The same model used for the *Ls*AA9 resting state used in the previous chapter was employed in this study as a starting point. Geometry optimizations were performed with the BP86 functional (with RI

approximation),[120] Def2-TZVP basis set on Cu and ligating atoms and Def-2-SVP on all the remaining atoms;[121] empirical dispersion correction were accounted using Grimme's D3 method with Becke-Johnson damping (D3BJ);[122] solvation effects were included with the conductor-like polarizable continuum model (CPCM, ε=4.0). The coordinates of all the optimized geometries can be found in **Appendix 2**.

The broken symmetry (BS) approach was used to optimize the singlet spin state geometry in each model. Single point energies were calculated using the B3LYP functional[123] and the Def2-TZVP basis set on all atoms. Corrected singlet state energies and exchange coupling constants (*J*) were computed with the Yamaguchi formula:[171]

$$J = \frac{E_{triplet} - E_{BS\ singlet}}{< S^2 >_{triplet} - < S^2 >_{singlet}}$$

UV-vis and Cu K-edge absorption spectra were calculated with the time-dependent density functional theory (TD-DFT) approach applying the Tamm−Dancoff approximation.[131] The UV-vis absorption spectra were computed with the B3LYP functional, Def2-TZVP basis set on all atoms, and RIJCOSX approximation,[133] with a dense integration grid (ORCA Grid5). The K-edge calculations were performed on the B3LYP functional together with the ZORA scalar relativistic approximation;[172] the CP(PPP) basis set[124] was used on the Cu and the ZORA-Def2-TZVP basis set[135] on all other atoms. In the TD-DFT approach, the description of the core hole leads to a systematic error in the absolute energy transitions, which can be compensated by a constant energy shift (which is characteristic for each functional and basis set).[173] Here, the calculated 1s → 3d pre-edge transition of the Cu(II) resting state model was used to calibrate the method. An energy shift of −5.8 eV was applied to all calculated transitions.

3.2.10 LC-MS/MS

Peptides derived from $H_2{}^{16}O_2$ treated protein were loaded onto a nanoAcquity UPLC system (Waters) equipped with a nanoAcquity Symmetry C_{18}, 5 µm trap (180 µm x 20 mm Waters) and a nanoAcquity HSS T3 1.8 µm C_{18} capillary column (75 µm x 250 mm,

Waters). The trap wash solvent was 0.1% (v/v) aqueous formic acid and the trapping flow rate was 10 µL min^{-1}. The trap was washed for 5 min before switching flow to the capillary column. Separation used a gradient elution of two solvents (solvent A: aqueous 0.1% (v/v) formic acid; solvent B: acetonitrile containing 0.1% (v/v) formic acid). The capillary column flow rate was 350 nL min^{-1} and the column temperature was 60°C. The gradient profile was linear 2-35% B over 20 min then proceeded to wash with 95% solvent B for 2.5 min. The nanoLC system was interfaced with a maXis HD LC-MS/MS system (Bruker Daltonics) with CaptiveSpray ionisation source (Bruker Daltonics). Positive ESI-MS and MS/MS spectra were acquired using AutoMSMS mode. Instrument control, data acquisition and processing were performed using Compass 1.7 software (microTOF control, Hystar and DataAnalysis, Bruker Daltonics). Instrument settings were: ion spray voltage: 1,450 V, dry gas: 3 L min^{-1}, dry gas temperature 150°C, ion acquisition range: *m/z* 150-2,000, MS spectra rate: 5 Hz, MS/MS spectra rate: 7 Hz at 2,500 cts to 27 Hz at 250,000 cts, cycle time: 1 s, quadrupole low mass: 300 *m/z*, collision RF: 1,400 Vpp, transfer time 120 ms. The collision energy and isolation width settings were automatically calculated using the AutoMSMS fragmentation table, absolute threshold 200 counts, preferred charge states: 2 – 4, singly charged ions excluded. A single MS/MS spectrum was acquired for each precursor and former target ions were excluded for 0.8 min unless the precursor intensity increased fourfold.

Peptides from $H_2{}^{18}O_2$ peroxide treated protein were loaded onto an UltiMate 3000 RSLCnano HPLC system (Thermo) equipped with a PepMap 100 Å C_{18}, 5 µm trap column (300 µm x 5 mm Thermo) and a PepMap, 2 µm, 100 Å, C_{18} EasyNano nanocapillary column (75 µm x 500 mm, Thermo). The trap wash solvent was aqueous 0.05% (v:v) trifluoroacetic acid and the trapping flow rate was 15 µL min^{-1}. The trap was washed for 3 min before switching flow to the capillary column. Separation used gradient elution of two solvents: solvent A, aqueous 1% (v:v) formic acid; solvent B, aqueous 80% (v:v) acetonitrile containing 1% (v:v) formic acid. The flow rate for the capillary column was 300 nL min^{-1} and the column temperature was 40 °C. The linear multi-step gradient profile was: 3-10% B over 7 mins, 10-35% B over 30 mins, 35-99% B over 5 mins and then proceeded to wash with 99% solvent B for 4 min. The nanoLC system was interfaced with an Orbitrap Fusion hybrid mass spectrometer (Thermo) with an EasyNano ionisation source (Thermo). Positive ESI-MS and MS^2 spectra were acquired using Xcalibur software (version 4.0, Thermo). Instrument source settings were: ion spray voltage, 1,900 V; sweep gas, 0 Arb; ion transfer tube temperature; 275 °C. MS^1 spectra were acquired

in the Orbitrap with: 120,000 resolution, scan range: *m/z* 375-1,500; AGC target, $4e^5$; max fill time, 100 ms. Data acquisition was performed in top speed mode using a 1 s cycle, selecting the most intense precursors with charge states >1. Easy-IC was used for internal calibration. Dynamic exclusion was performed for 50 s post precursor selection and a minimum threshold for fragmentation was set at $5e^3$. MS^2 spectra were acquired in the linear ion trap with: scan rate, turbo; quadrupole isolation, 1.6 *m/z*; activation type, HCD; activation energy: 32%; AGC target, $5e^3$; first mass, 110 *m/z*; max fill time, 100 ms. Acquisitions were arranged by Xcalibur to inject ions for all available parallelizable time.

Database Searching: Peak lists were imported into PEAKSX Studio (Build 20181106, Bioinformatics Solutions Inc.) for peak picking and database searching. Spectra were searched against the expected protein sequence specifying the following criteria: Parent Mass Error Tolerance, 10 ppm for qTOF data, 3.0 ppm for Orbitrap data; Fragment Mass Error Tolerance, 0.1 Da of qTOF data and 0.5 Da for ion trap data; Precursor Mass Search Type, monoisotopic; Enzyme, None; Digest Mode, Unspecific; Fixed Modifications, Carbamidomethylation: 57.02. To map positions of peroxide induced ^{18}O oxidation and background ^{16}O oxidation the following variable modifications were considered: ^{16}O oxidation, 15.99 Da, on H/M/Y/W residues; ^{18}O oxidation, 18.00 Da, on H/M/W/Y residues; ^{16}O di-oxidation, 31.99 Da, on M/W/Y residues; $^{18}O_2$ di-oxidation, 33.99 Da on M/W/Y residues; His → Asn degradation (with ^{16}O), –23.02 Da; His → Asn (with ^{18}O) degradation, –21.01 Da; His → Asp (with ^{16}O) degradation, –22.03 Da; His → Asp (with ^{18}O) degradation, –18.04 Da; Tyr → dopaquinine (with^{16}O) modification, 13.98; Tyr → dopaquinine (with ^{18}O) modification, 15.98; Tyr → topaquinine (with ^{16}O) modification, 29.97; Tyr → topaquinine (with ^{18}O) modification, 31.98. To account for expected N-terminal methylation and deamidation resulting from deglycosylation, methylation, 14.02 Da, protein N-term and deamidation, 0.98 Da, NQ, were also included as variable modifications. Resulting peptide matches were filtered to 1% false discovery rate as determined in PEAKSX.

3.2.11 SDS-PAGE

Samples for SDS-PAGE analysis were prepared by incubating Cu(II)-*Ls*AA9 or its deglycosylated version, with different amounts of H_2O_2 at room temperature for 2 hours. Each reaction contained 30 μM enzyme, 0.15/0.30/0.45/0.60 mM in HEPES 50 mM pH 7.0 or 8.0. When present, cellohexaose concentration was 0.30 mM; the reaction volume was 20 μL. Samples were then denatured and prepared for SDS-PAGE, mixing 10 uL of each sample with 10 uL of denaturing reagent (4% w/v SDS, 20% v/v glycerol, 25 mM EDTA, 0.4 mg mL^{-1} bromophenol blue, 0.29 M β-mercaptoethanol, 0.125 M Tris-HCl pH 6.8) and incubated at 95 °C for 5 min. Loaded 2.5 μg of protein per sample in the polyacrylamide gel.

In-gel protein digestion step. To increase potential sequence coverage the sample was split into two equal portions for parallel digestion with trypsin and Asp-N proteases, following deglycosylation. In-gel protease digestion was performed after reduction with dithioerythritol, *S*-carbamidomethylation with iodoacetamide and deglycosylation with the addition of 3 units of PNGaseF (Roche) and incubation at 37 ºC overnight. Gel pieces were washed two times with aqueous 50% (v:v) acetonitrile containing 25 mM ammonium bicarbonate, then once with acetonitrile to remove residual PNGaseF, then dried in a vacuum concentrator for 20 min. A 0.2 μg amount of sequencing-grade, modified trypsin (Promega) or Asp-N (Sigma) protease was added to the dry gel pieces in 10 μL, 25 mM ammonium bicarbonate and after 10 min enough 25 mM ammonium bicarbonate solution was added to cover the gel pieces. Digests were incubated overnight at 37 ºC. Peptides were extracted by washing three times with aqueous 50% (v:v) acetonitrile containing 0.1% (v:v) trifluoroacetic acid, before drying in a vacuum concentrator and reconstituting in aqueous 0.1% (v:v) trifluoroacetic acid. The two digests were pooled before LC-MS analysis.

3.3 Results

3.3.1 Formation of a purple-coloured LPMO species and its activity on oligosaccharides substrates

LPMOs catalyse the oxidation of oligosaccharide substrates with O_2 and reducing agent co-substrates (*e.g.* ascorbate). In addition to O_2 acting as a co-substrate, it has also recently been reported that hydrogen peroxide acts as a co-substrate for LPMOs, replacing the combination of O_2 and reducing agent, albeit in a reaction which is accompanied by significant protein degradation.[29] Despite the fact that the reaction with peroxide is deleterious to the enzyme, the addition of peroxide to LPMOs provides for a potential laboratory 'shunt' that avoids the complicating use of reducing agents within spectroscopic and activity studies. Thus, taking advantage of the peroxide shunt reaction with LPMOs, we added various concentrations of hydrogen peroxide (from 0 to 2 mM) to ~1 mM solutions of *Ls*AA9 which had previously been spectroscopically and structurally characterized (see **Chapter 2**)[65,82] This AA9 LPMO is active on soluble oligosaccharide substrates, affording the opportunity to be able to perform spectroscopic studies on optically transparent solutions. The addition of hydrogen peroxide to *Ls*AA9 was performed at room temperature (~290 K) over a range of pHs and peroxide concentrations (**Figure 3.2**). The reaction was also separately performed on both naturally glycosylated *Ls*AA9 (the enzyme was produced using *Aspergillus oryzae* and *Pichia pastoris* as expression systems, which maintain glycosylation patterns on the protein and, in the former expression system, the N_ε-methylation on His-1) and its de-N-glycosylated variant, which were prepared using previously reported methods.[65]

The resulting solutions were monitored over time by UV/vis and EPR spectroscopies. In the absence of substrate and at raised pHs (>7), following an initial burst of bubbling (presumably O_2 gas), a strongly colored purple solution formed over a period of minutes, which then appeared to be stable over a period of days. The UV-vis and CD spectra of this solution exhibit several intense bands in the visible region (**Figure 3.2**, see later for analysis). The addition of peroxide under anaerobic conditions to the Cu(I) form of *Ls*AA9 generated the same purple species but without the initial burst of bubbling observed for the addition of hydrogen peroxide to the Cu(II) form of *Ls*AA9. These

observations suggest that the appearance of bubbles following the addition of hydrogen peroxide to the Cu(II) form of *Ls*AA9 was associated with the reduction of the Cu(II) form by hydrogen peroxide and the concomitant formation of superoxide that disproportionated into O_2 and hydrogen peroxide. The rate of formation of the purple species and its final concentration depended on the pH and the initial concentration of hydrogen peroxide, with high pHs exhibiting the highest rate of formation (> 0.1 mM min^{-1}) and highest final concentrations (**Figure 3.2**).

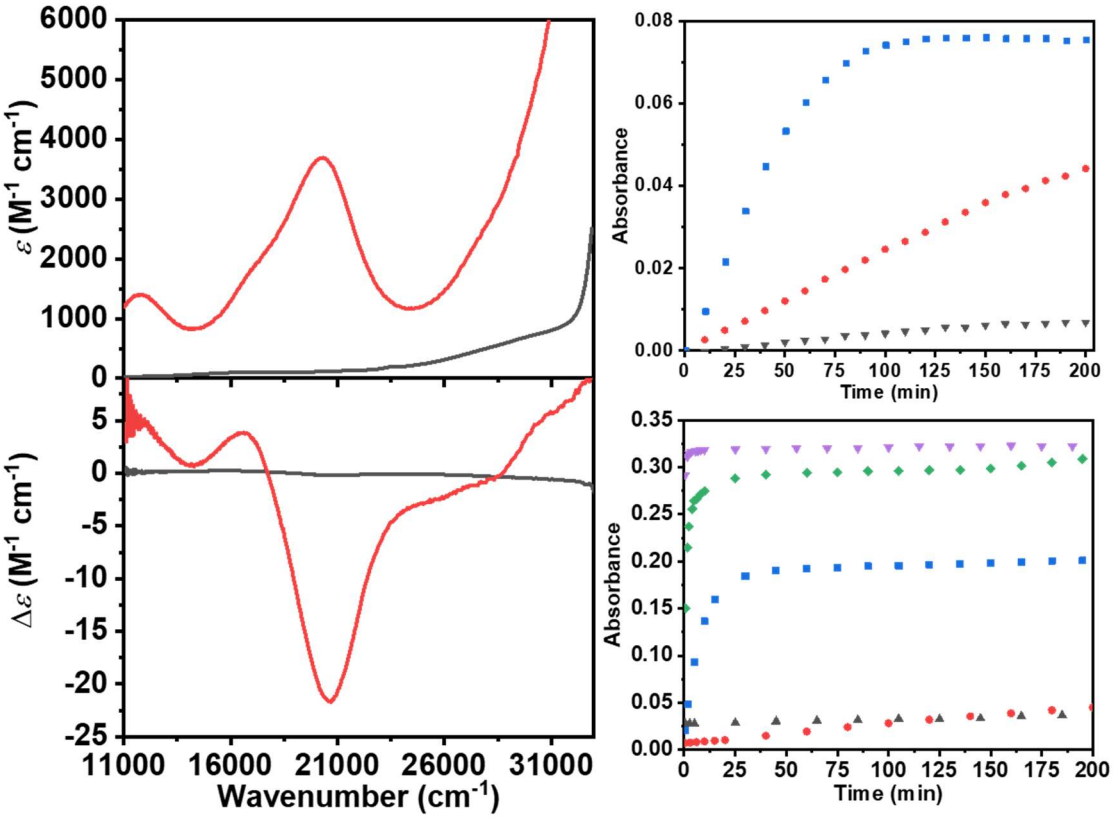

Figure 3.2 UV/vis (top left) and CD spectra (bottom left) of *Ls*AA9 resting state (black) and purple species (red), at pH 7.0. Growth of the absorption intensity at 20400 cm^{-1} at different H_2O_2 concentrations (top right): 0.10 mM, black triangles; 1.0 mM, red dots; 10.0 mM, blue squares. *Ls*AA9 0.1 mM, pH 7.0. Growth of the absorption intensity at 20400 cm^{-1} at different pHs (bottom right): 6.0 (black triangles); 7.0 (red dots); 8.0 (blue squares); 9.0 (green diamonds); 10.0 (purple triangles). *Ls*AA9 0.1 mM and 1.0 mM H_2O_2. All kinetic studies were carried out with glycosylated enzyme (*Aspergillus oryzae* as expression system) at 293 K. Maximal conversion was achieved at pH 10.0 with an addition of H_2O_2 1.0 mM to 0.1 mM *Ls*AA9 LPMO.

Once formed, the UV-vis spectrum of the purple species remained invariant across a pH range of 3.0–10.0 (**Figure 3.3**). At pHs lower than 3.0, the solution turned colorless with concomitant loss of the main bands (11790 cm^{-1}, 17100 cm^{-1}, 20400 cm^{-1}) in the visible part of the spectrum. Addition of H_2O_2 in the presence of cellohexaose (a known oligosaccharide substrate for *Ls*AA9)[65] gave the same purple species, but at a much lower rate (ca. 200 times slower, **Figure 3.4**).

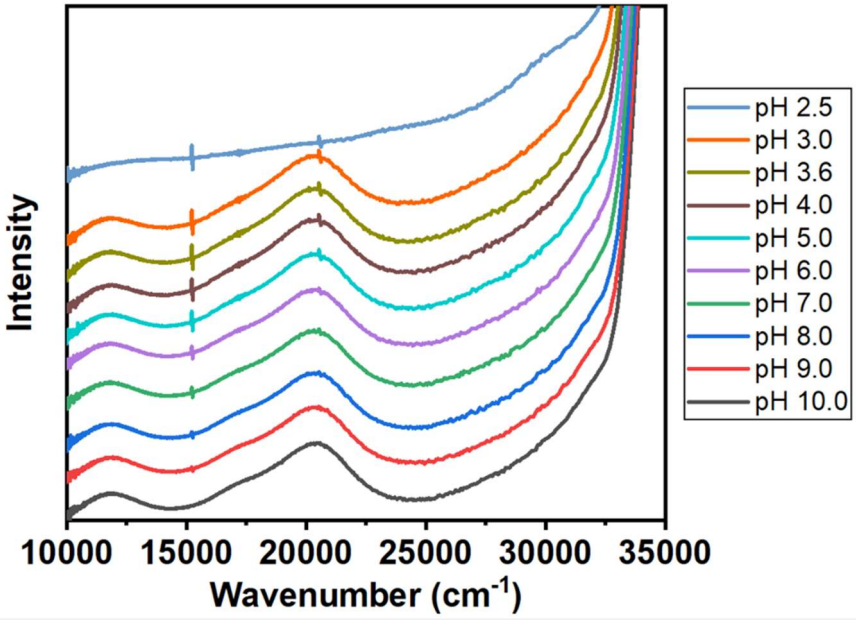

Figure 3.3 UV-vis spectrum of *Ls*AA9 purple at different pHs. The spectra were recorded with 30 µM *Ls*AA9, in a 10 mM sodium acetate, MES, HEPES and CAPS multi-buffer, adjusted to the relevant pH.

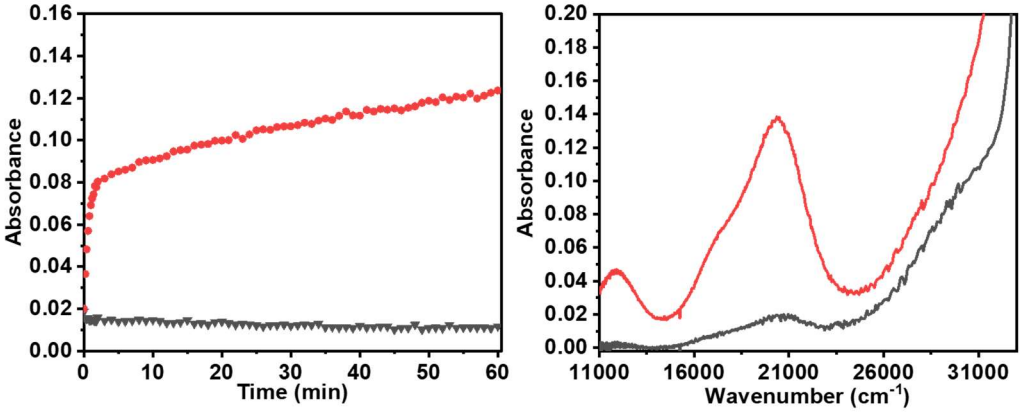

Figure 3.4 Absorbance at 20400 cm^{-1} *vs* time for the reaction between Cu(I)-*Ls*AA9 and H_2O_2 (left) in the presence (black triangles) and absence (red dots) of cellohexaose. UV-vis spectra of the same reaction after 16 hours incubation at room temperature (right). The reactions were performed with 50 µM Cu(I)-*Ls*AA9, 250 µM H_2O_2, 500 µM cellohexaose, in 50 mM CAPS pH 10.0.

To show that the formation of the chromophore, although not necessarily its location within the protein, is associated with the copper ion, the purple species was treated with a combination of reducing agent and EDTA at pH 10.0, as follows: the addition of sodium dithionite solution to the purple species gave a colorless and EPR-silent solution, which was then incubated with EDTA and passed through a size exclusion filter to remove the $[Cu(EDTA)]^{2-}$ complex. The amount of Cu leftover in the sample was measured by CW-EPR spectroscopy and determined by spin quantification to be less than 5% Cu content with respect to the resting state enzyme at the same concentration, as shown in **Figure 3.5** (see **Methods**). Re-addition of a Cu(II) solution to the protein solution in aerobic conditions immediately gave a purple-colored solution with the same visible spectrum as the original purple species (see **Discussion** for explanation of this effect). In the absence of a reducing agent it was not possible to decolorize the solution with the addition of EDTA alone, suggesting that the copper active site in the purple species is highly stable. In addition, we report that the same purple species could be formed under aerobic conditions at high pH, by addition of ascorbic acid as reducing agent to the enzyme solution but at a much slower rate than the reaction with peroxide.

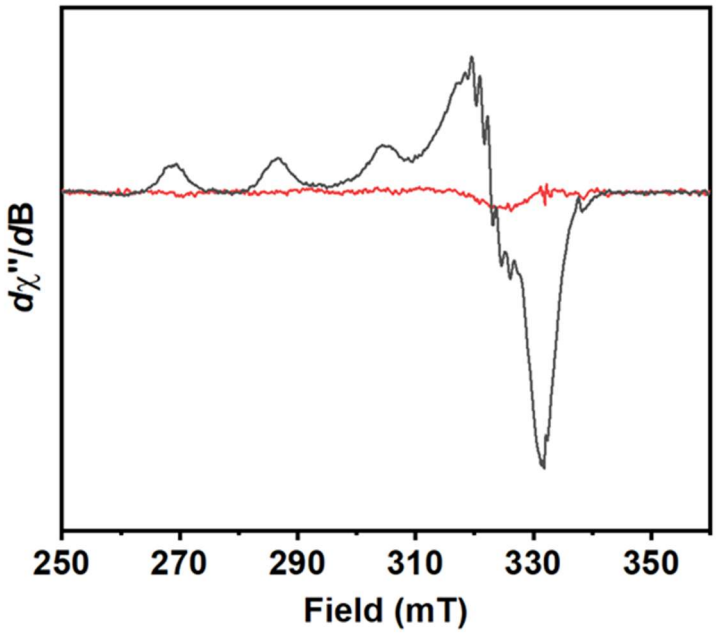

Figure 3.5 EPR spectrum of *Ls*AA9 purple species after incubation with $Na_2S_2O_4$/EDTA and washing step, to remove the Cu from the enzyme (red trace). As a comparison, the EPR spectrum of Cu(II)–*Ls*AA9 resting state at the same enzyme concentration is showed as black trace. Cu(II) concentration in the treated sample is less than 5% than the resting state, as determined by spin quantification. Enzyme concentration was 150 μM, in 50 mM CAPS pH 10.0.

The ability of the purple species to catalyse the oxidation of polysaccharides with either O_2 (and sodium ascorbate as reducing agent) or hydrogen peroxide was assessed using cellohexaose as substrate. To perform these experiments it was important to remove the small amounts of *Ls*AA9 that had not been converted to the purple species (see EPR discussion and **Methods**). Therefore, excess cellohexaose was added to a solution of the purple species that had previously been treated with Na_2EDTA and any $[Cu(EDTA)]^{2-}$ removed (*i.e.* retaining the purple species and removing any Cu(II) from unreacted Cu(II)−*Ls*AA9). The products of the reaction, *i.e.*, any oxidized oligosaccharides, were then analysed by MALDI-TOF MS. In both cases (hydrogen peroxide or O_2/ascorbate), the purple species did not generate any oxidized oligosaccharides under standard oxidation conditions after 24 h, and thus, the purple species appears to be catalytically inactive for the oxidation of polysaccharides (**Figure 3.6**). As a positive control, under the same conditions, *Ls*AA9 was shown by MALDI-TOF MS to generate C4 oxidized oligosaccharide products, as already demonstrated by Frandsen *et al*. (**Figure 3.6**).[65]

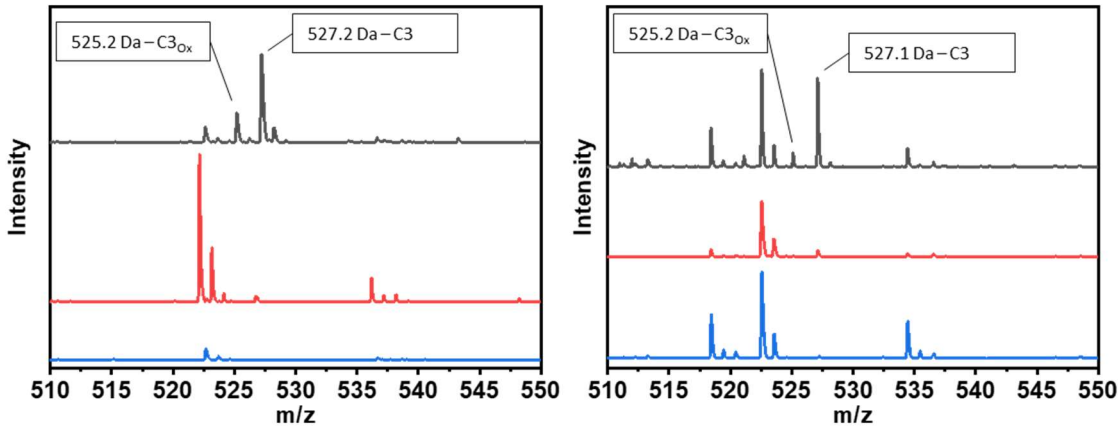

Figure 3.6 MALDI-TOF spectra showing the products of incubation of cellohexaose with *Ls*AA9 (black trace) or *Ls*AA9 purple (red trace), ascorbate and O_2 (left) or H_2O_2 (O_2 free atmosphere) (right). The blue trace represents a control reaction with only cellohexaose, ascorbate and with/without H_2O_2. *Ls*AA9 cleavage of this substrate yielded cellotriose (C3) and C4-oxidized cellotriose ($C3_{Ox}$). Products were detected as mono-sodiated adducts.

SDS-PAGE gel analyses of the purple-colored solutions were performed (**Figure 3.7**) to determine whether the lack of activity of the purple species was due to indiscriminate oxidation of the protein by the peroxide. The gels show that the purple species generated from *Ls*AA9 that had been de-N-glycosylated indeed underwent extensive proteolytic degradation at pHs 7.0−8.0, even upon addition of low concentrations of hydrogen peroxide (0.15 mM) or in the presence of substrate (cellohexaose). Such degradation is not surprising given the potent oxidizing power of hydrogen peroxide solutions. In contrast to the de-glycosylated sample, *Ls*AA9 left in its glycosylated form following its expression in *Aspergillus* or *Pichia* showed no signs of denaturation even upon treatment with a 20-fold molar excess of hydrogen peroxide with respect to the enzyme concentration (**Figure 3.7**).

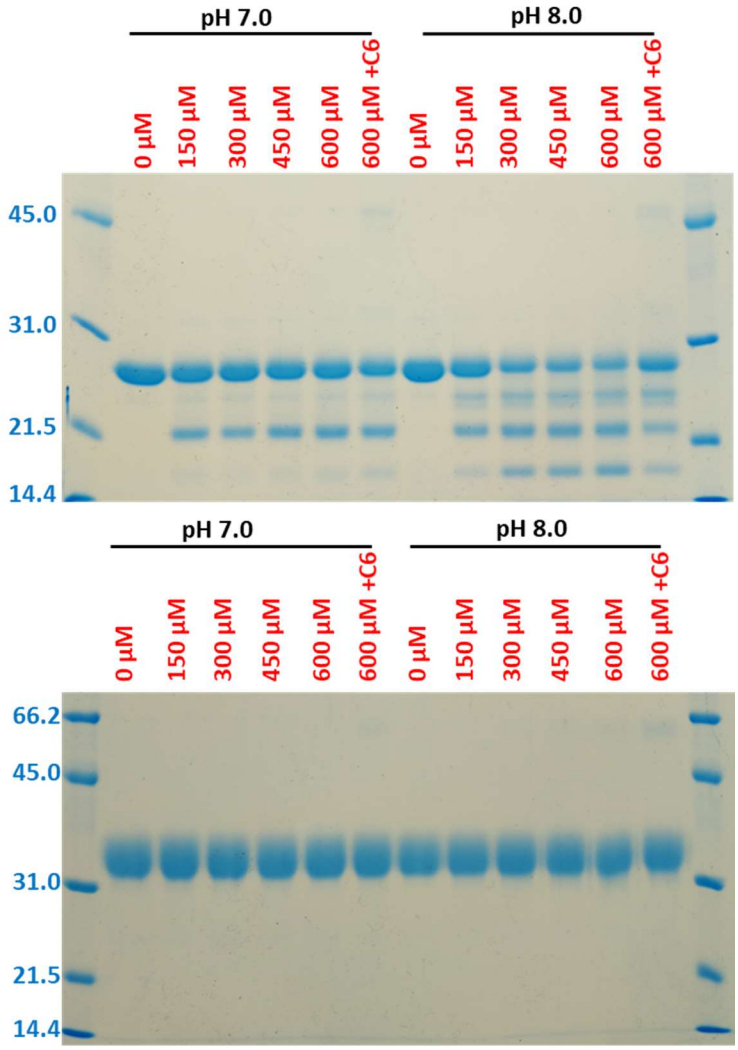

Figure 3.7 SDS-PAGE analysis of Cu(II)−*Ls*AA9 LPMO before and after peroxide treatment: (top) de-N-glycosylated *Ls*AA9 and (bottom) glycosylated *Ls*AA9 (produced in *Aspergillus oryzae*). The reactions were performed with 30 µM *Ls*AA9 with different amounts of H_2O_2 (red labels), in 50 mM HEPES at pH 7.0 or pH 8.0. The samples were incubated for 2 h at room temperature before the SDS-PAGE analysis. "C6" indicates the presence of 300 µM cellohexaose. Molecular weight markers are reported in kDa (blue labels).

The protective effect of the glycosylated side chains is evident from this experiment. Following treatment with hydrogen peroxide, glycosylated *Ls*AA9 remained essentially intact, save for some evidence from the SDS-PAGE gels (**Figure 3.7**) of the formation of a small amount (<1%) of a higher molecular weight species at *ca*. 60−65 kDa. The same experiment was repeated on *Ls*AA9 produced in *Pichia pastoris* as an expression system. *Pichia* can glycosylate but not methylate LPMOs with different glycosylation patterns/sites respect to *Aspergillus*.[174] Even in this case, no peptide fragments were generated upon incubation with hydrogen peroxide (**Figure 3.8**). The finding that

glycosylation protects eukaryotic LPMOs from oxidative damage by hydrogen peroxide serves as a useful reminder of the functional importance of glycosylated side chains in proteins and the need to be aware that the absence of glycosylation in AA9 LPMOs which have been expressed in prokaryotic hosts can significantly affect the stability of these proteins. Accordingly, in the studies reported below, the *Aspergillus*-produced, glycosylated *Ls*AA9 was used in all spectroscopic investigations.

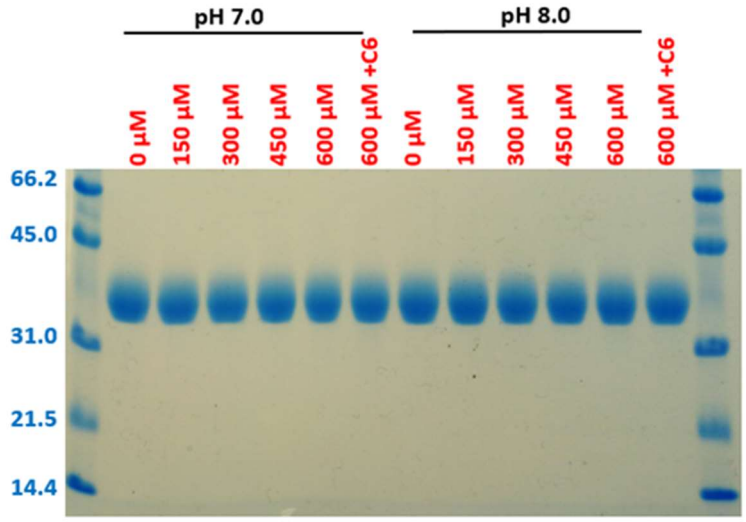

Figure 3.8. SDS-PAGE analysis of Cu(II)-*Ls*AA9 LPMO, produced in *Pichia pastoris* as expression system, before and after peroxide treatment. The reactions were performed with 30 µM *Ls*AA9 and different amounts of H_2O_2 (red labels), in 50 mM HEPES at pH 7.0 or pH 8.0. The samples were incubated for 2 hours at room temperature before the SDS-PAGE analysis. 'C6' indicates the presence of 300 µM cellohexaose. Molecular weight markers are reported in kDa (blue labels).

3.3.2 Sites of oxidative damage to the protein following addition of peroxide

The SDS-PAGE analysis described above does not provide detailed information about the sites of oxidative damage within the protein. In this regard, there is evidence from earlier studies that hydrogen peroxide treatment of LPMOs leads to significant oxidative damage of residues close to the copper active site.[29] Therefore, to determine the sites of oxidative damage and also to trace any potential redox active pathways in *Ls*AA9,[175] we performed LC-MS/MS analysis of the peroxide-treated glycosylated purple species

protein post protease digestion to determine the sites of oxidative modification (**Figure 3.9** and **Figure 3.10**).[176] This analysis was performed in two separate experiments, one employing $H_2{}^{16}O_2$ and the other $H_2{}^{18}O_2$ (**Figure 3.9** and **Figure 3.10**). The use of isotopically labeled hydrogen peroxide allowed for differentiation of peroxide treatment-induced oxidation (^{18}O) from oxidation which occurred during the protein purification procedure or sample preparation for LC-MS/MS analysis (^{16}O).

The analysis shows that the oxidative modification of amino acids by hydrogen peroxide occurred at several different sites across the protein, with measurable oxidation of some tryptophan, tyrosine, and methionine residues (**Figure 3.11**). Oxidation was also detected at other amino acid residues adjacent to the copper active site; as previously reported,[29] oxidation of the His-1 side chain was observed. Additional oxidative damage was seen on the active site residues His-79 and His-147, commensurate with the copper-histidine brace in LPMOs being a site that generates oxidizing species. Distant from the active site, oxidative modification of Tyr-65 (12.6 Å from Cu) and Trp-5 (17.6 Å) was observed (see **Section 3.4.3**). Also, several other aromatic residues (Tyr-137, Tyr-153, Trp- 98) were oxidized; most of them are close to the enzyme surface. There was additional oxidative modification of Tyr-85 (18.8 Å away from active site), which is notable as it forms one-half of a conserved tyrosine-dyad (Tyr-85, Tyr-191 in *Ls*AA9) that appears in all AA9 LPMOs and, furthermore, is not surface exposed.[114] Against expectations however, over all conditions there was no evidence for covalent modification of the active site tyrosine (Tyr-164). This is an important finding insofar as some copper-containing oxidases, including copper amine oxidases, are known to undergo oxidative maturation of nearby tyrosine residues into redox-active cofactors; this appears not to be the case in AA9 LPMOs.[91]

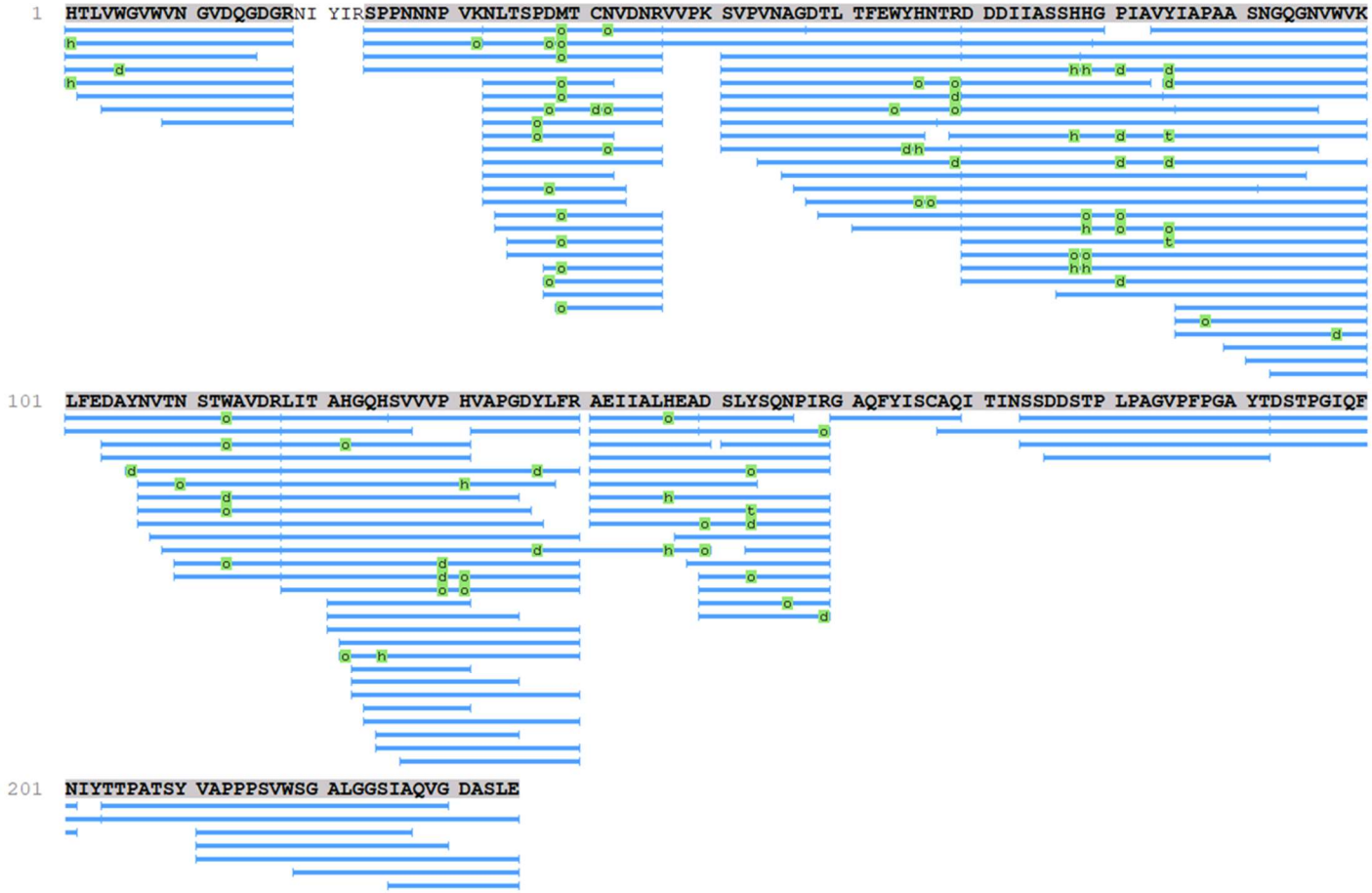

Figure 3.9 Annotation of sequence coverage and oxidised amino acid positions following peroxide treatment, identified by LC-MS/MS analysis. Blue bars indicate peptide identifications assigned by PEAKSX studio. Green boxes show identified positions of oxidation. Peroxide-induced and underlying or proteomic processing-induced oxidation cannot be distinguished in these data. No oxidative events were observed at the tyrosine active site (Y-164).

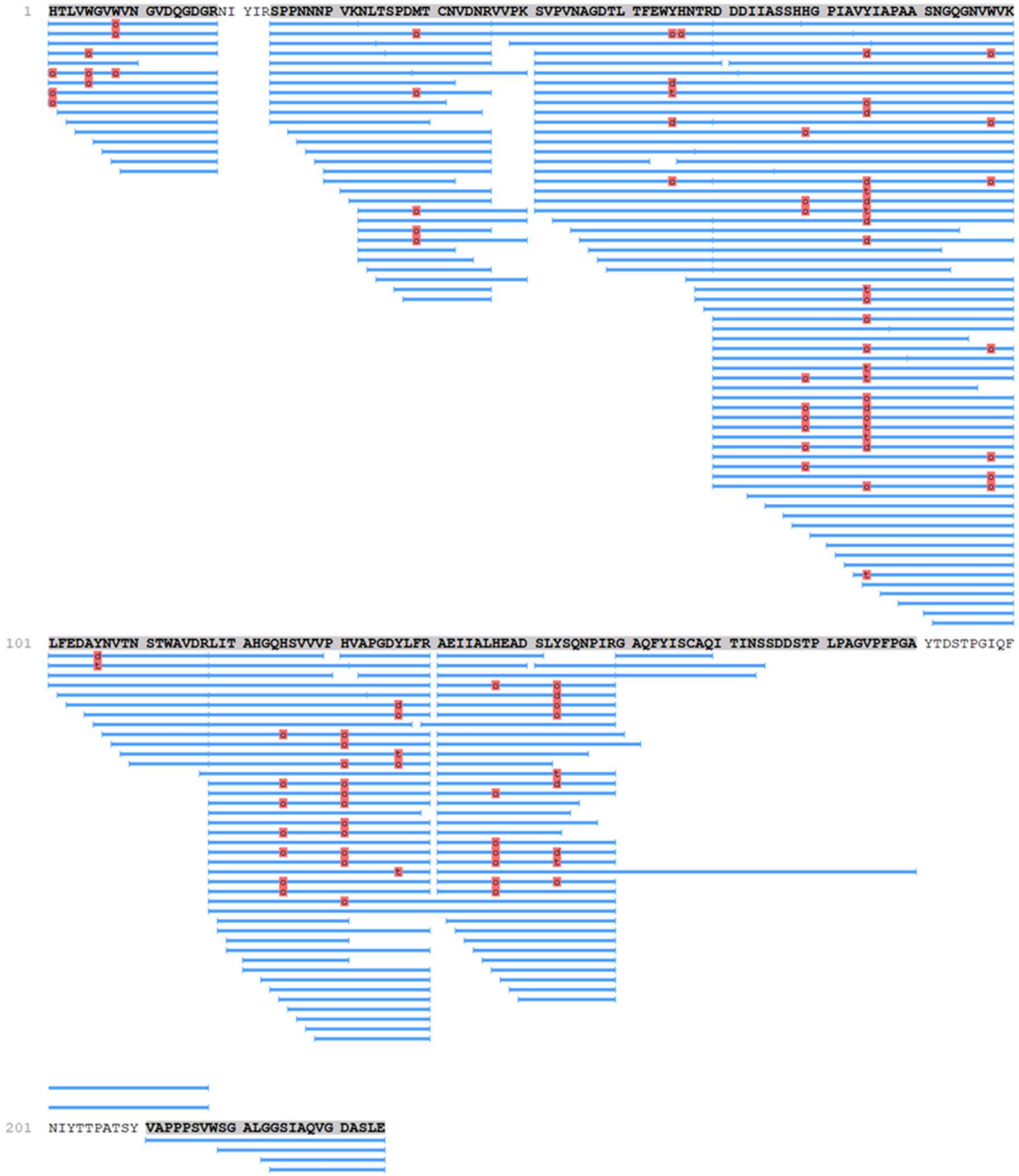

Figure 3.10 Annotation of sequence coverage and position of peroxide-induced ^{18}O oxidation, identified by LC-MS/MS analysis. Blue bars indicate peptide identifications assigned by PEAKSX studio. Red boxes within bars indicate identified peroxide-induced ^{18}O modifications, which can be distinguished from underlying or proteomic-induced ^{16}O oxidation.

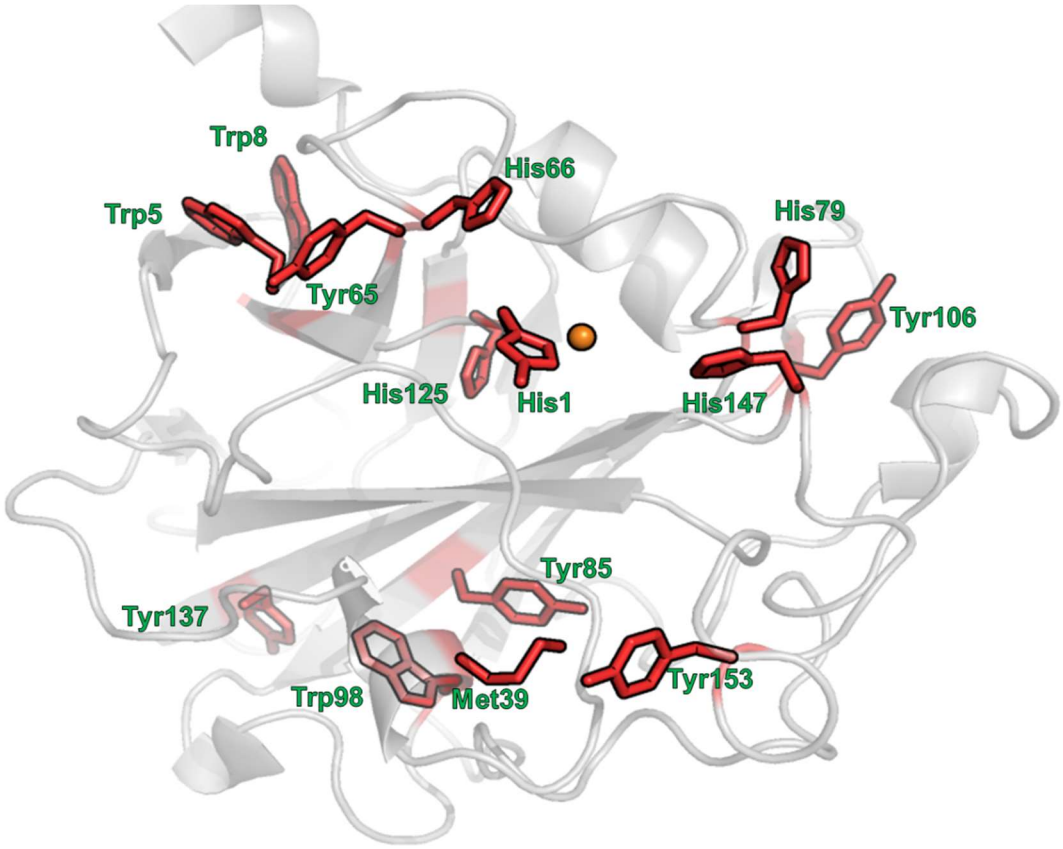

Figure 3.11 Ribbon view of *Ls*AA9 representing the amino acid side chains (PDB: 5ACG) where ^{18}O insertion was detected in amino acid side chains by LC-MS/MS, after treating the enzyme with $H_2{}^{18}O_2$ (depicted as red cylinder bonds). The results were analysed with PEAKSX Studio (Build 20181106, Bioinformatics Solutions Inc.) and resulting peptide matches were filtered to 1% false discovery rate in PEAKSX against a decoy database.

3.3.3 Spectroscopic characterization of the purple species

3.3.3.1 X-ray absorption spectroscopy of the purple species

To determine the oxidation state of the copper ion in the purple species, X-ray absorption studies at 77 K were performed. For reference, X-ray absorption spectra were also collected on the dithionite-reduced, EPR-silent Cu(I)−*Ls*AA9 and the Cu(II) resting state of *Ls*AA9. The combination of the XAS spectra of the purple species with those of the Cu(I) and Cu(II) forms of *Ls*AA9 reports on the changes at a single copper site over three oxidation levels (**Figure 3.12**).

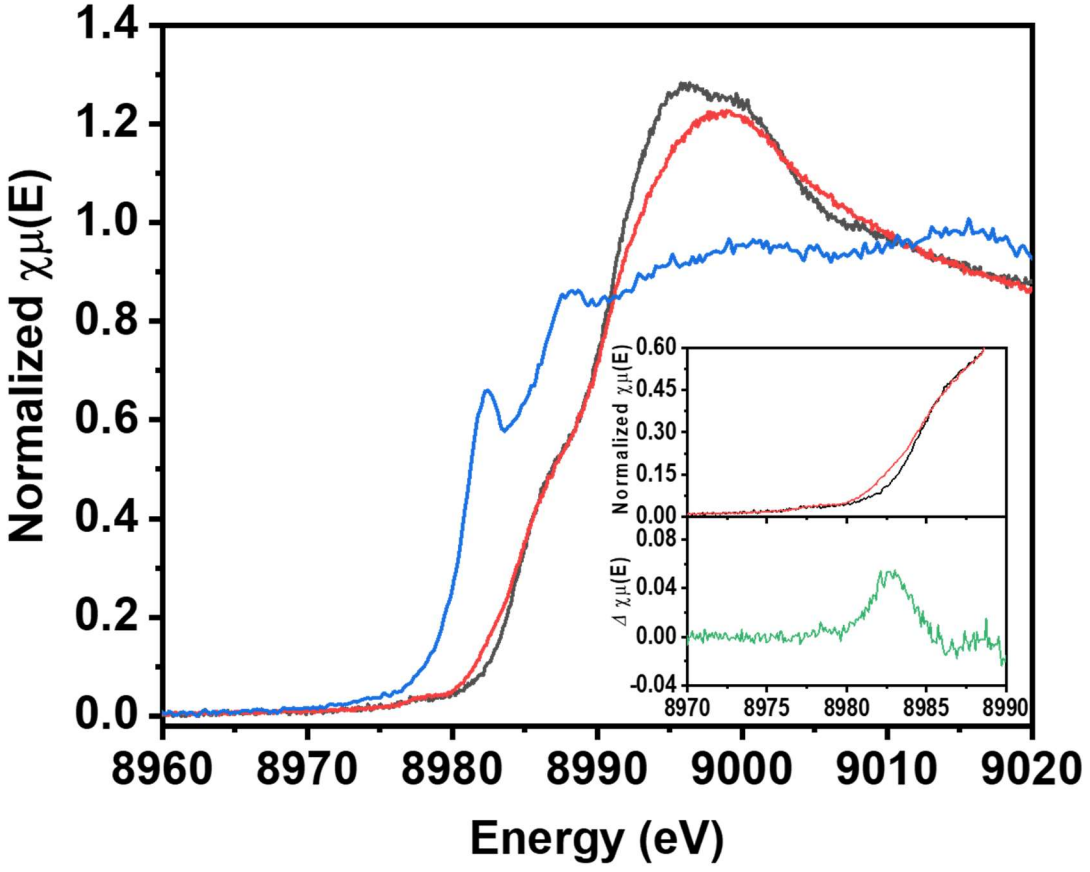

Figure 3.12 Normalized Cu K-edge XAS spectra (77 K) of purple species, Cu(II)−*Ls*AA9 (black), purple species *Ls*AA9 (red) and reduced Cu(I)−*Ls*AA9 (blue). In the inset, difference spectrum (green) between purple species *Ls*AA9 and Cu(II)−*Ls*AA9.

The X-ray absorption spectrum of Cu(I)−*Ls*AA9 exhibits a characteristic XAS feature at 8982.4 eV on the rising edge, which we assign as a Cu 1s to nonbonding 4p transition.[177] This peak is ca. 0.8−1.1 eV lower in energy than those reported for other three-coordinate Cu(I) complexes (8983.2−8983.8 eV).[177] The spectral profile is consistent with a Cu(I) oxidation state in which the coordination geometry at the copper is T-shaped N_3. For Cu(II)−*Ls*AA9, care was taken not to overexpose the sample to X-rays, which are known to photoreduce the copper from Cu(II) to Cu(I) in LPMOs; this was achieved by creating a raster pattern with the X-ray beam across the sample during collection.[60,61] Under these conditions, the subsequent XAS exhibits a weak pre-edge peak around 8977.4 eV which results from the dipole-disallowed, quadrupole-allowed Cu 1s to 3d(x^2-y^2) transition. Again, as for the Cu(I) spectrum, this transition is *ca*. 1−1.5 eV lower in energy than equivalent absorptions in XAS spectra of other Cu(II) complexes, save those of Cu zeolites (8977.5 eV) used as methane oxidation catalysts[178] and of distorted tetrahedral (D_{2d} symmetry) $[CuCl_4]^{2-}$ (8977.8 eV).[179] At higher energies a more intense band is observed on the rising edge at 8985.9 eV, which is assigned to a three-state Cu 1s to 4p+LMCT "shakedown" transition, often reported in the XAS of Cu(II) species and which typically appear in the range 8986−8988 eV.[177] (Aside: it was recently proposed that the energy at which the "shakedown" transitions of Cu(II) complexes occur may be associated with ligand charge donation to the Cu and the amount of ligand orbital overlap with the Cu 4p orbitals).[180]

The pre-edge peak at 8977.4 eV is slightly lower in energy than those reported for other Cu(II) complexes, indicative of some charge transfer to the Cu(II) center in *Ls*AA9. This observation is in accord with the high reduction potentials (>250 mV vs SHE) which are known for Cu(II) LPMOs.[61] The position of the rising edge band at 8985.9 eV is also commensurate with a Cu(II) oxidation state.[177,181] Both the Cu(I) and the Cu(II) XAS closely match those found in the analogous oxidation state of another AA9 LPMO and the Cu(I) state of a AA10 LPMO reported in earlier studies.[61,63] Overall, the spectral features are consistent with Cu(I) and Cu(II) oxidation states of the dithionite-reduced and resting states of LsAA9 LPMO, respectively.

The XAS spectrum of the purple species in the pre-edge and rising edge regions is almost identical (peaks at 8977.8 and 8986.0 eV) to that of Cu(II)−*Ls*AA9. Notwithstanding the similarity, an additional weak pre-edge feature at 8982.8 eV of similar intensity to the 8977.8 eV Cu 1s to 3d(x^2-y^2) transition is also resolved. In the

difference spectrum between the purple species spectrum and Cu(II)−*Ls*AA9 (inset, **Figure 3.12**), this extra peak could be cleanly fit with a single Gaussian (**Figure 3.13**).

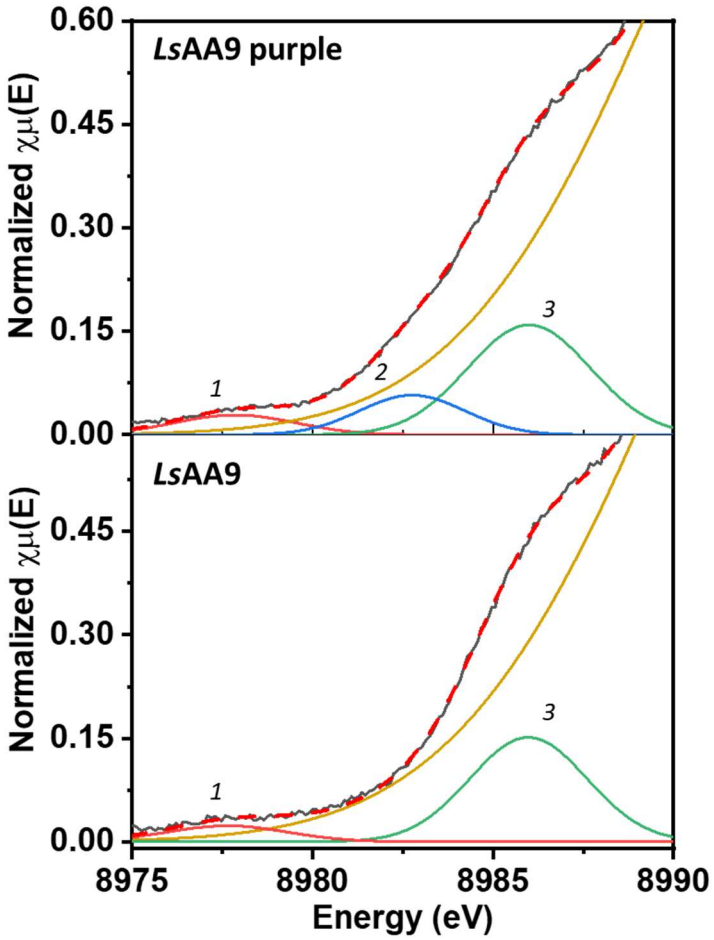

Figure 3.13 Fitting of the normalized Cu K-edge XAS spectra (77 K) of purple species (top) and Cu(II)−*Ls*AA9 (bottom). The fitting parameters for the single bands are reported in **Table 3.1**. The experimental spectrum is reported in black, while the relative fitting is reported as red dashed line.

The difference spectrum contains no other significant features in the pre-edge and rising edge regions, showing that the pre- edge 1s to 3d(x^2-y^2) transition and the 1s to 4p+MLCT shakedown transition are essentially unaffected in intensity and energy between the two different species. Thus, given the similarity in the XAS spectra the formal oxidation state of the Cu center in the purple species can be assigned as Cu(II). A higher oxidation state assignment would require that the pre-edge peak is upshifted by

the order of 1−2 eV.[181] The new peak at 8982.8 eV (**Table 3.1**) in the purple species falls outside the usual window (8986−8988 eV) of rising edge transitions, and it is also significantly shifted (+5.0 eV) from the Cu(II) 1s to 3d(x^2-y^2) transition, showing that it is not due to a Cu(III) 1s to 3d(x^2-y^2) transition. We can also rule out the possibility that this peak is due to a small amount of photoreduction, since the transition is at the wrong position (+ 0.4 eV) for the Cu(I) 1s to 4p transition and there is also no apparent drop in the intensity of the Cu(II) 1s to 3d(x^2-y^2) peak at 8977 eV between the purple species and Cu(II)–*Ls*AA9.

Table 3.1 Transitions energy (eV) and half width at half maximum (HWHM, eV) for the observed transition in the K-edge XAS spectra on *Ls*AA9 and *Ls*AA9 purple.

	***Ls*AA9**		***Ls*AA9 purple**	
Peak	**Energy**	**HWHM**	**Energy**	**HWHM**
1	8977.4	2.0	8977.8	2.0
2			8982.8	1.7
3	8985.9	1.9	8986.0	2.0
'*edge*'[1]	8996.2	7.1	8995.9	6.9

[1]-Band representing the rising edge absorption.

In summary, the positions of the shakedown transition and principal edge along with the position of the 1s to Cu 3d(x^2-y^2) pre-edge feature are commensurate with a Cu(II) oxidation state for both Cu(II)−*Ls*AA9 and the purple species. In addition, the appearance of a new pre-edge peak at 8982.8 eV is indicative of the formation of a new interaction between copper and a ligand (see **Discussion**, **Section 3.4.1**).[180,181]

3.3.3.2 Optical and magnetic spectroscopies

Simultaneous fitting of the UV-vis and CD spectra of the purple species (**Figure 3.14**) revealed the presence of six different absorption bands at 11790 (1400 M^{-1} cm^{-1}), 17100 (1800 M^{-1} cm^{-1}), 20400 (3600 M^{-1} cm^{-1}), 24560 (860 M^{-1} cm^{-1}), 28000 (2100 M^{-1} cm^{-1}), and 30810 cm^{-1} (3700 M^{-1} cm^{-1}). These bands all grew into the UV-vis and CD spectra at the same rate during the purple species formation, suggesting that they are all associated with a single species. This spectrum is quite different from the UV-vis absorption spectrum of *Ls*AA9 in its resting Cu(II) state, which is characterized by a weak and broad absorption band around 16600 cm^{-1}, typical for dipole-forbidden Cu(II) d-d transitions (**Figure 3.2**). All of the visible absorption bands of the purple species disappeared upon treatment with an aqueous solution of sodium dithionite.

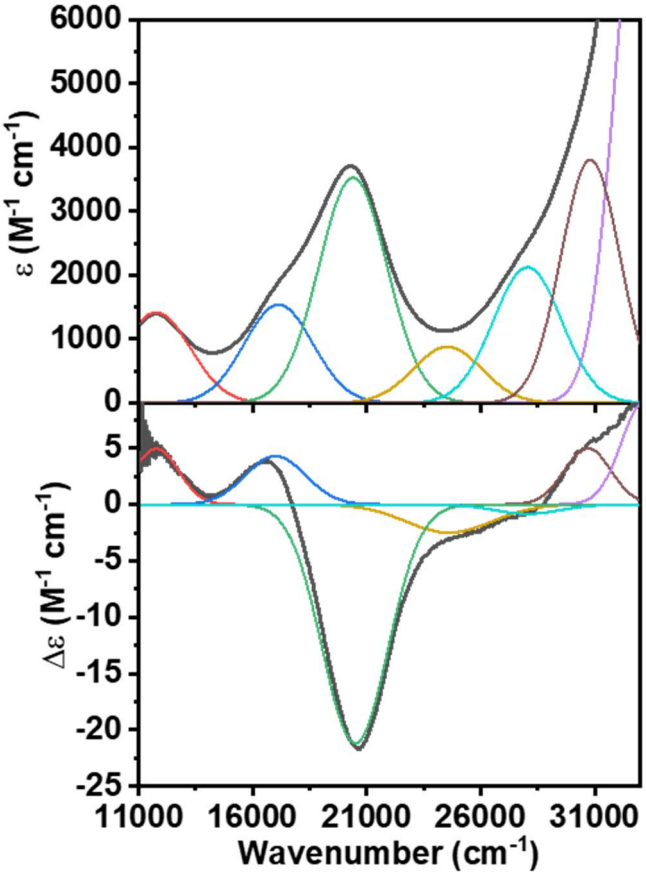

Figure 3.14 Room temperature UV-vis absorption and CD spectra of *Ls*AA9 purple together with the Gaussian fits of the absorption bands (coloured lines). The experimental spectrum is reported in black.

In generating the purple species, perpendicular-mode X-band CW-EPR spectroscopy showed that the axial type 2 copper signal of the Cu(II)−*Ls*AA9 slowly disappeared following treatment with hydrogen peroxide to a new EPR-silent species (**Figure 3.15**). EPR spectroscopy also demonstrated that the conversion of the resting state to the purple species was not complete, even at pH 10.0, as 15−20% of Cu(II) signal (as estimated by double integration of the EPR spectrum) remained following treatment of the Cu(II)−*Ls*AA9 form with hydrogen peroxide.

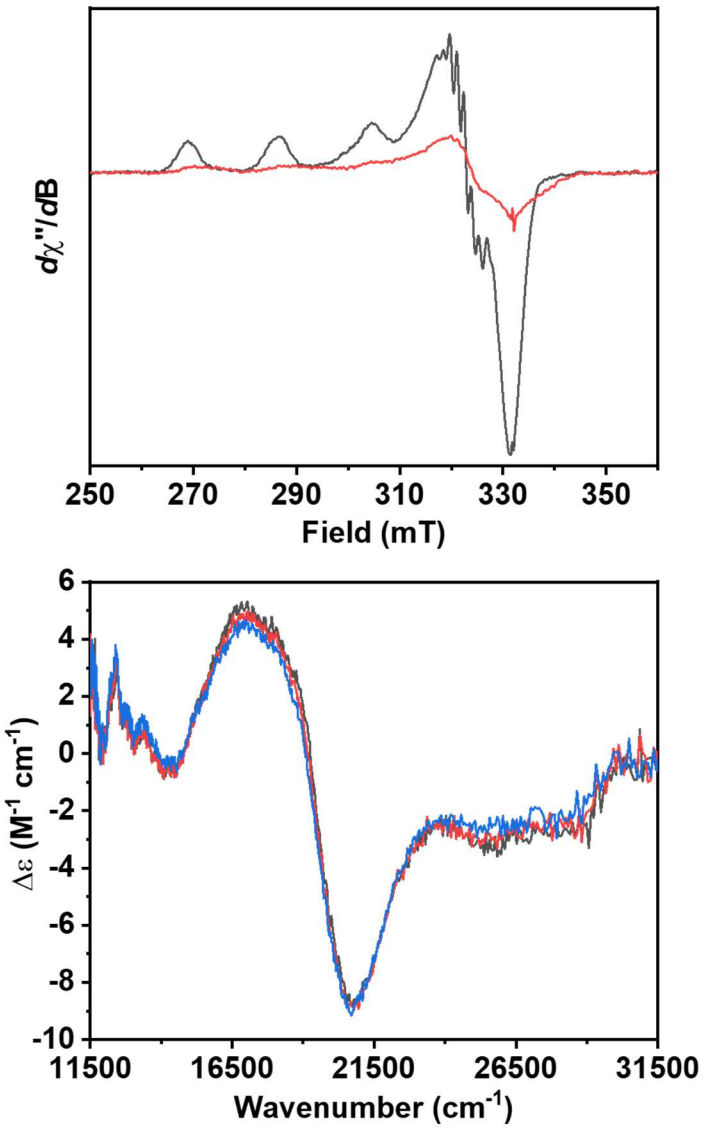

Figure 3.15 (Top) EPR spectra (160 K) of Cu(II)−*Ls*AA9 at pH 10.0 (black) and of *Ls*AA9-purple (red); in both samples the enzyme concentration was 200 μM, in 50 mM CAPS pH 10.0. (Bottom) Field dependence of the MCD spectrum of the purple species at 3 T (black), 5 T (red), and 7 T (blue), at 5 K. Enzyme concentration was 620 μM, 55% v/v glycerol, CAPS 50 mM, pH 10.0.

The EPR-silent nature of the purple species demonstrates that it is not a Kramers' spin doublet, although it is not possible to determine from this single observation whether it is a non- Kramers singlet or triplet state. Therefore, to determine the spin state, variable-temperature, variable-field magnetic circular dichroism (MCD) spectroscopy was carried out at pH 10. The MCD spectrum contained bands at 14300 cm^{-1} and 17000 cm^{-1} and shoulders at 18000 cm^{-1}, 14300 cm^{-1}, 25700 cm^{-1}, and 28400 cm^{-1}, all of which showed little/no field or temperature dependence across the full temperature (5−55 K) and full magnetic field ranges (3−7 T) employed in the study (**Figure 3.15** and **Figure 3.16**).

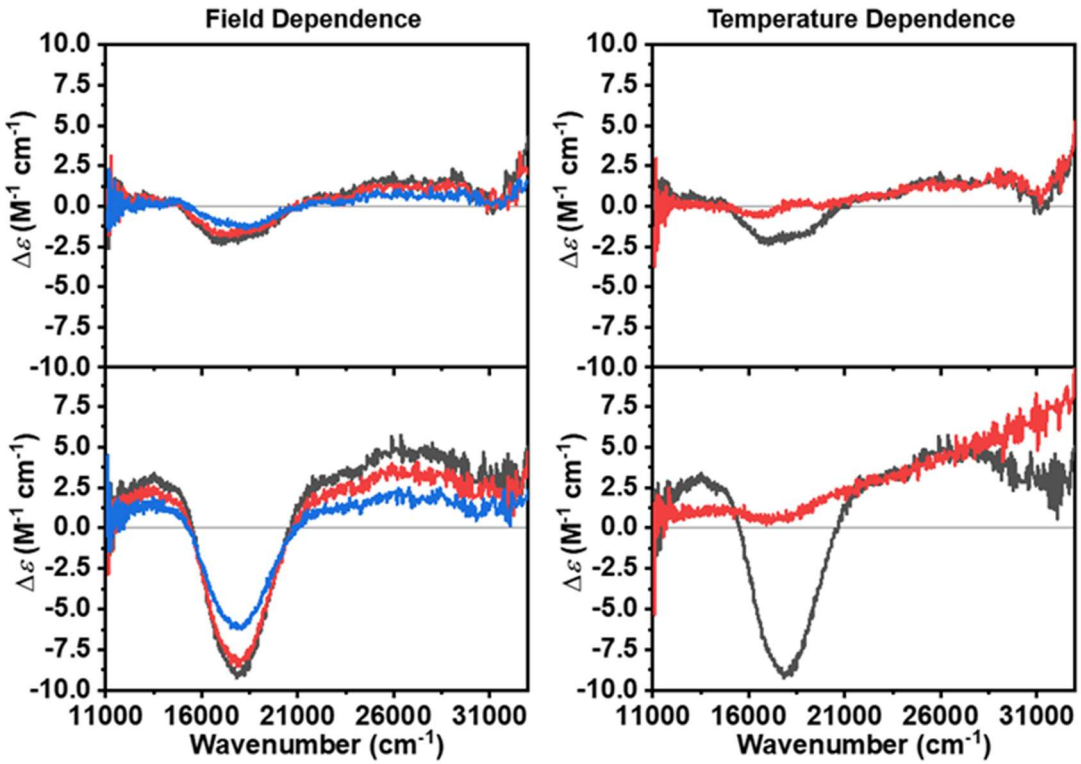

Figure 3.16 Field dependence (left) of the MCD spectrum of the *Ls*AA9 purple species (upper) and Cu(II)-*Ls*AA9 resting state (lower), recorded at 7 T (black), 5 T (red) and 3 T (blue), at 5 K. Temperature dependence (right) of the MCD spectrum of the *Ls*AA9 purple species (upper) and Cu(II)-*Ls*AA9 resting state (lower); 5 K (black) and 55 K (red), at 7 T. Protein concentration was 600 µM in CAPS 50 mM pH 10.0, glycerol 55% v/v. All the spectra are background subtracted, to remove the underlying zero field CD signal.

Thus, all of the bands in the MCD spectra (<55 K) arise from straightforward CD transitions. This observation establishes a singlet $S = 0$ ground state for the purple species ≤55 K, where the small variation recorded (<15% of band intensity) can be assigned to the 15−20% fraction of Cu(II)−*Ls*AA9 resting state that remained in the sample (**Figure 3.16**), consistent with the EPR studies described above. In regions of the spectrum that did not contain bands from the *C*-term transitions of Cu(II)−*Ls*AA9 (21000−23000 cm^{-1}) there was no change in signal intensity over the full temperature range (**Figure 3.16**).

Therefore, assuming that the lack of temperature variation seen in the MCD spectra requires a Boltzmann distribution of any higher spin state which is less than 2% (approximate signal-to-noise ratio) of the singlet species, an estimation of an upper limit of the exchange constant between singlet and higher order spin states of $-2J \approx 200$ cm^{-1} may be made (the negative sign indicates antiferromagnetic coupling). In practice, $2J$ is likely to be much more negative than −200 cm^{-1} since the low-temperature (5 K) CD spectrum is similar to the room-temperature CD spectrum, indicating that even at ~300 K there is no spectroscopically distinct higher spin state. The CD spectrum is not directly sensitive to the magnetic properties of the sample as there is no dependence on the magnetic field, but in switching from a singlet to a triplet electronic configuration, a change in the UV-vis electronic transitions is expected, which would be reflected in the CD spectrum as well.

3.3.3.3 Resonance Raman spectroscopy

Resonance Raman spectroscopy was carried out on the purple species under different isotopic conditions, including preparation of the sample in $H_2{}^{18}O$ water, preparation in $H_2{}^{16}O$ water with $H_2{}^{18}O_2$, and preparation in D_2O water with $H_2{}^{16}O_2$. Under all of these different conditions identical resonance Raman spectra were obtained and no bands were observed to be isotopically sensitive (**Figure 3.17**). This overall observation rules out the possibility of the spectroscopic features arising from a Cu−peroxide or Cu−superoxide unit. The resonance Raman spectra were obtained with 532 and 785 nm laser excitations, which are associated with the absorptions appearing at 11790 cm^{-1}, 17100 cm^{-1}, and 20400 cm^{-1} in the visible spectrum (**Figure 3.18**).

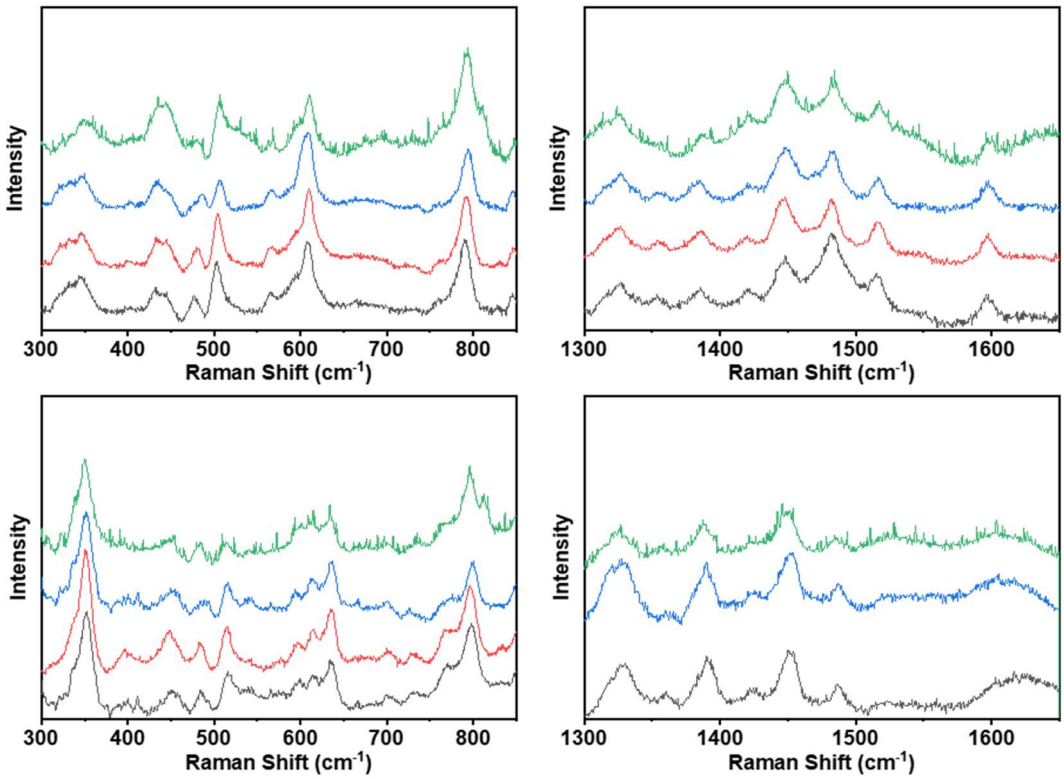

Figure 3.17 Resonance Raman spectra of *Ls*AA9 purple with 532 nm (upper) and 785 nm (lower) laser excitations measured at room temparature. The purple species formation reaction was performed using $H_2{}^{16}O/H_2{}^{16}O_2$ (black), $H_2{}^{16}O/H_2{}^{18}O_2$ (red), $D_2{}^{16}O/H_2{}^{16}O_2$ (blue) and $H_2{}^{18}O/H_2{}^{16}O_2$ (green).

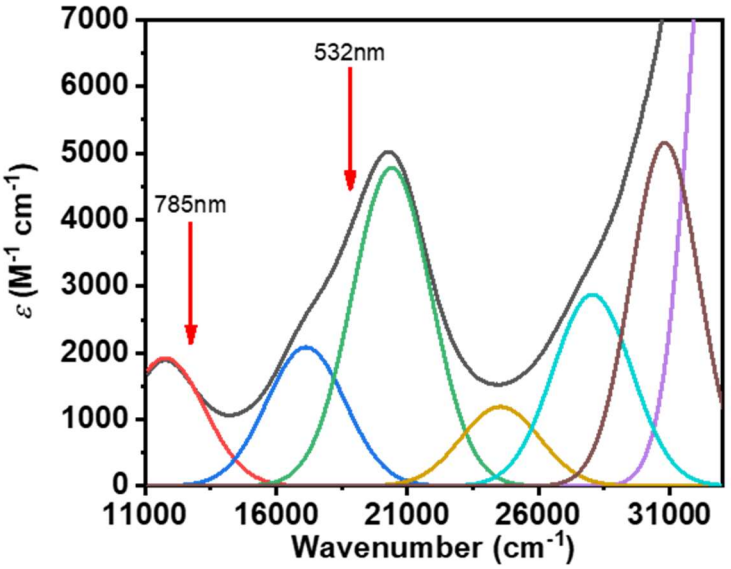

Figure 3.18 Gaussian fitting of the absorption spectrum of *Ls*AA9 purple. The red arrows indicate the position of the laser excitation wavelengths used in the resonance Raman data collection. The experimental spectrum is reported in black.

With 785 nm excitation, Raman bands in the spectrum appeared below 700 cm^{-1} with a prominent band appearing at 352 cm^{-1} (**Figure 3.19**, top). Using 532 nm laser excitation, a similar resonance Raman spectrum in the low-energy region was obtained, although the Raman band at 344 cm^{-1} was comparatively weaker. Conspicuously, excitation at 532 nm generated a rich Raman spectrum in the high-energy region (1300−1600 cm^{-1}), which is typical for ligand-based vibrational modes. Together, these results are consistent with the electronic transition at 20400 cm^{-1} being mostly ligand in character, whereas the transition at 11790 cm^{-1} is significantly metal in character.

A comparison of the resonance Raman spectra of the purple species with those of the oxidized form of galactose oxidase, which contains a Cu(II)−(modified)tyrosyl radical in the active site (**Table 3.2**), shows that bands at 1596 cm^{-1}, 1482 cm^{-1}, and 1386 cm^{-1} have a direct correspondence with bands in the resonance Raman spectra of galactose oxidase.[170] The similarity in the positions between the two proteins suggests that a Cu(II)−tyrosyl species is also the source of the these bands in the resonance Raman spectrum of the purple species. Bands at ~1330 cm^{-1} and 1515 cm^{-1} in the spectrum of the purple species are unassigned, but we note that the 7*a*′ (C−O) mode of a non-coordinated tyrosyl radical is reported at 1516 cm^{-1}.[182] While we do not have EPR

evidence of a free tyrosyl in the purple species (**Figure 3.15**), it is possible that a small amount of photodissociation of the Cu−OTyr bond occurs under the laser conditions used in the Raman experiment.

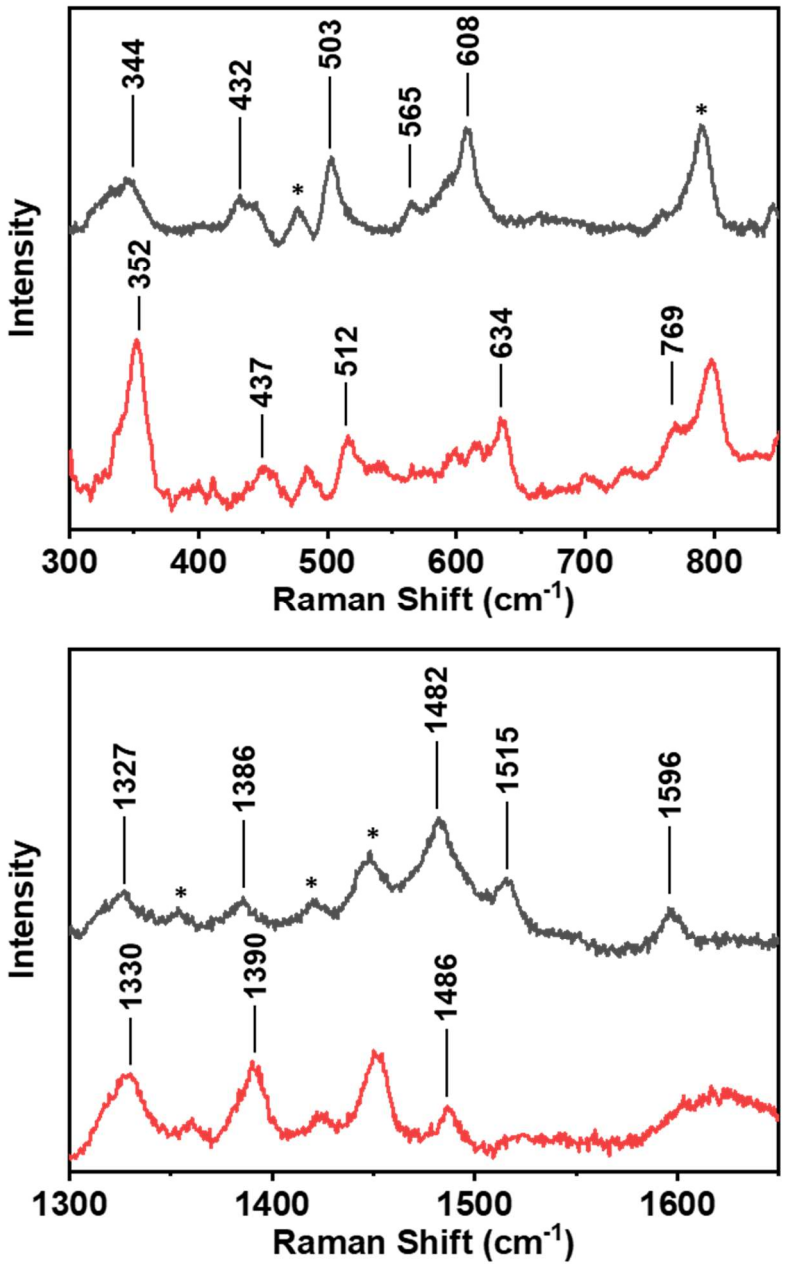

Figure 3.19 Resonance Raman spectra of the *Ls*AA9 purple species obtained with 532 nm (black) and 785 nm (red) excitation, at 293 K, 50 mM CAPS pH 10.0. Sample was prepared reacting *Ls*AA9 with $H_2{}^{16}O_2$ in $H_2{}^{16}O$. Asterisk (*) denotes vibrations due to CAPS buffer.

Table 3.2 Resonance Raman bands (cm^{-1}), above 1300 cm^{-1}, arising from irradiation at 532 nm and 785 nm of the purple species (CAPS buffer, pH 10.0), together with comparative assignments from Raman bands in active galactose oxidize (G.O.).[170]

532 nm	785 nm	Active G.O.	Normal mode assignment
1596	-	1595	Tyr 8*a*
1515	-	-	free-Tyr 7*a*'?
1482	1486	1487	Tyr 7*a*'
1386	1390	1382	Tyr 19*a*
1327	1330	-	?

3.3.3.4 DFT/TD-DFT analysis of the purple species

The spectroscopic studies are consistent with the presence of a Cu(II)−tyrosyl radical center at the active site of the purple species form of *Ls*AA9. In order to test this hypothesis and to provide a framework within which to interpret the spectroscopic results, we undertook DFT and TD-DFT calculations on models of *Ls*AA9 active site. The models were based on the coordinates of the X-ray crystal structure of *Ls*AA9. We used a cluster model of the active site (the same one used for the *Ls*AA9 resting state in **Chapter 2**), which is known from comparison with our previous QM/MM and DFT studies to model faithfully the active site structure of Cu(II)−*Ls*AA9.[101,103]

A Cu(II)−tyrosyl electronic state was optimized for both the triplet and the broken symmetry (BS) singlet electronic configurations using the BP86 functional. As the full coordination sphere of the copper in the purple species is unknown, we explored several different models that differed in the type of exogenous ligands (H_2O/HO^-) which coordinate to the copper and their *cis* or *trans* position with respect to the tyrosyl radical (**Figure 3.20**). The optimization on the BS singlet surface of these models showed differences with respect to those calculated on the triplet surfaces, most notably for Model3-OH_{trans} (**Table 3.3**), where the principal difference between the two structures was the length of the Cu···OTyr contact (*ca*. 2.0 Å in the singlet-optimized structure and *ca*. 2.4 Å in the triplet-optimized structure). Therefore, given the large differences in structures between singlet and triplet states, the exchange coupling constants were

calculated for both the broken-symmetry (BS) singlet and the triplet-optimized geometries.

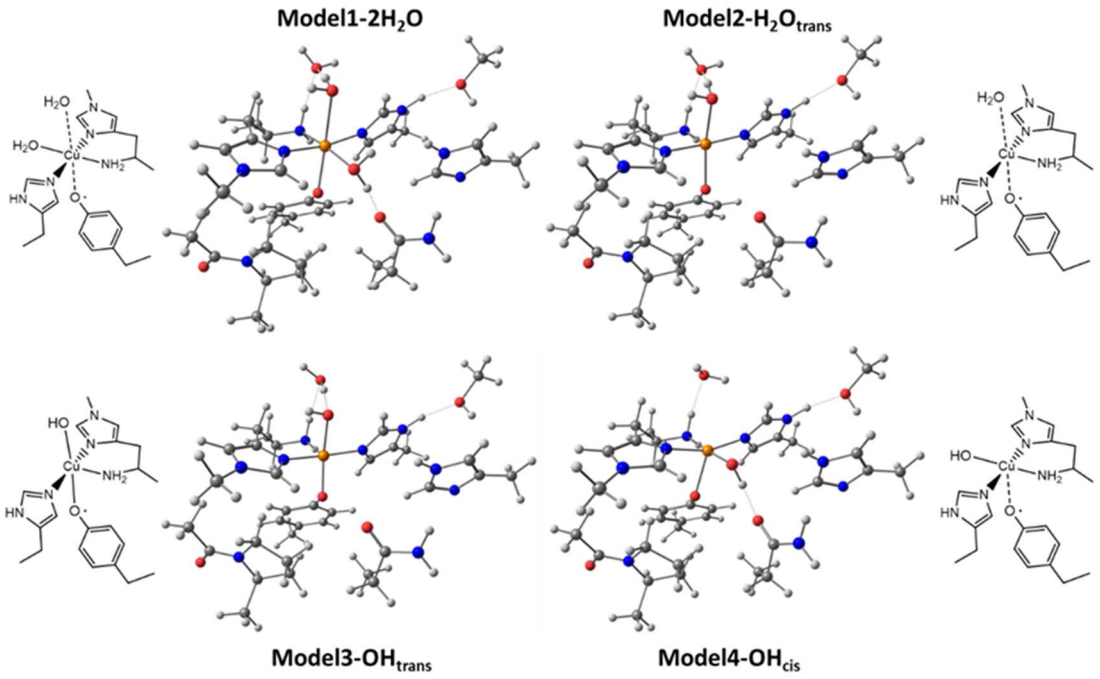

Figure 3.20 DFT optimized (broken symmetry singlet state) structures of the *Ls*AA9 cluster models together with their respective scheme, highlighting the different Cu coordination geometries considered.

Table 3.3 Selected structural parameters of the DFT optimized structures for both the triplet (T) and the singlet (broken symmetry, S) states. For comparison, the same parameters for the crystal structure (5ACF) are also included. Atom numbers refer to the numbers shown in the figure above.

Model	Electronic State	Cu–NH_2 (Å)	Cu–N_δ (Å)	Cu–N_ε (Å)	Cu–OTyr (Å)	Cu–X_{trans} (Å)	Cu–X_{cis} (Å)
Crystal Structure (5ACF)		2.2	1.9	2.00	2.8	3.3	2.09
	T	2.06	1.99	2.01	2.27	2.50	2.08
Model1-2H_2O	S	2.06	2.00	2.01	2.31	2.55	2.07
	T	2.12	1.95	1.95	2.20	2.29	-
Model2-H_2O_{trans}	S	2.13	1.93	1.93	2.19	2.23	-
	T	2.09	1.99	2.00	2.36	1.93	-
Model3-OH_{trans}	S	2.20	1.95	1.94	2.01	1.94	-
	T	2.10	2.01	2.01	2.26	-	1.93
Model4-OH_{cis}	S	2.03	2.00	2.00	2.26	-	1.90

In all cases, as expected, a single point BS calculation using B3LYP as functional from the triplet optimized geometry gave the lowest energy state with a positive *J* value (*i.e.*, ferromagnetic coupling). In contrast, performing the single point calculation with the singlet optimized geometry resulted in two structures with a modest (Model2-H_2O_{trans}, $J = -132$ cm^{-1}) and strong (Model3-OH_{trans}, $J = -1004$ cm^{-1}) antiferromagnetic coupling (**Table 3.4**). Both of these structures had a short Cu−OTyr bond, 2.19 and 2.01 Å, respectively, albeit slightly longer than the equivalent bond observed in Cu(II)−phenoxyl radical complexes (1.94 Å).[183]

Mindful of the well-known issues associated with the accuracy of BS calculations with transition metals and in particular their sensitivity to the degree of Hartree-Fock exchange included in the calculations,[90] a range of functionals was then employed to calculate the exchange constant on the BP86-optimized singlet structures (BP86, TPSSh, B3LYP, and PBE0) for all model structures. These functionals were selected to span a range of 0−25% of Hartree−Fock exchange contribution. Across all of the different functionals, each one predicted a large negative value of exchange constant (much more negative than −200 cm^{-1}) for when the hydroxide lies *trans* (Model3-OH_{trans}) to the tyrosyl ligand rather than

a water molecule in the same position, Model2-H_2O_{trans} (**Table 3.4**). The same functionals predicted small exchange constants for the *cis* configuration, incommensurate with experimental measurements. Thus, all functionals predict a large singlet−triplet energy gap for the trans hydroxide configuration.

Table 3.4 DFT calculated exchange coupling constant *J* for the different models starting from the triplet state (T) or the singlet state (S) optimized geometry. A positive *J* indicates ferromagnetic coupling, whilst a negative *J* indicates antiferromagnetic coupling.

Model	**Electronic State**	***J* (cm^{-1})**			
		BP86	**TPSSh**	**B3LYP**	**PBE0**
Model1-2H_2O	T	262	182	118	107
	S	201	141	93	84
Model2-H_2O_{trans}	T	22	17	21	11
	S	-220	-102	-118	-97
Model3-OH_{trans}	T	238	182	110	95
	S	-1277	-1059	-1004	-922
Model4-OH_{cis}	T	-171	129	88	79
	S	-631	-59	9	24

Time-dependent DFT calculations of the UV-vis spectra and Cu K-edge XAS were performed on Model2-H_2O_{trans} and Model3-OH_{trans} in their singlet electronic configuration using the B3LYP functional. For the UV-vis electronic transitions, at least one intense band was predicted in the visible region for both models, together with lower intensity bands (**Figure 3.21**). Moreover, a summary of the calculated transitions and their intensities are reported in **Table 3.5**.

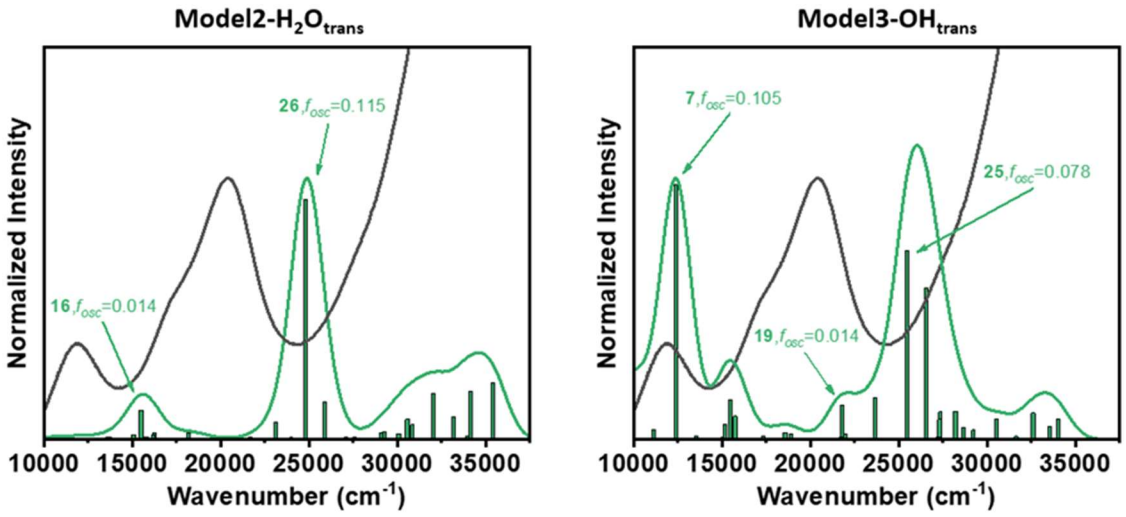

Figure 3.21 Overlay of *Ls*AA9 purple UV-vis spectrum (black) with the TD-DFT calculated spectrum of the singlet state (green), using a Gaussian broadening (HWHM = 2000 cm^{-1}) and normalized to the λ_{max} of the experimental spectrum. Labels indicate the number and the calculated oscillator strength (f_{osc}) for few selected transitions. The relation of the f_{osc} to the ε_{max} of a calculated transition is: $f_{osc} = 4.6 \cdot 10^{-9}\ \varepsilon_{max}\ \Delta\nu_{1/2}$, where $\Delta\nu_{1/2}$ is the HWHM of the relative Gaussian band.

In Model2-H_2O_{trans} the most intense band was calculated to appear at 24800 cm^{-1} and arose from a MLCT transition (Cu to Tyr-radical) according to its transition difference density (**Figure 3.22**). A second, less intense, transition at 15500 cm^{-1} came from a LMCT (Tyr-radical to Cu) transition. For Model3-OH_{trans} an intense MLCT (and with significant HO^- character) was predicted at 12390 cm^{-1}, together with a set of LLCT (histidine to tyrosine) and LMCT (histidine to Cu) transitions at higher energy (21800 cm^{-1} and 25500 cm^{-1}). These results assigned opposite character to the low-energy transition (~11800 cm^{-1}) in the UV-vis spectrum of the purple species, LMCT for Model2-H_2O_{trans}, and MLCT for Model3-OH_{trans}. Similarly, the nature of the higher energy transition (20400 cm^{-1}) between the two models was predicted to be different in nature: MLCT for Model2-H_2O_{trans}, His to Tyr (LLCT) and His to Cu (LMCT) for Model3-OH_{trans}. These results are in partial agreement with the experimental spectrum as the relative intensities of the experimental transitions are not modelled accurately. The discrepancy between experimental and calculated intensities likely arises from significant multi-configurational character of the copper(II)−tyrosyl species. In this case, multireference calculations would be needed to model the UV-vis spectrum; these calculations will be considered in a future study.

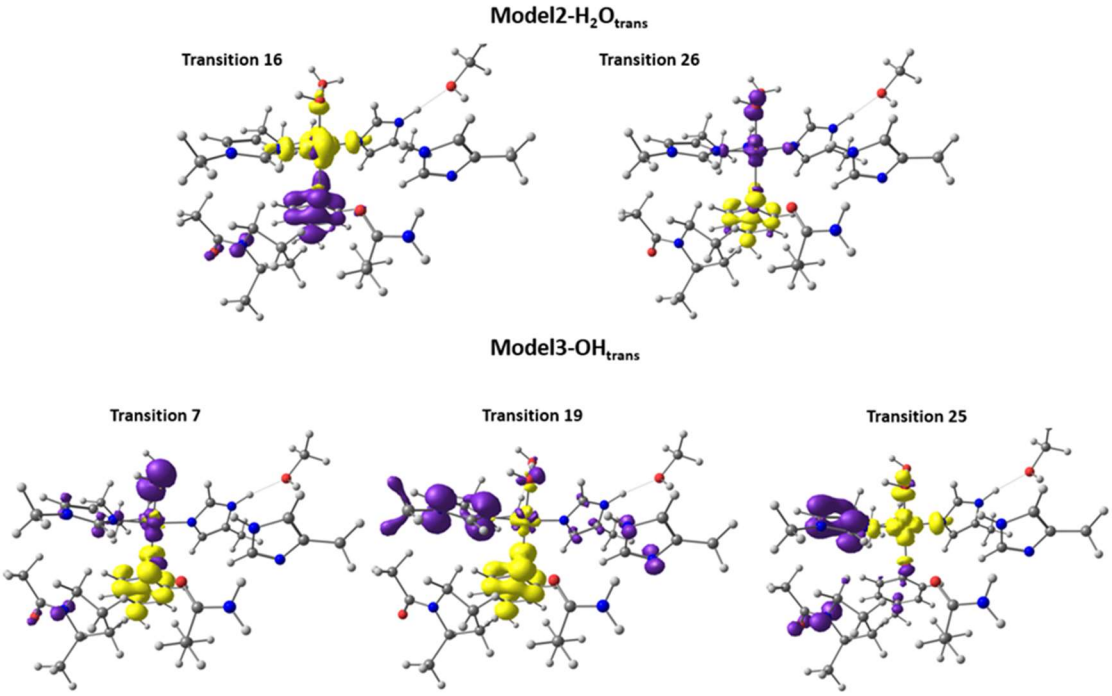

Figure 3.22 TD-DFT difference density plots of selected transitions (purple is loss of electron density, yellow gain of electron density) of Model2-H_2O_{trans} and Model3-OH_{trans}. Transition numbers refer to the labels reported in **Figure 3.21**.

Table 3.5 TD-DFT for Model2_H_2O_{trans} and Model3_OH_{trans} in the singlet state using B3LYP / Def2-TZVP of the first 40 excited states with an oscillator strength threshold of >0.001. Bolded values are pictured as difference density plots in **Figure 3.22**.

Model2_H_2O_{trans}			**Model3_OH_{trans}**		
Transition N°	**Wavenumber (cm^{-1})**	**f_{osc}**	**Transition N°**	**Wavenumber (cm^{-1})**	**f_{osc}**
1	8450	0.002	1	7987	0.002
3	7176	0.003	2	9950	0.02
10	15077	0.002	5	9878	0.002
11	13736	0.001	6	8601	0.003
12	10971	0.001	**7**	**12390**	**0.105**
13	16239	0.003	8	11142	0.004
15	16209	0.002	9	15740	0.010
16	**15502**	**0.014**	11	15175	0.006
17	15803	0.001	13	15467	0.016
21	18169	0.003	15	18895	0.002
25	21651	0.001	16	13527	0.001
26	**24821**	**0.115**	18	17331	0.001
30	23111	0.008	**19**	**21785**	**0.014**
32	25898	0.018	20	21760	0.001
34	27566	0.001	21	21959	0.002
35	29073	0.003	23	18563	0.003
36	27098	0.001	**25**	**25476**	**0.078**
37	29258	0.004	26	26562	0.063
38	30853	0.007	27	27361	0.011
39	32054	0.022	28	23680	0.018
40	30569	0.010	29	28213	0.012
			30	27315	0.008
			31	29227	0.004
			32	28659	0.005
			34	27247	0.001
			35	30544	0.009
			37	31640	0.001
			38	32612	0.011
			39	33550	0.006
			40	34023	0.009

The TD-DFT calculated K-pre-edge XAS of both Model2-H_2O_{trans} and Model3-OH_{trans} exhibit two weak features, the first at ~8977 eV (for both models) and another at higher energy 8981.5 and 8980.0 eV, respectively (**Figure 3.23** and **Table 3.6**). The first feature is assigned to a standard Cu 1s → 3d transition (8977 eV), while the second corresponds to a MLCT from Cu 1s to the tyrosyl radical. The calculated energy separation (4.3 and 2.3 eV, respectively) between the two features is smaller than that determined experimentally (5.0 eV); however, the exact energy of the calculated transitions is known to be heavily dependent on the functional chosen for the calculation and is therefore not generally predictive. On the other hand, the number and intensities of the calculated peaks are more reliably predicted from calculations, and from this perspective, the match between experiment and theory is excellent.[184]

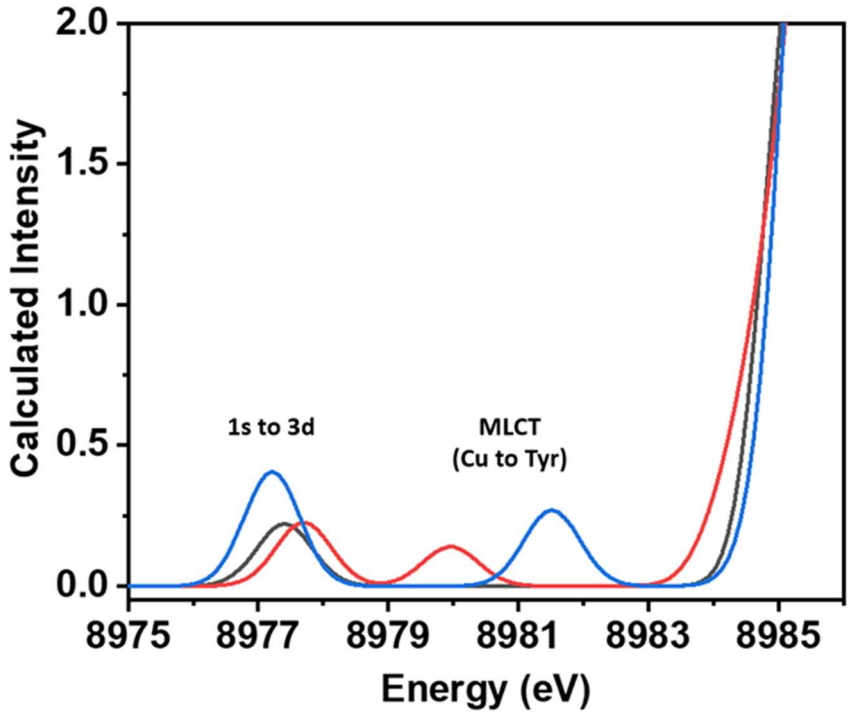

Figure 3.23 Calculated Cu K pre-edge regions for Model2-H_2O_{trans} (blue) or Model3-OH_{trans} (red) and for the Cu(II) resting state model (black). The calculation used the B3LYP functional, a -5.6 eV energy shift and a broadening of 1 eV have been applied to all calculated spectra.

Table 3.6 Comparison of experimental pre-edge energies of *Ls*AA9 purple species to calculated values using the B3LYP functional for Model2-H_2O_{trans} (blue) or Model3-OH_{trans} (red) in the singlet state.

Electronic Transition	Experiment (eV)	Model2_H_2Otrans (eV)	Model3_OHtrans (eV)
1s to 3d	8977.8	8977.2	8977.7
MLCT	8982.8	8981.5	8980.0
ΔE	5.0	4.3	2.3

Vibrational frequencies were calculated at the same level of theory used for geometry optimization (BP86, Def2-TZVP/ Def2-SVP, see DFT **Methods section 3.2.9**) and gave Raman active vibrations for both Model3-OH_{trans} and Model2-H_2O_{trans} at similar frequencies to those observed experimentally (**Table 3.7**). The C−O tyrosyl stretch (Tyr 7*a*′) is calculated at 1455 cm^{-1} and 1451 cm^{-1}, respectively (*cf.* ∼1482−1486 cm^{-1}), and a Cu−OTyr stretch at 375 cm^{-1} and 320 cm^{-1}, respectively (*cf.* 344−352 cm^{-1}).

Table 3.7 Comparison between selected *Ls*AA9 purple species experimental and Model2-H_2O_{trans}/Model3-OH_{trans} calculated Raman active vibrations (cm^{-1}).

***Ls*AA9-purple (532 nm excitation)**	***Ls*AA9-purple (785 nm excitation)**	**Model2-H_2O_{trans}**	**Model3-OH_{trans}**	**Normal mode assignment**
1596	-	1578	1574	Tyr 8*a*
1482	1486	1455	1451	Tyr 7*a*’
1386	1390	1294	1302	Tyr 19*a*
344	352	320	375	Tyr out of plane bending

On the basis of the calculated *J* value, TD-DFT, and vibrational calculations, the most plausible structure for the purple species possesses a hydroxide ligand that lies trans to the tyrosyl ligand (Model3-OH_{trans} in **Figure 3.20**), although we cannot rule out the model where a water molecule lies trans to the tyrosyl, Model2-H_2O_{trans}. From the DFT and TD-DFT studies it is not possible to make a definitive conclusion on which model (Model2-

H_2O_{trans} or Model3-OH_{trans}) best represents the structure of the purple species. Both are consistent with the experimental and calculated data. However, the lack of pH sensitivity of the purple species might argue more for Model3-OH_{trans} being the representative species.

3.4 Discussion

3.4.1 Assignment of spectroscopic features

The addition of hydrogen peroxide to a ~1 mM solution of *Ls*AA9 LPMO (in either the Cu(II) or Cu(I) form) at pHs > 7.0 affords a purple-colored species. The dependence of the absorptions within the visible spectrum on the presence of copper shows that they arise from transitions associated with the copper active site. The combined XAS, EPR, and MCD spectroscopic data establish the species as an open-shell singlet in which one unpaired electron is associated with the Cu(II) center (from XAS) and the other with a coordinating ligand. This ligand cannot be a peroxide or a coordinated water molecule, since the resonance Raman spectra are insensitive to the isotopic substitution of peroxide. The observation also rules out the formation of an antiferromagnetically coupled Cu_2−μ-peroxo dimer. Of the remaining ligands that could harbour an unpaired electron, the active site tyrosine offers the most reasonable possibility, and indeed, resonance Raman data of the purple species are best assigned by comparison to the oxidized form of galactose oxidase, which is known to contain a Cu(II)−(modified)tyrosyl radical pair.[170] We further considered the potential formation of an N-oxide at the amino terminus, but this species would be expected to have a prominent N−O vibration in the resonance Raman spectrum at 800 cm^{-1}, which is not observed. Also, while the spectroscopic data do not completely rule out a potential Cu(II)−semiquinone species which could arise from the covalent oxidative modification of the tyrosine, the possibility is very much reduced by the lack of any observable modification of the tyrosine in the mass spectrum of the purple species and by the absence of isotopic shifts in the resonance Raman spectra.[185]

To secure the assignment of the purple species as a Cu(II)−tyrosyl center, we note the appearance of a weak pre-edge feature in the XAS (8982 eV) which is not present in the Cu(II)−*Ls*AA9 spectrum. On the basis of previous examples of similar features in the XAS spectra of Cu(II) complexes and the TD-DFT calculations, this pre-edge feature is assigned to a 1s to SOMO transition where the SOMO has significant tyrosyl character.[180,181] The fact that this XAS transition has some intensity, along with the observed CT transition at 11790 cm^{-1} in the visible spectrum of the purple species, demonstrates that there is an appreciable overlap between the SOMOs of the tyrosyl and the Cu center. While unusual, the occurrence of second pre-edge peaks in the XAS spectra of metal complexes is not unprecedented, having been observed in complexes where strongly coordinated ligands which have low-lying empty π* orbitals gain σ-overlap with the Cu orbitals through distortion of the ligand.[180,181,184] Such an interaction could arise in *Ls*AA9 where structures show that the conformation of the tyrosine with respect to the Cu admits some overlap of the π-manifold orbitals of the tyrosyl with the Cu 3d(x^2-y^2) orbital (**Figure 3.24**). Notably, this orbital pathway can only exist if the 3d(x^2-y^2) orbital plane of the Cu is rotated out of the plane of the histidine brace toward the tyrosine O atom. This rotation further requires the presence of an exogenous ligand in the *trans* position to the tyrosyl (**Figure 3.24**), matching the best-fit models from DFT calculations. Previous structural studies have shown this exogenous ligand is displaced on the binding of substrate, thus linking the formation of the purple species with the absence of substrate, as also observed experimentally herein.

Further evidence that the purple species is a Cu(II)−tyrosyl pair is gained from comparison with known small-molecule complexes, where experimental determination of the value of the exchange constant *J* as a function of the Cu−O−C angle (**Figure 3.24**) shows that a singlet ground state is only observed when this angle is near 130° (and the Cu−O−C−C dihedral angle ≈ 90°).[186] In *Ls*AA9 the equivalent angles are 124° and 87°, respectively. Finally, we note here that careful inspection of the K-edge XAS spectrum of oxidized Cu(II) in galactose oxidase shows a similar pre-edge feature at ∼8985 eV, which was assigned at the time to small differences in coordination geometry between the oxidized and the reduced versions of the enzyme but now we would suggest represents the transition described above.[187]

Thus, the data presented herein are commensurate with the formation of an intensely colored, stable Cu(II)−tyrosyl complex, which is formed during the non-coupled turnover

of an AA9 LPMO with hydrogen peroxide. This species has an open-shell singlet ground state, in accord with the formation of a strong Cu(II)−O bond, leading to intense charge-transfer bands in its visible spectrum.

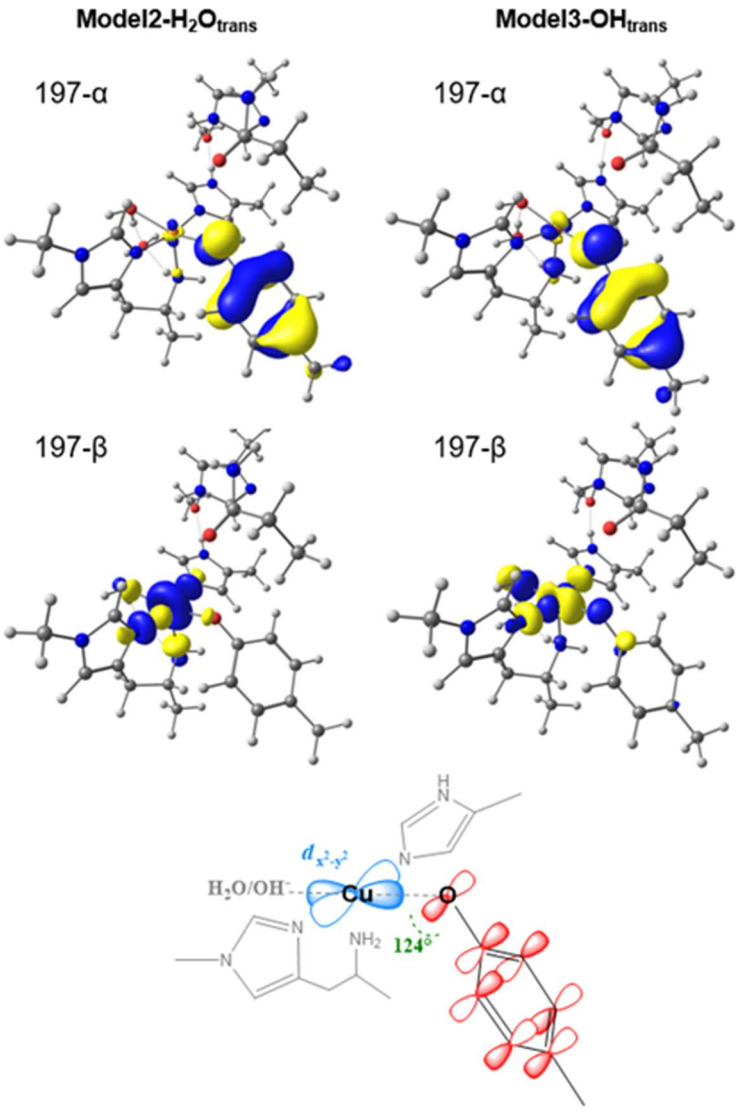

Figure 3.24 DFT calculated unrestricted corresponding orbitals representing the two magnetically coupled SOMO in the singlet state of Model2-H_2O_{trans} and Model3-OH_{trans}, together with a scheme showing the rotation of the 3d(x_2–y_2) orbital respect to the histidine brace plane. In the X-ray crystal structure of *Ls*AA9 (PDB 5ACG) the Cu–O–C angle is 124°, whilst the dihedral angle between the 3d(x_2–y_2) plane and the plane of the phenyl ring of the coordinated tyrosine is 87°.

3.4.2 Hydrogen peroxide as a co-substrate for LPMOs

Formation of the tyrosyl radical at the active site of *Ls*AA9 provides evidence that this is the site of generation of the oxidizing species in LPMOs, following addition of hydrogen peroxide. Hydrogen peroxide is a powerful oxidant, and its use as a co-substrate in the reactions of LPMOs has been the center of much recent debate.[29,106] This debate concerns itself with whether hydrogen peroxide or O_2/reducing agent are the *in vivo* co-substrates for LPMOs. While acknowledging that the peroxide/O_2 debate is not settled, our own working hypothesis for the work described herein is that hydrogen peroxide is a useful laboratory shunt for AA9 LPMOs for both coupled and uncoupled activities. In the former role it acts to simplify mechanistic studies, while in the latter it gives insight into the structural apparatus which LPMOs employ to deal with oxidizing intermediates generated at the active site in the absence of substrate. From this perspective we have shown herein that AA9 LPMOs are significantly protected from oxidative damage by their own glycosylation patterns. We also observe that some amino acid side chains (both at the surface and buried within the protein structure) are covalently modified after treatment with hydrogen peroxide (**Figure 3.11**), suggesting that these amino acids are redox active.

This last aspect directs us toward the possibility that LPMOs are equipped with specific internal charge-transfer mechanisms for dealing with the oxidizing species which are generated during its catalytic cycle – a proposal already made by others,[188] particularly given the parallels to P450 and also to the fact that the active site in LPMOs is surrounded by amino acid residues (e.g., tryptophans and tyrosines) that are in principle capable of translating a positive hole away from the active site.[189]

3.4.3 Role for the active site tyrosine in LPMOs

Mass spectrometry analysis shows that challenging *Ls*AA9 with hydrogen peroxide during uncoupled turnover does not lead to covalent oxidative modification of the active site tyrosine (Tyr-164). Not only does this observation take this LPMO away from the class of other copper-containing enzymes that possess tyrosine-derived redox-active cofactors (e.g., quinones), it also provides evidence that the tyrosyl is converted to a tyrosine by an efficient charge-transfer mechanism within the protein. Inspection of the

*Ls*AA9 structure shows that such mechanism could exist whereby the tyrosyl radical at the active site is quickly reduced to a tyrosine by a combination of rapid hole-hopping from Trp-64 (8.1 Å away, **Figure 3.25**) and back proton transfer from water. The tryptophan cation is subsequently reduced by other amino acid side chains along a charge-transfer pathway (see below).

Taking the above discussion as a basis for the role of the tyrosine in the active site of LPMOs, any potential hole-hopping pathways and the rates at which charge transfer occurs through these pathways can be examined using Marcus theory. The rate constant for any donor−acceptor pairwise interaction along a hole-hopping pathway can be estimated using a charge- transfer rate expression as follows:[190]

$$k_{DA} = \frac{2\pi}{\hbar} V_{DA}^2 \frac{1}{\sqrt{4\pi\lambda_{DA}T}} exp\left(-\frac{(\Delta G^0 + \lambda_{DA})^2}{4\lambda_{DA}k_B T}\right)$$

Elements of the equation can be calculated/estimated from the known self-exchange reorganization energies of the donor (λ_{DD}) and acceptor (λ_{AA}), the reduction potentials of the donor and acceptor, and the distances between the donor and the acceptor, the last of which is obtained from structural information. The effective electronic coupling (V_{DA}) can be estimated using Hopfield's equation.[191] On the basis of the charge transfer rate expression, a protein structure can then be searched for potential hole-hopping pathways and their rates calculated. To this end, a computer program, EHPath, is available to perform this search rapidly.[192]

Accordingly, we applied EHPath to all of the potential hole-hopping residues (tyrosine, tryptophan, cysteine) within the known structure of *Ls*AA9 using reduction potentials and reorganization energies at pH 7 and where the tyrosine at the active site (Tyr-164) acts as the hole donor. From this analysis a single and clear hole-hopping pathway in *Ls*AA9 emerges, which transfers a hole away from the tyrosyl radical (Tyr-164) to a surface residue (Trp-5) through Trp-64 and Tyr-65 with a mean-residence time of 6 ms (**Figure 3.25**). All other pathways in the protein have residence times of >1 s (**Table 3.8**).

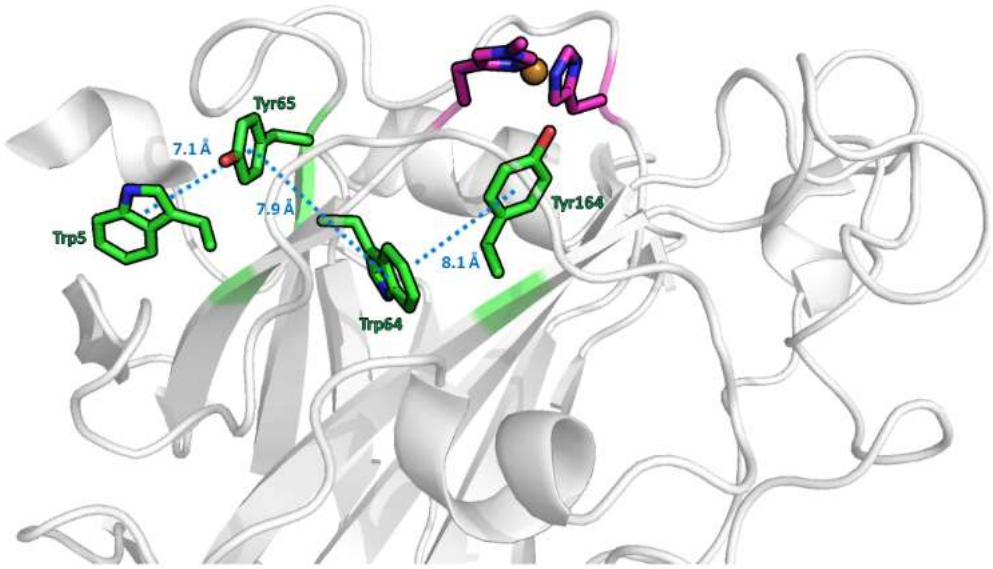

Figure 3.25 Depiction of *Ls*AA9 structure (grey ribbons) and amino acid side chains (cylinder bonds in green) involved in putative hole-hopping pathway. The Cu ion is represented as orange sphere and distances are given in Å.

Table 3.8 The five fastest accurate mean-residence times (AMRT) of hole-hopping pathways from Tyr-164 at pH 7 and 298.15 K through the structure of *Ls*AA9, as determined by EHPath.[192]

Pathway	AMRT /s
Tyr-164,Trp-64,Tyr65	$6.0 \cdot 10^{-3}$
Tyr-164,Trp-64,Tyr-65,Trp-5	$6.3 \cdot 10^{-3}$
Tyr-164,Tyr-65,Trp-5	1.2
Tyr-164,Trp-64,Trp-5	1.5
Tyr-164,Trp-64,Tyr-65,Tyr-21,Trp-5	1.8

The rapid rate of the Tyr-164···Trp-5 pathway parallels similar hole-hopping pathways seen in the enzymes P450 (37 ms), BSS (4.5 ms), and CCP1 (2.5 ms).[192] In a further parallel to these enzymes, the calculated activation energy of H-atom abstraction from substrate in coupled turnover by *Ls*AA9 is low ($\Delta G^{\ddagger}$= 5.5 kcal mol^{-1} from QM/MM calculations)[103] such that the rate of H-atom abstraction can be expected to be faster than the rate of hole hopping. As such, it is evident that the active-site tyrosine in *Ls*AA9 along with adjacent Trp-64 could form part of an efficient charge-transfer pathway through

LPMOs at pH 7, which is active during uncoupled turnover of the LPMO. It should be noted here that the network of aromatic residues connecting the Cu active site to the outside of the protein is largely conserved in the AA9 family.[50] The formation of the Cu(II)−tyrosyl species at pHs > 7 observed in our experiments is likely to be due to a combination of three factors. The first is, straightforwardly, that the active site tyrosine is easier to oxidize at higher pHs (reduction potential of tyrosyl is ~0.7 V at pH 10 and 0.93 V at pH 7).[193] The second is that our MS results show that several redox-active residues, including those in the hole-hopping pathway, are covalently modified in the experiment, thereby compromising the protein's capacity to transfer charge away from the active site tyrosine. In such circumstances it may be that there is an effective build-up of tyrosyl radical at the active site, which – under the conditions employed in our study – is eventually "extinguished" by the formation of a stable Cu(II)− tyrosyl bond (*i.e.*, purple species). Third, the formation of the bond occurs through a process which involves a pH-dependent reorganization of the Cu coordination sphere as described above.

3.4.4 Roles of Substrate in the Turnover of LPMOs

The Cu(II)−tyrosyl radical species does not form in the presence of substrate. This finding highlights two factors in AA9 LPMO (bio)chemistry. The first is that the presence of a bound substrate changes the mechanistic pathways available to AA9 LPMOs, ostensibly by locking the copper equatorial coordination sites into the plane of the histidine brace ligands. The locking is achieved by displacement of the axial water molecule in the Cu coordination sphere as previously demonstrated by spectroscopic studies on *Ls*AA9 (see **Chapter 2**).[65] Second, the presence of an efficient hole-hopping pathway in LPMOs confounds kinetic comparisons between the relative reactivity of H_2O_2 and O_2/reducing agent as co-substrates. The complication arises since the presence of a soluble reducing agent in the latter allows the hole-hopping mechanism to operate repeatedly to extinguish oxidizing equivalents generated at the active site. This pathway will compete against any weakly coupled pathway with substrate and thereby ostensibly lower the observed rate of reaction of substrate oxidation. Critical aspects in this regard are the availability (concentration) of substrate, its match to the LPMO under study, the presence of a carbohydrate-binding module, and the concentration and oxidation potential

of the reducing agent, all of which are factors known to affect the rate of substrate oxidation by LPMOs.[82,106,194]

3.5 Conclusions

The addition of hydrogen peroxide to an AA9 LPMO at high pHs in the absence of substrate results in the formation of a highly stable, purple-colored Cu(II)−tyrosyl complex that has been characterized using spectroscopic methods (UV−vis, CD, MCD, resonance Raman, EPR). The copper(II)−tyrosyl bond forms after the slow time scale "rotation" of the copper equatorial plane out of the plane of the histidine brace coordinating atoms. The redox activity of the active site tyrosine is indicative of its role in LPMOs, which is to act as part of an efficient charge-transfer pathway between the active site and the protein surface. Such a pathway, consisting of tyrosine and tryptophan residues and spanning ∼15 Å, has been identified in the LPMO used in our studies.

4 Characterization of the *Ao*AA11 LPMO

4.1 Introduction

Lytic polysaccharide monooxyganases are a recently discovered class of enzymes able to oxidize various polysaccharide substrates. They attract attention due to their potential use in biomass conversion, notably the production of biofuels (**Chapter 1**). LPMOs are classified in the CAZy database as Auxiliary Activity (AA) enzymes and divided in several different families according to their amino acidic sequence similarities[35]: AA9, AA10,[27,30] AA11,[37] AA13,[38,75] AA14,[39] AA15[40] and AA16.[41] Among these, the AA11 family was first identified by Hemsworth *et al*. in 2014 using a bioinformatics 'module walking' approach.[37] This approach is based on the discovery that many LPMOs from the AA9 family present additional domains at the C-terminus of the peptide chain, which are often carbohydrate binding modules (CBMs), used to enhance cellulose binding. However, some of these domains have unknown functions.[195] Sequence searches using one of these domains, called X278 at the time, returned hits where this particular domain was attached to potential LPMO domains, identified on the basis of their sequences (in particular the presence of an N-terminal histidine, which is a hallmark for LPMO enzymes). In general, LPMOs from different families share low sequence similarity and the AA11 enzymes are not an exception to this behaviour.

Despite many putative AA11 LPMOs sequences recorded in the CAZy database, today there are only two characterized enzymes belonging to this family: one from the fungi *Aspergillus oryzae* (*Ao*AA11)[37] and a second one from the fungi *Fusarium fujikuroi* (*Ff*AA11).[196] Both these enzymes have been shown to oxidize chitin as a substrate using O_2 and an external electron donor (sodium ascorbate in both cases). *Ao*AA11 was shown to be active on squid pen chitin (β-chitin), while *Ff*AA11 was reported to oxidize also shrimp shell chitin (α-chitin). Moreover, the catalytic activity of *Ff*AA11 was boosted by

addition of small amounts of H_2O_2 as oxidant (instead of O_2), but a large excess of peroxide was shown to be detrimental to the enzymatic activity.[197] This effect is common across the LPMO families AA9 and AA10, where enzymatic catalytic rates are enhanced by supplementing of small amounts of H_2O_2, while a too high concentration of H_2O_2 leads to oxidative damage and enzyme inactivation.[29,106,198,199] On the other hand, no activity tests of *Ao*AA11 using H_2O_2 as co-substrate have been reported so far, to best of our knowledge.

4.1.1 The structure of *Ao*AA11

Today, there is only one known X-ray structure of *Ao*AA11 (and the only available structure of an AA11 family member), characterized by Hemsworth *el al*.[37] The structure (PDB 4MAI, resolution 1.4 Å) shows that the overall fold of this enzyme is similar to that of other LPMOs with a largely antiparallel β-sandwich fold and three disulfide bonds (**Figure 4.1**).

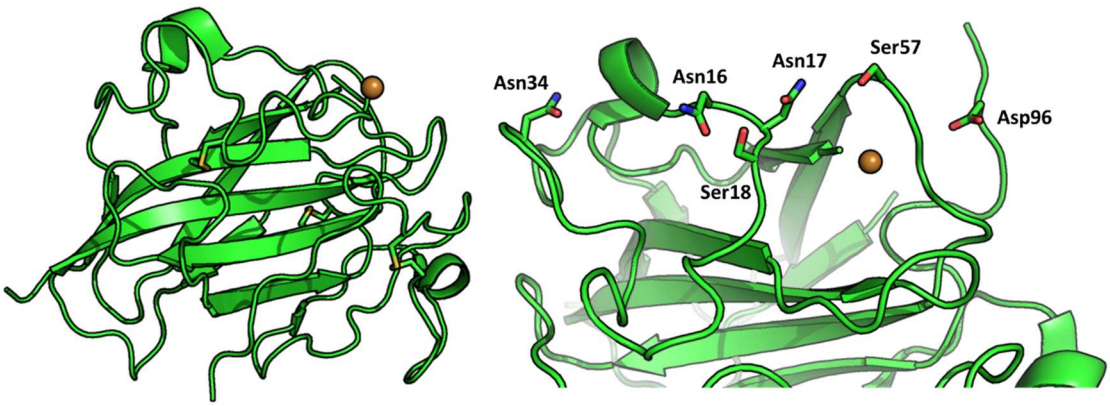

Figure 4.1 Cartoon representing the overall fold of *Ao*AA11, highlighting the disulfide bridges (in yellow) (left). Solvent exposed polar residues on the surface surrounding the Cu active site, potentially involved in substrate binding (right). The Cu ion is represented as a gold sphere. PDB code: 4MAI.

The N-terminus copper active site is solvent-exposed and sits on a flat surface that is also the substrate binding face, similar to all other LPMOs. However, in AA9 enzymes this surface has conserved aromatic residues (mainly Tyr residues) which are the main contributors to substrate binding, but they are not present in *Ao*AA11. In fact, its surface resembles more the substrate binding surface of AA10 LPMOs, characterized by residues

capable of forming hydrogen bonds with the polysaccharide chain like Asn-16/17/36, Ser-18/57 and Asp-96, even if none of these residues is strongly conserved in the AA11 family (**Figure 4.1**, see also **Section 1.7** on substrate binding).[37]

The *Ao*AA11 structure present a typical histidine brace copper active site, with the two conserved His residues coordinating the metal.[30] The absence of any other exogenous ligand in the free equatorial position, like H_2O or Cl^- (which are typically found in Cu(II)−LPMOs), suggests that the Cu ion has been photoreduced by the X-ray beam during data collection, and that it is best assigned as Cu(I) (**Figure 4.2**). Photoreduction of the Cu(II) state during data acquisition is a well-known problem in LPMOs X-ray structures and, more in general, with copper enzymes[60,61]. Similar to AA9, AA13, AA14 and AA15 families, one Cu axial position is occupied by the oxygen atom of a conserved Tyr residue (Tyr-140), with a long Cu−O(Tyr) distance of 3.1 Å. In this case, the other axial position, *trans* to the Tyr-140, is occupied by another oxygen atom from a glutamate residue of an adjacent *Ao*AA11 molecule in the crystal lattice at ~2.5 Å from the Cu (**Figure 4.2**); this interaction is an artefact due to crystallization as the enzyme is monomeric in solution.[37]

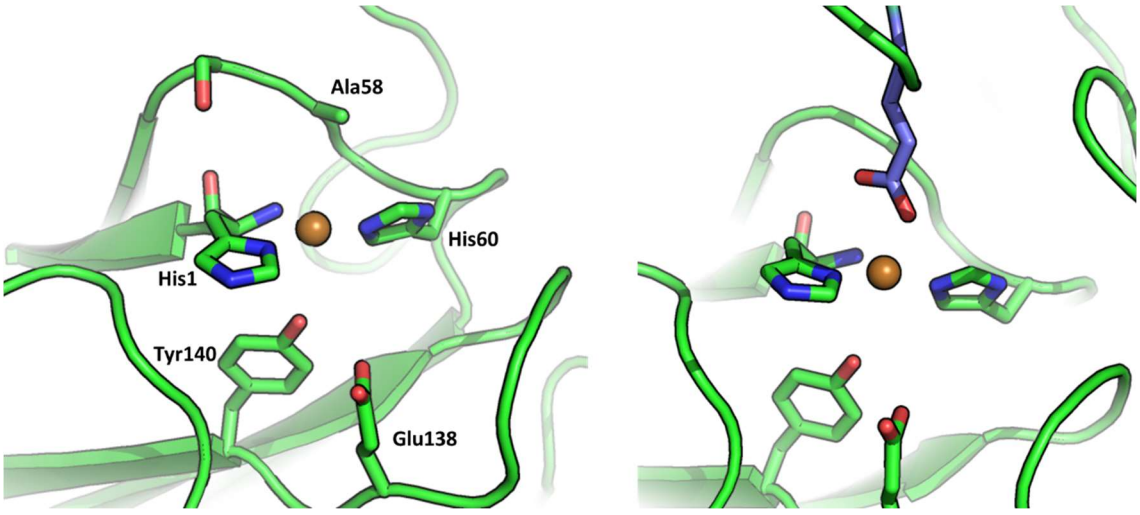

Figure 4.2 The active site of Cu(I)-*Ao*AA11, highlighting the two His residues forming the histidine brace and several copper secondary coordination sphere residues which are conserved in the AA11 family (left). The active site of Cu(I)-*Ao*AA11 showing the endogenous residues (green) together with the exogenous Glu residue (blue) from a second *Ao*AA11 molecule in the crystal lattice (right). The Cu ion is represented as a gold sphere.

In the copper secondary coordination sphere there are several other residues strongly conserved in the family that are probably important for the catalytic mechanism: Glu-138 is hydrogen bonded with the axial Tyr-140 and the Ala-58 side chain is positioned close to the other axial position (**Figure 4.2**). These two particular residues are found also in the AA10 (chitin active) and AA15 (cellulose and chitin active) families. Moreover, Tyr-140 is part of a conserved network of tryptophan, methionine and other tyrosine residues which connect the copper active site to another surface at the opposite side of the enzyme with respect to the active site (**Figure 4.3**). This network could act as electron transport chain, as already suggested for AA9 and AA10 families (see also **Section 3.4.3**).[50]

In general, LPMOs from eukaryotic organism feature a characteristic τ-N-methylation of the N-terminal histidine, which is not present in the *Ao*AA11 structure. The enzyme was produced in *E. coli*, an organism that lacks the appropriate enzymatic machinery to methylate proteins as post translational modification, therefore even if *Ao*AA11 would be naturally methylated, this feature cannot be reproduced with *E. coli* as expression system. Previous studies showed that the methylation is not required for enzymatic activity (and confirmed for this particular enzyme as well). Its functional role is not clearly understood and recent work by Petrović *et al*. suggested it protects the enzyme from auto-oxidative inactivation during uncoupled turnover.[53]

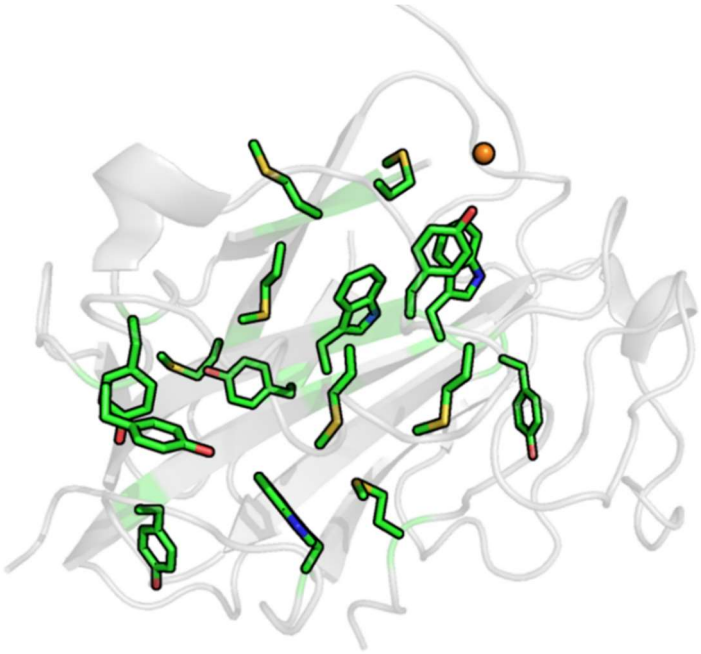

Figure 4.3 Cartoon representing the network of Tyr, Trp and Met residues connecting the Cu active site to different protein surfaces in *Ao*AA11 and putative electron transfer pathways. The Cu ion is depicted as gold sphere.

In summary, the *Ao*AA11 active site presents conserved residues that are typical of cellulose active AA9s (axial Tyr residue) and chitin active AA10s (distal Glu and Ala residues), families that show different Cu coordination geometries. Here, we report a multi-spectroscopic (EPR, UV-vis, CD and MCD) theoretical (DFT and CASSCF) investigation of the enzyme Cu(II) state electronic structure. We show that the *Ao*AA11 active site electronic structure is very similar to the one present in cellulose active AA9 LPMOs and consistent with a tetragonally distorted octahedral coordination for the Cu(II). Moreover, the addition of substrate (β-chitin) to the enzyme solution did not perturb the Cu(II) EPR parameters like it has been reported for several AA9 and AA10s LPMOs; potential implication for substrate binding are discussed. Lastly, we evaluated potential hole-hopping pathways through the enzyme network of redox active residues, like those found in *Ls*AA9 (**Section 3.4.3**), showing that they are possible also in *Ao*AA11 but appear to be less efficient as compared to those found in AA9 LPMOs.

4.2 Methods

4.2.1 *Ao*AA11 production and purification

The enzyme was produced in *E. coli* BL21* (DE3) competent cells. The cell growth was started in two 50 mL falcon tubes containing 15 mL of Luria-Bertani (LB) medium each, at 37 °C, shaking at 180 rpm, overnight. The following morning, the cell culture was transferred in 3 x 1000 mL LB cultures (inserting 10 mL of cell culture from the smaller falcon tubes) and the cell growth was continued at 37 °C shaking at 180 rpm. The growth was controlled measuring the absorbance of the suspension at 600 nm. At an Abs_{600nm} of 0.4, the temperature was lowered at 16 °C before the addition of isopropyl β-D-1-thiogalactopyranoside (IPTG) to a final concentration of 1 mM when Abs_{600nm}= 0.6–0.8. After the addition of IPTG, the cell culture was left at 16 °C, shaking at 180 rpm overnight.

The following day the cells where harvested by centrifugation at 11,000 *g* for 20 min at 4 °C. The cell paste was resuspended with two volumes of ice-cold Tris HCl 50 mM pH 8.0, 20% w/v sucrose. Afterwards, a 40 µL of 10 mg mL-1 lysozyme was added for every gram of cell paste, together with DNAase-I to a final concentration of 1 µg mL^{-1}; the suspension was incubated on ice for 1 hour, with occasional agitation. At this point, 60 µL of $MgSO_4$ 1 M per gram of cell paste were added to the suspension, which was then left on ice for further 30 min.

The suspension was centrifuged at 10,000 *g* for 20 min at 4 °C and the supernatant removed to a fresh tube. Following the centrifugation, the cell pellet underwent osmotic shock by resuspension in two volumes of ice-cold MilliQ water and was left on ice for 1 hour. The cell debris were removed by centrifugation at 10,000 *g* for 20 min and the supernatant was joined with that from the previous step. The supernatant was then sonicated on ice to reduce viscosity using a MSE Soniprep 150, with 20 seconds of sonic and 90 seconds resting, for 20 minutes. At this point, a small amount of Na−acetate 1 M pH 5.0 was added to the solution in order to lower the pH, before running the cation exchange chromatography. The solution was then concentrated under 50 mL using a VivaSpin 10 kDa molecular weight cut-off concentrator.

The protein solution was passed through a 5-mL HiTrap SP FF (GE Healthcare) column, equilibrated in 50 mM Na−acetate pH 5.0. Solid $(NH_4)_2SO_4$ was then added to the SP-column flow-through, which contained *Ao*AA11, to a final concentration of 1 M. The protein solution was then passed through a 5-mL Phenyl Sepharose HP column (GE Healthcare) equilibrated in 50 mM Na−acetate, 1 M $(NH_4)_2SO_4$ at pH 5.0. The flow-through of the Phenyl Sepharose column was collected and the protein was then precipitated by the addition of solid $(NH_4)_2SO_4$ to 85% saturation at 4 °C. The protein pellet was isolated by centrifugation at 50000 *g* for 20 min and the pallet was redissolved in ten volumes of 20 mM Na−acetate, 250 mM NaCl, pH 5.0. After this step, the solution was concentrated to a total volume of 2 mL, for size-exclusion chromatography on a Hi-Load 16/60 Superdex 75 column (GE Healthcare) equilibrated with 20 mM Na−acetate, 250 mM NaCl, pH 5.0. Before loading the protein solution into the column, the enzyme was copper loaded adding $CuSO_4$ 1 M to the concentrated protein solution to a final concentration of 5 mM $CuSO_4$. Th enzyme peak fractions were pooled together and concentrated by centrifugation on a VivaSpin 10 kDa molecular weight cut-off concentrator. Protein concentration were determined by measuring the $Abs_{280\ nm}$ with extinction coefficient of 25815 M^{-1} cm^{-1} and a molecular weight of 23055.8 Da, as reported in the previous work of Hemsworth *et al*.[37] The purified protein was judged to be >95% pure on SDS-PAGE analysis.

4.2.2 Activity Assays

Squid pen chitin was purchased from Mahtani Chitosan, while Shrimp shell Chitin was purchased from Sigma-Aldrich. Both substrates were washed with water before usage in the activity assays, to remove possible oligosaccharides contaminants. Reactions were set up in 0.5 mL total volume with 2 mg of solid substrate in 10 mM ammonium acetate, pH 6.0, 1 mM ascorbic acid and 1 μM Cu(II)-*Ao*AA11. The samples were incubated at 37 °C, rotating overnight. The tests involving hydrogen peroxide as co-substrate used an H_2O_2 concentration of 10 μM or 100 μM H_2O_2. After the reaction, the remaining solid substrate was removed by centrifugation at 14,000 *g* for 5 min and the supernatant used for the analysis. 1 μL of sample was mixed with 2 μL of 10 mg mL^{-1} 2,5-dihydroxybenzoic acid in 50% *v/v* acetonitrile, 0.1% *v/v* trifluoroacetic acid in water, on a SCOUT-MTP 384 target plate (Bruker). The spotted samples were then dried under a

lamp in air, before being analysed by mass spectrometry on a Ultraflex III matrix-assisted laser desorption ionization–time of flight (MALDI-TOF) instrument (Bruker), as described by Vaaje-Kolstad *et al.*[27] All samples were tested at least in triplicates.

4.2.3 Electronic spectroscopy: UV-vis, CD and MCD

The UV−vis absorption spectra were acquired on a Shimadzu UV-1800 spectrometer. CD spectra were recorded on a Jasco J810 spectropolarimeter. The spectra were recorded at room temperature with 0.5 mM Cu(II)–*Ao*AA11 in 20 mM MES pH 6.0. MCD spectra were recorded on a Jasco J-810 spectropolarimeter adapted to incorporate an Oxford Instruments Spectromag SM4000 magnetocryostat (MCD spectra were collected at the University of Nottingham). The samples were loaded into cells of ca. 2 mm path length constructed from quartz discs separated by a rubber ring spacer and frozen in liquid nitrogen. The spectra were collected at ±3, ±5 and ±7 T magnetic field and with temperatures between 5 and 15 K. The sample composition was: Cu(II)–*Ao*AA11 1.40 mM, 55% v/v glycerol, in MES 20 mM pH 6.0. Glycerol was used as glassing agent and its addition to the enzyme solution did not alter CD spectrum of the enzyme.

After the Gaussian deconvolution of UV-vis and MCD spectra of each sample, the C_0/D_0 ratio for each transition was determined with the following equation:

$$\frac{C_0}{D_0} = \frac{kT\ A_{MCD}}{\beta B\ A_{UV-}}$$

were A_{MCD} is the area under the MCD band, A_{UV-vis} is the area under the absorption band, k is the Boltzmann constant, β is the Bohr magneton and T and B are the temperature and the field at which the MCD spectra was recorded, respectively.

4.2.4 EPR Spectroscopy

CW X-band EPR spectra were acquired on a Bruker micro EMX spectrometer operating at ~9.30 GHz with a modulation amplitude of 4 G, modulation frequency of 100 kHz, and microwave power of 10.02 mW. The spectra reported are the summation of 3 scans and were recorded at 160 K. Enzyme concentration was 0.3 mM in MES 20 mM pH 6.0. The sample with the substrate was obtained by direct addition of solid squid pen chitin into the *Ao*AA11 solution. CW Q-band spectra were acquired on a Jeol JES-X320 spectrometer operating at ~34.7 GHz, with modulation width 0.8 mT and microwave power of 1.0 mW (8 scans). *Ao*AA11 concentration was 2 mM in MES 20 mM pH 6.0. Spectral simulations were carried out using EasySpin 5.2.21[117] integrated into MATLAB R2016b software. The spectra were simulated on the basis of a spin Hamiltonian description of the electronic ground state with $S = {}^1/_2$. Anisotropy between g_1/g_2 (namely degree of rhombicity) was quantified as R_g according to the following equation:[118]

$$R_g = \frac{2(\Delta g_2 - \Delta g_1)}{\Delta g_2 + \Delta g_1}$$

Simulation parameters are given in **Table 4.1**. g_3 and $|A_3|$ values were determined accurately from the absorptions at low magnetic field. It was assumed that g and A tensors were axially coincident. Accurate determination of the g_1, g_2, $|A_1|$ and $|A_2|$ was obtained by simultaneous fitting of both X- and Q-band spectra.[200] The superhyperfine coupling values for the nitrogen atoms could not be determined accurately, although it was noted that satisfactory simulation could only be achieved with the addition of two nitrogen atoms with the coupling values reported in **Table 4.1**.

Table 4.1 EPR spin Hamiltonian parameters from simulations of cw X-band and cw Q-band spectra, collected at 165 K and 113 K respectively.

Parameter		*Ao*AA11	
		X-band	Q-band
g values	g_1	2.042 (±5)	2.043
	g_2	2.073 (±5)	2.073
	g_3	2.276 (±2)	2.276
A^{Cu} (MHz) [1]	A_1	75	70
	A_2	40	40
	A_3	457	457
A^N (MHz) [1]		35, 45 (±5)	35, 35
H strains (MHz)		10, 15, 50	10, 15, 50
Line widths (Gaussian, Lorentzian)		1.2, 1.2	6.0, 6.0

[1]-The sign of the hyperfine coupling cannot be determined from the simulations, therefore they are all reported as positive. The nitrogen ligands are reported as single values as it is not possible to determine their anisotropicity from the experimental spectra; each reported value corresponds to a different nitrogen atom and is presumed to be the major axial coupling from nitrogen to the Cu(II). Estimated experimental errors are: ±0.005 for g_1/g_2; ±0.002 for g_3; ±5 MHz for A_1/ A_2; ±2 MHz for A_3 and ±5 MHz for A^N.

4.2.5 Theoretical Methods

Density Functional Theory (DFT) calculations were performed using the ORCA 4.0 Software package.[119] The starting point for the geometry optimized model of the Cu active site was obtained from the coordinates of the *A. orizae* crystal structure (PDB: 4MAI) and included seven amino acids residues (His-1, Pro-19, Ser-57, Ala-58, His-60, Glu-138, Tyr-140) with the following modifications: Carbonyl of His-1 and Pro-19 is replaced by a methyl group; the side chains of His-60, Glu-138 and Tyr-140 are truncated by methyl substitution of the Cβ. Ser-57 and Ala-58 form a chain truncated at the Cα and at the amide nitrogen of Ser-57 and Ala-58, respectively. Other than the residues that form the Cu first coordination sphere, the Ala-58 and Glu-138 residues were included because they are conserved in the AA11, hence probably important in determining the active site electronic structure (Glu-138 is H-bonded to the axial Tyr). The Pro-19 residue was found to be important in keeping the His-1 imidazole ring in the correct position during geometry optimizations. The Ser-57 residue, even if not strictly conserved in the AA11 family, was included because its side chain is located close to the Cu axial position

and therefore possibly important in H-bonding the other axial Cu ligand (likely to be an H_2O molecule in solution). Moreover, the Cu coordinating Glu residue from a different *Ao*AA11 molecule in the crystallographic lattice was initially included as well to better reproduce the Cu environment of the X-ray structure. This residue was then removed, in the following optimizations. During the geometry optimization, several atoms were kept fixed at their crystallographic position, as indicated in **Figure 4.4**. All the optimization were performed with the uBP86 functional (with RI approximation),[120] Def2-TZVP basis set on Cu and ligating atoms, and Def2-SVP on all of the remaining atoms;[121] empirical dispersion correction were accounted for using Grimme's D3 method with Becke−Johnson damping (D3BJ);[122] solvation effects were included with the conductor-like polarizable continuum model (CPCM, $\varepsilon = 4.0$). The CPCM model is a standard choice for cluster models calculations with DFT and was already successfully applied in previous studies on AA9 LPMOs active site.[63,103] The coordinates for all optimized models can be found in **Appendix 2**.

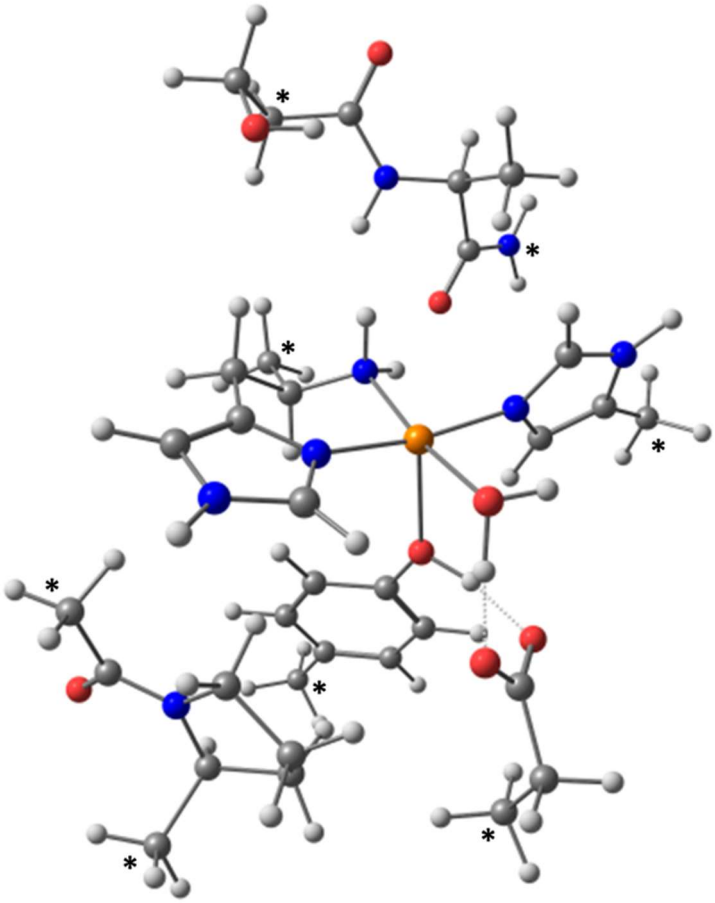

Figure 4.4 Cluster model of the *Ao*AA11 active site. Atoms with fixed coordinates during the geometry optimization are indicated with asterisks.

EPR properties were calculated at the DFT level of theory using B3LYP functional or B3LYP with 38% Hartree-Fock exact exchange (see discussion in **Section 2.3.4.1** for the choice of the functional).[123] The copper ion was described with the CP(PPP) basis set;[124] the amino terminus nitrogen atom, the coordinating water molecules and all the atoms on the imidazole rings where described with the IGLO-III basis set;[125] all the remaining atoms were treated with the Def2-SVP basis set. The integration grid was kept large thorough all the calculations (AngularGrid = 7 for all the atoms and IntAcc = 6 on the Cu(II) ion) to ensure that the core density was correctly described. Solvation effects were included with the conductor-like polarized continuum model (CPCM, ε = 4.0) as implemented in ORCA.

The *g* matrix was calculated through the solution of the coupled perturbed Kohn-Sham equations, as implemented in ORCA.[126] The origin was chosen as the centre of the electronic charge.[127] The calculations include the relativistic mass correction,

diamagnetic spin-orbit, and paramagnetic spin orbit terms. The hyperfine coupling calculations include the Fermi-contact term, the spin–dipolar contribution and the spin–orbit coupling correction (SOC) for the Cu(II) and the halides ions. The paramagnetic SOC term was calculated with the spin–orbit mean field concept (SOMF(1X) in ORCA).[128] The calculation of the nitrogen hyperfine tensors only included the first order terms, since SOC corrections are small for light ligand nuclei.[129,130]

Exited states calculations were performed with TD-DFT and CASSCF methods. The TD-DFT UV-vis spectra were calculated using the Tamm−Dancoff approximation,[131] the CAM-B3LYP functional,[132] the Def2-TZVP basis set on all atoms, together with the RIJCOSX approximation with a dense integration grid (ORCA Grid 5).[133]

The CASSCF method[134] was employed for calculation of the ligand field transition energies, together with the Def2-TZVP basis set on all the atoms in the models.[135] A minimal active space CAS(9,5), comprising only d-electrons was used in the calculation, together with the NEVPT2 methodology[136] to capture the effect of dynamic electron correlation. The effect of spin orbit coupling were considered using the spin–orbit mean-field (SOMF) approximation,[128] as implemented in ORCA. As an initial guess to the CASSCF calculations, the quasi-restricted orbitals (QROs) from DFT calculations (B3LYP/Def2-TZVP) were employed.[137]

4.3 Results

4.3.1 *Ao*AA11 enzymatic activity

After production and purification from *E. coli* the *Ao*AA11 LPMO was first tested for activity using β-chitin, the previously reported substrate for this enzyme.[37] The activity assays were prepared incubating the Cu-loaded enzyme with squid pen chitin (a very pure form of β-chitin) and Na−ascorbate as reducing agent, at 37 °C for 16 hours. The soluble products released in solution were then analysed by MALDI-TOF mass spectrometry. *Ao*AA11 resulted active on this substrate as expected, confirming that the purification procedure produced yielded a functional form of the enzyme. The product masses

(detected as Na^+ adducts in the MALDI-TOF conditions) are consistent with C1-oxidized (aldonic acid) chito-oligosaccharides with slightly higher abundance for even number degrees of polymerization (DP = 4, 6, 8, 10…), together with their respective native (non-oxidized) forms (**Figure 4.5**). Moreover, from the mass spectrum it is also evident the presence of species with a mass of −2 Da with respect to the native oligosaccharide, which could be assigned as unopened lactones in equilibrium with the aldonic acid (opened form) or as C4-oxidized (cheto-aldose) products (**Figure 1.7**). It should be noted that the hydrated form (gemdiol) of the 4-keto sugar has identical mass to the aldonic acid product, but because the aldonic acid is negatively charged, it tends to form double adducts with sodium in the MALDI-TOF conditions.[201] These Na^+ double adducts are indeed detected (**Figure 4.5**), therefore excluding a regiospecific C4-oxidation only for *Ao*AA11.

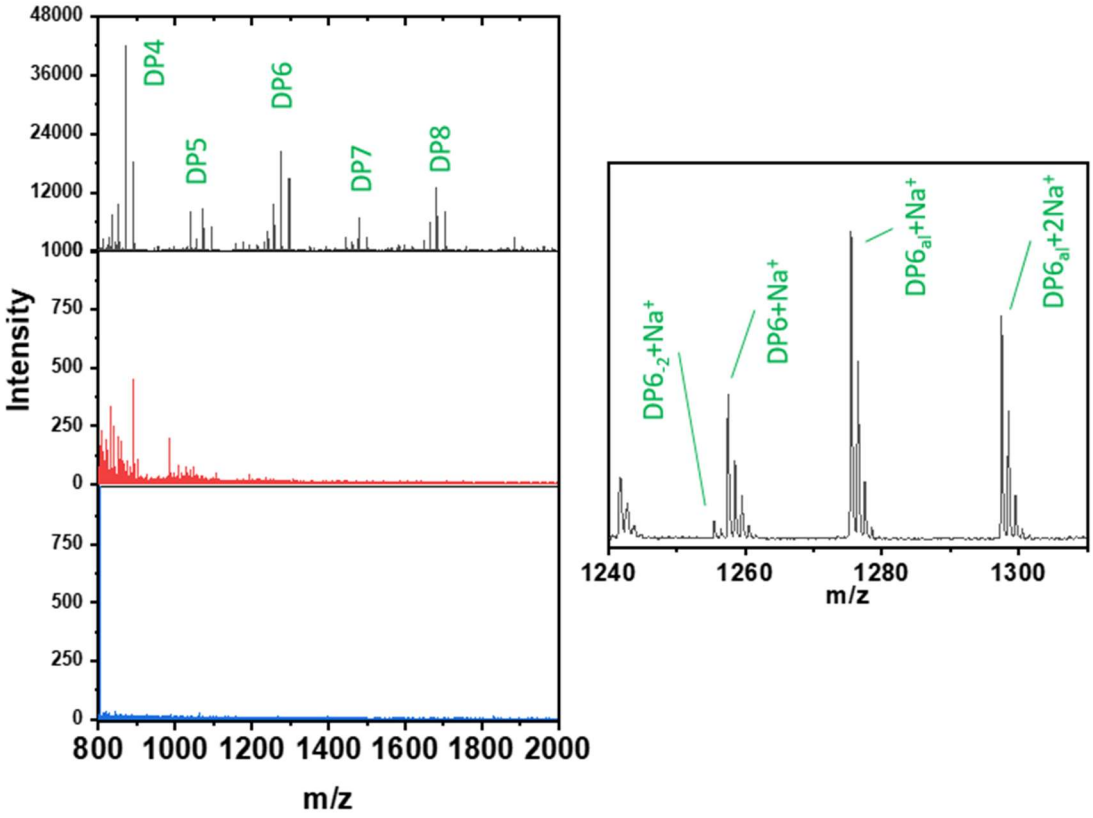

Figure 4.5 MALDI-TOF analysis of *Ao*AA11 activity on squid pen chitin (*β*-chitin): squid pen chitin + Na−ascorbate and *Ao*AA11 (black); squid pen chitin + *Ao*AA11 (red); squid pen chitin + Na−ascorbate (blue) (left). Expanded DP6 region of the spectrum for the black trace (right). Reactions were performed with 0.2% w/v squid pen chitin, 1 µM *Ao*AA11 and 1 mM Na−ascorbate, in 10 mM ammonium acetate at pH 6.0, 37 °C. DPn_{al}, aldonic acid; DPn_{-2} oxidation from R−OH to R=O (measured molecular weight). DP5/$DP5_{-2}$ + Na^+ (1056.4/1054.4), $DP5_{al}^-$ + Na^+ (1072.4), $DP5_{al}^-$ + $2Na^+$ (1094.4); DP6/$DP6_{-2}$ + Na^+ (1259.5.4/1257.5), $DP6_{al}$ + Na^+ (1275.5.4), $DP6_{al}^-$ + $2Na^+$ (1297.5); DP7/$DP7_{-2}$ + Na^+ (1462.6/1460.6), $DP7_{al}$ + Na^+ (1478.6), $DP7_{al}^-$ + $2Na^+$ (1500.6); DP8/$DP8_{-2}$ + Na^+ (1665.6/1663.6), $DP8_{al}$ + Na^+ (1681.6), $DP8_{al}^-$ + $2Na^+$ (1703.6).

The activity test was repeated in presence of hydrogen peroxide to test the ability of *Ao*AA11 to use H_2O_2 as co-substrate for chitin oxidation instead of O_2. In the absence of reducing agent, no reaction products were detected with MALDI-TOF, suggesting that the Cu(II) form of the enzyme and H_2O_2 alone cannot sustain the catalytic activity. This test was repeated at more basic pH (8.0) to increase the reducing power of H_2O_2 and activate the Cu(II) state to the reactive Cu(I) state as already seen for the *Ls*AA9 LPMO (see **Chapter 3**), but again no products were observed. Moreover, even when small amounts of Na–ascorbate (10 times less than the amount H_2O_2) were added to the reaction mixture to 'prime' the enzyme (reducing the Cu(II) resting state to the reactive Cu(I)), still no oligosaccharides were detected in mass spectrometry (**Figure 4.6**). This particular

reaction condition, with low amount of reducing agent, was found to be optimal for activity of several AA10 LPMOs with H_2O_2 by Bissaro *et al*.[29] Together these two results suggest that in the reaction conditions employed here, hydrogen peroxide is not a co-substrate for *Ao*AA11 in the oxidation of *β*-chitin.

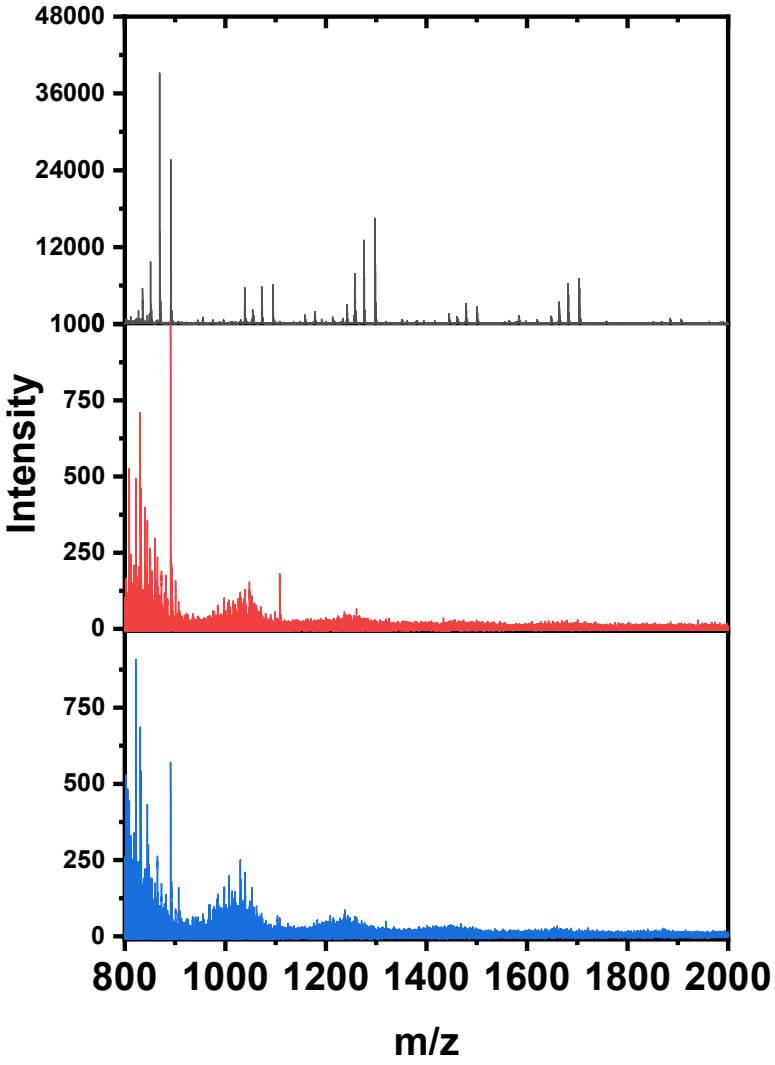

Figure 4.6 MALDI-TOF analysis of *Ao*AA11 activity on squid pen chitin with H_2O_2: squid pen chitin + Na−ascorbate and *Ao*AA11 as control reaction (black); squid pen chitin + *Ao*AA11 + H_2O_2 (red); squid pen chitin + Na−ascorbate + H_2O_2 + *Ao*AA11 (blue). Reactions were performed with 0.2% w/v squid pen chitin, 1 µM *Ao*AA11 and 10 µM Na−ascorbate, 100 µM H_2O_2 in 10 mM ammonium acetate at pH 6.0, 37°C. DPn_{al}, aldonic acid; DPn_{-2} oxidation from R−OH to R=O (measured molecular weight). DP5/$DP5_{-2}$ + Na^+ (1056.4/1054.4), $DP5_{al}^-$ + Na^+ (1072.4), $DP5_{al}^-$ + $2Na^+$ (1094.4); DP6/$DP6_{-2}$ + Na^+ (1259.5.4/1257.5), $DP6_{al}$ + Na^+ (1275.5.4), $DP6_{al}^-$ + $2Na^+$ (1297.5); DP7/$DP7_{-2}$ + Na^+ (1462.6/1460.6), $DP7_{al}$ + Na^+ (1478.6), $DP7_{al}^-$ + $2Na^+$ (1500.6); DP8/$DP8_{-2}$ + Na^+ (1665.6/1663.6), $DP8_{al}$ + Na^+ (1681.6), $DP8_{al}^-$ + $2Na^+$ (1703.6); DP9/$DP9_{-2}$ + Na^+ (1868.4/1866.4), $DP9_{al}$ + Na^+ (1884.4), $DP9_{al}^-$ + $2Na^+$ (1906.4).

To test the ability of *Ao*AA11 to degrade a different form of crystalline chitin, shrimp shell chitin was used as a form of α-chitin. In this case, it was possible to detect some soluble oligosaccharides in solution after the enzymatic treatment, but only in their native form without the corresponding oxidised forms. This is consistent with the weak background hydrolytic activity reported also for other AA9 LPMOs like *Hj*AA9 and *An*AA9.[46,202] However, no oxidative degradation is performed by *Ao*AA11 on *α*-chitin.

4.3.2 EPR Spectroscopy

The EPR transitions arising from the principal components of the *g* tensor are field dependent while the splitting patterns observed within these transitions due hyperfine interactions are not field dependent, therefore the frozen solution EPR spectrum of Cu(II)–*Ao*AA11 recorded at two different frequencies, X-band (~9.3 GHz) and Q-band (~34 GHz), gives more precise values for the Cu(II) spin Hamiltonian parameters (**Table 4.2**). The obtained X- and Q-band spectra have a near-axial envelope, typical for tetragonal type 2 copper sites (Peisach-Blumberg classification)[85] with $g_3 > g_{1,2} > 2.0$ indicating a mainly $d(x^2-y^2)$ ground state SOMO (**Figure 4.7**). The Cu hyperfine coupling is well resolved only in the parallel direction (g_3 direction) and simulation of the spectra yielded a $g_3 = 2.276$ and $|A_3^{Cu}| = 457$ MHz. The multi-frequency simulations also gave accurate values for $g_1 = 2.042$ and $g_2 = 2.073$, revealing some anisotropy in the perpendicular directions (with rhombicity R_g=0.56), and for the respective $|A_1^{Cu}| = 75$ MHz and $|A_2^{Cu}| = 40$ MHz. The obtained spin Hamiltonian parameters are very similar with those typical for AA9 LPMOs resting states, in agreement with their similar Cu active site structures.

On the other hand, the superhyperfine coupling (SHF) due to the ligating nitrogen atoms is not resolved and prevents an accurate determination from continuous wave EPR only. Notwithstanding the lack of resolution, inclusion in the simulations was necessary to better fit the overall line shape of the spectrum. Two N atoms with an estimated coupling of ~35 MHz were included in the simulations, a typical SHF coupling value for imidazole nitrogen atoms coordinated to Cu(II) ions.[139] It should be noted that the coupling with these ligands were simulated as isotropic even if this coupling is expected to be anisotropic with the largest component alongside the bond direction (see also

Section 4.3.5 on DFT calculations). The lack of resolution prevents any estimate of the degree of anisotropy.

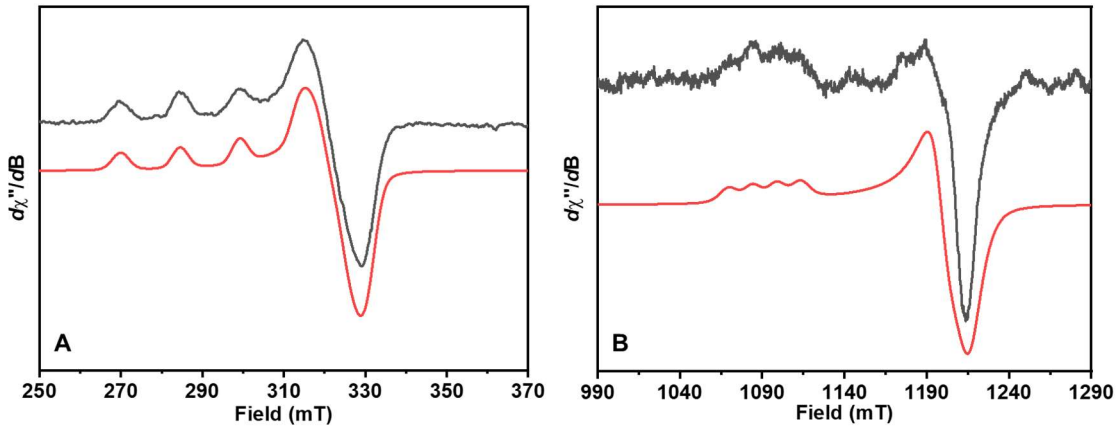

Figure 4.7 X-band EPR spectrum of Cu(II)–*Ao*AA11 at 160 K. Enzyme concentration was 0.3 mM in 20 mM MES pH 6.0 (left). Q-band EPR spectrum of Cu(II)–*Ao*AA11 at 77 K. Enzyme concentration was 2 mM in 20 mM MES pH 6.0 (right). The experimental spectrum is shown in black together with the corresponding simulation shown in red. Simulation parameters are reported in **Table 4.2**.

Table 4.2 Experimental *g* and *A* values for Cu(II)−*Ao*AA11 derived from simulation of frozen solution multifrequency (X- and Q-band) CW EPR spectra. *A* values are reported in MHz.

g_1	g_2	g_3	R_g [1]	A_1^{Cu} [2]	A_2^{Cu} [2]	A_3^{Cu} [2]	A^N [3]	
2.042	2.073	2.276	0.56	75	40	457	35	35

[1]-Rhombicity: $R_g = 2(\Delta g_2 - \Delta g_1)/(\Delta g_1 + \Delta g_2)$; $\Delta g_i = g_i - g_e$.

[2]- Signs of the hyperfine coupling cannot be determined from the simulations, so only their magnitude $|A|$ is reported. Estimated experimental errors are reported in **Table 4.1**.

[3]- The N atoms hyperfine coupling is reported as single values because the experimental spectra are not resolved enough to allow estimation of their anisotropicity. Estimated error for A^N are ±5 MHz

Addition of solid squid pen chitin (*β*-chitin) directly into the solution of *Ao*AA11 does not perturb the X-band EPR spectrum of the resting state, as the two spectra are basically identical (**Figure 4.8**). From this point of view, the enzyme behaves differently with respect to other previously characterised LPMOs from the AA9 and AA10 families where

substrate biding significantly perturbed the Cu(II) resting state spectrum.[65,77] In this case, it is clear, that the lack of spectroscopic perturbation does not imply a lack of activity on a certain substrate: the enzymatic activity on *β*-chitin is evident from the MALDI-TOF results. Indeed, two recent publications reported a similar effect in two different AA9 LPMOs *Hj*AA9A[59] or *Ta*AA9 [203] where activity on cellulose and the binding of the enzyme on the crystalline substrate were demonstrated, but the corresponding EPR spectrum did not show any perturbation upon interaction with the substrate.

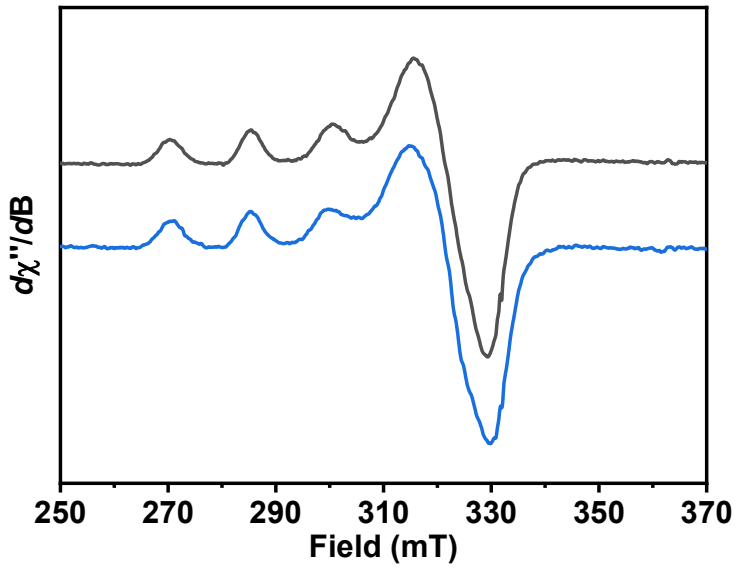

Figure 4.8 X-band EPR spectrum of Cu(II)–*Ao*AA11 recorded at 160 K in absence (black) and in presence (blue) of squid pen chitin. Enzyme concentration was 0.3 mM, in 20 mM MES pH 6.0. Solid chitin was directly added into the sample, until it completely covered the sample solution.

4.3.3 Electronic Spectroscopy: UV-vis/CD/MCD

A combination of UV-vis, circular dichroism and magnetic circular dichroism measurements were carried out with the aim of determining the d-d and charge transfer (CT) exited states transition energies. In particular, the ligand field (d-d) states are relevant for the interpretation of the EPR parameters of the *Ao*AA11 resting state. In UV-vis spectroscopy the dipole disallowed d-d transitions have very weak intensities (ε ~50–100 cm^{-1}) and are generally not well resolved for Cu(II) complexes.[91,140] On the other

hand, in MCD spectra d–d transitions are generally more intense than CT transitions and, being a signed quantity, MCD spectroscopy is able to better resolve these bands allowing the assignment of spectral features to individual d–d transitions.[140,141] This assignment is best performed by a simultaneous fitting of the UV-vis, CD and MCD spectra with Gaussian bands in order to obtain the maximum amount of information for a particular sample. As such, room temperature UV-vis, CD and low temperature (5 K) MCD spectra of the enzyme resting state were collected (**Figure 4.9**). The energies of identified transitions were allowed to vary on the order of few hundreds wavenumbers in the MCD relative to the CD and UV-vis spectra due to the difference in temperature at which they were collected and because of the overall broad band shapes, which lower the resolution. Overall, the error in the energy of the bands was estimated in the order of ±100 cm^{-1}. The results are reported in **Table 4.3** together with possible bands assignments. The bands were assigned on the basis of their energy, C_0/D_0 ratio and field/temperature dependence of the MCD spectrum, together with the results of the CASSCF and TD-DFT calculations (see **Section 4.3.6**).

Table 4.3 Gaussian band energies (cm^{-1}) for the fitting of the UV-vis, CD and MCD spectra of Cu(II)–*Ao*AA11, together with the respective C_0/D_0 ratio and assignment.

Band	UV-vis	CD	MCD	C_0/D_0	Assignment
1	12780	12700	12470	0.101	$d_{z^2} \rightarrow d_{x^2-y^2}$
2	14520	14560	14150	0.062	$d_{xz} \rightarrow d_{x^2-y^2}$
3	16400	16430	16150	0.227	$d_{yz} \rightarrow d_{x^2-y^2}$
4	18210	18160	18400	0.020	$Tyr \rightarrow d_{x^2-y^2}$
5	28540	28430	28860	0.008	CT
6	30820	30870	30920	0.009	CT

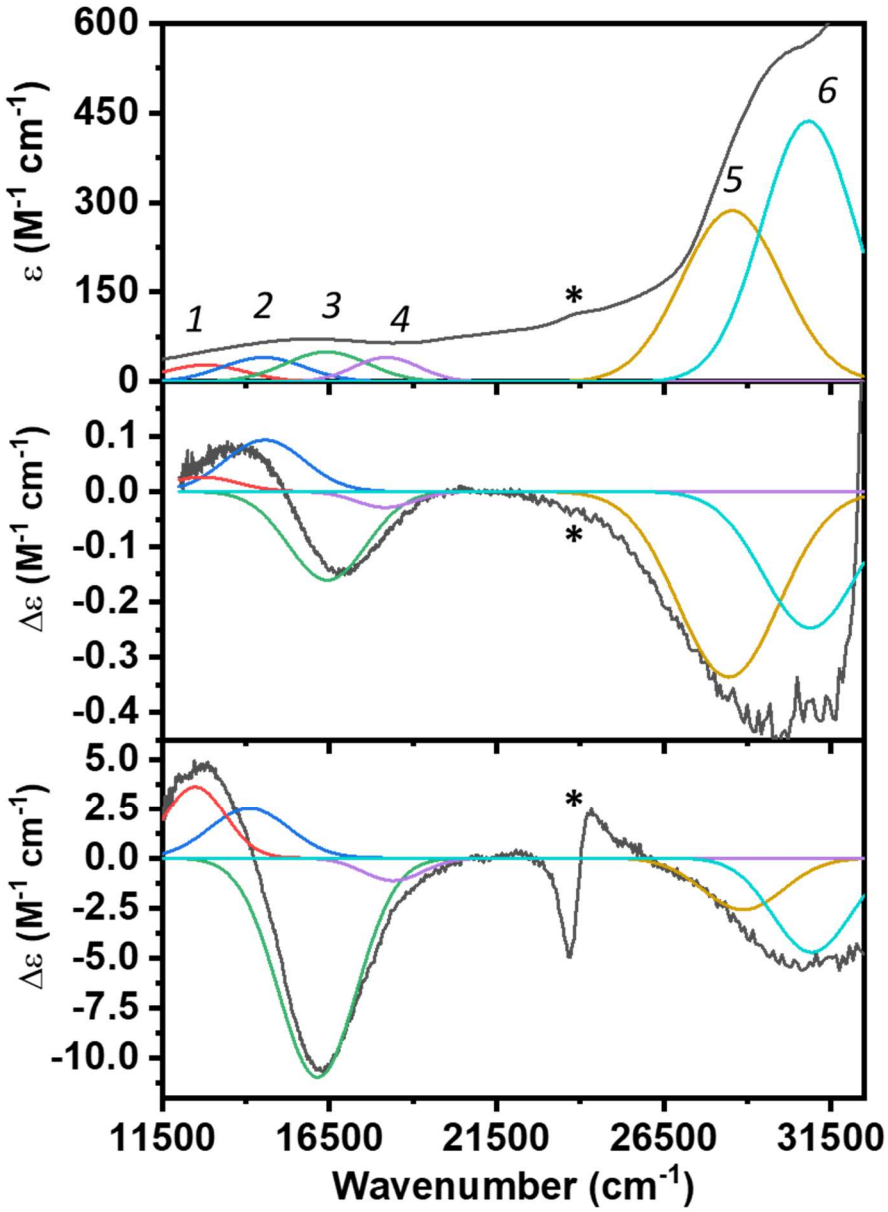

Figure 4.9 Room temperature UV-vis (top), CD (middle) and low temperature, 5 K, 7 T MCD (bottom) spectra of Cu(II)-*Ao*AA11, together with their Gaussian bands fitting. Experimental data are shown in black while peak fits as coloured lines. Enzyme concentration was 1.40 mM, 55% v/v glycerol, CAPS 50 mM, pH 10.0. The numbering of the individual transitions follows the numbering reported in table **Table 4.3**. The feature denoted by an asterisk at ~24000 cm^{-1} is due to a small heme contaminant where not considered in the fitting process.

The UV-vis spectrum shows a broad and asymmetric feature centred at ~16000 cm^{-1} (600 nm) with estimated ε around 70–75 M^{-1} cm^{-1}, typical for d–d transitions, and a more intense shoulder at higher energy ~30000 cm^{-1} and ε ~550 cm^{-1} more consistent with a weak charge transfer transition (**Figure 4.9**). The MCD spectrum displays a positive and a negative absorption band in the ligand field region at ~14500 cm^{-1} and ~16400 cm^{-1} respectively (bands *2* and *3*). This particular feature is typical for mononuclear Cu

complexes and is referred to as pseudo-*A* term, composed of two opposite sign *C*-term features assigned to d(xz/yz)→d(x^2–y^2) ligand field transitions which can spin–orbit couple.[91,142,143] Moreover bands *1*, *2* and *3* gain substantial MCD intensity with respect to bands *5* and *6*, consistent with their assignment as ligand field and charge transfer transitions, respectively (see **Table 4.3** for C_0/D_0 ratios). These bands are directly proportional to the intensity of the applied magnetic field, confirming that the measured circular dichroism is induced by the magnetic field, but inversely proportional to temperature, therefore classifying them as MCD *C*-terms (**Figure 4.10**).[140] Overall, the obtained transitions are similar to those already obtained for the *Ls*AA9 Cu(II) resting state.

The electronic spectra show evidence for a band at ~18200 cm^{-1} (*4* in **Figure 4.9**) with low intensity in the UV-vis spectrum (ε ~70 M^{-1} cm^{-1}) and which does not gain much intensity in the MCD spectrum, like the other d-d transitions. On the basis of its low C_0/D_0 ratio band *4* is classified as charge transfer transition and following the results obtained in **Chapter 2** for *Ls*AA9, it is tentatively assigned as Tyr → Cu(II) LMCT originating from the axial Tyr-140 residue (see also the discussion about the calculated spectra with TD-DFT below, **Section 4.3.6.1**).

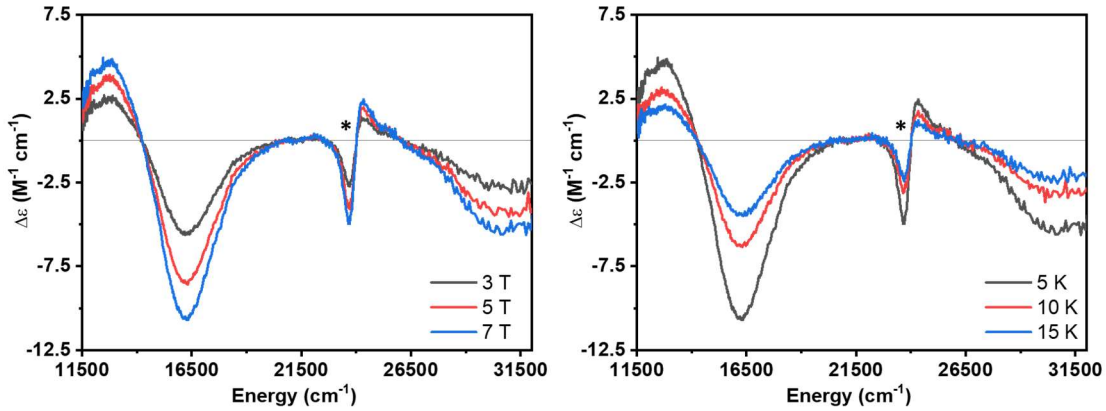

Figure 4.10 Field dependence at 5K (A) of the Cu(II)–*Ao*AA11 MCD spectrum, recorded at 3 T (black), 5 T (red) and 7 T (blue). Temperature dependence at 7 T (B) of the Cu(II)–*Ao*AA11 MCD spectrum, recorded at 5 K (black), 10 K (red) and 15 K (blue). Enzyme concentration was 1.40 mM, 55% v/v glycerol, MES 50 mM, pH 6.0. The asterisk marks a derivative shaped feature at ~24000 cm^{-1} due to a small heme contaminant.

4.3.4 Theoretical Calculations: Geometry Optimization

In order to obtain more insight into the electronic and structural origins of the spectroscopic features of the enzyme resting state, a series of DFT and CASSCF calculations were performed on the active site region of *Ao*AA11. To study the active site, the same cluster model approach already employed for the study of *Ls*AA9 in **Chapter 2** and **Chapter 3,** was applied also for this enzyme. The starting point for the modelling of the active site region was the X-ray crystal structure of *Ao*AA11 published by Hemsworth *et al*. (PDB 4MAI).[37]

The active model included the two histidine residues coordinating the copper ion, His-1 and His-60, the tyrosine residue in the Cu 'axial position' (Tyr-140), the glutamate that is hydrogen bonded to Tyr-140 and which is conserved across the AA11 family; the distal alanine (Ala-58, conserved in the family as well) and serine (Ser-57) which are close to the other Cu axial position and finally the proline (Pro-19) residue positioned directly below imidazole ring plane of His-1 (see **Figure 4.11**). In the crystal structure, a glutamate side chain from another *Ao*AA11 molecule in the crystal lattice occupied the axial position *trans* to Tyr-140 and coordinates the Cu, therefore this side chain was initially included in the model as well (Model1). The geometry was then optimized at the DFT level of theory, using BP86 as functional, the Def2-TZVP basis set for the Cu and the ligating atoms, and Def2-SVP on all other atoms. The copper ion in the structure is best described as Cu(I) as redox state, therefore the geometry was optimized for this redox state. The optimized geometry is in very good agreement with the X-ray structure, without unreasonable distortions as shown in **Figure 4.11** (see also **Table 4.4** for a comparison of few selected copper bond distances). The root mean square deviation (RMSD) for of the calculated Cu–ligand bond distances Model1 with respect to the experimental distances is 0.09 Å, with the largest variations observed for the Cu–O(Tyr) distance. It should be noted that for the resting state structure (4MAI) the resolution of 1.4 Å, a good resolution for typical protein structures, allows to estimate a bond distance RMSD of ~0.1–0.2 Å.[151] However, this value includes the entire protein and does not necessarily apply to the metal active site, where it could be even larger.[152]

The Cu(I) state is characterised by a Cu–NH_2 bond distance (2.1 Å) longer than the two Cu–N(His) bonds (1.9–2.0 Å), in agreement with the crystal structure. The Cu–O(Tyr) distance (3.08 Å and 3.2 Å in the optimized model and X-ray structure, respectively) is also longer as compared to the range typically found in LPMOs (between

2.5–2.8 Å) and probably due to the influence of the exogenous Glu side chain in the other axial position.

Table 4.4 Selected bond distances (Å) and angles (°) for the various optimized geometries, together with the corresponding metrics from the *Ao*AA11 crystal structure (PDB 4MAI, resolution 1.4 Å) as comparison.

Models	Cu–NH_2	Cu–N_δ	Cu–N_ε	Cu–O(Tyr)	Cu–O(Glu)	Cu–H_2O_{eq}	N_δ–Cu–N_ε(°)	NH_2–Cu–H_2O_{eq}(°)
4MAI	2.2	1.9	2.0	3.2	2.3	-	159	-
Cu(I)–Model1	2.12	1.97	1.93	3.08	2.39	-	145	-
Cu(I)–Model2	2.19	1.93	1.91	2.49	-		160	-
Cu(II)–Model3	2.06	1.98	1.98	2.30	-	2.07	167	170
Cu(II)–Model4	2.05	1.99	1.99	2.30		2.07	167	170

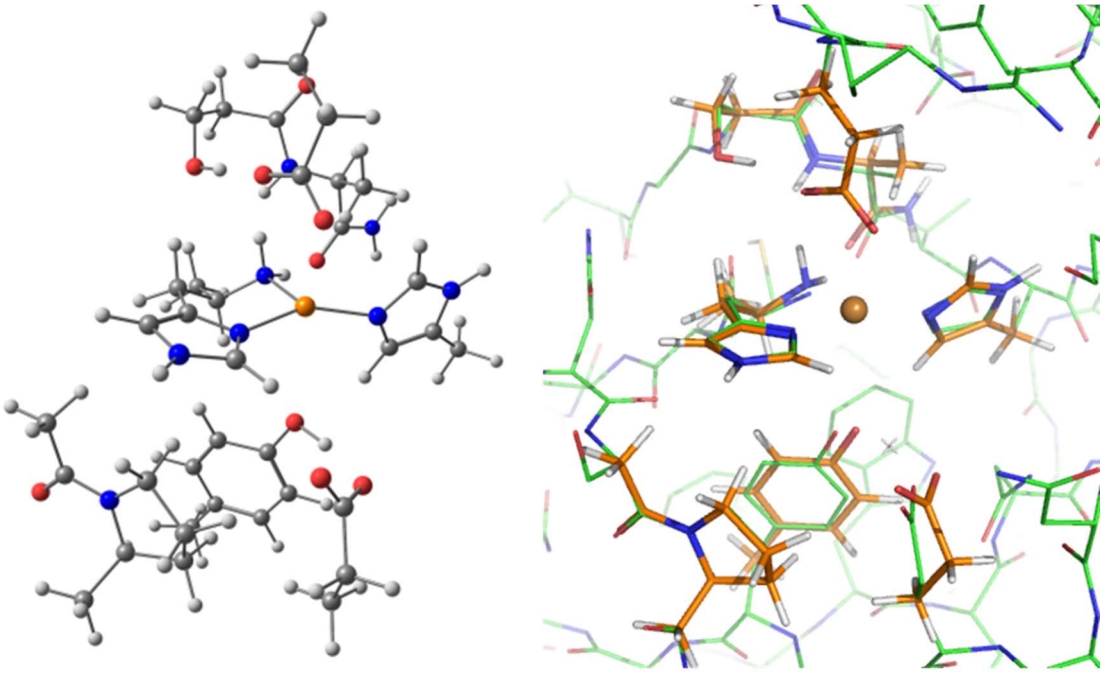

Figure 4.11 DFT-optimized structure of the *Ao*AA11 Model1 (left) and the overlay of the optimized geometry (orange) with the crystal structure of *Ao*AA11 (green), PDB 4MAI (right). The Cu ion is represented as gold sphere.

As the copper coordination by the exogenous glutamate side chain does not exist in solution (the enzyme is monomeric,) to obtain a more realistic model for the Cu(I) state of *Ao*AA11 the geometry was re-optimized after the removal of this extra Glu residue (Model2): the result is shown in **Figure 4.12**. Some small rearrangements are observed, where the overall geometry moves towards a flatter T-shaped coordination with a N_{δ}–Cu–N_{ε} angle of 160° with respect to 145°, observed in the previous model (**Table 4.4**). In terms of Cu bond distances, the only significant change is the Cu–O(Tyr-140) which shortens to 2.49 Å from 3.08 Å, consistent with the removal of the glutamate interaction in *trans* to the Tyr residue. This length now falls in the typical Cu–O(Tyr) range found in AA9 LPMOs (2.5–2.8).[8,57]

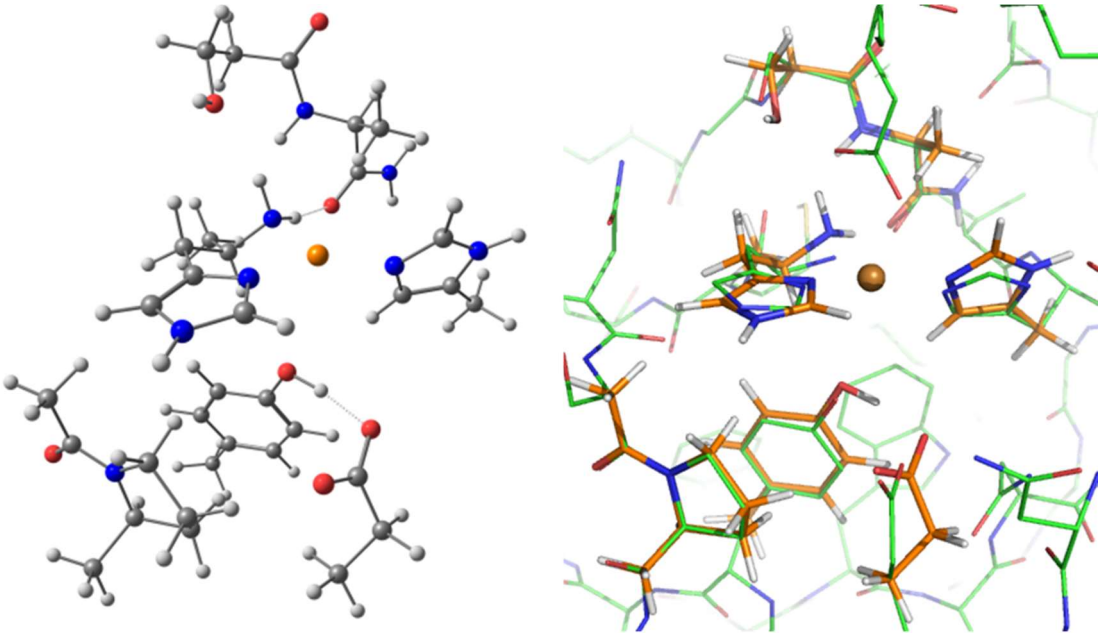

Figure 4.12 DFT-optimized structure of the *Ao*AA11 Model2 (left) and the overlay of the optimized geometry (orange) with the crystal structure of *Ao*AA11 (green), PDB 4MAI (right). The Cu ion is represented as a gold sphere.

The spectroscopic characterisation of *Ao*AA11 was performed on the Cu(II) resting state, therefore it was necessary to generate a DFT model also for the Cu(II) redox state. This was obtained staring from the Cu(I)–Model2 geometry and optimizing it for the Cu(II) state. In other characterised LPMOs Cu(II) X-ray structures an exogenous H_2O molecule in the equatorial plane of the His brace completes the copper coordination sphere, while a second H_2O molecule is often (but not always) found in the axial position *trans* to the tyrosine (as already seen for the *Ls*AA9 resting state); therefore two different Cu(II) models were tested: one starting with a single H_2O molecule in equatorial position (Cu(II)–Model3) and one with two H_2O molecules, in both the equatorial and axial position (Cu(II)–Model4). The resulting optimized geometries are shown in **Figure 4.13**.

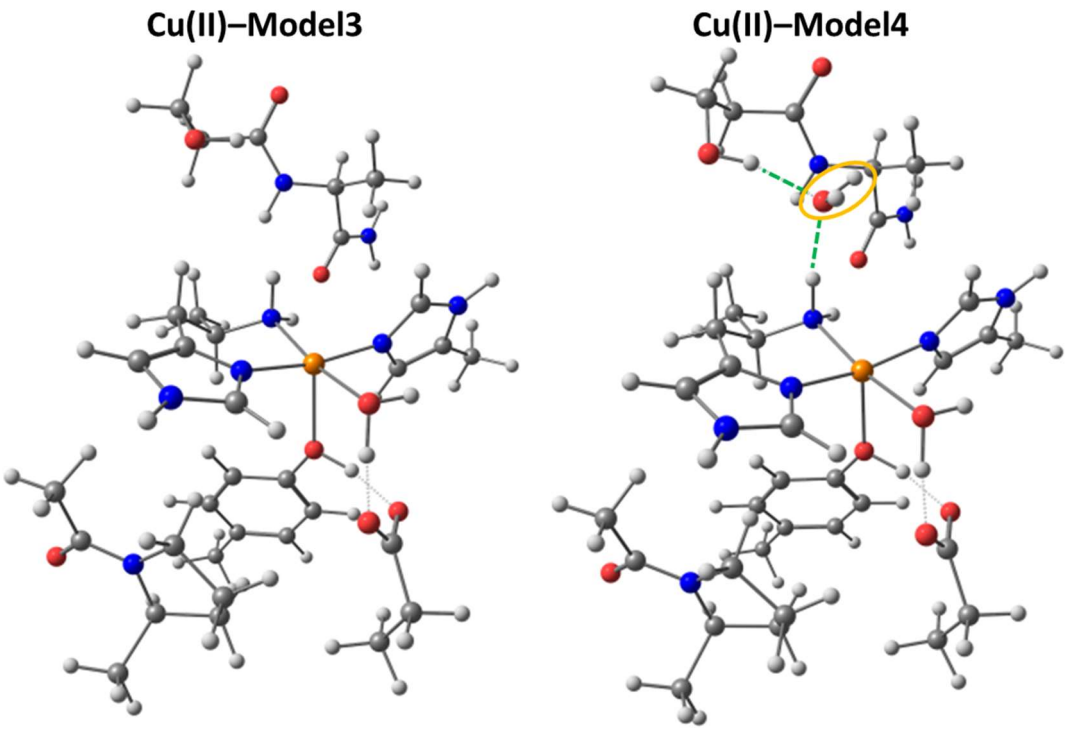

Figure 4.13 DFT-optimized structures of the *Ao*AA11 Model3 (left) and Model4 (right). In Model4, the water molecule that hydrogen bonds with the Ser residue and the amino terminus is highlighted in orange, while the two H-bonds are indicated in green.

In Model3, an almost flat equatorial coordination plane is obtained, with bond angles of 167° and 170° for N_{δ}–Cu–N_{ε} and NH_2–Cu–H_2O_{eq}, respectively (**Table 4.4**). The Cu–NH_2 shortens by ~0.1 Å and the two Cu–N(His) bonds elongate by 0.05–0.08 Å as compared to the reduced state. The Tyr-140 residue moves closer to the copper, with a Cu–O(Tyr) distance of 2.30 Å, slightly shorter with respect to the ones found in the resting state of AA9 LPMOs (the DFT calculated distance in Cu(II)–*Ls*AA9 is 2.55 Å, (**section 2.3.3**).[8,57] This difference can be rationalized considering that in *Ao*AA11 the Tyr-140 residue is hydrogen bonded to the distal Glu-138 residue, while in AA9 LPMOs this glutamate is replaced by a glutamine residue. The stronger H-bond formed by Glu with respect to Gln enhances the donor strength of the Tyr oxygen atom, shortening the Cu–O(Tyr) distance.

The addition of a second water molecule in positioned in *trans* to the Tyr in Model4, generates an almost identical optimized geometry. In fact, during the geometry optimization, this second H_2O moves away from the axial position ending closer to the serine residue (Ser-57), forming an H-bond with its side chain (2.8 Å), together with a weaker one with the *N*-terminal amino group (3.0 Å). The resulting effect on the Cu

coordination is minimal and the bonding metrics are almost identical to the ones in Model3. This water molecule is in an analogous position to the one referred as 'pocket' water molecule in AA9 LPMOs structures.[56,65] However, from the *Ao*AA11 crystal structure it is not possible to evaluate if this 'pocket' water molecule is present or not, because its expected position is occupied by the exogenous Glu residue, from the second *Ao*AA11 molecule in the crystal lattice.

In summary, the obtained geometries for the Cu(II) state (Model3 and Model4) are all plausible models for the *Ao*AA11 resting state and it is not possible to discriminate which one best represents the real system from a simple comparison with the X-ray structure of the enzyme; hence they will be both used for the calculations of the spectroscopic properties.

4.3.5 Theoretical Calculations: EPR spin Hamiltonian parameters

The EPR spin Hamiltonian parameters for the two resting state models were calculated at the DFT level of theory. As already discussed in **Chapter 2** for the calculations of EPR parameters in the *Ls*AA9 resting state, the accuracy of DFT predictions for these spectroscopic properties is dependent on the choice of the functional and with a different performance for *g* and *A* tensors.[89,90] Following the same methodology used for the *Ls*AA9 resting state, the EPR parameters were calculated with the B3LYP-38% Hartree-Fock exchange functionals, the CP(PPP) basis set on the Cu, the IGLO-III basis set for the Cu coordinating atoms and the Def2-SVP basis set for all other atoms. However, because the amount of H-F exchange was not optimized for this system, as a further comparison, the EPR parameters were calculated with the standard B3LYP functional, using the same basis sets defined above. The results are summarized in **Table 4.5**.

Table 4.5 Calculated *g* values, Cu and N hyperfine coupling constants (in MHz), together with the experimental values obtained for Cu(II)–*Ao*AA11. Estimated errors for the experimental values are reported in **Table 4.1**

Method [1]	g_1	g_2	g_3	R_g [2]	A_1^{Cu}	A_2^{Cu}	A_3^{Cu}	A^{NH_2} [3]	$A^{N\delta}$ [3]	$A^{N\varepsilon}$ [3]
Exp.	2.042	2.073	2.276	0.56	75	40	457			
				Cu(II)–Model3						
B3LYP	2.048	2.054	2.165	0.12	69	34	-550	41	38	41
B3LYP (38%HF)	2.061	2.073	2.222	0.18	86	32	-584	36	34	36
				Cu(II)–Model4						
B3LYP	2.050	2.051	2.163	0.05	29	37	-568	41	40	41
B3LYP (38%HF)	2.064	2.068	2.220	0.06	53	30	-604	36	35	36

[1]-'38%HF' refers to the B3LYP functional with 38% of Hartee-Fock exchange

[2]-Rhombicity: $R_g=2(\Delta g_2-\Delta g_1)/(\Delta g_1+\Delta g_2)$; $\Delta g_i=g_i-g_e$.

[3]-For the nitrogen ligands only A_{iso}^N is reported. Experimental values are not included as they cannot be assigned to specific nitrogen atoms from X/Q-band simulations only.

The calculated spin Hamiltonian parameters for Model3 and Model4 are very similar and they both are in reasonable agreement with the experimental values. On the other hand, the performance of B3LYP with respect to B3LYP(38%H-F) varies and depends on the specific EPR parameter considered. The g_3 value is significantly underestimated by both functionals, especially B3LYP because of its smaller amount of H-F exchange. The agreement with g_1 and g_2 is much better, but the two models are predicted to be more axial (with lower rhombicity, $R_g \sim 0.15$ and 0.05 for Model3 and Model4, respectively) with respect to the experiment ($R_g = 0.56$). A good agreement is found also for the Cu hyperfine coupling, where the relative magnitude of the $|A^{Cu}|$ principal components is correctly reproduced, in comparison with the experiment, with $A_2<A_1<A_3$; the only model that does not follow this pattern is Model4 with the B3LYP functional.

The calculated nitrogen super-hyperfine (SHF) couplings are all very similar, with B3LYP calculating slightly higher magnitudes (A^N ~40 MHz) with respect to B3LYP(38%H-F) (A^N ~35 MHz). Hence, the best agreement with the estimated experimental SHF couplings is obtained with B3LYP(38%H-F). The coupling for the amino terminus nitrogen (36–40 MHz), is in the same range as the other two imidazole nitrogen atoms, similar to what is already observed in the *Ls*AA9 case (**section 2.3.4.2**).

As previously discussed, this suggests a slightly higher covalency along the Cu–NH_2 bond as compared to the two Cu–N(His) bonds. Indeed, the Löwdin spin population analysis is consistent with this hypothesis, indicating a 7.9% of unpaired spin density of the amino terminus N and 5.4% and 5.8% on N_δ and N_ε respectively (**Table 4.6**). The differences in spin populations between the two models with the same functional are very small, while a significant difference is obtained considering the two different functionals: the B3LYP provides a more covalent description of the bonding as compared to B3LYP(38%H-F), giving a significantly lower spin population of the Cu(II) (66% *vs* 75%, respectively).[89,90] This more delocalized spin on the metal ligands is at the origin of the higher isotropic N SHF couplings with B3LYP, as compared to B3LYP(38%H-F). Overall, the spin density is mainly distributed in the equatorial plane of the histidine brace, with virtually no contribution from the Tyr ligand in axial position, and reflecting a σ* type of bonding between the Cu and the ligands (**Figure 4.14**).

Table 4.6 Löwdin spin population (%) of Cu and inner sphere ligand atoms calculated from DFT for Cu(II)–Model3 and Cu(II)–Model4 of *Ao*AA11.

	B3LYP		**B3LYP(38%H-F)**	
	Cu(II)–Model3	**Cu(II)–Model4**	**Cu(II)–Model3**	**Cu(II)–Model4**
Cu	65.9	65.6	75.0	74.8
NH_2 (His-1)	10.7	11.4	7.9	8.4
N_δ (His-1)	6.7	6.8	5.4	5.6
N_ε (His-2)	7.2	7.1	5.9	5.6
O (H_2O_{eq})	7.2	7.1	5.3	5.3

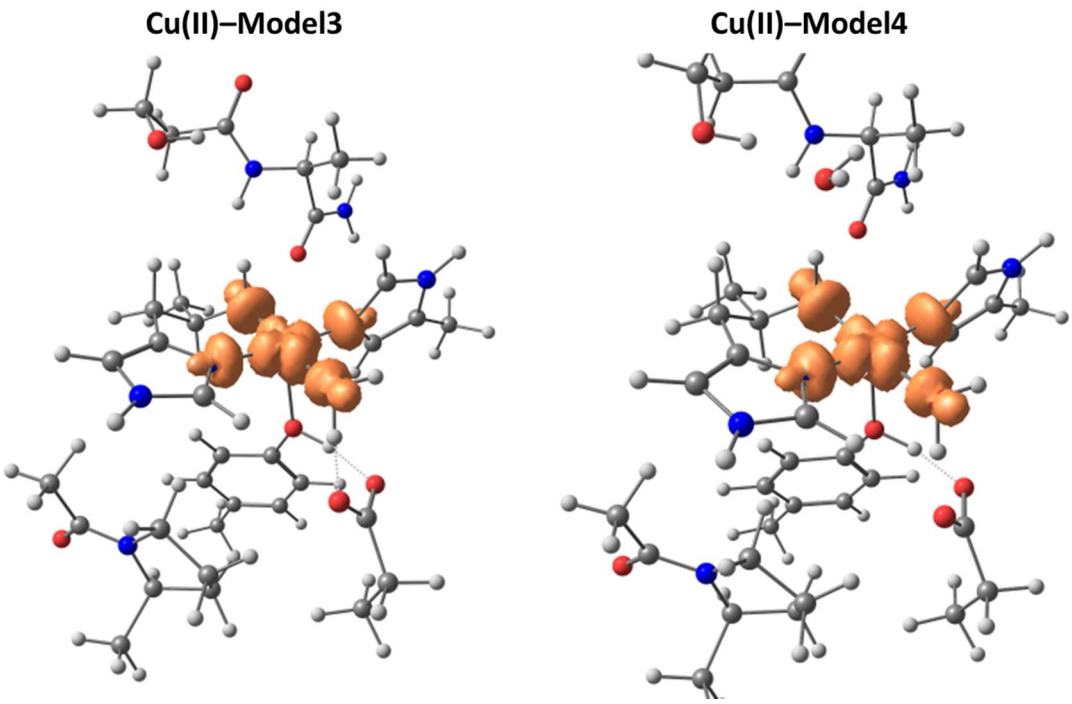

Figure 4.14 Calculated spin density (in orange) for the different models of the *Ao*AA11 active site. The spin density contour level for plotting is chosen at 0.003 Å^3.

Calculation of the SH parameters also affords the orientation of the *g* tensor and A^{Cu} tensor with respect to the reference molecular frame. From these orientations it is possible to make a connection with ligand field models of SH parameters (see discussion below). The molecular frame was defined with the origin on the Cu ion, the *x* axis along the Cu–N$_\delta$ (imidazole ring, His-1) bond, the *y* axis along the Cu–N (amino terminus) bond and *Z* axis normal to these two vectors. The calculated *g* principal components essentially align with the molecular frame with a small rotation (~5°) along the *z* axis (**Figure 4.15**); therefore it is possible to label the *g* values as follow, for both models: $g_1=g_x$, $g_2=g_y$ and $g_3=g_z$. This assignment is in agreement with a qualitative assignment based on ligand field theory for a square planar Cu(II) complex, where the largest *g* principal component is perpendicular with respect the Cu coordination plane. Moreover, the calculated A^{Cu} hyperfine tensor is essentially co-linear with the *g* frame, with a rotation of ~7° about the g_z direction (**Figure 4.15**).

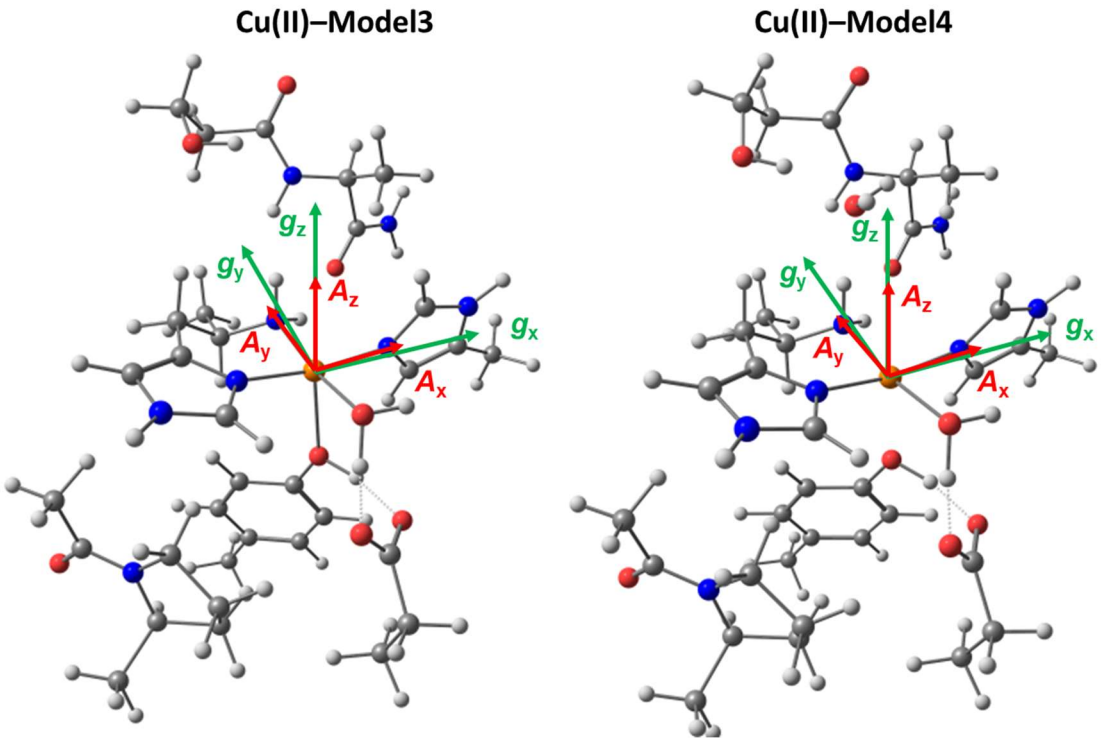

Figure 4.15 Cartoon representation of the calculated relative orientation of the *g* (green) and A^{Cu} (red) principal components, with labelling respect to the molecular frame, for *Ao*AA11 Model3 and Model4.

4.3.6 Theoretical Calculations: d-d and charge transfer electronic transitions

To further characterise the electronic structure of Cu(II)-*Ao*AA11, the ligand field (d-d) and charge transfer excited states were calculated at the TD-DFT level of theory (CAM-B3LYP functional and Def2-TZVP basis set on all atoms). However, TD-DFT is generally not a very accurate method for transition metal systems, with calculated transition energies sensitive to the choice of the functional.[89,90] Because d-d transition energies are important for the interpretation of the EPR spin Hamiltonian parameters, the ligand field excited states were also calculated with the CASSCF method together with NEVPT2 treatment of dynamic electron correlation, distributing all Cu(II) nine electrons in the five molecular orbitals with predominant metal 3d character, namely CAS(9,5). Although more computationally expensive compared to TD-DFT, the CASSCF method is multiconfigurational and is usually able to provide more accurate estimates of the d-d transitions, as already showed for the *Ls*AA9 active site (**section 2.3.5**). The energies and intensities of the calculated excitations were used to aid the assignment of the experimental electronic transitions (see **Section 4.3.3**). In this regard, in order to provide

a meaningful labelling of the d orbitals, the molecular frame reference axis were set in the same way as for the EPR calculations (**Figure 4.15**).

4.3.6.1 TD-DFT

The calculated UV-vis spectra for Model3 and Model4 are shown in **Figure 4.16**. The energies of the transitions and their relative assignments are reported in **Table 4.7** (the labelling of the different excited states follows to the one used in **Figure 4.16**). The assignments were based on the difference density plots of each transition. The two different models of the *Ao*AA11 active site gave essentially identical calculated electronic spectra. The first four calculated transitions can be assigned to ligand field (d-d) transitions (bands *1–4*): the first excited state is mainly represented by a $d(z^2)$ based SOMO; the second and the third excited states are represented by d(xz) and d(yz) SOMOs, respectively, while the fourth one is assigned as mainly d(xy) SOMO. Overall, the calculated ligand field transitions appear all blue shifted with respect to the experimental energies by about 1500–3000 cm^{-1}, depending on the particular transition, and with intensities in the 50–150 M^{-1} cm^{-1} range. After the ligand field transitions, the first charge transfer state (band *5*, ~23800 cm^{-1}) is represented by a Tyr → Cu(II) SOMO ligand to metal charge transfer (LMCT), with an intensity similar to the d-d excitations (**Figure 4.16**). This result is analogous to the one obtained in the *Ls*AA9 enzyme, which showed an analogue LMCT at ~25000 cm^{-1}. Even in this case, the unusually low intensity can be rationalised considering the low overlap between the Tyr π HOMO donor and the basically orthogonal Cu(II) SOMO acceptor (see difference density plot for transition *5* in **Figure 4.16**). At higher energies, the most intense transitions are represented by His → Cu(II) SOMO LMCTs: bands *6* and *7* at ~33800 cm^{-1} and ~35700 cm^{-1}, respectively. Band *6* is assigned as LMCT involving His-1, while band *7*, involves His-60 and has a much higher intensity as compared to band *6* (2000 M^{-1} cm^{-1} *vs* M^{-1} cm^{-1}, respectively). In addition, band *7* features a contribution also from the equatorial H_2O molecule, hence showing a mixed character (**Figure 4.16**). The appearance of these two LMCT is consistent with the experimental electronic spectra which show two CT transitions in the UV region of the electronic spectra; however their predicted energies appear again blue shifted by ~5000 cm^{-1} as compared to the experiment.

Table 4.7 TD-DFT calculated energies (cm^{-1}) for selected transitions in the UV-vis spectra of *Ls*AA9 active site models, together with their respective assignments.[1]

Nr.	Excitation	Model3	Model4
1	$d_{z^2} \rightarrow d_{x^2-y^2}$	13960	13950
2	$d_{xz} \rightarrow d_{x^2-y^2}$	17220	17340
3	$d_{yz} \rightarrow d_{x^2-y^2}$	17840	17850
4	$d_{xy} \rightarrow d_{x^2-y^2}$	19150	19310
5	$Tyr \rightarrow d_{x^2-y^2}$	23300	23840
6	$His_1 \rightarrow d_{x^2-y^2}$	33780	33870
7	$His_{60} \rightarrow d_{x^2-y^2}$	34580	35740

[1]-The numbering of the bands corresponds to the one used in **Figure 4.16**.

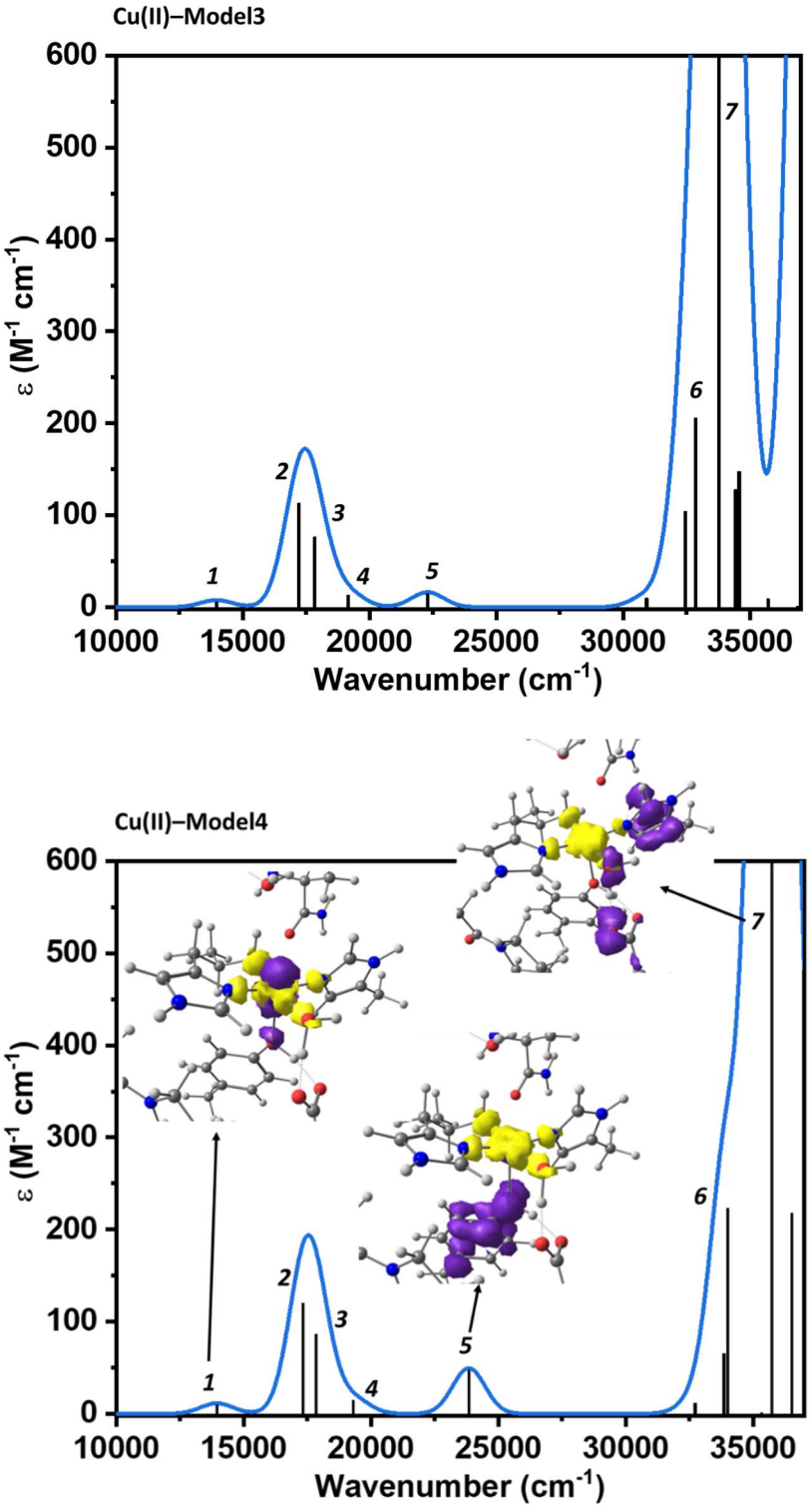

Figure 4.16 Calculated TD-DFT UV-vis spectra (blue) for Model3 and Model4 of the *Ao*AA11 active site. A band broadening of 1500 cm^{-1} was applied to each vertical transition. Vertical excitations are represented as black bars. The numbering of the transitions corresponds to the one reported in **Table 4.7**. Difference density plots for selected transitions are reported as insets: yellow indicates positive electron density and purple indicates negative electron density. The plotted surfaces were generated with a 0.003 e $Å^{-3}$ cut-off.

4.3.6.2 CASSCF/NEVPT2

The ligand field exited states were calculated with the CASSCF/NEVPT2 method and the results are summarised in **Table 4.8**. Even for this methodology, the d-d excitation energies are virtually identical between Model3 and Model4. The agreement with the experimental excitation energies is reasonably good (better than TD-DFT) with deviations between the calculated vertical excitation energies and the experimental band maxima in the order of 1000–2000 cm^{-1}, a typical result for this type of calculations.[204]

Table 4.8 CASSCF/NEVPT2 calculated excited state energies (cm^{-1}) for *Ao*AA11 Model3 and Model4 together with their relative assignments. The calculated energies are compared with those determined experimentally from the UV-vis, CD and MCD spectra.

Excitation	Model3	Model4	Experimental[1]
$d_{z^2} \rightarrow d_{x^2-y^2}$	13100	13100	12700
$d_{xy} \rightarrow d_{x^2-y^2}$	14150	14250	ND
$d_{xz} \rightarrow d_{x^2-y^2}$	15540	15610	14450
$d_{yz} \rightarrow d_{x^2-y^2}$	16480	16500	16400

[1]-Obtained from **Table 4.3**.

For both models the predicted ground state SOMO has mainly $d(x^2–y^2)$ character, consistent with the EPR spectra analysis reported above. This MO is of σ* character with respect to the four ligands in the equatorial plane and has little contribution form the Tyr-140 residue in axial position because the long Cu–O(Tyr) bond distance, ~2.3 Å for both models (**Figure 4.17**). The first excited state features a predominantly $d(z^2)$ SOMO, while the next excited state is mainly a d(xy) based SOMO. Lastly, the two highest lying excited states feature SOMOs that best represented by d(xz) and d(yz) orbitals, respectively, with some mixing between them due to spin–orbit coupling. The ordering of the d orbital excited states differs from the one obtained from TD-DFT calculations because in the TD-DFT case the highest ligand field excited state was represented by a d(xy) SOMO. However, the CASSCF/NEVPT2 result is more consistent with the EPR parameters obtained from the experimental spectra (and with those calculated by DFT as well), where the $d(xy) \rightarrow d(x^2–y^2)$ excitation is expected to be lower in energy with respect to the $d(xz/yz) \rightarrow d(x^2–y^2)$ excitations, as it is related to a bigger *g* shift (i.e. $g_z > g_{x,y}$). Following

this picture of the ligand field splitting, it is possible to make a partial assignment of the d-d bands in the electronic absorption spectra (**Figure 4.9**). The two highest energy transition (bands *2* and *3* in **Table 4.3**) correspond to the d(xz/yz)→d(x^2–y^2) transitions which form the pseudo-*A* pair in the MCD spectrum. On the other hand, the lowest energy transition (band *1* in **Table 4.3**) cannot be assigned with certainty: its energy (~12370 cm^{-1}) is lower with respect to both the calculated d(z^2)/d(xy)→d(x^2–y^2) transitions (13100 cm^{-1} and 14150 cm^{-1}, respectively). Nevertheless, the d(xy)→d(x^2–y^2) is typically found with negative sign in MCD spectra of monometallic Cu complexes, while d(z^2)/d(xy)→d(x^2–y^2) is generally positive.[91,144,145,149] Hence, the positive band *1* is tentatively assigned as d(z^2)→d(x^2–y^2), while the d(xy)→d(x^2–y^2) remains unresolved probably because of its overlap with another d-d transition.

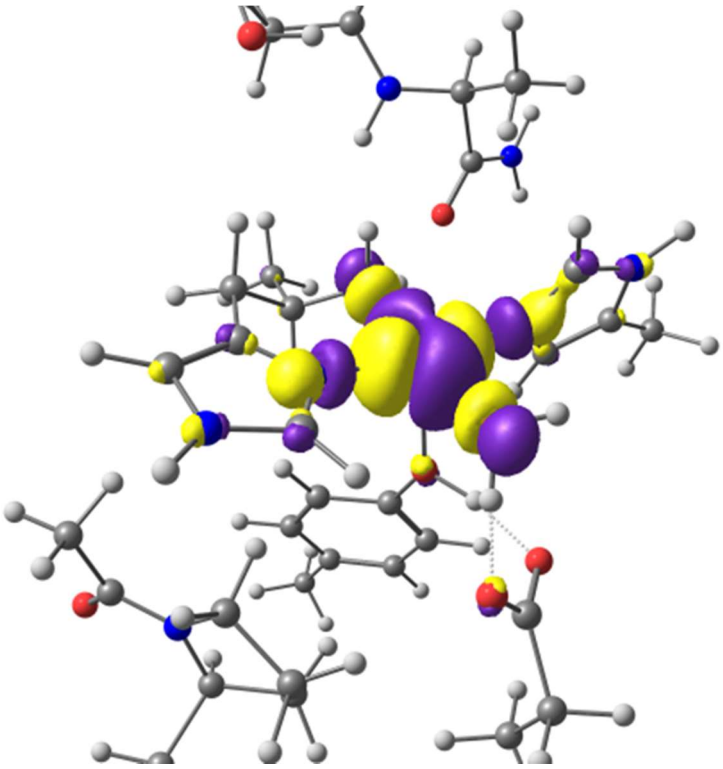

Figure 4.17 Ground state molecular orbital calculated by CASSCF for Model3 of *Ao*AA11 active site.

4.4 Discussion

4.4.1 Analysis of *Ao*AA11 Spectroscopy

Like all LPMOs, *Ao*AA11 contains a mononuclear type 2 copper active site, with the histidine brace defining the Cu coordination geometry. The analysis of the spectroscopic and computational data reported here allows a detailed description of the electronic structure of the Cu(II) resting state. The EPR spectra show that the enzyme is characterized by a d(x^2–y^2) SOMO ground state, with some anisotropy between the g_1/g_2 (g_x/g_y) directions in the His brace equatorial plane. The related EPR spin Hamiltonian parameters (**Table 4.2**) are similar to those already reported for AA9 LPMOs.[56,57,59,65] Indeed, from a structural point of view, the Cu first coordination sphere of AA11 and AA9 LPMOs are similar, with identical endogenous ligands (two His residues and a Tyr side chain in the axial position). The electronic absorption spectra show the presence of three absorption bands in the d-d transitions energy region, two of which form the MCD pseudo-*A* pair, assigned as d(xz/yz)→d(x^2–y^2) transitions. Spin Hamiltonian parameters and ligand field excitation energies can be analysed together within a ligand field theory model of EPR spin Hamiltonian parameters.[160,205] Similar to the analysis performed in **Chapter 2** for *Ls*AA9 (**Section 2.4**), the *Ao*AA11 experimental data were used to fit the following equations (see **Appendix 1** for full details about the methodology):

$$\Delta g_z \approx \frac{8\zeta_{\mathrm{Cu}}\,\gamma_{GS}^2\,\gamma_{xy}^2\,a^2}{\Delta E_{xy\rightarrow x^2-y^2}}$$

$$\Delta g_x \approx \frac{2\zeta_{\mathrm{Cu}}\,\gamma_{GS}^2\,\gamma_{yz}^2\,(a-\sqrt{3}b)^2}{\Delta E_{yz\rightarrow x^2-y^2}}$$

$$\Delta g_y \approx \frac{2\zeta_{\mathrm{Cu}}\,\gamma_{GS}^2\,\gamma_{xz}^2\,(a+\sqrt{3}b)^2}{\Delta E_{xz\rightarrow x^2-y^2}}$$

$$A_z = P_{\mathrm{d}}\left[-K-\frac{4}{7}\gamma_{GS}^2(a^2-b^2)+\Delta g_z+\frac{\Delta g_y\left(3a-\sqrt{3}b\right)}{14(a-\sqrt{3}b)}+\frac{\Delta g_x\left(3a+\sqrt{3}b\right)}{14(a-\sqrt{3}b)}\right]$$

ζ_{Cu} represents the one-electron quasi-atomic copper(II) spin–orbit coupling constant (usually taken as –830 cm^{-1}), the γ values are reduction factors which are sometimes associated with the 'covalent dilution' of the metal d-orbitals with the relative ligand orbitals, the ΔE values are excitation energies of the ligand field transitions, while a and b measure character of $d(x^2–y^2)$ and $d(z^2)$ in the ground state (GS), respectively ($a^2 + b^2 = 1$). $P_d = g_e g_{Cu} \mu_e \mu_{Cu}$ is the quasi atomic parameter usually taken as 1180 MHz, while the term $-P_d K$ represents the isotropic Fermi contact, which is treated phenomenologically in LFT. Lastly, A_{iso} is the isotropic Cu hyperfine coupling, the average of the hyperfine coupling over the x, y and z directions. Despite not being quantitatively accurate, these equations are useful tools which aid interpretation of spin Hamiltonian parameters and give chemical insight into the electronic structure of the Cu(II) ion.[160]

Rhombic splitting between g_x and g_y can be generated by several mechanisms (in an ideal axial systems, g_x and g_y would be identical): differences in transition energies of the d(xz) and d(yz) transitions; differences in the exited states covalency (γ_{xz}^2 and γ_{yz}^2); or $d(z^2)$ mixing into the ground state. The MCD spectrum reveals that the d(xz/yz) pair is not degenerate, therefore providing a mechanism for the rhombic splitting. However, the energy difference between these two transitions can only split g values by 0.01, which is too small with respect to the experimental $g_y - g_x = 0.03$. If all of the splitting is attributed to differences in exited state delocalization, than γ_{yz}^2 would be twice the value of γ_{xz}^2. This possibility is unlikely considering that none of the Cu(II) ligands is a strong π donor/acceptor (a strong difference in covalency would also be inconsistent with the spin density population obtained from DFT, **Table 4.6**, which gives similar spin distribution between the four equatorial ligands). Alternatively, anisotropy can introduce a certain amount of $d(z^2)$ mixing in the ground state. Following Gewirth *et al.*[161] the amount of $d(z^2)$ mixing can be estimated from the rhombicity parameter R_g (= 0.56), giving a $d(z^2)$ amount of ~0.3% (i.e. $b^2 \sim 0.003$) for Cu(II)–*Ao*AA11. The calculated parameters from the LF model are summarised in **Table 4.9** and the different contributions to the Cu A_z hyperfine coupling are compared with those calculated from DFT.

Table 4.9 Contributions to Cu A_z (MHz) and γ_{GS}^2 for *Ao*AA11 calculated with LFT, together with Cu A_z contribution calculated with DFT (MHz), using B3LYP(38%H-F) as functional.

	A_z^{total}	A_z^{FC}	A_z^{SD}	A_z^{SO}	γ_{GS}^2 [1]
LFT	–457	–265	–544	+352	0.81
DFT (Model3)	–584	–315	–567	+298	75.0
DFT (Model4)	–604	–332	–567	+295	74.8

[1]-The estimation of γ_{GS}^2 from DFT is taken from the Löwdin spin population analysis.

The LF analysis gives a ground state with 81% Cu character, of which 99.7% is d(x^2–y^2) and 0.3% is d(z^2), suggesting a complex with mainly ionic interaction with the ligands. The Löwdin spin population calculated with DFT (**Table 4.6**) is consistent with this description, giving a ~75% spin density on the Cu(II), with 0.4% of it in the d(z^2) orbital (using B3LYP 38% H-F).

The LF model decomposition of the Cu A_z into the three different contributions, gives a large and negative A_z^{FC} and A_z^{SD} together with an A_z^{SO} of opposite sign, a typical result for axial Cu(II) complexes. This decomposition is in qualitative agreement with DFT calculations, which correctly predict also the bigger relative magnitude of the different terms (**Table 4.9**). The largest variation respect to the LF model are the Fermi coupling term (notoriously a challenging contribution to calculate in DFT), and the spin–orbit contribution which is always underestimated in DFT calculations because of the underestimation of the g_z shift.[90]

The analysis of the electronic spectra together with the CASSCF/NEVPT2 calculations suggest a splitting of the d-orbitals due to the ligand field which follows the order: d(x^2–y^2) > d(z^2) > d(xy) > d(xz) > d(yz), suggesting that the interaction of the axial Tyr-140 with the Cu(II) is strong enough to define the d(z^2) as the first excited state SOMO (see **Figure 2.13**). In this respect, it should be noted that if we consider only the UV-vis/CD/MCD spectra for the analysis of the ligand field splitting, an alternative assignment for the d-d transitions is possible which follows the TD-DFT results: the experimental band *4* (**Figure 4.9**) could be assigned to a weak d(xy) → d(x^2–y^2) excitation instead of a Tyr π HOMO → d(x^2–y^2) LMCT. The obtained ligand field splitting would be: d(x^2–y^2) > d(z^2) > d(xz) > d(yz) > d(xy). This result, however, is not fully consistent with the EPR data because a $\Delta E_{xy\rightarrow x^2-y^2} > \Delta E_{xz/yz\rightarrow x^2-y^2}$ would require a $\gamma_{xy}^2 \approx$

$2\,\gamma^2_{xz/yz}$. Such a large difference in covalency is difficult to justify in the absence of strongly covalent ligands. Therefore, we conclude that the d orbitals splitting obtained from the CASSCF/NEVPT2 calculations is the one that best correlates with all the available experimental data. On the other hand, the putative Tyr → Cu LMCT appears at lower energy (18200 cm^{-1}) with respect to its position in the *Ls*AA9 resting state visible spectrum (21000 cm^{-1}). This red shift correlates with the predicted energy for this transition from TD-DFT: 23800 cm^{-1} and 25700 cm^{-1} for *Ao*AA11 and *Ls*AA9, respectively. This difference in energy could be explained considering the higher negative charge on the tyrosine oxygen atom in *Ao*AA11 as compared to *Ls*AA9 because of the hydrogen bond with the glutamate instead of a glutamine side chain (a weaker H bond acceptor). This additional negative charge increases the energy of the Tyr HOMO, moving it closer to the Cu(II) SOMO.

Finally, the two different computational models of the Cu(II)–*Ao*AA11 resting state studied in this work (Model3 and Model4) gave very similar results in terms of calculated Cu coordination geometries and spectroscopic properties, which are in reasonable agreement with the experimental data. Hence, it was not possible to establish which one of the two best represents the enzyme active site in solution. Moreover, the obtained results suggest that the weak H bond between the amino terminus and the H_2O molecule in the Cu secondary coordination sphere (in an analogue position with respect to the 'pocket' water molecule found in *Ls*AA9), do not affect significantly the Cu(II) spin Hamiltonian parameters and the d orbitals splitting.

4.4.2 Interaction with Substrate and Activity Profile

*Ao*AA11 showed enzymatic activity on *β*-chitin (**Figure 4.5**), but not on *α*-chitin where no oxidation products could be detected in MALDI-TOF mass spectrometry. Moreover, the addition of *β*-chitin to the enzyme resting state did not perturb the EPR spectrum (**Figure 4.8**), in contrast to what has been has been observed in several other AA9 or AA10 LPMOs.[62,65,77,82] This observation suggests a low binding affinity for β-chitin (high dissociation constant, K_d) or that the substrate binds to the enzyme in a way which does not affect the Cu(II) electronic structure. In this regard, we note that in the fungus *Aspergillus oryzae*, the *Ao*AA11 is likely to be produced together with a CBM domain

that would enhance substrate binding (see **section 4.1)**, therefore the substrate binding ability of the individual catalytic domain might not be very high. Indeed in a recent study on a AA9 LPMO, *Hj*AA9, Hansson et al. showed that when the CBM domain was removed from the catalytic domain, the enzyme exhibited significantly reduced binding and activity on cellulose compared with the full-length enzyme.[59] Even in this case, the EPR spectrum of the *Hj*AA9 catalytic domain was not perturbed upon addition of cellulose to the sample solution.

In addition, the potential of H_2O_2 to act as co-substrate (instead of O_2) for *Ao*AA11 was tested using *β*-chitin as polysaccharide substrate. Again, no oxidised chito-oligosaccharides were detected in the reaction solution, using MALDI-TOF mass spectrometry. Very little data are available in the literature about H_2O_2 activation in the AA11 family (only a very recent report on *Ff*AA11 LPMO),[196] so more studies will be needed in the future to obtain a detailed picture of the reactivity with hydrogen peroxide. However, it is possible to speculate that in case of *Ao*AA11, H_2O_2 is not the preferred co-substrate with respect to O_2 in the conditions used to assay the enzymatic activity, or that the enzyme is rapidly damaged by the action of the peroxide, abolishing catalytic activity. It should be noted that the action of H_2O_2 on the de-*N*-glycosylated version of *Ls*AA9 had an extremely deleterious effect on the enzyme, leading to extensive damage of the polypeptide chain (see **Chapter 3**). Being an enzyme of fungal origin, *Ao*AA11 is very likely to be glycosylated to a certain degree as well but, because it was produced in *E. coli* as expression system, the enzyme used in the experiments was completely without any glycosylation pattern. Therefore, if the glycosylation provides a protective role on this enzyme as well, its absence could explain the lack of detected enzymatic activity in presence of H_2O_2.

4.4.3 Possible Electron Transfer Pathways

The structure of *Ao*AA11 shows that the active site tyrosine (Tyr-140) is part of a network of aromatic (Trp and Tyr) and methionine residues which could form potential electron/hole hopping pathways to direct strongly oxidizing electron holes (generated at the Cu site during the catalytic cycle), away from the active site and thus protecting it from oxidative damage due to uncoupled turnover. This possibility was already discussed in **Chapter 3** for *Ls*AA9 LPMO and we showed that these networks of redox active residues can form efficient hole-hopping pathways, like in other monooxyganases and peroxidase enzymes.[188] The structure of *Ao*AA11 is richer in methionine and cysteine residues (which are involved in disulfide bridges) compared to *Ls*AA9 and other LPMOs in the AA9 family (in turn richer in tryptophan and tyrosine residues), therefore it was interesting to evaluate if efficient hole-hopping pathways could still be found also in *Ao*AA11. Accordingly, using the X-ray structure of *Ao*AA11 the potential pathways were evaluated with the EHPath computer program.[192]

The software calculates the rate of charge transfer through possible pathways in the enzyme using Marcus theory and estimating the charge transfer rate constant, for any donor-acceptor pair, using the following expression:

$$k_{DA} = \frac{2\pi}{\hbar} V_{DA}^2 \frac{1}{\sqrt{4\pi\lambda_{DA}T}} exp\left(-\frac{(\Delta G^0 + \lambda_{DA})^2}{4\lambda_{DA}k_B T}\right)$$

Elements of the equation can be calculated/estimated from the known self-exchange reorganization energies of the donor (λ_{DD}) and acceptor (λ_{AA}), the reduction potentials of the donor and acceptor, and the distances between the donor and the acceptor, the last of which is obtained from structural information. The effective electronic coupling (V_{DA}) can be estimated using Hopfield's equation. Thus, the possible pathways were calculated using reduction potential and reorganization energies at pH 7.0 and where the Tyr-140 act as hole donor (assuming that the axial Tyr would be the first oxidized residue by the Cu–O_x active intermediate).

Table 4.10 The five fastest accurate mean-residence times (AMRT) of hole-hopping pathways from Tyr-140 at pH 7 and 298.15 K through the structure of *Ao*AA11, as determined by EHPath.[192]

Pathway	AMRT /s
Tyr-140, Trp-128, Cys-143, Cys-29, Tyr-36	0.239
Tyr-140, Trp-128, Cys-143, Tyr-10, Tyr-36	0.239
Tyr-140, Trp-128, Cys-143, Tyr-36	0.239
Tyr-140, Trp-128, Cys-143, Trp-81, Tyr-36	0.244
Tyr-140, Trp-130, Trp-128, Cys-143, Tyr-36	0.246

Several hole transfer routes were identified, which are very similar to each other in term of residues involved and all have Tyr-36 as ending point, on the surface of the enzyme (**Figure 4.18**). Because of the similarity, their mean residence times are all around 230–250 ms (**Table 4.10**), significantly slower with respect to the fastest path found in *Ls*AA9 (~ 6 ms) and also compared to hole hopping paths seen in other redox enzymes, like P450 (37 ms) and CCP1 (2.5 ms), but still in the biologically relevant timescales. The analysis shows that chains of redox active residues (Tyr, Trp and Cys in this case) can support hole hopping in in *Ao*AA11, even if this mechanism appears to be less efficient respect to other AA9s LPMOs and potentially affecting the stability of the enzyme under uncoupled turnover.

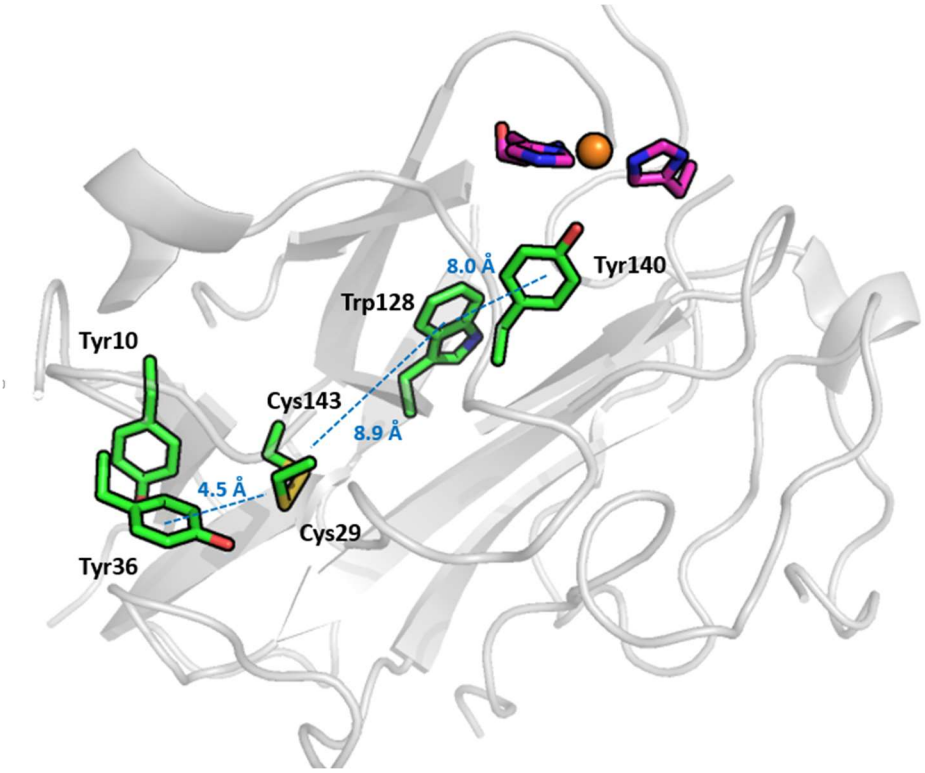

Figure 4.18 Cartoon representing the *Ao*AA11 structure (grey ribbons) and the amino acid side chains (in green) involved in putative hole-hopping pathways. The Cu ion is represented as orange sphere and distances are given in Å.

4.5 Conclusions

A combined experimental and theoretical using EPR, UV-vis, CD and MCD spectroscopies, together with DFT and CASSCF calculations allowed to obtain an accurate description of the Cu(II)–*Ao*AA11 Cu active site electronic structure. These data showed an Cu(II) electronic structure consistent with a Jahn-Teller distorted octahedral coordination geometry. Overall, the electronic structure is very similar to that found in AA9 LPMOs, suggesting a similar mechanism for the stabilization of the Cu–O_2 intermediates: the flat equatorial coordination plane generated by the His brace allows to have a high orbital overlap with the coordinating O_2^- at the beginning of the catalytic cycle. Moreover, the lack of EPR perturbation upon addition of β-chitin suggests that in some LPMOs, the catalytic domain alone might not be able to strongly bind to the substrate and that the relative CBM binding domain is needed to enhance this binding.

5 Conclusions and future perspectives

Although much progress has been made in LPMO research over the last years, many questions remain open about the detailed mechanism of action of these enzymes. LPMOs form a large and diverse class of enzymes with a wide array of substrate specificities. This range is reflected in the large number of different LPMOs which are often encoded within single genomes. Indeed, recent years have seen a surge in the number of reported LPMOs able to oxidize C–H bonds present in carbohydrates, characterized by high bond dissociation energies (BDE ~100–104 kcal mol^{-1}).[8,28] In this context, spectroscopic measurements and theoretical calculations are going to be fundamental in determining the nature of the relevant copper–oxygen intermediate species in the enzyme catalytic cycle and to explain their reactivity in terms of their electronic structure.

In studying LPMOs the solvent-accessible active site provides the opportunity to study the O_2 and H_2O_2 activation by a copper active site without the complexity of large protein domains interactions (or multiple metal center as seen in other Cu oxidases like the non-coupled bimetallic Cu monooxygenases, the coupled bimetallic Cu oxidases or the multicopper oxidases).[64,91] On the other hand, this accessibility makes the Cu(I) state of LPMOs very reactive indeed to species such as H_2O_2 and O_2, and therefore makes LPMOs prone to different kinds of redox reactions (most of which are considered off-pathway reactions).[95] Indeed, the Cu(I) state can activate both O_2 and H_2O_2,[29,106] and be obtained by using many different reducing agents[107,108] leading to oxidation of different substrates with different regioselectivities[82] or – in the absence of substrate – undergo oxidative damage and self-inactivation. Accordingly, it is clear that reaction conditions are a fundamental factor in determining the preferred reaction pathway and therefore they need to be carefully considered in designing experimental studies on LPMOs. Among these factors, one of the most important is surely the presence of the substrate because in the

substrate-bound state, the copper site is sheltered from solvent and precisely positioned relative to the target C–H bond. It is thus important for a reduced LPMO to bind to its substrate to prevent off-pathway reactions.[62,65,77,82,103,198]

In the work described herein, we showed that the His brace coordination provides a structurally rigid unit, with very small geometrical rearrangements upon change in Cu oxidation state and upon substrate binding. The spectroscopic and computational characterization of the cellulose active *Ls*AA9 resting state (**Chapter 2**), showed a mainly ionic Cu(II) ground state with a SOMO of σ* character (with an estimated γ_{GS}^2 from EPR parameters of 0.85, **Table 2.14**). Moreover, the Cu(II) based SOMO is oriented in order to have optimized interaction (high orbital overlap) with an exogenous ligand in the equatorial position. Indeed, this is a key requirement for efficient O_2 activation, where the high energetic cost of the one-electron reduction of dioxygen is counterbalanced by the formation of a strong covalent Cu–O_2^- bond.[63] Addition of substrate (cellohexaose) to the Cu(II) resting state of the enzyme only causes minor changes to the active site electronic structure. These changes are consistent with a shift from a 6 coordinate to a 5 coordinate Cu complex (the axial H_2O ligand in the resting state is displaced by the substrate, but the substrate does not bind to the Cu) and without significantly altering the orientation and composition of the ground state SOMO. Notwithstanding the slight structural changes brought about by substrate binding, interaction of the substrate with the active site forces any other Cu exogenous ligand (like O_2 or H_2O_2) to bind in the Cu equatorial coordination position. In this respect, several QM/MM and DFT studies showed that the substrate and few other residues in the Cu secondary coordination sphere interact with the bound O_2/H_2O_2 through H-bond interaction, stabilizing and properly orienting the reactivity of the active oxygen intermediate towards the target C–H bond.[99,103,104] Moreover, in presence of the substrate, small anions like Cl^- and Br^- can efficiently bind in this Cu equatorial position, forming a covalent bond with the metal and effectively reducing the spin density on the Cu(II) ion. This interaction possibly mimics the situation where the O_2 binds to the Cu active site forming an Cu(II)–superoxide intermediate as it has been already suggested for AA10 LPMOs (see below).[62] Future work directed at trapping and characterizing the Cu(II)–O_2–substrate ternary complex, through stopped flow and freeze-quench experiments will be important in the understanding the nature and the electronic structure of this state.

The results described in **Chapter 4** showed that the Cu(II) EPR spin Hamiltonian parameters and d-d transition energies for the chitin-active *Ao*AA11 are very similar to those obtained for *Ls*AA9, and therefore describe a similar electronic structure. The small differences in d-d excitation energies between *Ao*AA11 and *Ls*AA9 are likely due to differences in secondary coordination sphere interactions. The addition of *β*-chitin to *Ao*AA11 resting state did not generate a perturbation of the EPR spin Hamiltonian parameters as seen for *Ls*AA9; therefore it was not possible to conclude if the substrate was effectively bound or not to the enzyme. Nevertheless, the similarities with *Ls*AA9 suggests that that activation of O_2/H_2O_2 activation could follow the same mechanism.

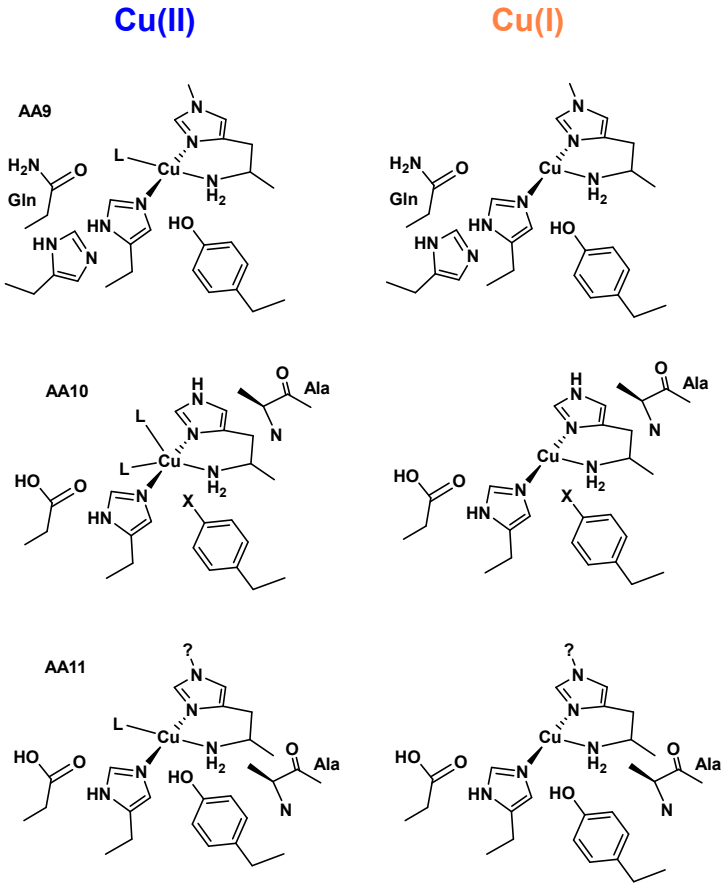

Figure 5.1 The active site structures of AA9, AA10 and AA11 LPMOs in the Cu(II) and Cu(I) states. 'L' refers to exogenous ligands, usually H_2O/OH^- or Cl^-. The wild-type AA11 LPMOs may contain a methylated N-terminal histidine side chain (depicted as '?'), like AA9, but this is unknown as the production systems (*E. coli* or *Pichia pastoris*) used to produce these enzymes lack the necessary enzymatic methylation apparatus.

In extending the comparison between different LPMOs, it is possible to consider also the characteristics of AA10 LPMO active sites. Because of the Cu distorted square pyramidal coordination geometry the EPR parameters for the Cu(II) resting state are significantly different (much more rhombic EPR spectra) from those typical for AA9 and AA11s (see **Section 1.8**). This difference would suggest that future work should be directed at the characterization of the ligand field splitting of the d orbitals in AA10s (and the effect of the substrate binding on this ligand field splitting), assessing possible differences and similarities with the AA9 and AA11 families. For example, a recent EPR, NMR and DFT study on an AA10 LPMO (*Bl*AA10) and its interaction with β-chitin showed that the Cu contribution to the SOMO ground state (γ^2_{GS} ~0.84) and the ligand N SHF coupling were very similar to those reported here for *Ls*AA9 and *Ao*AA11.[62] This consideration suggests that even the difference in coordination geometry and in the primary coordination sphere residues (a Phe residue replaces the axial Tyr residue) do not affect much the properties of the His brace structural unit between the different classes of LPMO enzymes. Furthermore, it should be considered that the reactive state of the enzyme is the Cu(I) state, in which the Cu ion is coordinated only by the three N atoms of the His brace, independently of what LPMO family is considered (**Figure 5.1**). Hence, it is possible to speculate that the His brace is the key structural element that is needed for O_2 and H_2O_2 activation in all LPMOs and that the substrate, together with secondary coordination sphere residues, helps to direct the reactivity of the Cu–O_2 species.

In the context of AA9 LPMOs reactivity with H_2O_2, we showed that the addition of hydrogen peroxide to Cu(I)–*Ls*AA9 LPMO at high pHs in the absence of substrate resulted in the formation of a highly stable, purple-coloured Cu(II)−tyrosyl complex that has been characterized using spectroscopic methods (UV−vis, CD, MCD, resonance Raman, EPR). This species is not a reactive intermediate of the enzyme catalytic cycle, but instead is formed (over the minute timescale) during un-coupled turnover. Despite the lack of catalytic activity of this species, its formation shows that the active site Tyr residue in AA9s is redox active. The redox activity of the active site tyrosine is indicative of its role in LPMOs, which is to act as part of an efficient charge-transfer 'hole-hopping' pathway between the active site and the protein surface. Such a pathway, consisting of tyrosine and tryptophan residues and spanning ∼15 Å, has been identified in the LPMO

used in our studies. The functional role of these pathways is not clear but it is possible to speculate that they can protect the protein active site from inactivation during uncoupled turnover. Importantly, this Cu(II)–tyrosyl species is formed at a much slower rate (hours timescale) in presence of cellohexaose, again indicating the importance of the substrate in preventing deleterious off-pathway side reactions.

Recently, Jones *et al*. published a spectroscopic study on the reaction of Cu(I)–*Hj*AA9 with H_2O_2, in the absence of substrate and at very short timescales (milliseconds and seconds timescale), which was issued after the publication of the results in **Chapter 3**.[102] The authors showed the formation of two intermediates corresponding to a neutral tyrosyl and tryptophan radicals, identified in the Cu axial Tyr residue and in a tryptophan residue at 5.4 Å from the Cu ion (this residue is present also in *Ls*AA9, but is positioned at a longer distance from the Cu ~10 Å, see **Figure 3.25**). Both radicals showed magnetic exchange coupling with the Cu(II) site reflecting facile electron transfer pathways which may be protective pathways against non-coupled turnover. In the light of these data, future work will certainly be directed towards investigating the charge transfer pathways in the AA9 LPMOs, and also in the other families and in particular in the AA10 LPMOs which do not have a Cu axial Tyr residue, but only present the tryptophan residue. Moreover, if these charge transfer pathways are indeed quickly reducing towards a Cu–oxygen intermediate during non-coupled turnover, it is possible to speculate that mutating these residues, and therefore interrupting the charge transfer pathways, could increase the lifetime of any Cu–oxygen intermediate, allowing its characterization. This strategy was already exploited in the past with success in cytochrome P450 enzymes, where the conversion and lifetime of the highly reactive compound I intermediate were increased by mutation of the tyrosine residues involved in non-coupled compound I decay pathways.[206]

The discovery of amino acid radical formation upon reaction of Cu(I)–AA9s and H_2O_2 now opens-up major new questions about the role of these species in the context of LPMOs reactivity (and possibly further complicating the picture) and will probably be the focus on many research efforts in the field for the next years.

Appendix 1
Ligand Field Theory and Spin Hamiltonian Parameters

Ligand Field Theory (LFT) can be used to derive equations for the EPR spin Hamiltonian parameters.[160] Even if they are not quantitatively accurate, they provide useful insight into EPR spectra of transition metal complexes and to correlate the spectroscopic data with electronic transitions involving electrons in d-orbitals.[91] In a distorted square planar Cu(II) complex, the Cu d based molecular orbitals (MO) are written as:[160,207]

$$\psi_{x^2-y^2} = \alpha_{\mathrm{GS}}\left(a\, d_{x^2-y^2} - b\, d_{z^2}\right) - \sqrt{1-\alpha_{\mathrm{GS}}^2}\ \psi_{L_1}$$

$$\psi_{z^2} = \alpha_{\mathrm{GS}}\left(b\, d_{x^2-y^2} + a\, d_{z^2}\right) - \sqrt{1-\alpha_{\mathrm{GS}}^2}\ \psi_{L_2}$$

$$\psi_{xy} = \alpha_{\mathrm{xy}} d_{\mathrm{xy}} - \sqrt{1-\alpha_{\mathrm{xy}}^2}\ \psi_{L_{xy}}$$

$$\psi_{xz} = \alpha_{\mathrm{xz}} d_{\mathrm{xz}} - \sqrt{1-\alpha_{\mathrm{xz}}^2}\ \psi_{L_{xz}}$$

$$\psi_{yz} = \alpha_{\mathrm{yz}} d_{\mathrm{yz}} - \sqrt{1-\alpha_{\mathrm{yz}}^2}\ \psi_{L_{yz}}$$

The $\psi_{x^2-y^2}$ orbital is the semi occupied MO (SOMO) and all other MOs are doubly occupied; in a molecular orbital context the α_i represent the metal d-orbital contribution to the molecular orbital (*i.e.* the 'covalent dilution' of the metal orbitals with the ligand orbitals), while a and b are the coefficients for the d(x^2–y^2) and d(z^2) orbitals in the ground state orbital (GS), with $a^2 + b^2 = 1$. The mixing of d(z^2) is due to the distortion from the ideal axial symmetry; in case of zero mixing ($b^2 = 0$), the ideal case for a square planar complex is recovered.

In this framework, if the relevant exited states are restricted to single excitation from the doubly occupied metal based MO to the SOMO, the g values can be expressed as:

$$\Delta g_z \approx \frac{8\zeta_{\mathrm{Cu}}\,\alpha_{GS}^2\,\gamma_{xy}^2\,a^2}{\Delta E_{xy\rightarrow x^2-y^2}}$$

$$\Delta g_y \approx \frac{2\zeta_{\mathrm{Cu}}\,\alpha_{GS}^2\,\alpha_{xz}^2\,(a+\sqrt{3}b)^2}{\Delta E_{xz\rightarrow x^2-y^2}}$$

$$\Delta g_x \approx \frac{2\zeta_{\mathrm{Cu}}\,\alpha_{GS}^2\,\alpha_{yz}^2\,(a-\sqrt{3}b)^2}{\Delta E_{yz\rightarrow x^2-y^2}}$$

$$\text{with } \Delta g_{\mathrm{i}} = g_{\mathrm{i}} - 2.0023$$

ζ_{Cu} represents the one-electron quasi-atomic copper spin–orbit coupling constant (usually taken as –830 cm^{-1}), and the ΔE values are excitation energies of the relevant ligand field transitions.

Similarly, the Cu hyperfine coupling can be written as:

$$A_z = P_{\mathrm{d}}\left[-K - \frac{4}{7}\alpha_{\mathrm{GS}}^2(a^2-b^2) + \Delta g_z + \frac{\Delta g_y(3a-\sqrt{3}b)}{14(a-\sqrt{3}b)} + \frac{\Delta g_x(3a+\sqrt{3}b)}{14(a-\sqrt{3}b)}\right]$$

$$A_y = P_{\mathrm{d}}\left[-K + \frac{2}{7}\alpha_{\mathrm{GS}}^2(a^2-b^2) - \frac{4\sqrt{3}}{7}\alpha_{\mathrm{GS}}^2(ab) + \Delta g_y - \frac{\Delta g_x(3a+\sqrt{3}b)}{14(a-\sqrt{3}b)}\right]$$

$$A_x = P_{\mathrm{d}}\left[-K + \frac{2}{7}\alpha_{\mathrm{GS}}^2(a^2-b^2) + \frac{4\sqrt{3}}{7}\alpha_{\mathrm{GS}}^2(ab) + \Delta g_x - \frac{\Delta g_y(3a-\sqrt{3}b)}{14(a-\sqrt{3}b)}\right]$$

$A_{\mathrm{x,y\ and\ z}}$ are the experimentally determined hyperfine couplings, $P_{\mathrm{d}} = g_{\mathrm{e}} g_{\mathrm{Cu}} \mu_{\mathrm{e}} \mu_{\mathrm{Cu}}$ is the quasi atomic parameter usually taken as 1180 MHz,[160] the term $-P_{\mathrm{d}}K$ (in blue) represents the isotropic Fermi contact (A^{Fermi}) term that is treated phenomenologically in LFT; the spin-dipolar (A^{SD}) contribution is in green and the spin–orbit contribution is indicated in red (A^{SO}).The different Cu hyperfine contributions, the % d(z^2) in the SOMO and the α_{GS}^2 can be determined as follows:

Following Gewirth *et al.*,[161] the values of a and b (and therefore the % d(z^2) in the ground state) can be estimated from the rhombicity parameter (R_g) and the above g values equations (see also **Figure A 1** below):

$$R_g = \frac{2(\Delta g_y - \Delta g_x)}{\Delta g_y + \Delta g_x} \approx 2\,\frac{\Delta E_{\mathrm{yz}}\left(a + \sqrt{3}b\right)^2 - \Delta E_{\mathrm{xz}}\left(a - \sqrt{3}b\right)^2}{\Delta E_{\mathrm{yz}}\left(a + \sqrt{3}b\right)^2 + \Delta E_{\mathrm{xz}}\left(a - \sqrt{3}b\right)^2}$$

Assuming $\alpha_{yz}^2 \approx \alpha_{xz}^2$ and where ΔE_{yz} and ΔE_{xz} are the experimental ligand field transitions $\Delta E_{yz \rightarrow x^2-y^2}$ and $\Delta E_{xz \rightarrow x^2-y^2}$, respectively.

Alternatively, the ratio a/b can be estimated from the $\Delta g_x / \Delta g_y$ ratio (using the same assumption as before):

$$\frac{\Delta g_x}{\Delta g_y} \approx \frac{\Delta E_{\mathrm{xz}}\left(a - \sqrt{3}b\right)^2}{\Delta E_{\mathrm{yz}}\left(a + \sqrt{3}b\right)^2}$$

The two approaches lead to equivalent results in terms of % d(z^2) mixing in the GS.

A^{SO} was obtained from the experimental Δg and the a and b values obtained above

A^{SO} was subtracted from A^{Total} to get $A^{\mathrm{Fermi}} + A^{\mathrm{SD}}$

The x, y and z components of $A^{\mathrm{Fermi}} + A^{\mathrm{SD}}$ were averaged to obtain A^{Fermi}

$A^{\mathrm{Fermi}} + A^{\mathrm{SO}}$ was subtracted from A^{Total} to get A^{SD}

α_{GS}^2 was calculated from A^{SD}

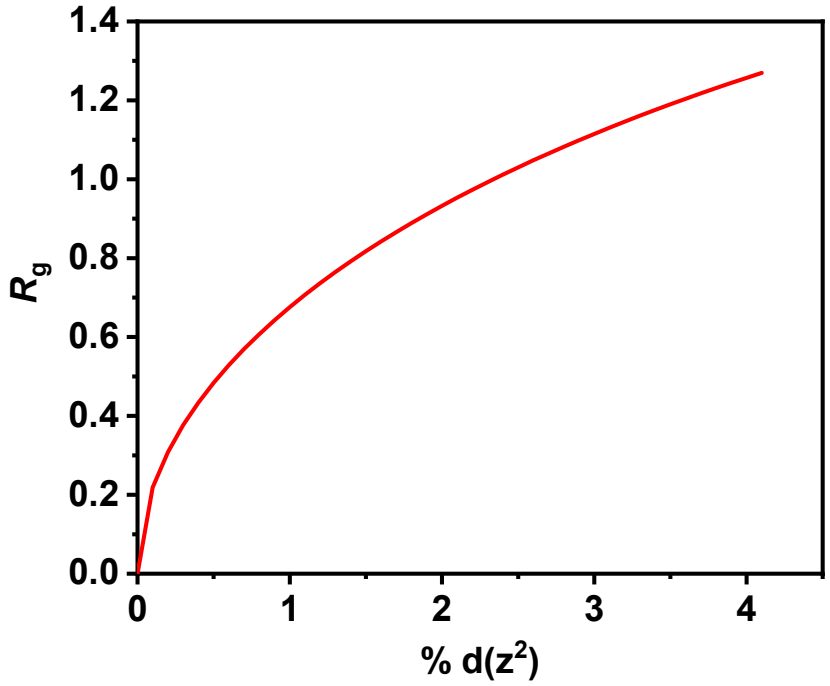

Figure A 1 Rhombicity of the *g* values as a function of the % d(z^2) mixing into the ground state. For this general case, is was assumed $\alpha_{yz}^2 \approx \alpha_{xz}^2$ and $\Delta E_{xz \rightarrow x^2-y^2} \approx \Delta E_{yz \rightarrow x^2-y^2}$.

The summary of parameters obtained for the different LPMOs in this work is reported below:

***Ls*AA9**

a^2=0.997, b^2=0.003, α_{GS}^2=0.85

$A^{Experimental}$[x, y, z] = [75, 125, –460] MHz

A^{Fermi}[x, y, z] = [–251, –251, –251] MHz

A^{SD}[x, y, z] = [260, 304, –564] MHz

A^{SO}[x, y, z] = [41, 72, 356] MHz

***Ls*AA9_C6**

a^2=1.000, b^2=0.000, α_{GS}^2=0.84

$A^{Experimental}$[x, y, z] = [35, 46, –518] MHz

A^{Fermi}[x, y, z] = [–295, –295, –295] MHz

A^{SD}[x, y, z] = [285, 383, –567] MHz

A^{SO}[x, y, z] = [45, 58, 344] MHz

***Ls*AA9_C6_Cl**

a^2=0.997, b^2=0.003, α^2_{GS}=0.81

$A^{\mathrm{Experimental}}$[x, y, z] = [10, 77, –517] MHz

A^{Fermi}[x, y, z] = [–275, –275, –275] MHz

A^{SD}[x, y, z] = [252, 289, –541] MHz

A^{SO}[x, y, z] = [33, 63, 299] MHz

***Ls*AA9_C6_Br**

a^2=0.995, b^2=0.005, α^2_{GS}=0.80

$A^{\mathrm{Experimental}}$[x, y, z] = [10, 55, –525] MHz

A^{Fermi}[x, y, z] = [–279, –279, –279] MHz

A^{SD}[x, y, z] = [316, 215, –532] MHz

A^{SO}[x, y, z] = [18, 74, 286] MHz

***Ao*AA11**

a^2=0.997, b^2=0.003, α^2_{GS}=0.81

$A^{\mathrm{Experimental}}$[x, y, z] = [75, 40, –457] MHz

A^{Fermi}[x, y, z] = [–265, –265, –265] MHz

A^{SD}[x, y, z] = [314, 230, –544] MHz

A^{SO}[x, y, z] = [26, 75, 352] MHz

Appendix 2

Cartesian coordinates of DFT models

The cartesian coordinates of the active site models optimized geometries are reported in the following pages. The names of the various models correspond to those used in the main text. Cartesian coordinates are reported using the [x y z] format.

Chapter 2

Model1_2H2O

N	-5.565570000	-4.435826000	18.116445000
C	-5.426348000	-4.257675000	16.644751000
C	-4.251984000	-5.075938000	16.102068000
C	-5.287325000	-2.761525000	16.326123000
C	-6.554981000	-1.997965000	16.534055000
C	-7.156443000	-1.042999000	15.730093000
N	-7.347858000	-2.164067000	17.661071000
C	-8.391205000	-1.333446000	17.550313000
N	-8.303588000	-0.631523000	16.391287000
C	-9.261286000	0.358270000	15.907158000
C	-9.558074000	-2.687084000	13.264063000
C	-10.228946000	-4.015867000	13.587864000
O	-10.225032000	-4.967346000	12.791746000
N	-10.860855000	-4.093125000	14.799306000
C	-11.639831000	-5.293194000	15.182897000
C	-12.940935000	-5.390955000	14.380011000
C	-11.858634000	-5.087606000	16.695168000
C	-11.852965000	-3.560501000	16.877318000
C	-10.799265000	-3.089107000	15.867200000
C	-4.835020000	-3.806054000	26.828752000
O	-5.538673000	-4.279079000	25.665814000
C	-5.687000000	-7.308018000	23.024170000
C	-5.926013000	-6.017975000	22.311582000
C	-6.398092000	-5.747631000	21.031886000
N	-5.684644000	-4.776247000	22.880190000
C	-6.002662000	-3.812416000	21.978363000
N	-6.439559000	-4.374336000	20.841421000
C	-9.370979000	-5.330981000	27.072937000
C	-9.085310000	-4.859465000	25.690487000
C	-8.638436000	-3.613895000	25.251724000
N	-9.289028000	-5.696036000	24.606055000
C	-8.968485000	-4.988802000	23.528768000
N	-8.586372000	-3.714853000	23.868473000
C	-12.033968000	-6.725964000	19.908925000
C	-12.454583000	-5.310665000	20.314226000
C	-11.370954000	-4.526405000	21.020313000
N	-11.714229000	-3.854562000	22.124762000
O	-10.183556000	-4.486142000	20.577533000
C	-8.003013000	-9.808969000	15.431019000
C	-8.193572000	-8.531826000	16.226592000
C	-8.201420000	-7.267647000	15.589718000
C	-8.393496000	-8.549677000	17.623626000
C	-8.401826000	-6.081633000	16.311200000
C	-8.591200000	-7.367326000	18.363405000
C	-8.600113000	-6.122822000	17.706102000
O	-8.795501000	-4.925287000	18.367681000
Cu	-6.956168000	-3.365364000	19.182462000
O	-5.632125000	-1.480121000	20.138505000
H	-8.800960000	-2.414333000	14.028573000
H	-11.018587000	-5.538282000	17.255398000
H	-12.793166000	-5.569227000	17.043290000
H	-11.601617000	-3.244227000	17.908206000
H	-12.844576000	-3.131352000	16.624778000
H	-9.787855000	-3.082474000	16.334397000
H	-11.008267000	-2.070927000	15.483930000
H	-11.017788000	-6.189723000	14.982979000
H	-4.914051000	-4.521379000	27.676362000
H	-5.203736000	-2.810862000	27.160179000
H	-6.494734000	-4.362680000	25.880036000
H	-9.105294000	-4.567988000	27.829618000
H	-8.807842000	-6.259425000	27.299416000
H	-8.403012000	-2.682780000	25.777693000
H	-8.240801000	-2.991072000	23.237546000
H	-8.989639000	-5.331046000	22.486548000
H	-11.765670000	-7.336155000	20.794098000
H	-11.166220000	-6.713218000	19.221454000
H	-13.364204000	-5.333485000	20.946072000
H	-12.716993000	-4.721238000	19.408192000
H	-11.014431000	-3.321404000	22.648175000
H	-7.964558000	-10.695364000	16.093043000
H	-7.064300000	-9.778942000	14.839683000
H	-8.073645000	-7.204716000	14.497410000
H	-8.400443000	-9.514442000	18.155440000
H	-8.453098000	-5.113989000	15.792699000
H	-8.762644000	-7.418759000	19.449986000
H	-4.681748000	-4.180892000	18.594926000
H	-6.366690000	-4.632273000	16.195626000
H	-4.211606000	-5.001898000	14.997314000
H	-4.468536000	-2.335364000	16.948496000
H	-4.969314000	-2.640926000	15.273047000
H	-6.860092000	-0.618451000	14.766125000
H	-9.197497000	-1.225628000	18.280457000
H	-10.082974000	0.452698000	16.638575000
H	-8.765267000	1.339588000	15.783694000
H	-9.674894000	0.037081000	14.932397000
H	-4.639746000	-7.382890000	23.380040000
H	-5.890709000	-8.159094000	22.349244000
H	-6.715022000	-6.451777000	20.256881000
H	-5.420686000	-4.594570000	23.878868000
H	-5.881964000	-2.738506000	22.151364000
H	-5.679476000	-0.765641000	19.475270000
H	-4.751004000	-1.919854000	19.973333000
H	-3.287793000	-4.708058000	16.510238000
H	-4.358232000	-6.146091000	16.369701000
H	-5.756461000	-5.421452000	18.325615000
H	-3.768391000	-3.708236000	26.550552000
H	-6.350396000	-7.399275000	23.908805000
H	-10.447703000	-5.573307000	27.192148000
H	-12.659469000	-3.910893000	22.508917000
H	-12.866687000	-7.230116000	19.382065000
H	-12.717816000	-5.427713000	13.296620000
H	-13.492136000	-6.314797000	14.651917000
H	-13.600556000	-4.521115000	14.579222000
H	-9.064540000	-2.773942000	12.280155000
H	-10.306276000	-1.868709000	13.223520000
O	-8.571409000	-2.475308000	20.207337000
H	-9.192794000	-3.205758000	20.540892000
H	-8.218654000	-1.994101000	20.979252000
H	-8.833200000	-9.956607000	14.708387000
H	-9.370873000	-5.027732000	19.181363000
O	-3.477849000	-3.081081000	19.648007000
H	-2.663620000	-2.716056000	19.245290000
H	-3.160362000	-3.519079000	20.463935000

Model2_Sub_H2O

N	-5.784018575	-4.675234919	18.109924705
C	-5.446573779	-4.284442539	16.709798347
C	-4.274000010	-5.115000010	16.157000000
C	-5.169970003	-2.773140758	16.663735122
C	-6.407577950	-1.956679204	16.835191810
C	-6.864632829	-0.873261698	16.107434247
N	-7.299453377	-2.169719807	17.877054949
C	-8.256355203	-1.234848125	17.796373780
N	-8.021513554	-0.432219561	16.727399766
C	-8.802716964	0.733216770	16.323398611
C	-9.596000039	-2.659000029	13.284000022
C	-10.244660664	-3.961469184	13.730005409
O	-10.122659892	-5.017807960	13.089984896
N	-10.993437330	-3.895374051	14.873270547
C	-11.767941891	-5.063196340	15.353193001
C	-12.994999970	-5.328999993	14.470000010
C	-12.109316897	-4.655318187	16.800519889
C	-12.218271749	-3.122708488	16.736718561
C	-11.089153772	-2.736424301	15.771380098
C	-4.967999957	-3.921999973	26.882000001
O	-5.041275167	-3.895575103	25.453461875
C	-5.832000094	-7.459999941	23.029000039
C	-6.097755949	-6.156719043	22.361153882
C	-6.480368569	-5.875382684	21.055752011
N	-6.005931319	-4.926179955	22.993069720
C	-6.318559184	-3.954479357	22.098770069
N	-6.609388692	-4.504107961	20.906165863
C	-9.497000084	-5.247000037	26.956000149
C	-9.583317265	-4.810541525	25.523868565
C	-9.952189814	-3.566680831	25.020314765
N	-9.322999879	-5.682000066	24.471999818
C	-9.531093028	-4.991923368	23.358263132

N	-9.906628514	-3.698109989	23.638228579
C	-12.209999999	-6.857999964	19.865999968
C	-12.797974867	-5.542575826	20.374374092
C	-11.861096660	-4.351707340	20.371097102
N	-12.422700224	-3.136982068	20.433385473
O	-10.599673157	-4.481731326	20.360943686
C	-8.093999994	-9.818000002	15.498999997
C	-8.288613519	-8.537456561	16.282178130
C	-8.311904744	-7.278424760	15.636277425
C	-8.483748729	-8.557369422	17.679955589
C	-8.524063534	-6.090774112	16.353082750
C	-8.693273314	-7.376290392	18.413866285
C	-8.716197608	-6.139622945	17.745333173
O	-8.916210831	-4.943961347	18.421761425
Cu	-7.114821270	-3.552906578	19.235230248
O	-5.642999999	2.009999996	17.125000004
C	-5.604954981	1.831766870	18.495868732
C	-6.954797394	2.201912481	19.112769251
O	-7.306932175	3.531700955	18.796771756
C	-6.883350843	2.001348011	20.627950274
O	-8.189880903	2.239595113	21.124593838
C	-6.362798691	0.603139277	20.980211795
O	-5.983028727	0.546509221	22.365919541
C	-5.127130275	0.196601764	20.151096797
O	-5.365931121	0.444080318	18.773886764
C	-4.825550935	-1.284185223	20.330422958
O	-3.676596518	-1.663057487	19.614981000
C	-6.954472467	0.153380983	23.263556320
C	-6.265074693	-0.518750571	24.456723363
O	-5.470134506	-1.617702917	24.010919441
C	-7.338204912	-1.039009760	25.394689463
O	-6.734296147	-1.580118637	26.549679559
C	-8.295798041	0.094732470	25.766341555
O	-9.400999975	-0.478999978	26.445999998
C	-8.810043738	0.867784868	24.548010995
O	-7.709453266	1.282371817	23.716983403
C	-9.593000002	2.080000002	25.009999995
O	-10.163586240	2.699477478	23.868220738
O	-3.524718044	-4.402739134	19.889937418
H	-8.922037953	-2.248240696	14.065322110
H	-11.271576052	-4.940423117	17.467769168
H	-13.029843662	-5.149205763	17.167107605
H	-12.116067229	-2.633355956	17.724525981
H	-13.198812128	-2.820169118	16.315437935
H	-10.127979132	-2.590982342	16.319148654
H	-11.304183596	-1.801610222	15.216129808
H	-11.107106524	-5.953696949	15.327747118
H	-5.972301744	-3.922517959	27.358979001
H	-4.398612524	-3.053663205	27.274160800
H	-5.260026158	-2.971852302	25.175876378
H	-9.758155521	-4.418544826	27.641842144
H	-8.474210943	-5.598311878	27.207104901
H	-10.214424650	-2.621124475	25.508510413
H	-10.245099591	-3.002556101	22.970769839
H	-9.452234359	-5.366654033	22.329757756
H	-11.334884286	-7.166054664	20.470975071
H	-11.885659318	-6.783836302	18.809535803
H	-13.122725774	-5.655930194	21.433999299
H	-13.715182028	-5.264889669	19.814709185
H	-4.929712215	-4.700126098	18.702148515
H	-6.350454532	-4.497688458	16.105409949
H	-4.115000821	-4.870862565	15.088516663
H	-4.439153931	-2.498062462	17.458461717
H	-4.704514698	-2.515060756	15.693902757
H	-6.444963368	-0.360440055	15.237704588
H	-9.099524847	-1.119935344	18.481922322
H	-9.675094646	0.833732969	16.992789225
H	-8.171265149	1.639246420	16.398147610
H	-9.152620264	0.610194865	15.280899629
H	-4.831231095	-7.475525604	23.506350456
H	-5.885060673	-8.282856324	22.293354746
H	-6.674844592	-6.572393674	20.235982520
H	-5.721651545	-4.734088777	23.991605625
H	-6.259310247	-2.889794777	22.348876576
H	-7.961228168	-10.687823501	16.170549470
H	-7.209458979	-9.754044457	14.832725410
H	-8.192013056	-7.219302498	14.543415958
H	-8.476615552	-9.521077367	18.213085272
H	-8.587638365	-5.122061672	15.837141527
H	-8.857501358	-7.418023856	19.501474232
H	-4.790175931	2.435588535	18.972833130
H	-7.700018785	1.471202834	18.712567009
H	-8.033424406	3.757644485	19.415283906
H	-6.151708413	2.741058386	21.035945033
H	-8.166078262	2.205374531	22.112753880
H	-7.187432961	-0.126029660	20.793626541
H	-4.251632676	0.795175568	20.504879590
H	-4.725853209	-1.469456468	21.424282476
H	-5.735060874	-1.849561296	19.984784150
H	-3.530420807	-2.628459921	19.788635186
H	-7.662149045	-0.575085188	22.781871072
H	-5.636984730	0.237515508	24.975262519
H	-4.618569163	-1.265001417	23.683167036
H	-7.921499595	-1.823069277	24.848769770
H	-7.465699965	-1.893045996	27.119998969
H	-7.734511541	0.792923082	26.426858639
H	-9.585765864	0.038754303	27.251125774
H	-9.484506521	0.203043188	23.954590089
H	-10.363957588	1.721344281	25.729827158
H	-8.898774827	2.761449916	25.556498941
H	-10.515924428	3.567486836	24.140281750
H	-2.653933002	-4.769601838	19.632930348
H	-3.698326811	-4.799112154	20.768213929
H	-4.736459182	1.888378986	16.780543118
H	-6.586513649	-7.650241720	23.821019540
H	-4.440274356	-4.850763594	27.179447896
H	-6.198250022	-5.616091668	18.110667719
H	-3.336386846	-4.895274004	16.707396212
H	-4.485512579	-6.199783334	16.236486218
H	-10.187386825	-6.093116835	27.153639637
H	-12.969867459	-7.659120087	19.934438639
H	-11.845972157	-2.293091283	20.479761346
H	-13.437976055	-3.019440189	20.455575455
H	-12.675305618	-5.510555854	13.426201582
H	-13.536670568	-6.227806625	14.828050789
H	-13.696120095	-4.469400679	14.481070772
H	-10.363536678	-1.887364072	13.069377789
H	-9.009567659	-2.852515425	12.368603216
H	-8.971057280	-10.021679490	14.848676176
H	-9.558603589	-5.072711089	19.175205342
O	-8.702844805	-2.654741385	20.417334248
H	-9.487485026	-3.308018075	20.364351923
H	-8.369674998	-2.802219775	21.326709201

Model3_Sub_Cl

N	-5.667692579	-4.567607584	18.181700845
C	-5.363579070	-4.216243681	16.768336852
C	-4.274000014	-5.115000044	16.156999984
C	-5.014607687	-2.718988110	16.707052057
C	-6.231572152	-1.867822772	16.851592873
C	-6.690885016	-0.832485550	16.058410836
N	-7.128173013	-2.031379303	17.898805412
C	-8.092661094	-1.116058103	17.752828633
N	-7.860308755	-0.372167513	16.642092610
C	-8.632136781	0.783652129	16.200572635
C	-9.596000029	-2.659000024	13.284000011
C	-10.282228301	-3.968154849	13.647928749
O	-10.283587761	-4.947528046	12.884046358
N	-10.922418382	-3.992050165	14.854392253
C	-11.703568809	-5.174763132	15.285510839
C	-12.994999976	-5.328999988	14.470000004
C	-11.943309559	-4.888908518	16.781634978
C	-11.954648315	-3.354103874	16.876040751
C	-10.861220166	-2.941920410	15.882866848
C	-4.967999899	-3.921999947	26.881999984
O	-4.973447754	-3.849426669	25.457270792
C	-5.832000099	-7.459999948	23.029000038
C	-6.036400178	-6.138584092	22.365710647
C	-6.398701037	-5.820187778	21.063110537
N	-5.920656726	-4.919105890	23.020523061
C	-6.217436569	-3.925126278	22.146765853

N	-6.506761539	-4.441354493	20.944438067
C	-9.497000228	-5.247000114	26.956000240
C	-9.479981554	-4.789448238	25.523458466
C	-9.569305484	-3.492074160	25.021844402
N	-9.322999783	-5.681999913	24.471999768
C	-9.285016190	-4.948272857	23.363915496
N	-9.437056222	-3.617283176	23.645322901
C	-12.210000035	-6.858000017	19.866000011
C	-12.473468173	-5.450524254	20.387581102
C	-11.212563915	-4.609373591	20.377040892
N	-11.344372615	-3.274258264	20.451360359
O	-10.083940151	-5.158200012	20.302905586
C	-8.093999978	-9.817999961	15.499000009
C	-8.240547818	-8.491498133	16.225189877
C	-8.206384036	-7.259074120	15.528543605
C	-8.436600142	-8.430890004	17.621918472
C	-8.356351796	-6.030741206	16.191415894
C	-8.589086089	-7.209139914	18.303326837
C	-8.548245802	-5.992712993	17.589107926
O	-8.701836021	-4.770082540	18.202315697
Cu	-6.970478777	-3.369430774	19.333686275
O	-5.643000000	2.010000000	17.125000000
C	-5.543072760	1.905906645	18.506631125
C	-6.874302771	2.281205968	19.157498986
O	-7.250959066	3.599628372	18.812090274
C	-6.753450638	2.131357732	20.677693063
O	-8.044674243	2.398259414	21.200908989
C	-6.234689970	0.740908890	21.050692611
O	-5.874658160	0.700695551	22.450019795
C	-4.993543624	0.341845119	20.224337997
O	-5.254382294	0.545991043	18.838784852
C	-4.654756154	-1.127903582	20.421842426
O	-3.471165544	-1.476964812	19.739580172
C	-6.850794372	0.241279440	23.319198513
C	-6.170012071	-0.408598110	24.529032267
O	-5.342444585	-1.493989724	24.109661588
C	-7.248085016	-0.963157398	25.446212302
O	-6.643460659	-1.483363744	26.616058604
C	-8.273613502	0.120411456	25.801776357
O	-9.400999964	-0.479000086	26.445999954
C	-8.770942952	0.886421879	24.568153781
O	-7.657356838	1.340789320	23.777467080
C	-9.593000002	2.080000022	25.009999991
O	-10.158752805	2.685536747	23.858354318
O	-3.433809213	-4.228505408	20.004183478
H	-8.843219824	-2.361907616	14.044498184
H	-11.100667787	-5.291807168	17.376143348
H	-12.876382114	-5.358758836	17.147872267
H	-11.751642925	-2.983674051	17.898710150
H	-12.936180186	-2.948845008	16.552846764
H	-9.862644001	-2.940269064	16.378783885
H	-11.032869978	-1.936515728	15.449562932
H	-11.074431627	-6.077754901	15.141256605
H	-5.994085134	-3.946595275	27.312675383
H	-4.426534740	-3.064361626	27.333062347
H	-5.156702768	-2.913267248	25.189385464
H	-9.676577572	-4.398847114	27.644957983
H	-8.529469440	-5.717509911	27.231701668
H	-9.727512092	-2.525841660	25.514597922
H	-9.385647049	-2.870575279	22.940470800
H	-9.174665635	-5.307467906	22.332224905
H	-11.470050304	-7.379610694	20.502481657
H	-11.804770782	-6.840511616	18.836536945
H	-12.845579654	-5.479560041	21.436372717
H	-13.261893783	-4.930146215	19.803310854
H	-4.802755796	-4.593805514	18.753199071
H	-6.303523299	-4.377166430	16.204353457
H	-4.147404926	-4.875083646	15.082836061
H	-4.286010936	-2.465884002	17.510783313
H	-4.527243247	-2.486432193	15.741211714
H	-6.272670441	-0.370601739	15.159669296
H	-8.938052025	-0.974272651	18.430696763
H	-9.549827079	0.857898919	16.810840669
H	-8.023333570	1.699221335	16.331776541
H	-8.910062596	0.669581441	15.135532277
H	-4.843744054	-7.519354384	23.529265725
H	-5.898240207	-8.274280436	22.284359827
H	-6.610172075	-6.495228141	20.229112306
H	-5.646962676	-4.736790919	24.020051461
H	-6.209825830	-2.867382744	22.418751778
H	-8.177363417	-10.671185593	16.199764788
H	-7.112313811	-9.891078793	14.985129775
H	-8.086035775	-7.253400910	14.433466682
H	-8.483509630	-9.367796190	18.200376818
H	-8.373072442	-5.088063421	15.625584852
H	-8.781522960	-7.192204084	19.385768800
H	-4.725943217	2.558433717	18.913168368
H	-7.625441210	1.532253191	18.803400852
H	-7.959366564	3.832758675	19.448609058
H	-6.006733010	2.883087354	21.037779634
H	-8.025026571	2.286390726	22.184108791
H	-7.045716947	0.003825663	20.861602882
H	-4.125328762	0.969255054	20.547883186
H	-4.582041574	-1.306949451	21.519696923
H	-5.534047306	-1.718077749	20.056644955
H	-3.352145096	-2.451309270	19.873967426
H	-7.512088663	-0.504342479	22.809639911
H	-5.571375812	0.365002055	25.059402077
H	-4.533696096	-1.119701104	23.706359919
H	-7.768622353	-1.773736841	24.883724615
H	-7.349511422	-1.942142459	27.113024501
H	-7.767041509	0.837611998	26.485082628
H	-9.455222491	-0.142235094	27.358846647
H	-9.409472865	0.208943506	23.950278499
H	-10.364919577	1.703117367	25.719364000
H	-8.922806731	2.778020140	25.566494340
H	-10.557988595	3.532593342	24.130827531
H	-2.575430870	-4.685676818	19.896841976
H	-3.780014678	-4.564169263	20.856548040
H	-4.762484198	1.808772383	16.751607211
H	-6.612796089	-7.630159214	23.800332348
H	-4.450141390	-4.857880549	27.176355480
H	-6.102673096	-5.496673045	18.219084804
H	-3.299002805	-4.963910693	16.665254106
H	-4.553232757	-6.184390588	16.241729698
H	-10.286973424	-6.007610729	27.128226382
H	-13.143840036	-7.453849358	19.860291923
H	-10.483613860	-2.699470455	20.497908606
H	-12.261322974	-2.832073912	20.526533374
H	-12.755043063	-5.424528468	13.393955520
H	-13.540338136	-6.240649466	14.788118131
H	-13.663823511	-4.454708666	14.609569797
H	-10.334361248	-1.833952644	13.211333257
H	-9.094062464	-2.783557866	12.308175790
H	-8.874522535	-9.936832482	14.718527788
H	-9.187302777	-4.899780618	19.093495443
Cl	-8.419736514	-2.077260298	20.752802620

Model4_Sub_Br

N	-5.688344330	-4.583646911	18.169355696
C	-5.358173498	-4.213429183	16.767105406
C	-4.274000006	-5.115000033	16.156999992
C	-4.985962270	-2.720869058	16.736226667
C	-6.199083315	-1.861970556	16.853041677
C	-6.631750702	-0.824746745	16.047957577
N	-7.131490339	-2.033230281	17.868450761
C	-8.092708657	-1.119108965	17.688578462
N	-7.822163913	-0.369675546	16.591106864
C	-8.580606823	0.787775786	16.131232892
C	-9.596000028	-2.659000019	13.284000010
C	-10.279104710	-3.967122891	13.658480462
O	-10.266288595	-4.957010660	12.908489182
N	-10.932758594	-3.977726768	14.857912543
C	-11.712809920	-5.158181668	15.296645979
C	-12.994999938	-5.328999969	14.470000029
C	-11.969257036	-4.853430462	16.786258653
C	-11.989318974	-3.317588757	16.860171743
C	-10.888575436	-2.912923315	15.871899493
C	-4.967999927	-3.921999967	26.881999988
O	-4.974840290	-3.858069415	25.455925147
C	-5.832000094	-7.459999941	23.029000034

C	-6.055901731	-6.141970139	22.359141130
C	-6.432703621	-5.826197765	21.058804970
N	-5.938534642	-4.919810921	23.009514043
C	-6.245816015	-3.928151189	22.136596048
N	-6.545147557	-4.446405130	20.936699044
C	-9.497000187	-5.247000063	26.956000371
C	-9.500541191	-4.793686081	25.523996902
C	-9.641703706	-3.500871246	25.023413602
N	-9.322999812	-5.682000018	24.471999546
C	-9.329820199	-4.948147833	23.362952732
N	-9.527354874	-3.624021531	23.646601605
C	-12.210000055	-6.858000056	19.866000039
C	-12.561983134	-5.470470867	20.381961883
C	-11.351892780	-4.557834591	20.372018845
N	-11.572059770	-3.234784451	20.461749715
O	-10.194050086	-5.036868001	20.288240006
C	-8.093999988	-9.817999972	15.499000003
C	-8.257389564	-8.492496372	16.228912607
C	-8.202276656	-7.257014819	15.538440386
C	-8.488524161	-8.433499956	17.621077391
C	-8.363707570	-6.029822208	16.201407557
C	-8.652030632	-7.212120096	18.302908483
C	-8.587632510	-5.993507536	17.594587351
O	-8.741369127	-4.768861212	18.205836201
Cu	-6.993994638	-3.381731167	19.305191173
O	-5.642999998	2.009999989	17.125000012
C	-5.522216189	1.920470332	18.507206492
C	-6.840044737	2.316299483	19.172731586
O	-7.208113839	3.634793296	18.817596878
C	-6.699966085	2.182268055	20.693438970
O	-7.981551370	2.470928593	21.229239415
C	-6.199683287	0.787042963	21.068809731
O	-5.845949144	0.736218517	22.470417187
C	-4.972267962	0.360800981	20.235635398
O	-5.241455510	0.561464558	18.849957612
C	-4.666592544	-1.116372468	20.435598878
O	-3.486263397	-1.491883947	19.760474531
C	-6.832583958	0.267568520	23.325333304
C	-6.175729502	-0.418143888	24.528770156
O	-5.360623214	-1.507922264	24.095540708
C	-7.273562863	-0.977715972	25.421600807
O	-6.692219006	-1.534895605	26.584824477
C	-8.278291086	0.117786304	25.791969341
O	-9.400999950	-0.478999966	26.445999979
C	-8.762273381	0.897470544	24.561933824
O	-7.636104893	1.364538796	23.795845687
C	-9.593000018	2.080000008	25.009999997
O	-10.139832956	2.708119723	23.861491140
O	-3.477150650	-4.246545269	20.021621315
H	-8.852064540	-2.348321464	14.047693525
H	-11.129931435	-5.243344743	17.393408745
H	-12.902919193	-5.323999021	17.150171785
H	-11.799618369	-2.931617186	17.879789064
H	-12.969650781	-2.922006716	16.521596268
H	-9.894240124	-2.897595023	16.376205915
H	-11.061835191	-1.914767060	15.422653043
H	-11.077947302	-6.059924454	15.170927970
H	-5.993206930	-3.947964501	27.313470287
H	-4.429917150	-3.058678999	27.326636264
H	-5.176822226	-2.926598678	25.186228540
H	-9.686744070	-4.400038370	27.643709921
H	-8.519208618	-5.699246095	27.226280520
H	-9.816416159	-2.537964218	25.516957922
H	-9.507608218	-2.875284938	22.940987635
H	-9.223696837	-5.302508388	22.329167558
H	-11.438041233	-7.329431310	20.503630549
H	-11.807573346	-6.819261745	18.835964186
H	-12.936048810	-5.518312708	21.429248600
H	-13.376670965	-4.999439969	19.792008185
H	-4.831882727	-4.624562710	18.752326029
H	-6.291924745	-4.349839576	16.186574642
H	-4.127534254	-4.858620884	15.089163287
H	-4.278529000	-2.486116988	17.563785835
H	-4.468114234	-2.481948770	15.788023832
H	-6.183213194	-0.360605991	15.165171803
H	-8.964484764	-0.978385565	18.332144998
H	-9.523561608	0.850116281	16.703031762
H	-7.981209209	1.703604272	16.298318118
H	-8.812892622	0.684879065	15.054288198
H	-4.837167552	-7.506120936	23.517187177
H	-5.900087667	-8.279208711	22.289979979
H	-6.648062945	-6.502790358	20.226956703
H	-5.660132335	-4.737653738	24.007615313
H	-6.236022566	-2.869988538	22.407701568
H	-8.196710087	-10.674039845	16.193535839
H	-7.099425472	-9.889053154	15.010669798
H	-8.055390752	-7.247941915	14.446643924
H	-8.552616853	-9.371343833	18.196406106
H	-8.361925197	-5.085916369	15.637355066
H	-8.864563555	-7.197360304	19.381919534
H	-4.693010344	2.570192700	18.892651929
H	-7.603466290	1.570718903	18.836158318
H	-7.904176279	3.883011642	19.461940107
H	-5.939316847	2.928204308	21.036535172
H	-7.962604764	2.338945411	22.209976690
H	-7.023869980	0.067050285	20.877072099
H	-4.087757862	0.970528116	20.548239778
H	-4.603473057	-1.296129510	21.533757686
H	-5.556525630	-1.687007715	20.064675290
H	-3.385324646	-2.467944185	19.898281076
H	-7.495531628	-0.461743486	22.796715525
H	-5.571352732	0.331926607	25.085802500
H	-4.538937105	-1.139181121	23.714011054
H	-7.805248555	-1.765063375	24.835023832
H	-7.425672599	-1.943728586	27.086621446
H	-7.755419719	0.822129801	26.476608503
H	-9.542615800	-0.027418762	27.297883451
H	-9.388903176	0.226515963	23.925199873
H	-10.378361387	1.689275013	25.697057267
H	-8.935499613	2.768570408	25.593063267
H	-10.547256781	3.547695696	24.144791677
H	-2.614816220	-4.700048448	19.931989019
H	-3.834470366	-4.575676446	20.872034678
H	-4.768882155	1.801487476	16.740750380
H	-6.602529240	-7.630894558	23.810249143
H	-4.443991465	-4.853138977	27.180468087
H	-6.132301535	-5.509154199	18.186320905
H	-3.304585302	-4.986430992	16.681913531
H	-4.568070235	-6.182097538	16.218410631
H	-10.271711881	-6.021192962	27.137694836
H	-13.102963900	-7.513795536	19.862602044
H	-10.754958108	-2.604486815	20.509070523
H	-12.515523535	-2.855214087	20.548742669
H	-12.743715303	-5.437292812	13.397734337
H	-13.539553894	-6.239012446	14.794148728
H	-13.669051926	-4.456053879	14.591541866
H	-10.337590024	-1.838703091	13.193853791
H	-9.084057977	-2.793893044	12.314837118
H	-8.854821619	-9.930483035	14.698604903
H	-9.265689048	-4.872844024	19.075876870
Br	-8.537712036	-1.979663135	20.783487408

Model5_Tyr

N	-5.796910764	-4.680870780	18.018278805
C	-5.402854434	-4.229434717	16.652768048
C	-4.252000023	-5.076000021	16.102000005
C	-5.057538998	-2.725053639	16.667702706
C	-6.266491126	-1.849079936	16.725658948
C	-6.867199214	-1.120193453	15.708759609
N	-7.053852619	-1.756644544	17.866527508
C	-8.105794335	-0.996244833	17.541932694
N	-8.027789286	-0.581329572	16.248543820
C	-8.951662506	0.327091614	15.579747938
C	-9.558000119	-2.687000149	13.264000425
C	-10.263671860	-3.989976254	13.591345117
O	-10.249090717	-4.964246936	12.813286847
N	-10.918242389	-4.020160805	14.781876835
C	-11.668286548	-5.217600003	15.214278107
C	-12.941000099	-5.391000021	14.380000023
C	-11.921805628	-4.937031747	16.710025047
C	-11.978529100	-3.401995027	16.795348117

C	-10.901217214	-2.956482209	15.800339278
C	-4.834999996	-3.806000002	26.829000000
O	-5.826112942	-4.282788708	25.900695441
C	-5.687000005	-7.307999992	23.023999993
C	-6.093595458	-6.057023163	22.324789055
C	-6.431249709	-5.832183793	20.999491885
N	-6.207907631	-4.820242768	22.943181292
C	-6.605382204	-3.908050700	22.013226325
N	-6.744516483	-4.491544403	20.817829021
C	-9.370999987	-5.331000011	27.073000057
C	-9.342282141	-5.611501133	25.597203821
C	-9.787695102	-4.803696867	24.552283573
N	-8.863015782	-6.809426395	25.080087484
C	-9.026761496	-6.722202610	23.759058088
N	-9.579055786	-5.529726922	23.394179914
C	-12.536999779	-5.420999858	20.422999471
C	-11.601418947	-4.255506310	20.592833093
N	-12.056950399	-3.031490017	20.286646187
O	-10.418492174	-4.434447010	20.994937599
C	-8.003000001	-9.808999958	15.431000033
C	-8.159268645	-8.406333924	15.989437661
C	-8.157199136	-7.265400426	15.152292787
C	-8.322134008	-8.180615457	17.381180503
C	-8.295756521	-5.968486434	15.665531956
C	-8.478216873	-6.891927801	17.908303556
C	-8.471017779	-5.735127584	17.063587753
O	-8.634071098	-4.509104445	17.536614785
Cu	-7.430116329	-3.872915797	18.965783304
O	-6.747512068	-0.959576099	20.522429581
H	-8.805267921	-2.436858933	14.040665876
H	-11.064836566	-5.306377401	17.306773539
H	-12.842760164	-5.433062041	17.074286249
H	-11.775193832	-3.020977941	17.812048302
H	-12.975330371	-3.025769863	16.482938185
H	-9.905182886	-2.926156543	16.296000637
H	-11.119123108	-1.967270516	15.351570333
H	-11.014144899	-6.103171523	15.072353328
H	-5.132885677	-4.000516158	27.882302891
H	-4.631897063	-2.718557337	26.709080981
H	-6.659360308	-3.807403446	26.086710090
H	-9.837936260	-4.349491632	27.283215647
H	-8.343244376	-5.320501447	27.496011669
H	-10.233205378	-3.802990842	24.536767195
H	-9.845078138	-5.228179025	22.433146982
H	-8.763201654	-7.491716860	23.022346132
H	-12.559983849	-6.006889373	21.362864975
H	-13.563238466	-5.117340628	20.148994761
H	-11.431425458	-2.222200074	20.342564980
H	-8.046459952	-7.396024632	14.063219348
H	-8.335252284	-9.043858577	18.067735195
H	-8.292064591	-5.102080302	14.989271922
H	-8.630982695	-6.741529915	18.989341622
H	-4.992979986	-4.600284266	18.652932895
H	-6.297433533	-4.378458128	16.016740661
H	-4.032271181	-4.789784778	15.054126171
H	-4.377527995	-2.516231867	17.522364782
H	-4.492897160	-2.491356729	15.744481047
H	-6.573304973	-0.936296440	14.670083194
H	-8.933300320	-0.736356302	18.209167490
H	-9.851786276	0.449101160	16.207856906
H	-8.477994621	1.316289533	15.425741296
H	-9.247591615	-0.085895038	14.598097867
H	-4.619306735	-7.278596241	23.328857802
H	-5.829219091	-8.177448762	22.355843686
H	-6.480126177	-6.557422570	20.182237039
H	-6.011948091	-4.617637402	23.945721029
H	-6.783083979	-2.852194831	22.235486723
H	-6.658316761	-1.277500654	19.573853267
H	-5.891053660	-1.190038522	20.930494322
H	-3.329099335	-4.933874420	16.702380756
H	-4.513730490	-6.153565905	16.115568399
H	-6.026718055	-5.682296854	17.975989272
H	-3.899390437	-4.360667792	26.622376110
H	-6.291136451	-7.465035598	23.941452768
H	-9.938700906	-6.112111669	27.621097140
H	-13.008162646	-2.882000869	19.947385095
H	-12.680259585	-5.482133465	13.308427279
H	-13.482498651	-6.309484986	14.686643688
H	-13.624960478	-4.526485454	14.506755606
H	-9.047718845	-2.790170180	12.289848216
H	-10.276564774	-1.844051481	13.210546775
O	-8.880980796	-2.673508536	19.902299903
H	-9.405205849	-3.317587159	20.486114313
H	-12.126382568	-6.083705755	19.635367748
H	-7.136750200	-10.333147006	15.887904217
H	-8.898858401	-10.431368932	15.643109401
H	-7.853007935	-9.791084232	14.333822087
H	-8.316565740	-2.115479721	20.492135089

Chapter 3

Model1-2H_2O (Triplet)

N	-5.527981781	-4.406591633	18.129869333
C	-5.403791155	-4.237256805	16.658987650
C	-4.251983999	-5.075937998	16.102067999
C	-5.262658175	-2.741923685	16.334804110
C	-6.539312628	-1.986996256	16.526515595
C	-7.142458096	-1.039873032	15.713962771
N	-7.350028129	-2.169714139	17.637559629
C	-8.406992399	-1.361471770	17.508292196
N	-8.311118643	-0.653999890	16.352778957
C	-9.281528895	0.316477373	15.854968239
C	-9.558073976	-2.687083968	13.264062945
C	-10.243902228	-4.026676475	13.505358661
O	-10.349105200	-4.878786628	12.609523146
N	-10.768174110	-4.233809533	14.754458835
C	-11.563105369	-5.448014204	15.048491869
C	-12.940935010	-5.390954993	14.380010984
C	-11.628663235	-5.456438091	16.586154747
C	-11.519516592	-3.975705709	16.993900763
C	-10.607214330	-3.355266971	15.921504667
C	-4.835019989	-3.806053995	26.828752007
O	-5.575857191	-4.197046275	25.659021820
C	-5.686999994	-7.308017991	23.024169995
C	-5.942684315	-6.021983272	22.312072910
C	-6.406371648	-5.765994611	21.027592384
N	-5.738402331	-4.773243074	22.880540544
C	-6.070601896	-3.820375857	21.970852160
N	-6.479656352	-4.397203735	20.832185895
C	-9.370978979	-5.330980991	27.072936992
C	-9.104239063	-4.852193175	25.688090190
C	-8.709885400	-3.590849144	25.243555909
N	-9.289028063	-5.696036026	24.606054976
C	-9.015123158	-4.975638511	23.523689586
N	-8.672857546	-3.690215106	23.859804358
C	-12.033967997	-6.725964038	19.908925101
C	-12.601274456	-5.418209958	20.468131205
C	-11.538060047	-4.545672075	21.114906050
N	-11.882684087	-3.882660671	22.234960142
O	-10.401119810	-4.445817709	20.595114315
C	-8.003013003	-9.808969005	15.431018997
C	-8.169860544	-8.511079396	16.165768965
C	-8.183764222	-7.269190434	15.461778907
C	-8.297696651	-8.483273406	17.586814087
C	-8.281276978	-6.061310502	16.134577954
C	-8.401044864	-7.286985114	18.281180602
C	-8.379563371	-6.013847921	17.584852452
O	-8.477865662	-4.904160236	18.214730972
Cu	-7.024340386	-3.426720941	19.152011181
O	-5.693555915	-1.529221468	20.099215157
H	-8.786017744	-2.469758942	14.030469622
H	-10.780266384	-6.034867610	16.998660004
H	-12.556775360	-5.935116249	16.953159385
H	-11.096829297	-3.851058321	18.009356539
H	-12.518096481	-3.492783274	16.971679206
H	-9.548713902	-3.352803432	16.266842968
H	-10.887990368	-2.308940909	15.683561125
H	-11.008679100	-6.325266474	14.654529197
H	-4.891949809	-4.574693186	27.630733417

H	-5.188148865	-2.833304360	27.235330201
H	-6.526459861	-4.289478891	25.892013714
H	-9.124287497	-4.560198948	27.828282050
H	-8.781880205	-6.243418913	27.298680514
H	-8.499932338	-2.651921128	25.766503687
H	-8.376249403	-2.951454920	23.221363901
H	-9.052152006	-5.312609768	22.479569542
H	-11.688446232	-7.391756573	20.725631172
H	-11.169965364	-6.515269778	19.250006509
H	-13.431179262	-5.602469229	21.180219260
H	-13.026351994	-4.807895629	19.640229914
H	-11.196375996	-3.298436540	22.718569031
H	-6.921507338	-10.010768438	15.258602624
H	-8.482401030	-9.776407144	14.433106352
H	-8.123726763	-7.276046754	14.361933007
H	-8.323604993	-9.438025495	18.135111362
H	-8.321538529	-5.111391479	15.584546606
H	-8.537290803	-7.267954187	19.372678052
H	-4.657967557	-4.100878949	18.605169542
H	-6.350738472	-4.601956631	16.217113786
H	-4.228025961	-5.008306887	14.996354727
H	-4.452173220	-2.310509031	16.964302505
H	-4.934808970	-2.623581370	15.284457488
H	-6.836226138	-0.608869276	14.755746449
H	-9.234408189	-1.283526324	18.218776116
H	-10.094335928	0.424404473	16.594367955
H	-8.792312957	1.296649343	15.700670589
H	-9.705192571	-0.029532799	14.893171273
H	-4.645430523	-7.361778630	23.400381634
H	-5.858464743	-8.160595594	22.342043669
H	-6.698546103	-6.479019697	20.252810547
H	-5.480483944	-4.579662596	23.877811710
H	-5.982167033	-2.743278894	22.142101071
H	-5.764604211	-0.846598540	19.405033263
H	-4.799943784	-1.946997157	19.952174794
H	-3.274698907	-4.724254562	16.492910550
H	-4.372082355	-6.142867732	16.377055703
H	-5.665787863	-5.396922437	18.355494512
H	-3.776782932	-3.693503812	26.525260119
H	-6.365224407	-7.418959937	23.895540084
H	-10.440361798	-5.602374599	27.195648915
H	-12.793756568	-4.016131412	22.676493842
H	-12.802406601	-7.267231470	19.324062499
H	-12.829092855	-5.281623415	13.284162634
H	-13.502922385	-6.326019195	14.580992579
H	-13.537577429	-4.537244476	14.764415540
H	-9.089532202	-2.708295872	12.264547799
H	-10.303967827	-1.865777140	13.293884756
O	-8.684899088	-2.616032625	20.102271179
H	-9.345462190	-3.351000256	20.399084055
H	-8.414671709	-2.116225604	20.894315443
H	-8.408439755	-10.663858225	16.005410023
O	-3.477848995	-3.081081001	19.648007002
H	-2.660846517	-2.692209872	19.274357555
H	-3.177969540	-3.515734870	20.472458280

Model1-2H_2O (singlet)

N	-5.524525426	-4.400011544	18.133011709
C	-5.401692225	-4.234530364	16.661194726
C	-4.251983983	-5.075938041	16.102067971
C	-5.258684658	-2.740040792	16.333021795
C	-6.532691491	-1.981815841	16.529239995
C	-7.146781605	-1.049311400	15.707927346
N	-7.328082390	-2.145629450	17.654200001
C	-8.386610673	-1.339649518	17.524874103
N	-8.306538210	-0.651580420	16.356476084
C	-9.282435255	0.310894401	15.854481395
C	-9.558073965	-2.687083991	13.264063010
C	-10.241255387	-4.028284614	13.503745719
O	-10.346981161	-4.879069149	12.606859148
N	-10.764617458	-4.237528010	14.753079714
C	-11.561306628	-5.451023045	15.044861078
C	-12.940934999	-5.390954993	14.380010995
C	-11.623918207	-5.464353237	16.582345915
C	-11.510169073	-3.985364323	16.995168377
C	-10.601558528	-3.361068484	15.921633453
C	-4.835019998	-3.806053996	26.828752013
O	-5.571625779	-4.195651569	25.656378172
C	-5.686999989	-7.308017996	23.024170002
C	-5.933657648	-6.017841445	22.315951693
C	-6.397338176	-5.753060731	21.033134941
N	-5.717556156	-4.773106802	22.888359319
C	-6.042582511	-3.814011156	21.982643654
N	-6.458149522	-4.382478522	20.842220751
C	-9.370979006	-5.330980960	27.072937018
C	-9.098986274	-4.853889985	25.688502011
C	-8.692390924	-3.596016225	25.244883313
N	-9.289027985	-5.696036063	24.606054920
C	-9.005624569	-4.978126713	23.524412825
N	-8.652567421	-3.695910887	23.861265951
C	-12.033968051	-6.725964018	19.908925076
C	-12.587982510	-5.412887200	20.468759322
C	-11.515089853	-4.541823119	21.101391124
N	-11.850103370	-3.864913547	22.215945929
O	-10.379734349	-4.453911862	20.575062885
C	-8.003012968	-9.808968951	15.431019013
C	-8.179024206	-8.508925541	16.155515443
C	-8.183342540	-7.272001261	15.441570679
C	-8.322519332	-8.474193149	17.575962244
C	-8.283409490	-6.060738208	16.104629405
C	-8.429956495	-7.275009241	18.261780956
C	-8.391560696	-6.004819476	17.556204870
O	-8.468858923	-4.893740069	18.177100887
Cu	-7.000012483	-3.406724450	19.165026002
O	-5.658717869	-1.477884762	20.144977439
H	-8.786412209	-2.467576632	14.030242420
H	-10.776404697	-6.047630593	16.989960952
H	-12.552186255	-5.942281877	16.949855829
H	-11.083986896	-3.864844848	18.009568138
H	-12.508315300	-3.501409135	16.978263609
H	-9.541931812	-3.356690560	16.263710731
H	-10.885684344	-2.314692199	15.687093593
H	-11.009043040	-6.327799825	14.646932000
H	-4.890676839	-4.577591888	27.628067056
H	-5.192926166	-2.836078816	27.237715550
H	-6.522872792	-4.291113269	25.886168677
H	-9.115286928	-4.563862291	27.829008919
H	-8.792119164	-6.250236016	27.297295431
H	-8.476310671	-2.658696188	25.768214657
H	-8.345205821	-2.960611792	23.223833003
H	-9.041374964	-5.314629554	22.480075265
H	-11.685722944	-7.391370162	20.724793007
H	-11.174231960	-6.523486160	19.242017256
H	-13.411253970	-5.590323896	21.190311948
H	-13.019710834	-4.803487614	19.643642647
H	-11.157781818	-3.278933392	22.688490041
H	-6.919699891	-10.002977945	15.259903384
H	-8.481220790	-9.786230213	14.432164369
H	-8.111348786	-7.288137571	14.342610254
H	-8.355328173	-9.426561628	18.127891309
H	-8.312623919	-5.112699262	15.551247219
H	-8.574651089	-7.246012900	19.351945535
H	-4.650996044	-4.100145839	18.605942745
H	-6.350327345	-4.597793839	16.221733709
H	-4.231955092	-5.010925098	14.996133320
H	-4.444643351	-2.309532140	16.958414653
H	-4.935493983	-2.624829745	15.280899565
H	-6.852745167	-0.632291498	14.739921545
H	-9.205854309	-1.250744240	18.243634325
H	-10.091937006	0.422779475	16.596991900
H	-8.799885180	1.292539417	15.688521469
H	-9.710039938	-0.047744769	14.898887069
H	-4.644812452	-7.371517750	23.397186824
H	-5.867540430	-8.157639526	22.340711417
H	-6.698717400	-6.460596818	20.256786815
H	-5.460630637	-4.585676456	23.887374265
H	-5.945459361	-2.738199784	22.157967314
H	-5.738708413	-0.813426990	19.434436487
H	-4.780990070	-1.919002300	19.977170405
H	-3.273198300	-4.723807089	16.488743540
H	-4.371560358	-6.142158821	16.380189045

H	-5.668078489	-5.389160613	18.360099696
H	-3.776563996	-3.688263834	26.528042663
H	-6.363484380	-7.415595445	23.897285084
H	-10.443317218	-5.590449569	27.195836142
H	-12.759444467	-3.987954174	22.664094658
H	-12.810866482	-7.264131288	19.332455224
H	-12.831754340	-5.278999080	13.284160439
H	-13.502719920	-6.326259128	14.580198691
H	-13.535928092	-4.537917453	14.768254612
H	-9.090523838	-2.705363191	12.264026147
H	-10.307376066	-1.868647486	13.294822415
O	-8.664396867	-2.611311691	20.114079254
H	-9.323343243	-3.352435159	20.400785148
H	-8.394688352	-2.121835172	20.912850276
H	-8.401962238	-10.663245413	16.010677047
O	-3.477849061	-3.081081007	19.648006980
H	-2.658047002	-2.696122714	19.276352175
H	-3.180357765	-3.520943633	20.470544341

Model2-H_2O_{trans} (triplet)

N	-5.421100562	-4.442159102	18.204764402
C	-5.426688893	-4.317781431	16.728372468
C	-4.252034015	-5.075954056	16.102082983
C	-5.453475990	-2.830029868	16.342863220
C	-6.757110907	-2.144076340	16.626585161
C	-7.407601570	-1.148923241	15.912314880
N	-7.524690420	-2.410763065	17.751920048
C	-8.595448218	-1.607184730	17.729646469
N	-8.549548068	-0.819291314	16.625647504
C	-9.544326458	0.175776920	16.231815898
C	-9.558090941	-2.687146944	13.264140943
C	-10.241797884	-4.033378939	13.483594776
O	-10.359238008	-4.865486611	12.571056300
N	-10.748128172	-4.269183332	14.735398853
C	-11.552100580	-5.479906353	15.021017664
C	-12.940926056	-5.390970981	14.380059954
C	-11.594737302	-5.510837061	16.559147533
C	-11.494103610	-4.033585775	16.980759134
C	-10.585993623	-3.405083188	15.910397478
C	-4.834950022	-3.806035018	26.828777005
O	-5.692921621	-4.000705778	25.688194602
C	-5.687006958	-7.308018004	23.024166002
C	-6.004452929	-6.016505147	22.366223380
C	-6.433822100	-5.758235233	21.076651378
N	-5.914454733	-4.777226094	22.984499165
C	-6.276128909	-3.821620395	22.093946273
N	-6.598543828	-4.393914720	20.923481965
C	-9.371035881	-5.330984965	27.072935953
C	-9.195530387	-4.826266242	25.678848518
C	-8.998401481	-3.525677601	25.214644159
N	-9.289016210	-5.696054997	24.606013965
C	-9.158992243	-4.952401223	23.511938302
N	-8.988525724	-3.629697281	23.830305182
C	-12.033947928	-6.725899104	19.908807184
C	-12.672220637	-5.373129507	20.258956293
C	-11.710768277	-4.442779827	21.000223394
N	-12.083765393	-4.109287816	22.265058914
O	-10.661884873	-4.019293875	20.484359285
C	-8.002994986	-9.808936936	15.431016017
C	-8.164577641	-8.569375017	16.262913121
C	-8.191576445	-7.270059600	15.676873946
C	-8.287397030	-8.668066606	17.684161409
C	-8.289345560	-6.126141847	16.458427321
C	-8.383091382	-7.541514006	18.483691143
C	-8.350919242	-6.208216803	17.908126032
O	-8.390851980	-5.173744539	18.665669784
Cu	-7.014178275	-3.541881622	19.230658854
O	-6.200002109	-1.652297019	20.182585846
H	-8.751136631	-2.510977972	14.005059954
H	-10.731295335	-6.082936548	16.950736806
H	-12.510818316	-6.004901755	16.935303479
H	-11.086149570	-3.912962034	18.004457508
H	-12.495345680	-3.556372255	16.951185967
H	-9.524326942	-3.406342399	16.243460576
H	-10.864751576	-2.355731693	15.686025719
H	-11.016023746	-6.358152319	14.604085546
H	-4.885570596	-4.660225107	27.538505183
H	-5.085271075	-2.869036431	27.371291300
H	-6.626274262	-4.063472283	25.986597055
H	-9.227034966	-4.527709726	27.821200983
H	-8.654393089	-6.148659136	27.294778186
H	-8.907969071	-2.562310060	25.727545484
H	-8.871210929	-2.860064041	23.167914431
H	-9.181964240	-5.295907063	22.468967132
H	-11.780269896	-7.297103199	20.825194138
H	-11.100475964	-6.573208588	19.331865049
H	-13.598535761	-5.521973493	20.850399533
H	-12.968278090	-4.846212759	19.327666611
H	-11.462694048	-3.532813521	22.836937956
H	-8.747883568	-10.580409588	15.716746538
H	-7.002925436	-10.261925882	15.612664638
H	-8.143640694	-7.175698797	14.580896635
H	-8.303308078	-9.667406226	18.146914778
H	-8.349450455	-5.133807447	15.991319310
H	-8.491124837	-7.623861890	19.575141920
H	-4.592427468	-3.992180914	18.631982460
H	-6.366956234	-4.788946819	16.380247606
H	-4.322080696	-5.046699687	14.996648643
H	-4.622128111	-2.307691156	16.868754385
H	-5.236740169	-2.731115494	15.262037861
H	-7.142670120	-0.641744323	14.979179901
H	-9.402350657	-1.593852690	18.469179325
H	-10.369930839	0.168293449	16.964506322
H	-9.083723393	1.181457156	16.206411824
H	-9.941508499	-0.068276727	15.228411867
H	-4.654945565	-7.316948317	23.431188555
H	-5.783280319	-8.136964790	22.299535069
H	-6.647806590	-6.463882741	20.271676358
H	-5.686978602	-4.587122857	23.993067172
H	-6.292184494	-2.750419203	22.306767820
H	-5.229917063	-1.910920842	20.123270379
H	-3.281354360	-4.630075803	16.402281662
H	-4.260903770	-6.138078270	16.417920829
H	-5.412016501	-5.427833630	18.484676713
H	-3.798999540	-3.726278999	26.448105183
H	-6.380657503	-7.505655561	23.868512614
H	-10.389517030	-5.750353044	27.211112018
H	-12.912515690	-4.507387500	22.707443106
H	-12.724071048	-7.341290369	19.299232015
H	-12.850369634	-5.268641036	13.283716474
H	-13.514276237	-6.318754153	14.579036832
H	-13.514390706	-4.532822539	14.786864503
H	-9.132422537	-2.669577077	12.245771166
H	-10.292148509	-1.860854960	13.365216145
H	-8.093843390	-9.598664450	14.349114673
O	-3.752096992	-2.769402981	19.892349012
H	-2.991478187	-2.217190020	19.617570784
H	-3.437913165	-3.217715106	20.704537791
H	-6.301208958	-0.917325269	19.546143291

Model2-H_2O_{trans} (singlet)

N	-5.448926000	-4.482510000	18.200781000
C	-5.440208000	-4.342908000	16.724689000
C	-4.252034000	-5.075954000	16.102083000
C	-5.484052000	-2.851207000	16.354358000
C	-6.794203000	-2.173561000	16.630912000
C	-7.428700000	-1.163793000	15.921919000
N	-7.578603000	-2.448209000	17.744140000
C	-8.640252000	-1.632753000	17.720177000
N	-8.574808000	-0.831070000	16.626984000
C	-9.556791000	0.176742000	16.234265000
C	-9.558091000	-2.687147000	13.264141000
C	-10.234155000	-4.038055000	13.481713000
O	-10.341854000	-4.872877000	12.570961000
N	-10.746441000	-4.275559000	14.732016000
C	-11.550416000	-5.486076000	15.015430000
C	-12.940926000	-5.390971000	14.380060000
C	-11.591213000	-5.521516000	16.552939000
C	-11.496207000	-4.044851000	16.979045000
C	-10.602527000	-3.402974000	15.903225000

C	-4.834950000	-3.806035000	26.828777000
O	-5.711324000	-3.991797000	25.700126000
C	-5.687007000	-7.308018000	23.024166000
C	-6.038092000	-6.026543000	22.367196000
C	-6.474715000	-5.783404000	21.077727000
N	-5.985478000	-4.785081000	22.984400000
C	-6.376300000	-3.841790000	22.091765000
N	-6.680819000	-4.426400000	20.923146000
C	-9.371036000	-5.330985000	27.072936000
C	-9.219811000	-4.821914000	25.677320000
C	-9.077162000	-3.515540000	25.209867000
N	-9.289016000	-5.696055000	24.606014000
C	-9.200879000	-4.949374000	23.510162000
N	-9.077658000	-3.620888000	23.825537000
C	-12.033948000	-6.725899000	19.908807000
C	-12.696249000	-5.384824000	20.259671000
C	-11.763776000	-4.462112000	21.045422000
N	-12.169418000	-4.165376000	22.309488000
O	-10.707332000	-4.016338000	20.565432000
C	-8.002995000	-9.808937000	15.431016000
C	-8.140683000	-8.563252000	16.261473000
C	-8.202889000	-7.265462000	15.669821000
C	-8.218606000	-8.653846000	17.687734000
C	-8.311541000	-6.120238000	16.447508000
C	-8.320543000	-7.524858000	18.483683000
C	-8.360633000	-6.193628000	17.900203000
O	-8.489138000	-5.153614000	18.640760000
Cu	-7.081212000	-3.581970000	19.229365000
O	-6.221875000	-1.735071000	20.134183000
H	-8.779673000	-2.486586000	14.028350000
H	-10.725690000	-6.092164000	16.941856000
H	-12.505274000	-6.020470000	16.927539000
H	-11.078015000	-3.925876000	17.999021000
H	-12.501054000	-3.574745000	16.962674000
H	-9.541014000	-3.379826000	16.234368000
H	-10.902897000	-2.360704000	15.672686000
H	-11.017402000	-6.363594000	14.593386000
H	-4.902826000	-4.647660000	27.552097000
H	-5.050497000	-2.853918000	27.359905000
H	-6.641383000	-4.021685000	26.011693000
H	-9.241711000	-4.524294000	27.820247000
H	-8.632166000	-6.130180000	27.289109000
H	-9.016803000	-2.548893000	25.720904000
H	-9.003305000	-2.849187000	23.159232000
H	-9.226367000	-5.293798000	22.467751000
H	-11.790527000	-7.303036000	20.824233000
H	-11.091334000	-6.553030000	19.352162000
H	-13.639325000	-5.550710000	20.819132000
H	-12.965466000	-4.844723000	19.327874000
H	-11.570293000	-3.594062000	22.909245000
H	-8.789823000	-10.545566000	15.698362000
H	-7.031276000	-10.306136000	15.645508000
H	-8.176714000	-7.175379000	14.572795000
H	-8.202664000	-9.649952000	18.157139000
H	-8.396396000	-5.130240000	15.978629000
H	-8.409423000	-7.607651000	19.576690000
H	-4.614609000	-4.044289000	18.625557000
H	-6.371068000	-4.818090000	16.359782000
H	-4.302652000	-5.035118000	14.995615000
H	-4.661905000	-2.327148000	16.893639000
H	-5.257192000	-2.737114000	15.276887000
H	-7.148038000	-0.647221000	14.998590000
H	-9.453166000	-1.618890000	18.453210000
H	-10.375831000	0.189060000	16.974410000
H	-9.079766000	1.174315000	16.197586000
H	-9.967867000	-0.066409000	15.236206000
H	-4.658102000	-7.288013000	23.438851000
H	-5.753791000	-8.138437000	22.297874000
H	-6.657143000	-6.496484000	20.271468000
H	-5.754232000	-4.589630000	23.990041000
H	-6.421964000	-2.770974000	22.301626000
H	-5.245776000	-1.984674000	20.082855000
H	-3.290108000	-4.623952000	16.421842000
H	-4.251636000	-6.142337000	16.404274000
H	-5.426527000	-5.472773000	18.462037000
H	-3.801403000	-3.763429000	26.435696000
H	-6.380489000	-7.527003000	23.863472000
H	-10.377403000	-5.776205000	27.219429000
H	-13.008493000	-4.576507000	22.719234000
H	-12.703228000	-7.344123000	19.279245000
H	-12.853716000	-5.257241000	13.284674000
H	-13.514061000	-6.320515000	14.571382000
H	-13.512260000	-4.536857000	14.798290000
H	-9.099808000	-2.680507000	12.259829000
H	-10.307458000	-1.870634000	13.324828000
H	-8.057509000	-9.595630000	14.347723000
O	-3.752097000	-2.769403000	19.892349000
H	-3.015000000	-2.188845000	19.612421000
H	-3.427766000	-3.182718000	20.718888000
H	-6.329017000	-1.005114000	19.492994000

Model3-OH$_{trans}$ (triplet)

N	-5.441237000	-4.344682000	18.163320000
C	-5.382714000	-4.229674000	16.688318000
C	-4.252062000	-5.075951000	16.102093000
C	-5.280492000	-2.742240000	16.308621000
C	-6.557369000	-1.993276000	16.533713000
C	-7.216032000	-1.093590000	15.708669000
N	-7.309016000	-2.133953000	17.690692000
C	-8.385523000	-1.352537000	17.575484000
N	-8.360092000	-0.695618000	16.384691000
C	-9.361296000	0.245526000	15.895580000
C	-9.558087000	-2.687147000	13.264145000
C	-10.250119000	-4.025544000	13.492857000
O	-10.372816000	-4.861052000	12.582043000
N	-10.760036000	-4.247528000	14.743152000
C	-11.552394000	-5.465242000	15.027999000
C	-12.940922000	-5.390967000	14.380066000
C	-11.586409000	-5.503104000	16.566455000
C	-11.478499000	-4.029608000	16.999951000
C	-10.584615000	-3.387751000	15.924321000
C	-4.835028000	-3.806064000	26.828752000
O	-5.606166000	-4.370504000	25.756615000
C	-5.687009000	-7.308026000	23.024174000
C	-5.902638000	-6.007384000	22.336346000
C	-6.299872000	-5.725954000	21.037298000
N	-5.747340000	-4.773699000	22.949612000
C	-6.056817000	-3.803183000	22.049152000
N	-6.395056000	-4.357579000	20.879995000
C	-9.370995000	-5.330978000	27.072929000
C	-9.114082000	-4.843765000	25.681851000
C	-8.752324000	-3.574654000	25.221849000
N	-9.288973000	-5.696027000	24.606019000
C	-9.048996000	-4.972797000	23.515014000
N	-8.730890000	-3.680746000	23.836684000
C	-12.033945000	-6.725892000	19.908808000
C	-12.627444000	-5.414942000	20.431679000
C	-11.572714000	-4.548685000	21.124445000
N	-11.966944000	-3.952975000	22.285332000
O	-10.443363000	-4.383806000	20.642984000
C	-8.002981000	-9.808948000	15.431013000
C	-8.129407000	-8.501930000	16.172298000
C	-8.161187000	-7.260711000	15.471468000
C	-8.201153000	-8.462747000	17.595855000
C	-8.225772000	-6.047756000	16.144798000
C	-8.267615000	-7.261192000	18.291761000
C	-8.265960000	-5.985760000	17.598777000
O	-8.332066000	-4.872282000	18.228584000
Cu	-6.893820000	-3.302646000	19.249386000
H	-8.794550000	-2.474762000	14.039852000
H	-10.722177000	-6.079039000	16.949766000
H	-12.501940000	-5.996645000	16.945250000
H	-11.041701000	-3.924371000	18.012355000
H	-12.479626000	-3.550908000	16.998720000
H	-9.521392000	-3.384433000	16.254789000
H	-10.875435000	-2.339677000	15.706510000
H	-11.005811000	-6.335389000	14.608112000
H	-5.046119000	-4.312311000	27.795954000
H	-5.014637000	-2.714309000	26.948596000
H	-6.565775000	-4.238188000	25.931323000
H	-9.156931000	-4.549893000	27.828088000

H	-8.748571000	-6.219977000	27.303584000
H	-8.567666000	-2.625233000	25.735992000
H	-8.495543000	-2.943224000	23.165436000
H	-9.104292000	-5.300701000	22.468408000
H	-11.724494000	-7.384944000	20.746072000
H	-11.135900000	-6.513337000	19.295900000
H	-13.489027000	-5.599991000	21.106341000
H	-13.016713000	-4.812157000	19.581785000
H	-11.286590000	-3.400681000	22.812265000
H	-8.405091000	-10.655338000	16.020800000
H	-6.932117000	-10.029886000	15.223523000
H	-8.143410000	-7.266863000	14.369559000
H	-8.211985000	-9.413877000	18.151866000
H	-8.282289000	-5.103363000	15.586557000
H	-8.357429000	-7.241082000	19.388073000
H	-4.586026000	-3.947427000	18.601296000
H	-6.343482000	-4.619159000	16.300877000
H	-4.278285000	-5.050246000	14.994045000
H	-4.449479000	-2.282785000	16.889460000
H	-5.001871000	-2.651375000	15.241125000
H	-6.962695000	-0.697726000	14.720500000
H	-9.187414000	-1.257344000	18.314216000
H	-10.163933000	0.341340000	16.648096000
H	-8.902195000	1.237775000	15.724005000
H	-9.794101000	-0.120645000	14.945133000
H	-4.664049000	-7.383098000	23.447032000
H	-5.831325000	-8.142344000	22.313447000
H	-6.540632000	-6.421762000	20.229881000
H	-5.528600000	-4.610153000	23.960662000
H	-6.064448000	-2.726760000	22.246317000
H	-3.260269000	-4.706129000	16.436369000
H	-4.351284000	-6.132797000	16.421168000
H	-5.501049000	-5.329273000	18.437291000
H	-3.766751000	-3.959876000	26.581300000
H	-6.403789000	-7.438257000	23.862085000
H	-10.430615000	-5.640895000	27.188000000
H	-12.859748000	-4.171522000	22.727592000
H	-12.765789000	-7.279038000	19.287463000
H	-12.842807000	-5.260244000	13.285173000
H	-13.503957000	-6.327734000	14.570715000
H	-13.528063000	-4.542904000	14.790320000
H	-9.081734000	-2.702459000	12.268149000
H	-10.304085000	-1.865463000	13.292225000
O	-7.400168000	-1.900409000	20.479910000
H	-7.446957000	-1.076179000	19.958211000
H	-8.518089000	-9.771243000	14.451165000
O	-3.498735000	-2.848962000	19.738629000
H	-4.017892000	-2.988788000	20.557951000
H	-3.631736000	-1.895826000	19.563511000

Model3-OH$_{trans}$ (singlet)

N	-5.406085000	-4.578116000	18.230949000
C	-5.400504000	-4.346825000	16.774936000
C	-4.252062000	-5.075951000	16.102093000
C	-5.399419000	-2.829540000	16.498487000
C	-6.729485000	-2.163343000	16.680707000
C	-7.329076000	-1.155602000	15.939238000
N	-7.586234000	-2.459092000	17.733901000
C	-8.645910000	-1.650511000	17.656480000
N	-8.521777000	-0.838845000	16.573789000
C	-9.488441000	0.158945000	16.127198000
C	-9.558087000	-2.687147000	13.264145000
C	-10.260102000	-4.026530000	13.464700000
O	-10.392251000	-4.843063000	12.538703000
N	-10.754719000	-4.273197000	14.716030000
C	-11.545901000	-5.490348000	15.003019000
C	-12.940922000	-5.390967000	14.380066000
C	-11.564833000	-5.534978000	16.542053000
C	-11.477433000	-4.059111000	16.969804000
C	-10.574248000	-3.425614000	15.899728000
C	-4.835028000	-3.806064000	26.828752000
O	-5.703547000	-4.219094000	25.760919000
C	-5.687009000	-7.308026000	23.024174000
C	-6.091065000	-6.039726000	22.377268000
C	-6.587686000	-5.822075000	21.105969000
N	-6.011503000	-4.787493000	22.969893000
C	-6.441408000	-3.861781000	22.074181000
N	-6.800612000	-4.471837000	20.941590000
C	-9.370995000	-5.330978000	27.072929000
C	-9.221858000	-4.821616000	25.676462000
C	-9.073715000	-3.515797000	25.208304000
N	-9.288973000	-5.696027000	24.606019000
C	-9.194359000	-4.950557000	23.510065000
N	-9.072281000	-3.622526000	23.824442000
C	-12.033945000	-6.725892000	19.908808000
C	-12.726374000	-5.395135000	20.245199000
C	-11.816645000	-4.462266000	21.046464000
N	-12.184446000	-4.262342000	22.343246000
O	-10.808078000	-3.933483000	20.553873000
C	-8.002981000	-9.808948000	15.431013000
C	-8.107258000	-8.542595000	16.266576000
C	-8.131277000	-7.249506000	15.669901000
C	-8.184566000	-8.591694000	17.684768000
C	-8.194720000	-6.083089000	16.436237000
C	-8.239240000	-7.434229000	18.467275000
C	-8.239806000	-6.121504000	17.877120000
O	-8.408704000	-5.045909000	18.613129000
Cu	-7.122263000	-3.631944000	19.219968000
H	-8.688938000	-2.579921000	13.946498000
H	-10.685156000	-6.092048000	16.917577000
H	-12.469773000	-6.044158000	16.926185000
H	-11.068107000	-3.937422000	17.992683000
H	-12.481965000	-3.586886000	16.942459000
H	-9.511863000	-3.441984000	16.226923000
H	-10.843541000	-2.371105000	15.688080000
H	-11.012181000	-6.361951000	14.569931000
H	-5.007219000	-4.398705000	27.753574000
H	-4.948862000	-2.725502000	27.067668000
H	-6.637944000	-4.079054000	26.024756000
H	-9.268443000	-4.518869000	27.818621000
H	-8.611803000	-6.109035000	27.297123000
H	-9.011071000	-2.548770000	25.718704000
H	-8.974490000	-2.855378000	23.155652000
H	-9.206804000	-5.297893000	22.468881000
H	-11.786180000	-7.291180000	20.830669000
H	-11.089833000	-6.539322000	19.357418000
H	-13.675559000	-5.576763000	20.790369000
H	-12.987237000	-4.861105000	19.308144000
H	-11.575465000	-3.715750000	22.956186000
H	-8.394956000	-10.687344000	15.978382000
H	-6.939857000	-10.016143000	15.179824000
H	-8.118153000	-7.162466000	14.571196000
H	-8.215566000	-9.573329000	18.184407000
H	-8.262993000	-5.104968000	15.939907000
H	-8.353970000	-7.514365000	19.558090000
H	-4.576451000	-4.140985000	18.674298000
H	-6.345090000	-4.763612000	16.377271000
H	-4.292566000	-4.972977000	14.997458000
H	-4.647368000	-2.359407000	17.171217000
H	-5.057153000	-2.638187000	15.463289000
H	-7.002465000	-0.635334000	15.033567000
H	-9.494819000	-1.642917000	18.346974000
H	-10.316370000	0.211738000	16.856047000
H	-9.002724000	1.150296000	16.053219000
H	-9.891863000	-0.121601000	15.135452000
H	-4.625091000	-7.285532000	23.346061000
H	-5.817560000	-8.150453000	22.320059000
H	-6.781402000	-6.543364000	20.310876000
H	-5.743084000	-4.583146000	23.959510000
H	-6.450601000	-2.781717000	22.236525000
H	-3.272245000	-4.684275000	16.448820000
H	-4.290007000	-6.157702000	16.342943000
H	-5.367721000	-5.582189000	18.427128000
H	-3.795371000	-3.981717000	26.491231000
H	-6.300814000	-7.514544000	23.926044000
H	-10.366303000	-5.802580000	27.212773000
H	-12.973528000	-4.753397000	22.763326000
H	-12.685721000	-7.362485000	19.278174000
H	-12.860095000	-5.247032000	13.285357000
H	-13.515368000	-6.321543000	14.567442000
H	-13.508734000	-4.540173000	14.810592000

H	-9.207766000	-2.628997000	12.218816000
H	-10.248682000	-1.842540000	13.466379000
O	-6.169243000	-2.115766000	19.966518000
H	-6.318574000	-1.386451000	19.332902000
H	-8.548079000	-9.704705000	14.472384000
O	-3.498735000	-2.848962000	19.738629000
H	-4.433115000	-2.503238000	19.879803000
H	-3.089952000	-2.169431000	19.169323000

Model4-OH$_{cis}$ (triplet)

N	-5.475019000	-4.333031000	18.149891000
C	-5.376836000	-4.209711000	16.674814000
C	-4.252062000	-5.075951000	16.102093000
C	-5.238137000	-2.722009000	16.308832000
C	-6.493806000	-1.941980000	16.550541000
C	-7.153731000	-1.045828000	15.723221000
N	-7.220663000	-2.046722000	17.727564000
C	-8.285818000	-1.252250000	17.621913000
N	-8.277103000	-0.616931000	16.419043000
C	-9.278938000	0.322543000	15.930530000
C	-9.558087000	-2.687147000	13.264145000
C	-10.251068000	-4.022863000	13.497401000
O	-10.370546000	-4.865137000	12.592091000
N	-10.766692000	-4.234115000	14.746789000
C	-11.555891000	-5.451639000	15.036732000
C	-12.940922000	-5.390967000	14.380066000
C	-11.598823000	-5.480169000	16.575280000
C	-11.475654000	-4.006162000	17.004967000
C	-10.587870000	-3.366651000	15.922630000
C	-4.835028000	-3.806064000	26.828752000
O	-5.617765000	-4.097076000	25.660781000
C	-5.687009000	-7.308026000	23.024174000
C	-5.917148000	-6.019588000	22.316655000
C	-6.329578000	-5.765490000	21.016080000
N	-5.771752000	-4.773207000	22.905606000
C	-6.108020000	-3.823207000	21.990761000
N	-6.446438000	-4.401942000	20.833825000
C	-9.370995000	-5.330978000	27.072929000
C	-9.124454000	-4.838911000	25.680630000
C	-8.776055000	-3.567918000	25.216423000
N	-9.288973000	-5.696027000	24.606019000
C	-9.048863000	-4.976795000	23.514620000
N	-8.745373000	-3.679536000	23.831729000
C	-12.033945000	-6.725892000	19.908808000
C	-12.555102000	-5.379135000	20.412730000
C	-11.459153000	-4.533828000	21.056296000
N	-11.838868000	-3.755511000	22.100062000
O	-10.293678000	-4.543023000	20.620093000
C	-8.002981000	-9.808948000	15.431013000
C	-8.141965000	-8.478278000	16.118868000
C	-8.131535000	-7.268328000	15.364277000
C	-8.269493000	-8.385512000	17.535447000
C	-8.207653000	-6.030275000	15.984599000
C	-8.358748000	-7.156738000	18.178940000
C	-8.317595000	-5.916779000	17.429294000
O	-8.418412000	-4.775553000	18.002307000
Cu	-7.053181000	-3.416039000	19.187402000
H	-8.798188000	-2.466451000	14.041775000
H	-10.746239000	-6.067939000	16.965061000
H	-12.523481000	-5.960350000	16.949515000
H	-11.022658000	-3.902076000	18.009605000
H	-12.473714000	-3.521448000	17.016759000
H	-9.524288000	-3.362136000	16.251288000
H	-10.883444000	-2.320480000	15.701346000
H	-11.003524000	-6.322373000	14.625777000
H	-4.864633000	-4.635509000	27.570348000
H	-5.168241000	-2.868179000	27.325339000
H	-6.562592000	-4.202545000	25.911557000
H	-9.156656000	-4.550728000	27.828871000
H	-8.742531000	-6.217412000	27.296480000
H	-8.591529000	-2.616934000	25.727409000
H	-8.502912000	-2.947406000	23.155721000
H	-9.094163000	-5.316438000	22.471692000
H	-11.730067000	-7.377812000	20.753301000
H	-11.146678000	-6.571073000	19.264603000
H	-13.405815000	-5.506298000	21.114190000
H	-12.943124000	-4.779354000	19.559561000
H	-11.140488000	-3.182495000	22.578561000
H	-8.355659000	-10.642169000	16.068792000
H	-6.935350000	-10.005399000	15.185584000
H	-8.067496000	-7.322735000	14.265718000
H	-8.310421000	-9.314912000	18.125390000
H	-8.222882000	-5.104024000	15.394711000
H	-8.499660000	-7.082986000	19.267502000
H	-4.636234000	-3.930489000	18.612723000
H	-6.337115000	-4.574491000	16.263289000
H	-4.254786000	-5.036311000	14.994134000
H	-4.390165000	-2.291084000	16.887129000
H	-4.964665000	-2.630786000	15.239815000
H	-6.915837000	-0.670603000	14.723061000
H	-9.051702000	-1.150988000	18.398634000
H	-10.062894000	0.444371000	16.698911000
H	-8.817288000	1.306812000	15.722540000
H	-9.739467000	-0.062187000	14.999964000
H	-4.667602000	-7.362270000	23.458355000
H	-5.811357000	-8.153124000	22.322430000
H	-6.562941000	-6.479801000	20.221989000
H	-5.541530000	-4.581261000	23.908105000
H	-6.120451000	-2.747827000	22.191717000
H	-3.259139000	-4.732982000	16.460960000
H	-4.381838000	-6.134594000	16.404994000
H	-5.513534000	-5.322760000	18.410796000
H	-3.787711000	-3.670352000	26.497563000
H	-6.411721000	-7.439393000	23.855298000
H	-10.428253000	-5.646722000	27.193971000
H	-12.776657000	-3.806859000	22.498733000
H	-12.809327000	-7.258704000	19.324121000
H	-12.836840000	-5.270208000	13.284581000
H	-13.499503000	-6.329297000	14.576366000
H	-13.535740000	-4.542454000	14.778475000
H	-9.078153000	-2.706961000	12.269888000
H	-10.304447000	-1.865248000	13.285519000
O	-8.355002000	-2.472362000	20.263514000
H	-8.984857000	-3.203707000	20.483734000
H	-8.556161000	-9.827226000	14.470908000
O	-3.498735000	-2.848962000	19.738629000
H	-3.885377000	-3.115073000	20.597911000
H	-3.792941000	-1.920219000	19.649651000

Model4-OH$_{cis}$ (singlet)

N	-5.464127000	-4.323453000	18.150412000
C	-5.368361000	-4.195215000	16.673496000
C	-4.252062000	-5.075951000	16.102093000
C	-5.206873000	-2.709708000	16.313970000
C	-6.449107000	-1.920559000	16.582910000
C	-7.138679000	-1.040427000	15.763987000
N	-7.141739000	-2.015563000	17.780621000
C	-8.218736000	-1.233638000	17.694518000
N	-8.247074000	-0.614176000	16.484414000
C	-9.269203000	0.311642000	16.010733000
C	-9.558087000	-2.687147000	13.264145000
C	-10.256536000	-4.020271000	13.491636000
O	-10.382188000	-4.856884000	12.581516000
N	-10.768446000	-4.232896000	14.740844000
C	-11.553077000	-5.452579000	15.031464000
C	-12.940922000	-5.390967000	14.380066000
C	-11.585156000	-5.486028000	16.570254000
C	-11.463890000	-4.012639000	17.003532000
C	-10.581674000	-3.369765000	15.918853000
C	-4.835028000	-3.806064000	26.828752000
O	-5.609111000	-4.110303000	25.658579000
C	-5.687009000	-7.308026000	23.024174000
C	-5.875265000	-6.010551000	22.318366000
C	-6.250078000	-5.743611000	21.009038000
N	-5.720449000	-4.769753000	22.916523000
C	-6.014477000	-3.807807000	22.001165000
N	-6.333197000	-4.374873000	20.832611000
C	-9.370995000	-5.330978000	27.072929000
C	-9.111207000	-4.842791000	25.681302000
C	-8.734188000	-3.579217000	25.218380000

N	-9.288973000	-5.696027000	24.606019000
C	-9.027362000	-4.982963000	23.515376000
N	-8.696995000	-3.692691000	23.833670000
C	-12.033945000	-6.725892000	19.908808000
C	-12.527604000	-5.365529000	20.402178000
C	-11.412500000	-4.534693000	21.029573000
N	-11.773894000	-3.727252000	22.057328000
O	-10.247395000	-4.579906000	20.592610000
C	-8.002981000	-9.808948000	15.431013000
C	-8.123901000	-8.469340000	16.110299000
C	-8.108145000	-7.265302000	15.354367000
C	-8.240236000	-8.363710000	17.524898000
C	-8.169705000	-6.020049000	15.970887000
C	-8.319160000	-7.128628000	18.162663000
C	-8.274302000	-5.894247000	17.411336000
O	-8.365228000	-4.742831000	17.979148000
Cu	-6.966009000	-3.430425000	19.189030000
H	-8.797678000	-2.474221000	14.043645000
H	-10.726303000	-6.069197000	16.952902000
H	-12.505902000	-5.970050000	16.949507000
H	-11.002034000	-3.912764000	18.004112000
H	-12.462415000	-3.528733000	17.022535000
H	-9.516257000	-3.368563000	16.242999000
H	-10.878829000	-2.322749000	15.702774000
H	-11.000377000	-6.320562000	14.615256000
H	-4.869372000	-4.627905000	27.578414000
H	-5.173209000	-2.863542000	27.312789000
H	-6.556613000	-4.212345000	25.902438000
H	-9.140169000	-4.556903000	27.830327000
H	-8.762782000	-6.231618000	27.295240000
H	-8.535030000	-2.631347000	25.729630000
H	-8.438012000	-2.965877000	23.158485000
H	-9.073970000	-5.322696000	22.472334000
H	-11.738929000	-7.375604000	20.758111000
H	-11.146704000	-6.593526000	19.259343000
H	-13.376354000	-5.469278000	21.109918000
H	-12.908877000	-4.766163000	19.545695000
H	-11.062945000	-3.164352000	22.528951000
H	-8.413128000	-10.625542000	16.056889000
H	-6.935679000	-10.051786000	15.229839000
H	-8.054832000	-7.322694000	14.254911000
H	-8.283567000	-9.288306000	18.123229000
H	-8.193114000	-5.098478000	15.372954000
H	-8.452481000	-7.051103000	19.252278000
H	-4.620572000	-3.924959000	18.614373000
H	-6.333235000	-4.552218000	16.265257000
H	-4.257518000	-5.025886000	14.995024000
H	-4.343564000	-2.293868000	16.879930000
H	-4.951626000	-2.618880000	15.240788000
H	-6.931024000	-0.676893000	14.752860000
H	-8.970400000	-1.139327000	18.485079000
H	-10.051297000	0.411670000	16.784168000
H	-8.826345000	1.305937000	15.809505000
H	-9.726230000	-0.074041000	15.078903000
H	-4.678672000	-7.383804000	23.480248000
H	-5.812094000	-8.146253000	22.314612000
H	-6.484875000	-6.448693000	20.207623000
H	-5.508030000	-4.586026000	23.926028000
H	-6.012533000	-2.733902000	22.209957000
H	-3.254625000	-4.749385000	16.462972000
H	-4.399987000	-6.134453000	16.396386000
H	-5.521422000	-5.314415000	18.406530000
H	-3.785536000	-3.672601000	26.503683000
H	-6.432326000	-7.429327000	23.838396000
H	-10.435150000	-5.623325000	27.191983000
H	-12.712124000	-3.752671000	22.457704000
H	-12.822056000	-7.249316000	19.332734000
H	-12.840552000	-5.266517000	13.284648000
H	-13.498903000	-6.330033000	14.575009000
H	-13.534916000	-4.544016000	14.783114000
H	-9.077482000	-2.704416000	12.270077000
H	-10.299730000	-1.861151000	13.289501000
O	-8.296621000	-2.572288000	20.231971000
H	-8.968438000	-3.285443000	20.393646000
H	-8.521031000	-9.814915000	14.451412000
O	-3.498735000	-2.848962000	19.738629000
H	-3.879022000	-3.104629000	20.604128000
H	-3.764226000	-1.911084000	19.654460000

Chapter 4

Cu(I)-Model1

N	28.215565000	43.833603000	14.802045000
C	28.237036000	45.242815000	15.258656000
C	29.222563000	45.459548000	16.416980000
C	26.807082000	45.692606000	15.636391000
C	25.839986000	45.836122000	14.490270000
C	24.679648000	46.583774000	14.437286000
N	26.024907000	45.227324000	13.250860000
C	25.023865000	45.621153000	12.460982000
N	24.177613000	46.428454000	13.156958000
C	25.273394000	50.134919000	14.692992000
C	26.230616000	50.867845000	13.769258000
O	26.873841000	51.868114000	14.139473000
N	26.321595000	50.375974000	12.500144000
C	27.083647000	51.096626000	11.459159000
C	26.361783000	52.400819000	11.091048000
C	27.147479000	50.065801000	10.313926000
C	25.831945000	49.277348000	10.459084000
C	25.663582000	49.164411000	11.982562000
C	28.249623000	41.484476000	19.386365000
C	28.681778000	40.578429000	18.229595000
O	28.541822000	39.344472000	18.272106000
C	26.960492000	42.282839000	19.099724000
O	27.133339000	43.223681000	18.052722000
N	29.242463000	41.210464000	17.149285000
C	29.726447000	40.458581000	15.992765000
C	30.933867000	41.196377000	15.379389000
O	30.872680000	42.408883000	15.109909000
C	28.656447000	40.241828000	14.904211000
N	32.026877000	40.438232000	15.109548000
C	31.328008000	41.248216000	10.406980000
C	29.971724000	41.524580000	10.953197000
C	29.347092000	42.700975000	11.305393000
N	29.039606000	40.530403000	11.216484000
C	27.908757000	41.109855000	11.714417000
N	28.069076000	42.431370000	11.787541000
C	31.653272000	50.515371000	11.949050000
C	30.725100000	49.344542000	11.732896000
C	30.800070000	48.565648000	10.555840000
C	29.788054000	48.952164000	12.715367000
C	30.019577000	47.413991000	10.380551000
C	28.996388000	47.805042000	12.554277000
C	29.124663000	46.994642000	11.398453000
O	28.408738000	45.858420000	11.305410000
C	24.693272000	39.845507000	16.704954000
C	24.783616000	40.247010000	15.231736000
C	25.558864000	41.546652000	14.941735000
O	26.095906000	42.153949000	15.925156000
O	25.627120000	41.914152000	13.729543000
C	28.070210000	48.035912000	7.294083000
C	26.821280000	47.146788000	7.399281000
C	26.835426000	46.167792000	8.599595000
O	27.959471000	45.583803000	8.840756000
O	25.771379000	46.009832000	9.253852000
Cu	27.132548000	43.621120000	12.990419000
H	25.550546000	49.064251000	14.784464000
H	28.015313000	49.392603000	10.468717000
H	27.259635000	50.551497000	9.324159000
H	24.986294000	49.855262000	10.027838000
H	25.841343000	48.283392000	9.971177000
H	26.169042000	48.254766000	12.378141000
H	24.600092000	49.115521000	12.290242000
H	28.095039000	51.328331000	11.855754000
H	26.673501000	42.821891000	20.031839000
H	26.134089000	41.573077000	18.861980000
H	26.734405000	42.812287000	17.234664000
H	28.094353000	40.825886000	20.264268000
H	27.782015000	39.726806000	15.345248000

H	29.064791000	39.616578000	14.084906000
H	28.310900000	41.200225000	14.471465000
H	30.033578000	39.467780000	16.386133000
H	29.177560000	42.232829000	17.078737000
H	32.075426000	39.447389000	15.349576000
H	31.880692000	42.198066000	10.278690000
H	31.280799000	40.742255000	9.419202000
H	29.709643000	43.726140000	11.247377000
H	27.032406000	40.567249000	12.061662000
H	32.613475000	50.192158000	12.410643000
H	31.910481000	51.020944000	10.994912000
H	31.498560000	48.866015000	9.755804000
H	29.666708000	49.565139000	13.624592000
H	30.072376000	46.822391000	9.454739000
H	28.248269000	47.522570000	13.309945000
H	28.227032000	45.628395000	10.295122000
H	24.195967000	40.634221000	17.305330000
H	25.703333000	39.695406000	17.139607000
H	23.771806000	40.360097000	14.783775000
H	25.276008000	39.448349000	14.633211000
H	28.221407000	48.624323000	8.220574000
H	28.976518000	47.411978000	7.157765000
H	25.896287000	47.756547000	7.469947000
H	26.718709000	46.533857000	6.473826000
H	27.632234000	43.256030000	15.434929000
H	29.167790000	43.431923000	14.815821000
H	28.571321000	45.848904000	14.389900000
H	26.869083000	46.673822000	16.152456000
H	26.409726000	44.979018000	16.392796000
H	24.171856000	47.191659000	15.181615000
H	24.945060000	45.414266000	11.392403000
H	23.343525000	46.882528000	12.784032000
H	29.173662000	39.530471000	11.061318000
H	24.119786000	38.903484000	16.831539000
H	31.209361000	51.273835000	12.627064000
H	27.998136000	48.741667000	6.440008000
H	26.940094000	52.966241000	10.330448000
H	25.354595000	52.191099000	10.674579000
H	26.249494000	53.039425000	11.988605000
H	31.918008000	40.597004000	11.086610000
H	32.829702000	40.867336000	14.642527000
H	30.230204000	45.087311000	16.140149000
H	29.310156000	46.534501000	16.683503000
H	28.876942000	44.896561000	17.310160000
H	25.307570000	50.608225000	15.690712000
H	24.233649000	50.167887000	14.306377000
H	29.061940000	42.204092000	19.626647000

Cu(I)-Model2

N	28.144764000	43.604936000	15.152636000
C	28.190443000	45.071818000	15.357143000
C	29.223990000	45.461007000	16.419997000
C	26.775023000	45.575744000	15.702182000
C	25.782343000	45.570622000	14.573910000
C	24.785086000	46.475511000	14.334569000
N	25.734393000	44.604113000	13.577450000
C	24.756281000	44.940115000	12.753892000
N	24.150252000	46.062484000	13.184952000
C	25.273002000	50.134996000	14.693019000
C	26.211210000	50.876503000	13.765762000
O	26.838676000	51.871380000	14.141085000
N	26.312521000	50.392421000	12.505971000
C	27.089786000	51.114205000	11.484368000
C	26.362000000	52.401011000	11.091000000
C	27.196549000	50.081364000	10.352582000
C	25.883477000	49.293328000	10.459274000
C	25.672147000	49.180914000	11.973632000
C	28.251000000	41.485900000	19.380103000
C	28.716837000	40.524512000	18.299596000
O	28.473172000	39.321228000	18.344003000
C	26.819612000	41.949961000	19.110105000
O	26.787326000	42.676555000	17.883970000
N	29.376048000	41.098954000	17.263823000
C	29.808277000	40.338420000	16.105486000
C	30.928641000	41.133484000	15.434554000
O	30.804548000	42.338799000	15.202566000
C	28.671688000	40.061680000	15.108031000
N	32.026001000	40.438000000	15.110998000
C	31.330006000	41.247995000	10.405998000
C	29.994347000	41.400534000	11.036333000
C	29.381268000	42.472642000	11.617938000
N	29.080307000	40.369631000	11.132280000
C	27.972121000	40.829444000	11.756236000
N	28.124262000	42.102741000	12.068129000
C	31.652997000	50.514998000	11.949000000
C	30.737058000	49.315497000	11.925415000
C	30.835660000	48.360629000	10.900279000
C	29.781467000	49.086376000	12.929307000
C	30.031527000	47.221316000	10.875021000
C	28.964813000	47.951873000	12.918558000
C	29.078634000	46.999881000	11.889539000
O	28.281618000	45.910686000	11.902394000
C	28.070004000	48.035992000	7.293985000
C	28.144330000	46.509181000	7.450928000
C	27.541550000	45.989316000	8.775404000
O	28.248963000	45.164654000	9.446381000
O	26.413044000	46.402844000	9.107797000
Cu	27.135741000	43.243633000	13.291180000
H	25.653843000	49.119988000	14.880497000
H	28.051798000	49.414052000	10.541789000
H	27.342910000	50.551573000	9.369130000
H	25.056926000	49.868844000	10.009852000
H	25.930573000	48.314097000	9.965526000
H	26.164364000	48.280096000	12.378601000
H	24.607639000	49.132029000	12.247123000
H	28.077240000	51.364225000	11.901446000
H	26.475143000	42.579468000	19.951127000
H	26.159154000	41.064675000	19.058192000
H	25.863454000	42.826200000	17.639944000
H	28.273781000	40.950684000	20.339867000
H	27.881005000	39.491925000	15.615533000
H	29.041915000	39.471369000	14.256366000
H	28.245833000	40.997676000	14.720267000
H	30.191104000	39.374337000	16.472384000
H	29.486262000	42.106839000	17.231781000
H	32.123097000	39.451625000	15.318312000
H	31.868390000	42.204444000	10.439643000
H	31.247080000	40.936800000	9.351980000
H	29.744774000	43.480791000	11.744426000
H	27.107503000	40.220231000	11.969191000
H	32.627952000	50.269401000	12.406741000
H	31.859555000	50.885907000	10.932476000
H	31.563064000	48.511338000	10.096053000
H	29.655971000	49.819280000	13.732235000
H	30.110830000	46.495492000	10.065458000
H	28.211781000	47.804402000	13.695562000
H	28.220174000	45.514282000	10.962259000
H	27.028491000	48.376000000	7.397961000
H	28.660970000	48.541856000	8.074607000
H	27.577993000	46.032759000	6.629462000
H	29.183455000	46.154909000	7.368280000
H	27.735376000	43.164255000	15.980616000
H	29.097824000	43.234102000	15.090298000
H	28.487889000	45.512048000	14.392993000
H	26.840259000	46.606146000	16.082500000
H	26.397817000	44.966017000	16.543448000
H	24.471883000	47.355013000	14.870490000
H	24.462159000	44.401378000	11.866630000
H	23.371459000	46.525646000	12.733755000
H	29.210002000	39.426254000	10.788056000
H	31.220911000	51.343997000	12.531250000
H	28.449786000	48.358427000	6.311450000
H	26.946266000	52.963542000	10.344495000
H	25.374783000	52.177920000	10.656270000
H	26.221548000	53.040817000	11.973044000
H	31.938213000	40.493014000	10.930584000
H	32.780482000	40.902802000	14.615265000
H	30.209330000	45.043571000	16.161877000
H	29.322099000	46.555636000	16.501495000
H	28.932039000	45.064111000	17.406974000
H	25.219750000	50.675370000	15.645854000

H	24.263361000	50.039039000	14.266240000
H	28.914042000	42.362673000	19.452480000

Cu(II)-Model3

N	28.212351000	44.157197000	14.520018000
C	28.170369000	45.418058000	15.315898000
C	29.224000000	45.461000000	16.420000000
C	26.752152000	45.596270000	15.866323000
C	25.720387000	45.881734000	14.817432000
C	24.545680000	46.607970000	14.931837000
N	25.809645000	45.419593000	13.506542000
C	24.727000000	45.853849000	12.848569000
N	23.945291000	46.568867000	13.688996000
C	25.273000000	50.135000000	14.693000000
C	26.233670000	50.869412000	13.780159000
O	26.873614000	51.870971000	14.155914000
N	26.335777000	50.383822000	12.512679000
C	27.100788000	51.112950000	11.480564000
C	26.362000000	52.401000000	11.091000000
C	27.207936000	50.075687000	10.348534000
C	25.909550000	49.256998000	10.472862000
C	25.682385000	49.173954000	11.990294000
C	28.289239000	41.930153000	19.249097000
C	28.799213000	40.842646000	18.314765000
O	28.792033000	39.644992000	18.636639000
C	26.758400000	41.869500000	19.357100000
O	26.117785000	42.263441000	18.143441000
N	29.191926000	41.260826000	17.073835000
C	29.826228000	40.352841000	16.127593000
C	30.907667000	41.141031000	15.379021000
O	30.715337000	42.321193000	15.031992000
C	28.844900000	39.742300000	15.115700000
N	32.026000000	40.438000000	15.111000000
C	31.330000000	41.248000000	10.406000000
C	30.067669000	41.684680000	11.070482000
C	29.629958000	42.929497000	11.496637000
N	29.028524000	40.816665000	11.370294000
C	28.013000000	41.511685000	11.942844000
N	28.356348000	42.800044000	12.026912000
C	31.653000000	50.515000000	11.949000000
C	30.753883000	49.311836000	11.827646000
C	30.914524000	48.411795000	10.752047000
C	29.751617000	49.025069000	12.779085000
C	30.132084000	47.257386000	10.638091000
C	28.946832000	47.878716000	12.669059000
C	29.141558000	46.976312000	11.604989000
O	28.368334000	45.852254000	11.499351000
C	28.070000000	48.036000000	7.294000000
C	27.091639000	46.846563000	7.339927000
C	27.125006000	46.047526000	8.644181000
O	28.228455000	45.526962000	9.006232000
O	26.035902000	45.929617000	9.308795000
Cu	27.217741000	44.271558000	12.711624000
H	25.560261000	49.069421000	14.809254000
H	28.090426000	49.427341000	10.520637000
H	27.325809000	50.559337000	9.359708000
H	25.065952000	49.794710000	9.992297000
H	25.974333000	48.251341000	10.016252000
H	26.161436000	48.264050000	12.415128000
H	24.607966000	49.142997000	12.258587000
H	28.097573000	51.368583000	11.894809000
H	26.412810000	42.575918000	20.137795000
H	26.455923000	40.842632000	19.668188000
H	26.368602000	41.619598000	17.451635000
H	28.735778000	41.743017000	20.246965000
H	28.058566000	39.172922000	15.648509000
H	29.374655000	39.056747000	14.425146000
H	28.362780000	40.541121000	14.517893000
H	30.283191000	39.533099000	16.718504000
H	29.314695000	42.261037000	16.883459000
H	32.152269000	39.482990000	15.448143000
H	31.987246000	42.120398000	10.236304000
H	31.122760000	40.770999000	9.425980000
H	30.134166000	43.897623000	11.450487000
H	27.065983000	41.070878000	12.266875000
H	32.614565000	50.253396000	12.442783000
H	31.906265000	50.935291000	10.955102000
H	31.676342000	48.620098000	9.983271000
H	29.577033000	49.722403000	13.614030000
H	30.258725000	46.573792000	9.786963000
H	28.134659000	47.697699000	13.387241000
H	28.327003000	45.583825000	10.478347000
H	27.766665000	48.833439000	7.998251000
H	29.095471000	47.714072000	7.562867000
H	26.050223000	47.178582000	7.158197000
H	27.351866000	46.129492000	6.530547000
H	27.759611000	43.395038000	15.040930000
H	29.177341000	43.834290000	14.360060000
H	28.391876000	46.233812000	14.600616000
H	26.746918000	46.427248000	16.598907000
H	26.486135000	44.681739000	16.447814000
H	24.095175000	47.126151000	15.783070000
H	24.492077000	45.666903000	11.799466000
H	23.053670000	47.004023000	13.438063000
H	29.014850000	39.811596000	11.175213000
H	31.185116000	51.317085000	12.554990000
H	28.099350000	48.474087000	6.276506000
H	26.945192000	52.970530000	10.338410000
H	25.366620000	52.171779000	10.658712000
H	26.222744000	53.042193000	11.982309000
H	31.880291000	40.511723000	11.028422000
H	32.779224000	40.861398000	14.562843000
H	30.236200000	45.267213000	16.013522000
H	29.227974000	46.460755000	16.897355000
H	29.018401000	44.708934000	17.211409000
H	25.276185000	50.619674000	15.685451000
H	24.242975000	50.148113000	14.280897000
H	28.597264000	42.941071000	18.912819000
O	26.072531000	44.083098000	11.002554000
H	26.485451000	43.352804000	10.500252000
H	26.104463000	44.925430000	10.303661000

Cu(II)-Model4

N	28.190460000	44.178058000	14.524300000
C	28.179810000	45.446291000	15.304309000
C	29.224000000	45.461000000	16.420000000
C	26.769055000	45.674139000	15.855552000
C	25.724785000	45.919847000	14.808420000
C	24.537148000	46.625761000	14.922788000
N	25.808047000	45.435938000	13.505064000
C	24.710745000	45.838873000	12.851494000
N	23.924707000	46.554572000	13.687409000
C	25.273000000	50.135000000	14.693000000
C	26.234464000	50.863966000	13.776708000
O	26.882891000	51.860475000	14.151485000
N	26.328219000	50.380140000	12.507839000
C	27.093869000	51.107388000	11.474848000
C	26.362000000	52.401000000	11.091000000
C	27.190241000	50.072878000	10.339333000
C	25.885961000	49.263681000	10.466249000
C	25.666471000	49.175084000	11.984454000
C	28.291220000	41.765179000	19.292367000
C	28.731029000	40.741087000	18.265418000
O	28.607156000	39.521729000	18.462715000
C	26.758400000	41.869500000	19.357100000
O	26.198210000	42.687302000	18.343368000
N	29.224135000	41.229943000	17.090598000
C	29.839100000	40.338174000	16.120915000
C	30.906352000	41.136652000	15.370825000
O	30.704844000	42.313637000	15.021098000
C	28.844900000	39.742300000	15.115700000
N	32.026000000	40.438000000	15.111000000
C	31.330000000	41.248000000	10.406000000
C	30.070631000	41.687607000	11.076240000
C	29.635043000	42.933686000	11.502682000
N	29.031486000	40.821430000	11.380809000
C	28.018351000	41.519434000	11.955615000
N	28.363047000	42.807650000	12.036816000
C	31.653000000	50.515000000	11.949000000
C	30.752534000	49.312997000	11.825203000

C	30.918603000	48.411212000	10.751259000
C	29.742168000	49.030505000	12.768780000
C	30.134441000	47.258824000	10.633363000
C	28.935480000	47.885484000	12.654648000
C	29.137204000	46.980153000	11.594887000
O	28.367100000	45.855084000	11.488846000
C	28.070000000	48.036000000	7.294000000
C	27.082642000	46.854706000	7.341515000
C	27.118896000	46.052403000	8.643555000
O	28.224545000	45.532057000	9.000411000
O	26.032203000	45.932624000	9.310913000
Cu	27.223064000	44.288631000	12.715348000
H	25.553279000	49.067163000	14.804826000
H	28.068652000	49.417782000	10.507279000
H	27.309103000	50.558848000	9.351604000
H	25.044676000	49.811907000	9.993455000
H	25.939479000	48.260802000	10.001775000
H	26.143692000	48.261259000	12.402675000
H	24.593227000	49.147940000	12.258016000
H	28.093718000	51.355896000	11.885969000
H	26.476211000	42.332271000	20.325745000
H	26.330567000	40.838301000	19.354118000
H	26.314721000	42.268223000	17.454781000
H	28.668447000	41.405831000	20.271386000
H	28.014034000	39.243928000	15.654208000
H	29.338435000	38.984417000	14.476326000
H	28.451660000	40.532337000	14.444021000
H	30.302018000	39.503249000	16.685569000
H	29.408049000	42.231462000	16.974067000
H	32.154103000	39.484436000	15.451437000
H	31.988313000	42.119343000	10.234991000
H	31.117425000	40.772777000	9.426301000
H	30.140394000	43.901162000	11.454562000
H	27.070098000	41.079560000	12.277514000
H	32.664209000	50.227163000	12.310674000
H	31.794909000	51.020518000	10.971814000
H	31.687624000	48.615731000	9.988457000
H	29.564250000	49.729759000	13.601507000
H	30.264776000	46.572772000	9.784659000
H	28.117547000	47.706914000	13.366637000
H	28.322952000	45.586529000	10.466353000
H	27.782327000	48.828247000	8.010467000
H	29.096183000	47.702912000	7.546116000
H	26.042503000	47.195333000	7.168272000
H	27.331253000	46.138121000	6.528033000
H	27.677623000	43.430361000	15.026254000
H	29.146019000	43.822106000	14.383186000
H	28.431345000	46.254147000	14.589721000
H	26.786476000	46.543723000	16.542176000
H	26.498478000	44.798439000	16.489598000
H	24.085033000	47.148739000	15.770223000
H	24.468140000	45.627404000	11.808852000
H	23.022576000	46.969057000	13.438976000
H	29.015596000	39.816366000	11.185926000
H	31.247022000	51.257640000	12.665078000
H	28.089098000	48.484189000	6.280583000
H	26.946768000	52.968818000	10.338342000
H	25.363843000	52.179592000	10.661006000
H	26.229428000	53.040547000	11.984507000
H	31.880716000	40.509696000	11.025538000
H	32.779916000	40.860299000	14.562626000
H	30.233057000	45.227601000	16.027030000
H	29.258874000	46.461637000	16.894531000
H	28.975159000	44.718322000	17.207519000
H	25.285061000	50.617582000	15.686390000
H	24.240943000	50.155472000	14.286343000
H	28.721420000	42.769389000	19.101778000
O	26.073242000	44.082163000	11.004751000
H	26.492469000	43.356810000	10.501018000
H	26.100888000	44.923703000	10.308913000
O	26.504972000	41.990824000	15.671823000
H	26.951903000	41.129021000	15.538966000
H	25.638215000	41.878982000	15.230866000

List of abbreviations

AA	Auxiliary Activity
AMRT	Accurate mean-residence times
BDE	Bond dissociation energy
BS	Broken symmetry
CASSCF	Complete active space self-consistent field
CAZy	Carbohydrate-active enzymes
CBM	Carbohydrate binding module
CBP	Chitin-binding protein
CD	Circular dichroism
CDH	Cellobiose dehydrogenase
CT	Charge transfer
DFT	Density functional theory
DHB	2,5-dihydroxybenzoic acid
DP	Degree of polymerisation
EDTA	Ethylenediaminetetraacetic acid
ENDOR	Electron nuclear double resonance
EPR	Electron paramagnetic resonance
EXAFS	Extended X-ray absorption fine structure
FC	Fermi coupling
GH	Glycoside hydrolase
HF	Hartree-Fock
HYSCORE	Hyperfine sub-level correlation
LB	Luria-Bertani broth
LC-MS/MS	Liquid chromatography-mass spectrometry/mass spectrometry
LFT	Ligand field theory
LMCT	Ligand to metal charge transfer
LPMO	Lytic polysaccharide monooxygenase
MALDI-TOF	Matrix-assisted laser desorption/ionisation-time of flight
MCD	Magnetic circular dichroism
MLCT	Metal to ligand charge transfer

NEVPT2	N-electron valence second order perturbation theory
NMR	Nuclear magnetic resonance
PASC	Phosphoric acid swollen cellulose
P-B	Peisach-Blumberg
PCR	Polymerase chain reaction
PDB	Protein data bank
RMSD	Root mean square deviation
SD	Spin-dipolar
SDS-PAGE	Sodium dodecyl sulfate-poly acrylamide gel electrophoresis
SH	Spin Hamiltonian
SHF	Super-hyperfine
SO	Spin–orbit
SOMO	Singly occupied molecular orbital
TD-DFT	Time dependent-density functional theory
UV-vis	Ultraviolet-visible spectroscopy
VT-VH MCD	Variable temperature-variable field MCD
XANES	X-ray absorption near edge structure
XAS	X-ray absorption spectroscopy
ZORA	Zeroth-order regular approximation

Bibliography

1. Dale, B. E.; Anderson, J. E.; Brown, R. C.; Csonka, S.; Dale, V. H.; Herwick, G.; Jackson, R. D.; Jordan, N.; Kaffka, S.; Kline, K. L.; Lee, R. M.; Ong, R. G.; Richard, T. L.; Taylor, C.; Wang, M. Q.; Take a Closer Look: Biofuels Can Support Environmental, Economic and Social Goals. *Environ. Sci. Technol.* **2014**, 48, 7200−7203.

2. Robak, K.; Balcerek, M., Review of Second Generation Bioethanol Production from Residual Biomass. *Food Technol. Biotechnol.* **2018** Jun; 56(2), 174–187.

3. Himmel, M. E.; Ding, S. Y.; Johnson, D. K.; Adney, W. S.; Nimlos, M. R.; Brady, J. W.; Foust, T. D., Biomass Recalcitrance: Engineering Plants and Enzymes for Biofuels Production. *Science (80-.).* **2007**, *315* (5813), 804–807.

4. Gupta, V. K.; Kubicek, C. P.; Berrin, J. G.; Wilson, D. W.; Couturier, M.; Berlin, A.; Filho, E. X. F.; Ezeji, T., Fungal Enzymes for Bio-Products from Sustainable and Waste Biomass. *Trends Biochem. Sci.* **2016**, *41* (7), 633–645.

5. Gloster, T. M., Exploitation of Carbohydrate Processing Enzymes in Biocatalysis. *Current Opinion in Chemical Biology*, **2020,** 55, 180–188.

6. Godfray, H. C. J.; Beddington, J. R.; Crute, I. R.; Haddad, L.; Lawrence, D.; Muir, J. F.; Pretty, J.; Robinson, S.; Thomas, S. M.; Toulmin, C., Food Security: The Challenge of Feeding 9 Billion People. *Science*, **2010**, 812–818.

7. Lynd, L. R., The Grand Challenge of Cellulosic Biofuels. *Nat. Biotechnol.* **2017**, *35* (10), 912–915.

8. Meier, K. K.; Jones, S. M.; Kaper, T.; Hansson, H.; Koetsier, M. J.; Karkehabadi, S.; Solomon, E. I.; Sandgren, M.; Kelemen, B., Oxygen Activation by Cu LPMOs in Recalcitrant Carbohydrate Polysaccharide Conversion to Monomer Sugars. *Chem. Rev.* **2018**, *118* (5), 2593–2635.

9. Burton, R. A.; Gidley, M. J.; Fincher, G. B., Heterogeneity in the Chemistry, Structure and Function of Plant Cell Walls. *Nature Chemical Biology*. Nature Publishing Group October 22, 2010, pp 724–732.

10. Loqué, D.; Scheller, H. V.; Pauly, M., Engineering of Plant Cell Walls for Enhanced Biofuel Production. *Current Opinion in Plant Biology*, **2015**, 25, 151–161.

11. Wolfenden, R.; Lu, X.; Young, G., Spontaneous Hydrolysis of Glycosides. *J. Am. Chem. Soc.* **1998**, *120* (27), 6814–6815.

12. Atalla, R. H.; VanderHart, D. L., Native Cellulose: A Composite of Two Distinct Crystalline Forms. *Science (80-.).* **1984**, *223* (4633), 283–285.

13. Stipanovic, A. J.; Sarko, A., Packing Analysis of Carbohydrates and Polysaccharides. 6. Molecular and Crystal Structure of Regenerated Cellulose II. *Macromolecules* **1976**, *9* (5), 851–857.

14. Wada, M.; Chanzy, H.; Nishiyama, Y.; Langan, P., Cellulose III I Crystal Structure and Hydrogen Bonding by Synchrotron X-Ray and Neutron Fiber Diffraction. *Macromolecules* **2004**, *37* (23), 8548–8555.

15. Wood, T. M., Preparation of Crystalline, Amorphous, and Dyed Cellulase Substrates. *Methods Enzymol.* **1988**, *160* (C), 19–25.

16. Gomes, T. C. F.; Skaf, M. S., Cellulose-Builder: A Toolkit for Building Crystalline Structures of Cellulose. *J. Comput. Chem.* **2012**, *33* (14), 1338–1346.

17. Scheller, H. V.; Ulvskov, P., Hemicelluloses. *Annu. Rev. Plant Biol.* **2010**, *61* (1), 263–289.

18. Willats, W. G. T.; Mccartney, L.; Mackie, W.; Knox, J. P., Pectin: Cell Biology and Prospects for Functional Analysis. *Plant Molecular Biology*. Springer 2001, pp 9–27.

19. Burton, R. A.; Fincher, G. B., Current Challenges in Cell Wall Biology in the Cereals and Grasses. *Frontiers in Plant Science*, **2012**, https://doi.org/10.3389/fpls.2012.00130.

20. Merzendorfer, H., Insect Chitin Synthases: A Review. *Journal of Comparative Physiology B: Biochemical, Systemic, and Environmental Physiology*. Springer January 2, 2006, pp 1–15.

21. Sikorski, P.; Hori, R.; Wada, M., Revisit of R-Chitin Crystal Structure Using High Resolution X-Ray Diffraction Data. *Biomacromolecules* **2009**, 10 (5), 1100–1105.

22. Stankiewicz, B. A.; Briggs, D. E. G.; Evershed, R. P.; Flannery, M. B.; Wuttke, M., Preservation of Chitin in 25-Million-Year-Old Fossils. *Science (80-.).* **1997**, *276* (5318), 1541–1543.

23. Sharp, R., A Review of the Applications of Chitin and Its Derivatives in Agriculture to Modify Plant-Microbial Interactions and Improve Crop Yields. *Agronomy* **2013**, *3* (4), 757–793.

24. Kubicek, C. P.; Kubicek, E. M., Enzymatic Deconstruction of Plant Biomass by Fungal Enzymes. *Curr. Opin. Chem. Biol.* **2016**, *35*, 51–57.

25. Levasseur, A.; Drula, E.; Lombard, V.; Coutinho, P. M.; Henrissat, B., Expansion of the Enzymatic Repertoire of the CAZy Database to Integrate Auxiliary Redox Enzymes. *Biotechnol. Biofuels* **2013**, *6* (1), article no. 41.

26. Payne, C. M.; Knott, B. C.; Mayes, H. B.; Hansson, H.; Himmel, M. E.; Sandgren, M.; Ståhlberg, J.; Beckham, G. T., Fungal Cellulases. *Chem. Rev.* **2015**, *115* (3), 1308–1448.

27. Vaaje-Kolstad, G.; Westereng, B.; Horn, S. J.; Liu, Z.; Zhai, H.; Sorlie, M.; Eijsink, V. G. H., An Oxidative Enzyme Boosting the Enzymatic Conversion of Recalcitrant Polysaccharides. *Science (80).* **2010**, *330* (6001), 219–222.

28. Hangasky, J. A.; Detomasi, T. C.; Marletta, M. A., Glycosidic Bond Hydroxylation by Polysaccharide Monooxygenases. *Trends Chem.* **2019**, 26–30.

29. Bissaro, B.; Røhr, Å. K.; Müller, G.; Chylenski, P.; Skaugen, M.; Forsberg, Z.; Horn, S. J.; Vaaje-Kolstad, G.; Eijsink, V. G. H., Oxidative Cleavage of Polysaccharides by Monocopper Enzymes Depends on H_2O_2. *Nat. Chem. Biol.* **2017**, *13* (10), 1123–1128.

30. Quinlan, R. J.; Sweeney, M. D.; Lo Leggio, L.; Otten, H.; Poulsen, J.-C. N.; Johansen, K. S.; Krogh, K. B. R. M.; Jorgensen, C. I.; Tovborg, M.; Anthonsen, A.; et al., Insights into the Oxidative Degradation of Cellulose by a Copper Metalloenzyme that Exploits Biomass Components. *Proc. Natl. Acad. Sci.* **2011**, *108* (37), 15079–15084.

31. Phillips, C. M.; Beeson, W. T.; Cate, J. H.; Marletta, M. A., Cellobiose Dehydrogenase and a Copper-Dependent Polysaccharide Monooxygenase Potentiate Cellulose Degradation by Neurospora Crassa. *ACS Chem. Biol.* **2011**, *6* (12), 1399–1406.

32. Hemsworth, G. R.; Johnston, E. M.; Davies, G. J.; Walton, P. H., Lytic Polysaccharide Monooxygenases in Biomass Conversion. *Trends Biotechnol.* **2015**, *33* (12), 747–761.

33. Eibinger, M.; Ganner, T.; Bubner, P.; Rošker, S.; Kracher, D.; Haltrich, D.; Ludwig, R.; Plank, H.; Nidetzky, B., Cellulose Surface Degradation by a Lytic Polysaccharide Monooxygenase and its Effect on Cellulase Hydrolytic Efficiency. *J. Biol. Chem.* **2014**, *289* (52), 35929–35938.

34. Jagadeeswaran, G.; Gainey, L.; Prade, R.; Mort, A. J., A Family of AA9 Lytic Polysaccharide Monooxygenases in Aspergillus Nidulans is Differentially Regulated by Multiple Substrates and at Least One is Active on Cellulose and Xyloglucan. *Appl. Microbiol. Biotechnol.* **2016**, *100* (10), 4535–4547.

35. Cantarel, B. L.; Coutinho, P. M.; Rancurel, C.; Bernard, T.; Lombard, V.; Henrissat, B., The Carbohydrate-Active EnZymes Database (CAZy): An Expert Resource for Glycogenomics. *Nucleic Acids Res.* **2009**, *37* (Database), D233–D238.

36. Main Page, CAZypedia, © 2007-2019 The Authors and Curators of CAZypedia. https://www.cazypedia.org/index.php?title=Special:CiteThisPage&page=Main_Page&id=13510 (accessed Apr 28, 2020).

37. Hemsworth, G. R.; Henrissat, B.; Davies, G. J.; Walton, P. H., Discovery and Characterization of a New Family of Lytic Polysaccharide Monooxygenases. *Nat. Chem. Biol.* **2014**, *10* (2), 122–126.

38. Vu, V. V.; Beeson, W. T.; Span, E. A.; Farquhar, E. R.; Marletta, M. A., A Family of Starch-Active Polysaccharide Monooxygenases. *Proc. Natl. Acad. Sci.* **2014**, *111* (38), 13822–13827.

39. Couturier, M.; Ladevèze, S.; Sulzenbacher, G.; Ciano, L.; Fanuel, M.; Moreau, C.; Villares, A.; Cathala, B.; Chaspoul, F.; Frandsen, K. E.; et al., Lytic Xylan Oxidases from Wood-Decay Fungi Unlock Biomass Degradation. *Nat. Chem. Biol.* **2018**, *14* (3), 306–310.

40. Sabbadin, F.; Hemsworth, G. R.; Ciano, L.; Henrissat, B.; Dupree, P.; Tryfona, T.; Marques, R. D. S.; Sweeney, S. T.; Besser, K.; Elias, L.; et al., An Ancient Family of Lytic Polysaccharide Monooxygenases with Roles in Arthropod Development and Biomass Digestion. *Nat. Commun.* **2018**, *1723*, 0–38.

41. Filiatrault-Chastel, C.; Navarro, D.; Haon, M.; Grisel, S.; Herpoël-Gimbert, I.; Chevret, D.; Fanuel, M.; Henrissat, B.; Heiss-Blanquet, S.; Margeot, A.; et al., AA16, a New Lytic Polysaccharide Monooxygenase Family Identified in Fungal Secretomes. *Biotechnol. Biofuels* **2019**, *12*, 55–70.

42. Vu, V. V.; Beeson, W. T.; Phillips, C. M.; Cate, J. H. D.; Marletta, M. A., Determinants of Regioselective Hydroxylation in the Fungal Polysaccharide Monooxygenases. *J. Am. Chem. Soc.* **2014**, *136* (2), 562–565.

43. Book, A. J.; Yennamalli, R. M.; Takasuka, T. E.; Currie, C. R.; Phillips, G. N.; Fox, B. G., Evolution of Substrate Specificity in Bacterial AA10 Lytic Polysaccharide Monooxygenases. *Biotechnol. Biofuels* **2014**, *7* (1), 109–125.

44. Reese, E. T.; Siu, R. G.; Levinson, H. S.; The Biological Degradation of Soluble Cellulose Derivatives and its Relationship to the Mechanism of Cellulose Hydrolysis. *J. Bacteriol.* **1950**, *59* (4), 485–497.

45. Eriksson, K. E.; Pettersson, B.; Westermark, U., Oxidation: An Important Enzyme Reaction in Fungal Degradation of Cellulose. *FEBS Lett.* **1974**, *49* (2), 282–285.

46. Karlsson, J.; Saloheimo, M.; Siika-aho, M.; Tenkanen, M.; Penttilä, M.; Tjerneld, F., Homologous Expression and Characterization of Cel61A (EG IV) of *Trichoderma Reesei*. *Eur. J. Biochem.* **2001**, *268* (24), 6498–6507.

47. Forsberg, Z.; Vaaje-Kolstad, G.; Westereng, B.; Bunsæ, A. C.; Stenstrøm, Y.; Mackenzie, A.; Sørlie, M.; Horn, S. J.; Eijsink, V. G. H., Cleavage of Cellulose by a Cbm33 Protein. *Protein Sci.* **2011**, *20* (9), 1479–1483.

48. Karkehabadi, S.; Hansson, H.; Kim, S.; Piens, K.; Mitchinson, C.; Sandgren, M., The First Structure of a Glycoside Hydrolase Family 61 Member, Cel61B from Hypocrea Jecorina, at 1.6 Å Resolution. *J. Mol. Biol.* **2008**, *383* (1), 144–154.

49. Harris, P. V.; Welner, D.; McFarland, K. C.; Re, E.; Navarro Poulsen, J. C.; Brown, K.; Salbo, R.; Ding, H.; Vlasenko, E.; Merino, S.; et al., Stimulation of Lignocellulosic Biomass Hydrolysis by Proteins of Glycoside Hydrolase Family 61:

Structure and Function of a Large, Enigmatic Family. *Biochemistry* **2010**, *49* (15), 3305–3316.

50. Beeson, W. T.; Vu, V. V.; Span, E. A.; Phillips, C. M.; Marletta, M. A., Cellulose Degradation by Polysaccharide Monooxygenases. *Annu. Rev. Biochem.* **2015**, *84* (1), 923–946.

51. Forsberg, Z.; Mackenzie, A. K.; Sørlie, M.; Røhr, Å. K.; Helland, R.; Arvai, A. S.; Vaaje-Kolstad, G.; Eijsink, V. G. H., Structural and Functional Characterization of a Conserved Pair of Bacterial Cellulose-Oxidizing Lytic Polysaccharide Monooxygenases. *Proc. Natl. Acad. Sci. U. S. A.* **2014**, *111* (23), 8446–8451.

52. Vaaje-Kolstad, G.; Forsberg, Z.; Loose, J. S.; Bissaro, B.; Eijsink, V. G., Structural Diversity of Lytic Polysaccharide Monooxygenases. *Curr. Opin. Struct. Biol.* **2017**, *44*, 67–76.

53. Petrović, D. M.; Bissaro, B.; Chylenski, P.; Skaugen, M.; Sørlie, M.; Jensen, M. S.; Aachmann, F. L.; Courtade, G.; Várnai, A.; Eijsink, V. G. H., Methylation of the N-Terminal Histidine Protects a Lytic Polysaccharide Monooxygenase from Auto-Oxidative Inactivation. *Protein Sci.* **2018**, *27* (9), 1636–1650.

54. Frandsen, K. E. H.; Tovborg, M.; Jørgensen, C. I.; Spodsberg, N.; Rosso, M. N.; Hemsworth, G. R.; Garman, E. F.; Grime, G. W.; Poulsen, J. C. N.; Batth, T. S.; et al., Insights into an Unusual Auxiliary Activity 9 Family Member Lacking the Histidine Brace Motif of Lytic Polysaccharide Monooxygenases. *J. Biol. Chem.* **2019**, *294* (45), 17117–17130.

55. Ciano, L.; Davies, G. J.; Tolman, W. B.; Walton, P. H., Bracing Copper for the Catalytic Oxidation of C–H Bonds. *Nat. Catal.* **2018**, *1* (8), 571–577.

56. Span, E. A.; Suess, D. L. M.; Deller, M. C.; Britt, R. D.; Marletta, M. A., The Role of the Secondary Coordination Sphere in a Fungal Polysaccharide Monooxygenase. *ACS Chem. Biol.* **2017**, *12* (4), 1095–1103.

57. Vu, V. V; Ngo, S. T., Copper Active Site in Polysaccharide Monooxygenases. *Coord. Chem. Rev.* **2018**, *368* (May), 134–157.

58. O'Dell, W. B.; Agarwal, P. K.; Meilleur, F., Oxygen Activation at the Active Site of a Fungal Lytic Polysaccharide Monooxygenase. *Angew. Chemie Int. Ed.* **2017**, *56* (3), 767–770.

59. Hansson, H.; Karkehabadi, S.; Mikkelsen, N.; Douglas, N. R.; Kim, S.; Lam, A.; Kaper, T.; Kelemen, B.; Meier, K. K.; Jones, S. M.; et al., High-Resolution Structure of a Lytic Polysaccharide Monooxygenase from Hypocrea Jecorina Reveals a Predicted Linker as an Integral Part of the Catalytic Domain. *J. Biol. Chem.* **2017**, *292* (46), 19099–19109.

60. Gudmundsson, M.; Kim, S.; Wu, M.; Ishida, T.; Momeni, M. H.; Vaaje-Kolstad, G.; Lundberg, D.; Royant, A.; Ståhlberg, J.; Eijsink, V. G. H.; et al., Structural and Electronic Snapshots during the Transition from a Cu(II) to Cu(I) Metal Center of a Lytic Polysaccharide Onooxygenase by X-Ray Photoreduction. *J. Biol. Chem.* **2014**, *289* (27), 18782–18792.

61. Hemsworth, G. R.; Taylor, E. J.; Kim, R. Q.; Gregory, R. C.; Lewis, S. J.; Turkenburg, J. P.; Parkin, A.; Davies, G. J.; Walton, P. H., The Copper Active Site of CBM33 Polysaccharide Oxygenases. *J. Am. Chem. Soc.* **2013**, *135* (16), 6069–6077.

62. Courtade, G.; Ciano, L.; Paradisi, A.; Lindley, P. J.; Forsberg, Z.; Sørlie, M.; Wimmer, R.; Davies, G. J.; Eijsink, V. G. H.; Walton, P. H.; et al., Mechanistic Basis of Substrate–O 2 Coupling within a Chitin-Active Lytic Polysaccharide Monooxygenase: An Integrated NMR/EPR Study. *Proc. Natl. Acad. Sci.* **2020**, *117* (32), 19178–19189.

63. Kjaergaard, C. H.; Qayyum, M. F.; Wong, S. D.; Xu, F.; Hemsworth, G. R.; Walton, D. J.; Young, N. A.; Davies, G. J.; Walton, P. H.; Johansen, K. S.; et al., Spectroscopic and Computational Insight into the Activation of O_2 by the Mononuclear Cu Center in Polysaccharide Monooxygenases. *Proc. Natl. Acad. Sci. U. S. A.* **2014**, *111* (24), 8797–8802.

64. Paradisi, A.; Steward, M. J.; Lindley, P.; Davies, G. J.; Walton, P. H., Copper Oxygenases. In *Comprehensive Coordination Chemistry III*; Elsevier, 2020; p Accepted.

65. Frandsen, K. E. H.; Simmons, T. J.; Dupree, P.; Poulsen, J. N.; Hemsworth, G. R.; Ciano, L.; Johnston, E. M.; Tovborg, M.; Johansen, K. S.; von Freiesleben, P.; et al., The Molecular Basis of Polysaccharide Cleavage by Lytic Polysaccharide Monooxygenases. *Nat. Chem. Biol.* **2016**, *12* (4), 298–303.

66. Bacik, J. P.; Mekasha, S.; Forsberg, Z.; Kovalevsky, A. Y.; Vaaje-Kolstad, G.; Eijsink, V. G. H.; Nix, J. C.; Coates, L.; Cuneo, M. J.; Unkefer, C. J.; et al., Neutron and Atomic Resolution X-Ray Structures of a Lytic Polysaccharide Monooxygenase Reveal Copper-Mediated Dioxygen Binding and Evidence for N-Terminal Deprotonation. *Biochemistry* **2017**, *56* (20), 2529–2532.

67. Lombard, V.; Golaconda Ramulu, H.; Drula, E.; Coutinho, P. M.; Henrissat, B., The Carbohydrate-Active Enzymes Database (CAZy) in 2013. http://www.cazy.org/Citing-CAZy.html

68. Creagh, A. L.; Ong, E.; Jervis, E.; Kilburn, D. G.; Haynes, C. A., Binding of the Cellulose-Binding Domain of Exoglucanase Cex from Cellulomonas Fimi to Insoluble Microcrystalline Cellulose Is Entropically Driven. *Proc. Natl. Acad. Sci. U. S. A.* **1996**, *93* (22), 12229–12234.

69. Forsberg, Z.; Røhr, Å. K.; Mekasha, S.; Andersson, K. K.; Eijsink, V. G. H.; Vaaje-Kolstad, G.; Sørlie, M., Comparative Study of Two Chitin-Active and Two Cellulose-Active AA10-Type Lytic Polysaccharide Monooxygenases. *Biochemistry* **2014**, *53* (10), 1647–1656.

70. Borisova, A. S.; Isaksen, T.; Dimarogona, M.; Kognole, A. A.; Mathiesen, G.; Várnai, A.; Røhr, Å. K.; Payne, C. M.; Sørlie, M.; Sandgren, M.; et al., Structural and Functional Characterization of a Lytic Polysaccharide Monooxygenase with Broad Substrate Specificity. *J. Biol. Chem.* **2015**, *290* (38), 22955–22969.

71. Amore, A.; Knott, B. C.; Supekar, N. T.; Shajahan, A.; Azadi, P.; Zhao, P.; Wells, L.; Linger, J. G.; Hobdey, S. E.; Vander Wall, T. A.; et al., Distinct Roles of N- and O-Glycans in Cellulase Activity and Stability. *Proc. Natl. Acad. Sci. U. S. A.* **2017**, *114* (52), 13667–13672.

72. Spiro, R. G., *Protein Glycosylation: Nature, Distribution, Enzymatic Formation, and Disease Implications of Glycopeptide Bonds*; 2002; Vol. 12 (4), 43R–56R.

73. Isaksen, T.; Westereng, B.; Aachmann, F. L.; Agger, J. W.; Kracher, D.; Kittl, R.; Ludwig, R.; Haltrich, D.; Eijsink, V. G. H.; Horn, S. J., A C4-Oxidizing Lytic Polysaccharide Monooxygenase Cleaving Both Cellulose and Cello-Oligosaccharides. *J. Biol. Chem.* **2014**, *289* (5), 2632–2642.

74. Agger, J. W.; Isaksen, T.; Várnai, A.; Vidal-Melgosa, S.; Willats, W. G. T.; Ludwig, R.; Horn, S. J.; Eijsink, V. G. H.; Westereng, B., Discovery of LPMO Activity on Hemicelluloses Shows the Importance of Oxidative Processes in Plant Cell Wall Degradation. *Proc. Natl. Acad. Sci. U. S. A.* **2014**, *111* (17), 6287–6292.

75. Lo Leggio, L.; Simmons, T. J.; Poulsen, J. C. N.; Frandsen, K. E. H.; Hemsworth, G. R.; Stringer, M. A.; Von Freiesleben, P.; Tovborg, M.; Johansen, K. S.; De Maria, L.; et al., Structure and Boosting Activity of a Starch-Degrading Lytic Polysaccharide Monooxygenase. *Nat. Commun.* **2015**, *6*.

76. Aachmann, F. L.; Sorlie, M.; Skjak-Braek, G.; Eijsink, V. G. H.; Vaaje-Kolstad, G., NMR Structure of a Lytic Polysaccharide Monooxygenase Provides Insight into Copper Binding, Protein Dynamics, and Substrate Interactions. *Proc. Natl. Acad. Sci.* **2012**, *109* (46), 18779–18784.

77. Bissaro, B.; Isaksen, I.; Vaaje-Kolstad, G.; Eijsink, V. G. H.; Røhr, Å. K., How a Lytic Polysaccharide Monooxygenase Binds Crystalline Chitin. *Biochemistry* **2018**, *57* (12), 1893–1906.

78. Wu, M.; Beckham, G. T.; Larsson, A. M.; Ishida, T.; Kim, S.; Payne, C. M.; Himmel, M. E.; Crowley, M. F.; Horn, S. J.; Westereng, B.; et al., Crystal Structure and Computational Characterization of the Lytic Polysaccharide Monooxygenase GH61D from the Basidiomycota Fungus Phanerochaete Chrysosporium. *J. Biol. Chem.* **2013**, *288* (18), 12828–12839.

79. Davies, G. J.; Ducros, V.; Lewis, R. J.; Borchert, T. V.; Schülein, M., Oligosaccharide Specificity of a Family 7 Endoglucanase: Insertion of Potential Sugar-Binding Subsites. *J. Biotechnol.* **1997**, *57* (1–3), 91–100.

80. Courtade, G.; Wimmer, R.; Røhr, Å. K.; Preims, M.; Felice, A. K. G.; Dimarogona, M.; Vaaje-Kolstad, G.; Sørlie, M.; Sandgren, M.; Ludwig, R.; et al., Interactions of a Fungal Lytic Polysaccharide Monooxygenase with β-Glucan Substrates and Cellobiose Dehydrogenase. *Proc. Natl. Acad. Sci. U. S. A.* **2016**, *113* (21), 5922–5927.

81. Zhou, X.; Zhu, H., Current Understanding of Substrate Specificity and Regioselectivity of LPMOs. *Bioresources and Bioprocessing*. Springer December 1, 2020, pp 1–19.

82. Simmons, T. J.; Frandsen, K. E. H.; Ciano, L.; Tryfona, T.; Lenfant, N.; Poulsen, J. C.; Wilson, L. F. L.; Tandrup, T.; Tovborg, M.; Schnorr, K.; et al., Structural and Electronic Determinants of Lytic Polysaccharide Monooxygenase Reactivity on Polysaccharide Substrates. *Nat. Commun.* **2017**, *8* (1).

83. Forsberg, Z.; Bissaro, B.; Gullesen, J.; Dalhus, B.; Vaaje-Kolstad, G.; Eijsink, V. G. H., Structural Determinants of Bacterial Lytic Polysaccharide Monooxygenase Functionality. *J. Biol. Chem.* **2018**, *293* (4), 1397–1412.

84. Danneels, B.; Tanghe, M.; Desmet, T., Structural Features on the Substrate-Binding Surface of Fungal Lytic Polysaccharide Monooxygenases Determine their Oxidative Regioselectivity. *Biotechnol. J.* **2018**, *1800211*, 1–10.

85. Peisach, J.; Blumberg, W. E., Structural Implications Derived from the Analysis of Electron Paramagnetic Resonance Spectra of Natural and Artificial Copper Proteins. *Arch. Biochem. Biophys.* **1974**, *165* (2), 691–708.

86. Hemsworth, G. R.; Ciano, L.; Davies, G. J.; Walton, P. H., Production and Spectroscopic Characterization of Lytic Polysaccharide Monooxygenases. In *Methods in Enzymology*; Academic Press Inc., 2018; Vol. 613, pp 63–90.

87. Chaplin, A. K.; Wilson, M. T.; Hough, M. A.; Svistunenko, D. A.; Hemsworth, G. R.; Walton, P. H.; Vijgenboom, E.; Worrall, J. A. R., Heterogeneity in the Histidine-Brace Copper Coordination Sphere in Auxiliary Activity Family 10 (AA10) Lytic Polysaccharide Monooxygenases. *J. Biol. Chem.* **2016**, *291* (24), 12838–12850.

88. Munzone, A.; El Kerdi, B.; Fanuel, M.; Rogniaux, H.; Ropartz, D.; Réglier, M.; Royant, A.; Simaan, A. J.; Decroos, C., Characterization of a Bacterial Copper-dependent Lytic Polysaccharide Monooxygenase with an Unusual Second Coordination Sphere. *FEBS J.* **2020**, febs.15203.

89. Neese, F., A Critical Evaluation of DFT, Including Time-Dependent DFT, Applied to Bioinorganic Chemistry. *J. Biol. Inorg. Chem.* **2006**, *11* (6), 702–711.

90. Neese, F., Prediction of Molecular Properties and Molecular Spectroscopy with Density Functional Theory: From Fundamental Theory to Exchange-Coupling. *Coord. Chem. Rev.* **2009**, *253* (5–6), 526–563.

91. Solomon, E. I.; Heppner, D. E.; Johnston, E. M.; Ginsbach, J. W.; Cirera, J.; Qayyum, M.; Kieber-Emmons, M. T.; Kjaergaard, C. H.; Hadt, R. G.; Tian, L., Copper Active Sites in Biology. *Chem. Rev.* **2014**, *114* (7), 3659–3853.

92. Tan, T. C.; Kracher, D.; Gandini, R.; Sygmund, C.; Kittl, R.; Haltrich, D.; Hällberg, B. M.; Ludwig, R.; Divne, C., Structural Basis for Cellobiose Dehydrogenase Action during Oxidative Cellulose Degradation. *Nat. Commun.* **2015**, *6*.

93. Hedegård, E. D.; Ryde, U., Targeting the Reactive Intermediate in Polysaccharide Monooxygenases. *JBIC J. Biol. Inorg. Chem.* **2017**, *22* (7), 1029–1037.

94. Walton, P. H.; Davies, G. J., On the Catalytic Mechanisms of Lytic Polysaccharide Monooxygenases. *Curr. Opin. Chem. Biol.* **2016**, 1–13.

95. Chylenski, P.; Bissaro, B.; Sørlie, M.; Røhr, Å. K.; Várnai, A.; Horn, S. J.; Eijsink, V. G. H., Lytic Polysaccharide Monooxygenases in Enzymatic Processing of Lignocellulosic Biomass. *ACS Catal.* **2019**, *9* (6), 4970–4991.

96. Elwell, C. E.; Gagnon, N. L.; Neisen, B. D.; Dhar, D.; Spaeth, A. D.; Yee, G. M.; Tolman, W. B., Copper–Oxygen Complexes Revisited: Structures, Spectroscopy, and Reactivity. *Chem. Rev.* **2017**, 117 (3), 2059–2107.

97. Liu, J. J.; Diaz, D. E.; Quist, D. A.; Karlin, K. D., Copper(I)-Dioxygen Adducts and Copper Enzyme Mechanisms. *Isr. J. Chem.* **2016**, *56* (9–10), 738–755.

98. Beeson, W. T.; Phillips, C. M.; Cate, J. H. D.; Marletta, M. A., Oxidative Cleavage of Cellulose by Fungal Copper-Dependent Polysaccharide Monooxygenases. *J. Am. Chem. Soc.* **2012**, *134* (2), 890–892.

99. Bertini, L.; Breglia, R.; Lambrughi, M.; Fantucci, P.; De Gioia, L.; Borsari, M.; Sola, M.; Bortolotti, C. A.; Bruschi, M., Catalytic Mechanism of Fungal Lytic Polysaccharide Monooxygenases Investigated by First-Principles Calculations. *Inorg. Chem.* **2017**, acs.inorgchem.7b02005.

100. Hedegård, E. D.; Ryde, U., Molecular Mechanism of Lytic Polysaccharide Monooxygenases. *Chem. Sci.*, **2018**, 9 (15), 3866–3880.

101. Wang, B.; Walton, P. H.; Rovira, C., Molecular Mechanisms of Oxygen Activation and Hydrogen Peroxide Formation in Lytic Polysaccharide Monooxygenases. *ACS Catal.* **2019**, *9*, 4958–4969.

102. Jones, S. M.; Transue, W. J.; Meier, K. K.; Kelemen, B.; Solomon, E. I., Kinetic Analysis of Amino Acid Radicals Formed in H_2O_2-Driven Cu(I) LPMO Reoxidation Implicates Dominant Homolytic Reactivity. *Proc. Natl. Acad. Sci.* **2020**, PNAS Latest Articles.

103. Wang, B.; Johnston, E. M.; Li, P.; Shaik, S.; Davies, G. J.; Walton, P. H.; Rovira, C., QM/MM Studies into the H_2O_2-Dependent Activity of Lytic Polysaccharide Monooxygenases: Evidence for the Formation of a Caged Hydroxyl Radical Intermediate. *ACS Catal.* **2018**, *8* (2), 1346–1351.

104. Bissaro, B.; Streit, B.; Isaksen, I.; Eijsink, V. G. H.; Beckham, G. T.; DuBois, J. L.; Røhr, Å. K., Molecular Mechanism of the Chitinolytic Peroxygenase Reaction. *Proc. Natl. Acad. Sci. U. S. A.* **2020**, *117* (3), 1504–1513.

105. Kuusk, S.; Bissaro, B.; Kuusk, P.; Forsberg, Z.; Eijsink, V. G. H.; Sørlie, M.; Väljamäe, P., Kinetics of H_2O_2-Driven Degradation of Chitin by a Bacterial Lytic Polysaccharide Monooxygenase. *J. Biol. Chem.* **2018**, *293* (2), 523–531.

106. Hangasky, J. A.; Iavarone, A. T.; Marletta, M. A., Reactivity of O 2 versus H 2 O 2 with Polysaccharide Monooxygenases. *Proc. Natl. Acad. Sci.* **2018**, 201801153.

107. Frommhagen, M.; Westphal, A. H.; van Berkel, W. J. H.; Kabel, M. A., Distinct Substrate Specificities and Electron-Donating Systems of Fungal Lytic Polysaccharide Monooxygenases. *Front. Microbiol.* **2018**, *9*, 1–22.

108. Kracher, D.; Scheiblbrandner, S.; Felice, A. K. G.; Breslmayr, E.; Preims, M.; Ludwicka, K.; Haltrich, D.; Eijsink, V. G. H.; Ludwig, R., Extracellular Electron Transfer Systems Fuel Cellulose Oxidative Degradation. *Science*, **2016**; 352, 1098–1101.

109. Westereng, B.; Cannella, D.; Agger, J. W.; Jørgensen, H.; Andersen, M. L.; Eijsink, V. G. H.; Felby, C., Enzymatic Cellulose Oxidation Is Linked to Lignin by Long-Range Electron Transfer. *Scientific Reports,* **2015**, *5*, Article no. 18561.

110. Várnai, A.; Umezawa, K.; Yoshida, M.; Eijsink, V. G. H., The Pyrroloquinolinequinone- Dependent Pyranose Dehydrogenase from Coprinopsis Cinerea Drives Lytic Polysaccharide Monooxygenase Action. *Appl. Environ. Microbiol.* **2018**, *84* (11), e00156-18.

111. Frommhagen, M.; Westphal, A. H.; Hilgers, R.; Koetsier, M. J.; Hinz, S. W. A.; Visser, J.; Gruppen, H.; van Berkel, W. J. H.; Kabel, M. A., Quantification of the Catalytic Performance of C1-Cellulose-Specific Lytic Polysaccharide Monooxygenases. *Appl. Microbiol. Biotechnol.* **2018**, *102* (3), 1281–1295.

112. Loose, J. S. M.; Forsberg, Z.; Kracher, D.; Scheiblbrandner, S.; Ludwig, R.; Eijsink, V. G. H.; Vaaje-Kolstad, G., Activation of Bacterial Lytic Polysaccharide Monooxygenases with Cellobiose Dehydrogenase. *Protein Sci.* **2016**, *25* (12), 2175–2186.

113. Martin Hallberg, B.; Henriksson, G.; Pettersson, G.; Divne, C., Crystal Structure of the Flavoprotein Domain of the Extracellular Flavocytochrome Cellobiose Dehydrogenase. *J. Mol. Biol.* **2002**, *315* (3), 421–434.

114. Li, X.; Beeson IV, W. T.; Phillips, C. M.; Marletta, M. A.; Cate, J. H. D., Structural Basis for Substrate Targeting and Catalysis by Fungal Polysaccharide Monooxygenases. *Structure* **2012**, *20* (6), 1051–1061.

115. Zhang, R., Functional Characterization of Cellulose-Degrading AA9 Lytic Polysaccharide Monooxygenases and Their Potential Exploitation. *Appl. Microbiol. Biotechnol.* **2020**.

116. Hangasky, J. A.; Marletta, M. A., A Random-Sequential Kinetic Mechanism for Polysaccharide Monooxygenases. *Biochemistry* **2018**, *57* (22), 3191–3199.

117. Stoll, S.; Schweiger, A., EasySpin, a Comprehensive Software Package for Spectral Simulation and Analysis in EPR. *J. Magn. Reson.*, **2005**, 178 (1), 42–55.

118. Hitchman, M. A.; Olson, C. D.; Belford, R. L.; Belford, A. R. L., Behavior of the In-Plane g Tensor in Low-Symmetry d^1 and d^9 Systems with Application to Copper and Vanadyl Chelates. *J. Chem. Phys.* **1969**, *50*, 2571.

119. Neese, F., Software Update: The ORCA Program System, Version 4.0. *Wiley Interdiscip. Rev. Comput. Mol. Sci.* **2018**, *8* (1), e1327.

120. Becke, A. D., Density-Functional Exchange-Energy Approximation with Correct Asymptotic Behavior. *Phys. Rev. A* **1988**, *38* (6), 3098–3100.

121. Weigend, F.; Ahlrichs, R., Balanced Basis Sets of Split Valence, Triple Zeta Valence and Quadruple Zeta Valence Quality for H to Rn: Design and Assessment of Accuracy. *Phys. Chem. Chem. Phys.* **2005**, *7* (18), 3297–3305.

122. Grimme, S.; Ehrlich, S.; Goerigk, L., Effect of the Damping Function in Dispersion Corrected Density Functional Theory. *J. Comput. Chem.* **2011**, *32* (7), 1456–1465.

123. Becke, A. D., Density-Functional Thermochemistry. III. The Role of Exact Exchange. *J. Chem. Phys.* **1993**, *98* (7), 5648–5652.

124. Neese, F., Prediction and Interpretation of the ^{57}Fe Isomer Shift in Mossbauer Spectra by Density Functional Theory. *Inorganica Chim. Acta* **2002**, *337* (1), 181–192.

125. Kutzelnigg, W.; Fleischer, U.; Schindler, M., The IGLO-Method: Ab-Initio Calculation and Interpretation of NMR Chemical Shifts and Magnetic Susceptibilities; Springer, Berlin, Heidelberg, **1990**; 165–262, https://doi.org/10.1007/978-3-642-75932-1_3.

126. Neese, F., Prediction of Electron Paramagnetic Resonance g Values Using Coupled Perturbed Hartree-Fock and Kohn-Sham Theory. *J. Chem. Phys.* **2001**, *115* (24), 11080–11096.

127. Luzanov, A. V.; Babich, E. N.; Ivanov, V. V., Gauge-Invariant Calculations of Magnetic Properties in Semiempirical Approaches. Application to Full-CI π-Electron Scheme. *J. Mol. Struct. THEOCHEM* **1994**, *311*, 211–220.

128. Heß, B. A.; Marian, C. M.; Wahlgren, U.; Gropen, O., A Mean-Field Spin-Orbit Method Applicable to Correlated Wavefunctions. *Chem. Phys. Lett.* **1996**, *251* (5–6), 365–371.

129. Neese, F., Metal and Ligand Hyperfine Couplings in Transition Metal Complexes: The Effect of Spin-Orbit Coupling as Studied by Coupled Perturbed Kohn-Sham Theory. *J. Chem. Phys.* **2003**, *118* (9), 3939–3948.

130. Neese, F., Theoretical Study of Ligand Superhyperfine Structure. Application to Cu(II) Complexes. *J. Phys. Chem. A* **2001**, *105* (17), 4290–4299.

131. Hirata, S.; Head-Gordon, M., Time-Dependent Density Functional Theory within the Tamm-Dancoff Approximation. *Chem. Phys. Lett.* **1999**, *314* (3–4), 291–299.

132. Yanai, T.; Tew, D. P.; Handy, N. C., A New Hybrid Exchange-Correlation Functional Using the Coulomb-Attenuating Method (CAM-B3LYP). *Chem. Phys. Lett.* **2004**, *393* (1–3), 51–57.

133. Neese, F.; Wennmohs, F.; Hansen, A.; Becker, U., Efficient, Approximate and Parallel Hartree-Fock and Hybrid DFT Calculations. A "Chain-of-Spheres" Algorithm for the Hartree-Fock Exchange. *Chem. Phys.* **2009**, *356* (1–3), 98–109.

134. Malmqvist, P. Å.; Roos, B. O., The CASSCF State Interaction Method. *Chem. Phys. Lett.* **1989**, *155* (2), 189–194.

135. Pantazis, D. A.; Chen, X. Y.; Landis, C. R.; Neese, F., All-Electron Scalar Relativistic Basis Sets for Third-Row Transition Metal Atoms. *J. Chem. Theory Comput.* **2008**, *4* (6), 908–919.

136. Angeli, C.; Cimiraglia, R.; Evangelisti, S.; Leininger, T.; Malrieu, J. P., Introduction of *N*-Electron Valence States for Multireference Perturbation Theory. *J. Chem. Phys.* **2001**, *114* (23), 10252.

137. Neese, F., Importance of Direct Spin-Spin Coupling and Spin-Flip Excitations for the Zero-Field Splittings of Transition Metal Complexes: A Case Study. *J. Am. Chem. Soc.* **2006**, *128* (31), 10213–10222.

138. Figgis, B. N.; Hitchman, M. A., *Ligand Field Theory and Its Applications*; Wiley-VCH, 2000.

139. Iwaizumi, M.; Kudo, T.; Kita, S., Correlation between the Hyperfine Coupling Constants of Donor Nitrogens and the Structures of the First Coordination Sphere in Copper Complexes as Studied by Nitrogen-14 ENDOR Spectroscopy. *Inorg. Chem.* **1986**, *25* (10), 1546–1550.

140. Lawrence Que, J., *Physical Methods in Bioinorganic Chemistry: Spectroscopy and Magnetism*, 1st edition.; University Science Books, 2000.

141. Gewirth, A. A.; Solomon, E. I., Electronic Structure of Plastocyanin: Excited State Spectral Features; *J. Am. Chem. Soc*. **1988**, 110 (12), 3811–3819.

142. Stephens, P. J., Magnetic Circular Dichroism. *Adv. Chem. Phys,*. **1976**, 35, 197-264.

143. Gerstman, B. S.; Brill, A. S., Magnetic Circular Dichroism of Low Symmetry Cupric Sites. *J. Chem. Phys.* **1985**, *82* (3), 1212–1230.

144. Chen, P.; Bell, J.; Eipper, B. A.; Solomon, E. I., Oxygen Activation by the Noncoupled Binuclear Copper Site in Peptidylglycine R-Hydroxylating Monooxygenase. Spectroscopic Definition of the Resting Sites and the Putative Cu(II) M–OOH Intermediate. *Biochemistry*, **2004,** 43, 5735–5747.

145. Adelson, C. N.; Johnston, E. M.; Hilmer, K. M.; Watts, H.; Dey, S. G.; Brown, D. E.; Broderick, J. B.; Shepard, E. M.; Dooley, D. M.; Solomon, E. I., Characterization of the Preprocessed Copper Site Equilibrium in Amine Oxidase and Assignment of the Reactive Copper Site in Topaquinone Biogenesis. *J. Am. Chem. Soc.* **2019**, *141* (22), 8877–8890.

146. Ghosh, S.; Cirera, J.; Vance, M. A.; Ono, T.; Fujisawa, K.; Solomon, E. I., Spectroscopic and Electronic Structure Studies of Phenolate Cu (II) Complexes: *J. Struct. Biol.* **2008**, *130* (48), 16262–16273.

147. Dick, A.; Rahemi, H.; Krausz, E. R.; Hanson, G. R.; Riley, M. J., The Highly Resolved Electronic Spectrum of the Square Planar $[CuCl_4]^{2-}$ Ion. *J. Chem. Phys.* **2008**, *129* (21), 214505.

148. Desjardins, S. R.; Penfield, K. W.; Cohen, S. L.; Solomon, E. I.; Musselman, R. L., Detailed Absorption, Reflectance, and UV Photoelectron Spectroscopic and Theoretical Studies of the Charge-Transfer Transitions of $[CuCl_4]^{2-}$: Correlation of the Square-Planar and the Tetrahedral Limits. *J. Am. Chem. Soc.* **1983**, *105* (14), 4590–4603.

149. Solomon, E. I.; Szilagyi, R. K.; DeBeer George, S.; Basumallick, L., Electronic Structures of Metal Sites in Proteins and Models: Contributions to Function in Blue Copper Proteins. *Chemical Reviews*. **2004**, 104, 419–458.

150. Rivoal, J. C.; Briat, B., Magnetic Circular Dichroism Studies of the Charge-Transfer Transitions in Tetrachloro and Tetrabromocomplexes of Transition Metal Ions. *Mol. Phys.* **1974**, *27* (4), 1081–1108.

151. Carugo, O., How Root-Mean-Square Distance (r.m.s.d.) Values Depend on the Resolution of Protein Structures that are Compared. *J. Appl. Crystallogr.* **2003**, *36* (1), 125–128.

152. Sinnecker, S.; Neese, F., QM/MM Calculations with DFT for Taking into Account Protein Effects on the EPR and Optical Spectra of Metalloproteins. Plastocyanin as a Case Study. *J. Comput. Chem.* **2006**, *27* (12), 1463–1475.

153. Szilagyi, R. K.; Metz, M.; Solomon, E. I., Spectroscopic Calibration of Modern Density Functional Methods Using $[CuCl_4]^{2-}$. *J. Phys. Chem. A,* **2002,** 106 (12), 2994–3007.

154. Remenyi, C.; Reviakine, R.; Kaupp, M., Density Functional Study of EPR Parameters and Spin-Density Distribution of Azurin and Other Blue Copper Proteins. *J. Phys. Chem. B* **2007**, *111* (28), 8290–8304.

155. Hedegård, E. D.; Kongsted, J.; Sauer, S. P. A., Optimized Basis Sets for Calculation of Electron Paramagnetic Resonance Hyperfine Coupling Constants: Aug-Cc-PVTZ-J for the 3d Atoms Sc-Zn. *J. Chem. Theory Comput.* **2011**, *7* (12), 4077–4087.

156. Szilagyi, R. K.; Metz, M.; Solomon, E. I., Spectroscopic Calibration of Modern Density Functional Methods Using $[CuCl_4]^{2-}$. *J. Phys. Chem. A* **2002**, *106* (12), 2994–3007.

157. Pierloot, K.; De Kerpel, J. O. A.; Ryde, U.; Roos, B. O., Theoretical Study of the Electronic Spectrum of Plastocyanin. *J. Am. Chem. Soc.* **1997**, *119* (1), 218–226.

158. Pierloot, K.; De Kerpel, J. O. A.; Ryde, U.; Olsson, M. H. M.; Roos, B. O., Relation between the Structure and Spectroscopic Properties of Blue Copper Proteins. *J. Am. Chem. Soc.* **1998**, *120* (50), 13156–13166.

159. Jazdzewski, B. A.; Holland, P. L.; Pink, M.; Young, V. G.; Spencer, D. J. E.; Tolman, W. B., Three-Coordinate Copper(II)-Phenolate Complexes. *Inorg. Chem.* **2001**, *40* (24), 6097–6107.

160. Neese, F.; Solomon, E. I., Interpretation and Calculation of Spin-Hamiltonian Parameters in Transition Metal Complexes; *Magnetism: Molecules to Materials* **2003**, Vol. 4–5, 345–466.

161. Gewirth, A. A.; Cohen, S. L.; Schugar, H. J.; Solomon, E. I., Spectroscopic and Theoretical Studies of the Unusual EPR Parameters of Distorted Tetrahedral Cupric Sites: Correlations to X-Ray Spectral Features of Core Levels. *Inorg. Chem.* **1987**, *26* (7), 1133–1146.

162. Kuska, H. A.; Rogers, M. T.; Drullinger, R. E., Effect of Substituents on the Anisotropic Electron Spin Resonance Parameters in Copper Acetylacetonates. *J. Phys. Chem.* **1967**, *71* (1), 109–114.

163. Singh, R. K.; Blossom, B. M.; Russo, D. A.; Singh, R.; Weihe, H.; Andersen, N. H.; Tiwari, M. K.; Jensen, P. E.; Felby, C.; Bjerrum, M. J., Detection and Characterization of a Novel Copper-Dependent Intermediate in a Lytic Polysaccharide Monooxygenase. *Chem. – A Eur. J.* **2020**, *26* (2), 454–463.

164. Gao, J.; Thomas, D. A.; Sohn, C. H.; Beauchamp, J. L., Biomimetic Reagents for the Selective Free Radical and Acid–Base Chemistry of Glycans: Application to Glycan Structure Determination by Mass Spectrometry. *J. Am. Chem. Soc.* **2013**, *135* (29), 10684–10692.

165. Mann, S. I.; Heinisch, T.; Ward, T. R.; Borovik, A. S., Peroxide Activation Regulated by Hydrogen Bonds within Artificial Cu Proteins. *J. Am. Chem. Soc.* **2017**, 139 (48), 17289–17292.

166. Loose, J. S. M.; Arntzen, M.; Bissaro, B.; Ludwig, R.; Eijsink, V. G. H.; Vaaje-Kolstad, G., Multipoint Precision Binding of Substrate Protects Lytic Polysaccharide Monooxygenases from Self-Destructive Off-Pathway Processes. *Biochemistry* **2018**, *57* (28), 4114–4124.

167. Lucarini, M.; Pedrielli, P.; Pedulli, G. F.; Cabiddu, S.; Fattuoni, C., Bond Dissociation Energies of O-H Bonds in Substituted Phenols from Equilibration Studies. *J. Org. Chem.* **1996**, *61* (26), 9259–9263.

168. Hedegård, E. D.; Ryde, U., Molecular Mechanism of Lytic Polysaccharide Monooxygenases. *Chem. Sci.* **2018**.

169. Whittaker, M. M.; Ekberg, C. A.; Peterson, J.; Sendova, M. S.; Day, E. P.; Whittaker, J. W., Spectroscopic and Magnetochemical Studies on the Active Site Copper Complex in Galactose Oxidase. *J. Mol. Catal. - B Enzym.* **2000**, *8* (1–3), 3–15.

170. McGlashen, M.; Eads, D., Resonance Raman Spectroscopy of Galactose Oxidase: A New Interpretation Based on Model Compound Free Radical Spectra. *J. Phys. Chem,* **1995,** 99, 4918-4922.

171. Yamaguchi, K.; Takahara, Y.; Fueno, T., Ab-Initio Molecular Orbital Studies of Structure and Reactivity of Transition Metal-oxo Compounds. In *Applied Quantum Chemistry*; Springer Netherlands: Dordrecht, 1986; pp 155–184.

172. Van Wüllen, C., Molecular Density Functional Calculations in the Regular Relativistic Approximation: Method, Application to Coinage Metal Diatomics, Hydrides, Fluorides and Chlorides, and Comparison with First-Order Relativistic Calculations. *J. Chem. Phys.* **1998**, *109* (2), 392–399.

173. DeBeer George, S.; Petrenko, T.; Neese, F., Prediction of Iron K-Edge Absorption Spectra Using Time-Dependent Density Functional Theory. *J. Phys. Chem. A* **2008**, *112* (50), 12936–12943.

174. Kittl, R.; Kracher, D.; Burgstaller, D.; Haltrich, D.; Ludwig, R., Production of Four *Neurospora Crassa* Lytic Polysaccharide Monooxygenases in *Pichia Pastoris* Monitored by a Fluorimetric Assay. *Biotechnol. Biofuels* **2012**, *5* (1), 79.

175. Bhattacharjee, S.; Deterding, L. J.; Jiang, J. J.; Bonini, M. G.; Tomer, K. B.; Ramirez, D. C.; Mason, R. P., Electron Transfer between a Tyrosyl Radical and a Cysteine Residue in Hemoproteins: Spin Trapping Analysis. *J. Am. Chem. Soc.* **2007**, *129* (44), 13493–13501.

176. Kathiresan, M.; English, A. M., LC-MS/MS Suggests That Hole Hopping in Cytochrome c Peroxidase Protects its Heme from Oxidative Modification by Excess H_2O_2. *Chem. Sci.* **2017**, *8* (2), 1152–1162.

177. Kau, L. shan; Spira-Solomon, D. J.; J. E.; Hodgson, K. O.; Solomon, E. I., X-Ray Absorption Edge Determination of the Oxidation State and Coordination Number of Copper: Application to the Type 3 Site in *Rhus Vernicifera* Laccase and its Reaction with Oxygen. *J. Am. Chem. Soc.* **1987**, *109* (21), 6433–6442.

178. Borfecchia, E.; Lomachenko, K. A.; Giordanino, F.; Falsig, H.; Beato, P.; Soldatov, A. V.; Bordiga, S.; Lamberti, C., Revisiting the Nature of Cu Sites in the Activated Cu-SSZ-13 Catalyst for SCR Reaction. *Chem. Sci.* **2015**, *6* (1), 548–563.

179. Shadle, S. E.; Hodgson, K. O.; Solomon, E. I.; Hedman, B.; Schugar, H. J., X-Ray Absorption Spectroscopic Studies of the Blue Copper Site: Metal and Ligand K-Edge Studies To Probe the Origin of the EPR Hyperfine Splitting in Plastocyanin. *J. Am. Chem. Soc.* **1993**, *115* (2), 767–776.

180. Walroth, R. C.; Miles, K. C.; Lukens, J. T.; MacMillan, S. N.; Stahl, S. S.; Lancaster, K. M., Electronic Structural Analysis of Copper(II)-TEMPO/ABNO Complexes Provides Evidence for Copper(I)-Oxoammonium Character. *J. Am. Chem. Soc.* **2017**, *139* (38), 13507–13517.

181. Lim, H.; Thomas, K. E.; Hedman, B.; Hodgson, K. O.; Ghosh, A.; Solomon, E. I., X-Ray Absorption Spectroscopy as a Probe of Ligand Noninnocence in Metallocorroles: The Case of Copper Corroles. *Inorg. Chem.* **2019**, *58* (10), 6722–6730.

182. Cappuccio, J. A.; Ayala, I.; Elliott, G. I.; Szundi, I.; Lewis, J.; Konopelski, J. P.; Barry, B. A.; Einarsdóttir, Ó., Modeling the Active Site of Cytochrome Oxidase: Synthesis and Characterization of a Cross-Linked Histidine-Phenol. *J. Am. Chem. Soc.* **2002**, *124* (8), 1750–1760.

183. Thomas, F., Ten Years of a Biomimetic Approach to the Copper(II) Radical Site of Galactose Oxidase. *Eur. J. Inorg. Chem.* **2007**, No. 17, 2379–2404.

184. Roemelt, M.; Beckwith, M. A.; Duboc, C.; Collomb, M. N.; Neese, F.; Debeer, S., Manganese K-Edge X-Ray Absorption Spectroscopy as a Probe of the Metal-Ligand Interactions in Coordination Compounds. *Inorg. Chem.* **2012**, *51* (1), 680–687.

185. Verma, P.; Weir, J.; Mirica, L.; Stack, T. D. P., Tale of a Twist: Magnetic and Optical Switching in Copper(II) Semiquinone Complexes. *Inorg. Chem.* **2011**, *50* (20), 9816–9825.

186. Müller, J.; Weyhermüller, T.; Bill, E.; Hildebrandt, P.; Ould-Moussa, L.; Glaser, T.; Wieghardt, K., Why does the Active Form of Galactose Oxidase Possess a Diamagnetic Ground State? *Angew. Chemie Int. Ed.* **1998**, *37* (5), 616–619.

187. Clark, K.; Penner-Hahn, J. E.; Whittaker, M. M.; Whittaker, J. W., Oxidation-State Assignments for Galactose Oxidase Complexes from X-Ray Absorption Spectroscopy. Evidence for Cu(II) in the Active Enzyme. *J. Am. Chem. Soc.* **1990**, *112* (17), 6433–6434.

188. Winkler, J. R.; Gray, H. B., Electron Flow through Biological Molecules: Does Hole Hopping Protect Proteins from Oxidative Damage? *Q. Rev. Biophys.* **2015**, *48* (4), 411–420.

189. Warren, J. J.; Winkler, J. R.; Gray, H. B., Redox Properties of Tyrosine and Related Molecules. *FEBS Lett.* **2012**, *586* (5), 596–602.

190. Teo, R. D.; Rousseau, B. J. G.; Smithwick, E. R.; Di Felice, R.; Beratan, D. N.; Migliore, A., Charge Transfer between [4Fe4S] Proteins and DNA Is Unidirectional: Implications for Biomolecular Signaling. *Chem* **2019**, *5* (1), 122–137.

191. Hopfield, J. J., Electron Transfer between Biological Molecules by Thermally Activated Tunneling. *Proc. Natl. Acad. Sci. U. S. A.* **1974**, *71* (9), 3640–3644.

192. Teo, R. D.; Wang, R.; Smithwick, E. R.; Migliore, A.; Therien, M. J.; Beratan, D. N., Mapping Hole Hopping Escape Routes in Proteins. *Proc. Natl. Acad. Sci.* **2019**, *116* (32), 15811–15816.

193. Harriman, A., Further Comments on the Redox Potentials of Tryptophan and Tyrosine. *J. Phys. Chem.* **1987**, *91* (24), 6102–6104.

194. Kuusk, S.; Kont, R.; Kuusk, P.; Heering, A.; Sørlie, M.; Bissaro, B.; Eijsink, V. G. H.; Väljamäe, P., Kinetic Insights into the Role of the Reductant in H_2O_2-Driven Degradation of Chitin by a Bacterial Lytic Polysaccharide Monooxygenase. *J. Biol. Chem.* **2019**, *294* (5), 1516–1528.

195. Jarle Horn, S.; Vaaje-Kolstad, G.; Westereng, B.; Eijsink, V. G., Novel Enzymes for the Degradation of Cellulose; *Biotechnology for Biofuels*, **2012**; Vol. 5 (1), 45.

196. Wang, D.; Li, J.; Salazar-Alvarez, G.; McKee, L. S.; Srivastava, V.; Sellberg, J. A.; Bulone, V.; Hsieh, Y. S. Y., Production of Functionalised Chitins Assisted by Fungal Lytic Polysaccharide Monooxygenase. *Green Chem.* **2018**, *20* (9), 2091–2100.

197. Wang, D.; Li, J.; Wong, A. C. Y.; Aachmann, F. L.; Hsieh, Y. S. Y., A Colorimetric Assay to Rapidly Determine the Activities of Lytic Polysaccharide Monooxygenases. *Biotechnol. Biofuels* **2018**, *11* (1), 215.

198. Paradisi, A.; Johnston, E. M.; Tovborg, M.; Nicoll, C. R.; Ciano, L.; Dowle, A.; McMaster, J.; Hancock, Y.; Davies, G. J.; Walton, P. H., Formation of a Copper(II)–Tyrosyl Complex at the Active Site of Lytic Polysaccharide Monooxygenases Following Oxidation by H_2O_2. *J. Am. Chem. Soc.* **2019**, *141* (46), 18585–18599.

199. Bissaro, B.; Streit, B.; Isaksen, I.; Eijsink, V. G. H.; Beckham, G. T.; DuBois, J. L.; Røhr, Å. K., Molecular Mechanism of the Chitinolytic Peroxygenase Reaction. *Proc. Natl. Acad. Sci.* **2020**, *117* (3), 1504–1513.

200. Mabbs, F. E., Some Aspects of the Electron Paramagnetic Resonance Spectroscopy of D-Transition Metal Compounds. *Chemical Society Reviews*. The Royal Society of Chemistry January 1, 1993, pp 313–324.

201. Westereng, B.; Loose, J. S. M.; Vaaje-Kolstad, G.; Aachmann, F. L.; Sørlie, M.; Eijsink, V. G. H., Analytical Tools for Characterizing Cellulose-Active Lytic Polysaccharide Monooxygenases (LPMOs). In *Cellulases: Methods and Protocols*; Lubeck, M., Ed.; Methods in Molecular Biology; Springer: Totowa, NJ, 2018; Vol. 1796, pp 219–246.

202. Bauer, S.; Vasu, P.; Persson, S.; Mort, A. J.; Somerville, C. R., Development and Application of a Suite of Polysaccharide-Degrading Enzymes for Analyzing Plant Cell Walls. *Proc. Natl. Acad. Sci. U. S. A.* **2006**, *103* (30), 11417–11422.

203. Ciano, L.; Paradisi, A.; Hemsworth, G. R.; Tovborg, M.; Davies, G. J.; Walton, P. H., Insights from Semi-Oriented EPR Spectroscopy Studies into the Interaction of Lytic Polysaccharide Monooxygenases with Cellulose. *Dalt. Trans.* **2020**, *49* (11), 3413–3422.

204. Singh, S. K.; Eng, J.; Atanasov, M.; Neese, F., Covalency and Chemical Bonding in Transition Metal Complexes: An Ab Initio Based Ligand Field Perspective. *Coord. Chem. Rev.* **2017**, *344*, 2–25.

205. Mabbs, F. E.; Collison, D., *Electron Paramagnetic Resonance of d Transition Metal Compounds*, 1st ed.; Elsevier, 1992; Vol. 16.

206. Yosca, T. H.; Rittle, J.; Krest, C. M.; Onderko, E. L.; Silakov, A.; Calixto, J. C.; Behan, R. K.; Green, M. T., Iron(IV)–Hydroxide pKa and the Role of Thiolate Ligation in C-H Bond Activation by Cytochrome P450. *Science (80-.).* **2013**, *342* (6160), 825–829.

207. Abragam, A.; Bleaney, B., *Electron Paramagnetic Resonance of Transition Ions,* Oxford University Press: Oxford, 1970.